Search for New Particles Decaying to a Top Quark Pair with the CMS Experiment

Von der Fakultät für Mathematik, Informatik und Naturwissenschaften der RWTH Aachen University zur Erlangung des akademischen Grades eines Doktors der Naturwissenschaften genehmigte Dissertation

vorgelegt von

Diplom-Physiker

Jan Steggemann

aus Neuss

Berichter: Universitätsprofessor Dr. Martin Erdmann

Universitätsprofessor Dr. Thomas Hebbeker

Tag der mündlichen Prüfung: 5. November 2012

Contents

1 Introduction

After a successful start of its operations at the end of 2009, the Large Hadron Collider (LHC) began to deliver proton-proton collisions at a centre-of-mass energy of 7 TeV in March 2010. All four major detectors, ATLAS, ALICE, CMS, and LHCb, recorded these collisions and have effectively operated since. In the 2010 proton-proton run, the LHC provided an amount of data corresponding to an integrated luminosity of close to 50 pb^{-1} to the CMS experiment. The dataset was increased by two orders of magnitude in 2011, with a delivered integrated luminosity of more than 6 fb^{-1}.

The top quark, the heaviest elementary particle known to date, was discovered at the Tevatron collider by the CDF and D0 collaborations in 1995. Both collaborations have measured the properties of the top quark, most importantly its mass, and the production cross section in proton-antiproton collisions at centre-of-mass energies of 1.8 TeV and 1.96 TeV. Measurements of the production and decay of top quarks in a new energy regime have also been performed by the ATLAS and CMS collaborations.

There are several indications why the top quark may guide the way to the discovery of new particles. The high top quark mass involves a high coupling to the Higgs boson, with a Yukawa coupling constant close to unity, and may hence play a special role in electroweak symmetry breaking. It is the only quark that decays before hadronisation and therefore offers the unique opportunity to study a bare quark. There is also strong motivation to study the top quark from the experimental side. The CDF and D0 collaborations measured a top quark charge asymmetry that is substantially larger than predicted by the Standard Model of particle physics [1,2]. At high invariant mass of the top-antitop quark system, an increased asymmetry is measured in the CDF analysis, which has been reported as evidence for a deviation from the Standard Model (SM).

This thesis reports on a search for resonant new particles decaying to a top quark and an antitop quark. The data analysis is carried out with 5 fb^{-1} of data taken with the CMS detector at the LHC in 2011. New particles decaying to a $\mathrm{t\bar{t}}$ pair are predicted by a number of models for physics beyond the Standard Model, e.g. by models with an additional strong interaction and by models involving extra space dimensions. Moreover, the production of such a new particle may also explain the top quark charge asymmetry measurement by the CDF collaboration.

The new particles are searched for in the final state of the $\mathrm{t\bar{t}}$ decay with either a muon or an electron, jets, amongst which are b quark jets, and missing transverse energy. To be able to identify the new particles, the invariant mass of the top-antitop quark system is reconstructed. A resonant new particle would then show up as a local excess or bump in addition to the invariant mass distribution from the SM background processes, most importantly SM $\mathrm{t\bar{t}}$ production.

Searches for new particles decaying to top-antitop quark pairs have been performed at the Tevatron and at the LHC. Using a dataset of 5.3 fb^{-1} of $p\bar{p}$ collisions at 1.96 TeV, the D0 collaboration sets a lower limit on a narrow-width leptophobic topcolour Z′ of $m_{\text{Z}'} > 835$ GeV [3]. The CDF collaboration provides the best limits on the mass of a narrow leptophobic topcolour Z′ to date, $m_{\text{Z}'} > 900$ GeV, with a slightly smaller dataset of 4.8 fb^{-1} [4]. In an analysis using 1.9 fb^{-1} of $p\bar{p}$ collision data, the CDF collaboration also sets limits on the coupling strength to quarks of a massive gluon with masses in the range 400 GeV $< m_{g'} < 800$ GeV [5]. At the LHC, the ATLAS collaboration excludes a narrow-width topcolour leptophobic Z′ with mass < 880 GeV and a Kaluza-Klein gluon with mass $m_{g'} < 1130$ GeV using a dataset of 2.05 fb^{-1} of pp collisions at 7 TeV [6].

The thesis is structured as follows. The first chapter introduces the role of the top quark in the Standard Model of particle physics, explains which models of new physics predict new particles decaying to top-antitop quarks, and describes the experimental signature. Then, the experimental setup will be discussed, focussing on the LHC accelerator and the CMS experiment, followed by a description of the reconstruction of physics objects that are relevant for the data analysis. The discussion of the main analysis begins with the selection of events. After that, the reconstruction of the invariant mass of the $\text{t}\bar{\text{t}}$ system is illustrated. In the subsequent chapter, it is described how events from background processes are treated, and the comparison of kinematic distributions in data and simulated events is discussed. This is followed by an account of the statistical treatment, including a detailed description of the relevant systematic uncertainties, leading to the results and the conclusions.

2 The Top Quark in the Standard Model and Beyond

This chapter first gives a brief recapitulation of the Standard Model of particle physics. The description starts with the particle content of the Standard Model and continues with an overview of the theoretical structure. Then, an introduction to top quark physics at hadron colliders is given, including a brief overview of proton-proton collision physics and a recapitulation of the properties of the top quark as well as the production mechanisms and decay modes. Finally, the limitations and open questions of the Standard Model are discussed, and extensions of the Standard Model are presented that predict new particles decaying to top-antitop-quark pairs.

2.1 Standard Model of particle physics

2.1.1 Particle content

The Standard Model of particle physics summarises our present knowledge of the constituents of matter and the interactions between them, which are both represented by particles. All constituents of matter are called fermions and are characterised by a spin of $1/2$, whereas the particles representing the interactions, the bosons, have integer spin of either 0 or 1. The matter particles can be subdivided into quarks and leptons, each coming in three generations. Of the quarks and charged leptons, only those of the first generation, electrons, u and d quarks, make up "ordinary" matter. The additional leptons, neutrinos, are massless in the original formulation of the Standard Model. The discovery of neutrino oscillations however means that neutrinos have non-zero mass. The Standard Model can be extended to accommodate the non-zero neutrino masses.

Table 2.1: Bosons (force-carrying particles and the Higgs boson) in the Standard Model.

Name	Symbol	Spin	El. Charge (e)	Interaction	Subject to
photon	γ	1	0	EM	-
W boson	W^-/W^+	1	-1/+1	weak	EM, weak
Z boson	Z	1	0	weak	weak
gluon	g	1	0	strong	strong (self)
Higgs boson	H	0	0	-	Higgs (self), weak

A summary of the bosons in the Standard Model is given in table 2.1. For each boson, the symbols that are used throughout this work are listed with its spin, electric charge, and the interaction that it mediates. In addition, the last column shows the interactions that the boson is subject to.

The massless photon with spin 1 mediates the electromagnetic interaction between charged particles. Electromagnetic interactions are described by the relativistic quantum field theory of *quantum electrodynamics* (QED). Precise predictions of e.g. scattering cross sections can be calculated within QED with the help of perturbation theory.

The W bosons, i.e. the W^- boson and its antiparticle, the W^+ boson (together in the following often denoted as the W boson), and the Z boson are the particles mediating the *weak interaction*. The W and Z bosons are massive spin-1 particles; the masses of $m_W = 80.399 \pm 0.023$ GeV[1] and $m_Z = 91.1876 \pm 0.0021$ GeV [7] imply that the weak force is of short range. Since the W boson carries electric charge, it is also subject to the electromagnetic interaction.

Gluons are the interaction particles of the strong interactions that are described by the theory of *quantum chromodynamics* (QCD). Gluons are colour octets, meaning that there are 8 linearly independent states with different colour charges, the charges of the strong interactions. As gluons carry colour charge, they are self-interacting, unlike e.g. photons that do not carry electric charge. This implies that neither quarks nor gluons are observed as free particles, which is referred to as colour confinement. Gluons only take part in strong interactions.

The remaining boson within the Standard Model is the yet unobserved Higgs boson[2], a spin-0 particle. The Higgs mechanism explains how the W and Z bosons acquire mass within electroweak theory, and it also gives rise to the masses of quarks and charged leptons via the Yukawa couplings.

In table 2.2, an overview of quarks and leptons in the Standard Model is given with their respective symbols that are used in the text. Also shown are their electric charge, the interactions they are affected by, and their generation. All fundamental fermions have spin $1/2$ and appear in three generations. The three charged leptons, the electron, the muon, and the tau lepton, have charge -1, whereas their antiparticles have charge $+1$; all are subject to the electromagnetic as well as the weak interactions. The three corresponding neutrinos carry no electric charge and are only affected by the weak interactions.

The six different types of quarks are subject to all interactions of the Standard Model. The up quark, the charm quark, and the top quark are up-type quarks and have charge $2/3$, whereas the down-type quarks, the down quark, the strange quark, and the bottom quark, have charge $-1/3$.

A summary of the measured fermion masses, which are not predicted by the Standard Model, is given in table 2.3. It is noteworthy that there is a large mass hierarchy between the different generations that is present for both quarks and charged leptons.

[1] As common in particle physics, natural units will be used throughout this work. The units are defined by setting $\hbar = c = 1$ and by setting the unit for energies to eV. Energies and masses are then measured in units of eV, whereas time and length are given in units of $\frac{1}{\mathrm{eV}}$.

[2] In a seminar at CERN on 4 July 2012, the ATLAS and CMS collaborations showed preliminary results of the search for the Higgs boson and announced the observation of a new boson in the mass region of 125–126 GeV that is consistent with the Higgs boson [8].

Table 2.2: Leptons and quarks in the Standard Model.

Name	Type	Symbol	El. Charge (e)	Interactions	Generation
electron	lepton	e	-1	EM, weak	1
muon	lepton	μ	-1	EM, weak	2
tau lepton	lepton	τ	-1	EM, weak	3
electron neutrino	lepton	ν_e	0	weak	1
muon neutrino	lepton	ν_μ	0	weak	2
tau neutrino	lepton	ν_τ	0	weak	3
up quark	quark	u	2/3	EM, weak, strong	1
down quark	quark	d	-1/3	EM, weak, strong	1
charm quark	quark	c	2/3	EM, weak, strong	2
strange quark	quark	s	-1/3	EM, weak, strong	2
top quark	quark	t	2/3	EM, weak, strong	3
bottom quark	quark	b	-1/3	EM, weak, strong	3

Table 2.3: Fermion masses [7].

	electron	**muon**	**tauon**
Mass (MeV)	0.511	105.658	1776.82±0.16
	electron neutrino	**muon neutrino**	**tau neutrino**
Mass	< 2 eV (95% CL)	< 0.19 MeV (90% CL)	< 18.2 MeV (95% CL)
	up quark	**charm quark**	**top quark**
Mass (GeV)	0.0017-0.0031 ($\overline{MS}$)	$1.29^{+0.05}_{-0.11}$ ($\overline{MS}$)	173.2±0.9 [9]
	down quark	**strange quark**	**bottom quark**
Mass (GeV)	0.0041-0.0057 ($\overline{MS}$)	0.080-0.130 ($\overline{MS}$)	$4.19^{+0.18}_{-0.06}$ ($\overline{MS}$)

The relative uncertainty of the electron (muon) mass is less than $1/10^6$ ($1/10^7$).
All quark masses are well defined only in the context of perturbation theory and, except for the top quark mass, are given in the modified minimal subtraction ($\overline{MS}$) renormalisation scheme.

2.1.2 Structure of the Standard Model

The general structure of the Standard Model is as follows. It has a global Poincare symmetry in accordance with special relativity. This implies that the theory is invariant with respect to the choice of the reference frame, and it imposes symmetries of translation and rotation. In addition, there is a local gauge symmetry with the groups U(1) x SU(2) x SU(3). The *gauge* is connected to degrees of freedom in the formulation of the theory. The term *local* means that the symmetry holds at every point in spacetime. While the SU(3) symmetry is responsible for the strong interactions, the U(1) x SU(2) is the symmetry group for the electromagnetic and weak interactions.

In the following two sections, quantum chromodynamics and the electroweak theory will be briefly introduced in the Lagrangian formalism, roughly following references [10–12]. In the Standard Model, particles are described by the following fields:

- Particles with spin 0 are represented by scalar fields $\Phi(x)$,
- particles with spin $1/2$ are represented by spinor fields $\Psi(x)$, and
- particles with spin 1 are represented by vector fields $A_\mu(x)$.

The dynamics of the physical system can be calculated from a given Lorentz-invariant Lagrangian $\mathcal{L}$. For a field ϕ, the action is given by

$$S[\phi] = \int \mathrm{d}^4x \; \mathcal{L}(\phi(x)), \tag{2.1}$$

from which the equations of motion for the field can be calculated following Hamilton's principle. The Lagrangians for free fields, $\mathcal{L} = \mathcal{L}_0$, are quadratic in the field variables and give rise to linear equations of motion. If one adds an interaction term $\mathcal{L}_{int}$,

$$\mathcal{L} = \mathcal{L}_0 + \mathcal{L}_{int}, \tag{2.2}$$

the field equations typically become non-linear and cannot be solved exactly. By treating the interaction as a small perturbation to the Lagrangian of the free field, one can calculate the probability amplitudes for physics processes with perturbation theory. The perturbative contributions are often visualised as Feynman diagram and are calculated with the help of an expansion in terms of leading order (LO) and higher order diagrams.

Since all Lagrangians in the Standard Model have to obey special relativity and are hence Lorentz-invariant, they are subject to the global symmetries of special relativity, i.e. translations in space-time, rotations in space, and changes of the inertial reference system. According to Noether's theorem, each symmetry is connected with a conserved quantity, in this case energy, momentum, and angular momentum.

Quantum Chromodynamics

Quantum Chromodynamics (QCD) is based on the symmetry group colour SU(3) and describes the strong interactions, i.e. the interactions between quarks and gluons. Quarks q_i, which come in three different colour states $i = 1, 2, 3$, transform under the fundamental representation of colour SU(3) symmetry, while antiquarks $\bar{q}_i$ transform under the adjoint representation. The quarks are represented by

$$\Psi = (q_1, q_2, q_3)^T \tag{2.3}$$

for the six different quark flavours $q = u, d, c, s, t, b$. Gluons are the quanta of the SU(3) gauge field; they can have 8 different colour states, $a = 1, .., 8$ and are written as G^a_μ. The structure constants of colour SU(3) are f^{abc} (with a, b, $c = 1, ..., 8$), and the generators of the colour group SU(3) are given by T_a. The field strength tensor of the strong interaction is given by

$$G^a_{\mu\nu} = \partial_\mu G^a_\nu - \partial_\nu G^a_\mu - g_s f^{abc} G^b_\mu G^c_\nu. \tag{2.4}$$

The strength of these interactions is determined by the strong coupling constant g_s. In analogy to quantum electrodynamics, it is common to define

$$\alpha_S = g_s^2/(4\pi) \tag{2.5}$$

as the fine-structure constant for the strong interactions.

By requiring invariance under local colour SU(3) gauge transformations, the QCD Lagrangian for one quark species can be constructed and is given by

$$\mathcal{L}_{QCD} = \bar{\Psi}(i\gamma^\mu\partial_\mu - m)\Psi + g_s G_\mu^a \bar{\Psi}\gamma^\mu T_a \Psi - \frac{1}{4} G_{\mu\nu}^A G_A^{\mu\nu}. \tag{2.6}$$

It is individually invariant under charge conjugation C, parity transformation P, and time reversal T. In addition, two gauge-fixing terms for the gluon fields need to be introduced that are omitted here.

The first term of the Lagrangian gives the quark propagator; note that a proper summation over the different quark species with their individual masses m_q, which appear as free parameters, needs to be performed. The interactions between quarks and gluons, which correspond to the quark-gluon vertex, are described by the second term. The third term gives three contributions, the gluon propagator and the two vertices for the gluon self-interaction, the triple-gluon vertex and the quartic-gluon vertex.

Perturbative calculations within QCD are possible at high momentum transfers Q^2 of the order of GeV^2. To calculate physical quantities in perturbation theory at some energy scale Q, which needs to be sufficiently high, the perturbation series requires *renormalisation* in order to remove ultraviolet divergences. Yet, renormalisation introduces a second mass scale μ_R (the point at which the subtractions to remove the ultraviolet divergences are performed), which is arbitrary, and hence physical quantities cannot depend on μ_G. From this follows that the coupling α_S is not constant, but depends on the chosen scales. For calculations, the standard approach is to set μ_G to some convenient value, e.g. the Z boson mass; one can then determine α_S at that scale and calculate α_S at any other large scale Q^2 using perturbation theory.

It is also often useful to define a QCD scale parameter Λ, indicating the scale at which α_S becomes strong. The dependence of α_S on Q^2 can then be written as

$$\alpha_S(Q^2) = \frac{1}{b\ln(Q^2/\Lambda^2)}\left(1 - \frac{b'}{b}\frac{\ln\ln(Q^2/\Lambda^2)}{\ln(Q^2/\Lambda^2)} + ...\right), \tag{2.7}$$

where the coefficients b and b' have to be determined from experiment, typically by measuring α_S and comparing leading order with next-to-leading order (NLO) calculations. The definition of the scale Λ follows from

$$\ln\frac{Q^2}{\Lambda^2} = \int_{\alpha_S(Q^2)}^{\infty} \frac{dx}{bx^2(1 + b'x + ...)}, \tag{2.8}$$

where Λ is the constant of integration. Depending on the exact definition, Λ has a magnitude of the order of 200 MeV.

The running of the coupling α_S in this way also illustrates asymptotic freedom, $\alpha_S \to 0$ for $Q^2 \to \infty$. Asymptotic freedom means that the interaction strength of QCD becomes smaller with increasing energy and implies that QCD interactions are weak at high energies or momentum transfers.

For sufficiently strong coupling, i.e. at lower energy scales, QCD entails the so-called *confinement of colour*. This means that the only possible states with finite energy are colour-free states, i.e. singlets of colour SU(3). The only hadrons that are invariant under SU(3) symmetry transformations are hence of the following types,

$$\bar{q}^i q_i, \;\; \epsilon^{ijk} q_i q_j q_k, \;\; \epsilon^{ijk} \bar{q}_i \bar{q}_j \bar{q}_k, \tag{2.9}$$

with the total invariant tensor ϵ^{ijk}. Under the assumption that physical hadrons are singlets under colour, this implies that mesons, baryons, and antibaryons are the only possible light hadrons (apart from exotic hadrons like tetraquarks or pentaquarks which have not been observed yet).

In high-energy physics experiments, quasi-free quarks or gluons are produced in the hard interaction. In the transition from high energy scales to lower energy scales, the coloured quarks and gluons form colour-singlet hadrons. This process is called *hadronisation*. As hadronisation cannot be calculated by perturbation theory, event generators make use of phenomenological models to describe this process [7]. In these models, the transition from the perturbative to the non-perturbative regime takes place at the so-called *hadronisation scale*.

Electroweak Theory and Electroweak Symmetry Breaking

The Standard Electroweak Model provides a unified description of the weak and electromagnetic interactions. The underlying symmetry group is a SU(2) x U(1) with the charges weak isospin I and weak hypercharge Y. The third component of the isospin I_3 is related to the electric charge Q by

$$Q = I_3 + \frac{Y}{2}. \tag{2.10}$$

The fermions are the fundamental representations of SU(2) x U(1). The different families of leptons and quarks are described by left-handed and right-handed fields since the representations of the gauge group are different for the different chirality states. The left-handed fields are written with an index L, have isospin $I = 1/2$, and are doublets,

$$\Psi_L^j = \begin{pmatrix} \Psi_{L+}^i \\ \Psi_{L-}^j \end{pmatrix}, \tag{2.11}$$

with $+$ denoting up-type fermions and $-$ down-type fermions.

In the general form, the right-handed fields are written as Ψ^j_{R+} and Ψ^j_{R-} (with an index R); they have isospin $I = 0$ and are singlets.

In the explicit form, the leptons are then represented by

$$\begin{pmatrix}\nu_e\\ e\end{pmatrix}_L, \begin{pmatrix}\nu_\mu\\ \mu\end{pmatrix}_L, \begin{pmatrix}\nu_\tau\\ \tau\end{pmatrix}_L, e_R, \mu_R, \tau_R, \tag{2.12}$$

with the neutrinos being purely left-handed, and the quarks are denoted by

$$\begin{pmatrix}u\\ d\end{pmatrix}_L, \begin{pmatrix}c\\ s\end{pmatrix}_L, \begin{pmatrix}t\\ b\end{pmatrix}_L, u_R, d_R, c_R, s_R, t_R, b_R. \tag{2.13}$$

The Lagrangian for the electroweak theory needs to be invariant under SU(2) x U(1) gauge transformations. For the W and Z bosons to acquire mass, the electroweak symmetry must be broken to the electromagnetic gauge symmetry U$(1)_{EM}$. In the Standard Model, this is achieved by the *Higgs mechanism*.

In the following, the different parts of the electroweak Lagrangian

$$\mathcal{L}_{EW} = \mathcal{L}_G + \mathcal{L}_F + \mathcal{L}_H + \mathcal{L}_Y \tag{2.14}$$

will be explained, the gauge, the fermion, the Higgs, and the Yukawa part.

The Lagrangian for the gauge fields can be written as

$$\mathcal{L}_G = -\frac{1}{4}W^{i\mu\nu}W_{i\mu\nu} - \frac{1}{4}B^{\mu\nu}B_{\mu\nu}, \tag{2.15}$$

with the field strength tensors associated with the bosons introduced above,

$$W^i_{\mu\nu} = \partial_\mu W^i_\nu - \partial_\nu W^i_\mu - g_2\epsilon^{ijk}W^j_\mu W^k_\nu \text{ and} \tag{2.16}$$

$$B_{\mu\nu} = \partial_\mu B_\nu - \partial_\nu B_\mu. \tag{2.17}$$

where g_2 is the SU(2) gauge coupling.

The U(1) group has a different gauge coupling g_1. There are no explicit mass terms for the gauge bosons in the gauge field Lagrangian as they would violate scale invariance; the masses are introduced in the spontaneous symmetry breaking discussed below.

To write the coupling of the gauge fields to fermionic matter fields, the covariant derivative for both left- and right-handed fields is introduced,

$$D^{L,R}_\mu = \partial^\mu - ig_2 I^{L,R}_a W^a_\mu + ig_1\frac{Y}{2}B_\mu, \tag{2.18}$$

where I_a are the SU(2) isospin operators $I_a^L = \frac{1}{2}\sigma_a$ and $I_a^R = 0$, and Y is the Abelian hypercharge from the U(1) group. The Lagrangian describing the interactions of fermions and gauge fields is then given by

$$\mathcal{L}_F = \sum_j \bar{\Psi}_L^j i\gamma^\mu D_\mu^L \Psi_L^j + \sum_{j,\sigma=+,-} \bar{\Psi}_{R\sigma}^j i\gamma^\mu D_\mu^R \Psi_{R\sigma}^j. \tag{2.19}$$

There are again no mass terms for the fermion fields as they would break gauge invariance. The masses are introduced below with the help of Yukawa interactions that are gauge invariant.

To arrive at the Lagrangian for the Higgs field, a single isospin doublet of scalar fields is introduced,

$$\Phi(x) = \begin{pmatrix} \Phi^+(x) \\ \Phi^0(x) \end{pmatrix}. \tag{2.20}$$

The covariant derivative, given by equation 2.18, becomes

$$D_\mu = \partial_\mu - ig_2 \frac{\sigma_a}{2} W_\mu^a + i\frac{g_1}{2} B_\mu \tag{2.21}$$

for $I = \frac{1}{2}$ and $Y = 1$, with which the Higgs Lagrangian can be written as

$$\mathcal{L}_H = D^\mu \Phi^\dagger D_\mu \Phi - V(\Phi^\dagger \Phi). \tag{2.22}$$

The first term in the Lagrangian gives rise to the masses of the W and Z bosons. By performing transformations of the fields W_μ^a and B_μ, one can define the physical fields for the W bosons,

$$W_\mu^\pm = \frac{1}{\sqrt{2}}(W_\mu^1 \mp iW_\mu^2), \tag{2.23}$$

and for the Z boson and the photon,

$$\begin{pmatrix} Z_\mu \\ A_\mu \end{pmatrix} = \begin{pmatrix} \cos\theta_W & \sin\theta_W \\ -\sin\theta_W & \cos\theta_W \end{pmatrix} \begin{pmatrix} W_\mu^3 \\ B_\mu \end{pmatrix}. \tag{2.24}$$

The mass terms now become diagonal and are given by

$$M_W = \frac{1}{2} g_2 v, \quad M_Z = \frac{1}{2}\sqrt{g_1^2 + g_2^2}\, v \tag{2.25}$$

for the W and Z bosons, and zero for photons - no new free parameters are introduced. The electroweak mixing angle θ_W is related to the electroweak coupling constants g_1 and g_2, and to the W and Z boson masses, by

$$cos\theta_W = \frac{g_2}{\sqrt{g_1^2 + g_2^2}} = \frac{M_W}{M_Z}. \tag{2.26}$$

The second term in the Higgs Lagrangian is the Higgs potential V,

$$V(\Phi) = \frac{\lambda}{4}(\Phi^\dagger\Phi)^2 - \mu^2\Phi^\dagger\Phi, \tag{2.27}$$

with constants λ and μ^2. It gives rise to the self-interactions of the Higgs field. The minimum of the Higgs potential defines the ground state, the vacuum. If both λ and μ^2 are positive, the minimum does not arise for $\Phi = 0$, but for all field configurations that satisfy $\Phi^\dagger\Phi = 2\mu^2/\lambda$. By choosing the one that is electrically neutral and real, one arrives at the vacuum expectation value

$$< \Phi >= \frac{1}{\sqrt{2}}\begin{pmatrix}0\\v\end{pmatrix}, \text{ with } v = \frac{2\mu}{\sqrt{\lambda}}. \tag{2.28}$$

The vacuum configuration is only symmetric under U(1)$_{em}$ transformations; the full symmetry has been broken spontaneously. When expanding the potential $V(\Phi)$ around the vacuum configuration, the Φ^+ component of equation 2.20 as well as the imaginary part of Φ_0, denoted as χ in the following, are massless. The real part of Φ_0 gives the field $H(x)$. Furthermore, Φ^+ and the imaginary part of Φ_0 are unphysical degrees of freedom. By choosing the unitary gauge where $\Phi^+ = \chi = 0$, one can write the Higgs doublet field as

$$\frac{1}{\sqrt{2}}\begin{pmatrix}0\\v + H(x)\end{pmatrix}. \tag{2.29}$$

The potential then becomes

$$V = \frac{M_H^2}{2}H^2 + \frac{M_H^2}{2v}H^3 + \frac{M_H^2}{8v^2}H^4 \tag{2.30}$$

when identifying $M_H = \mu\sqrt{2}$. This means that the real field $H(X)$ describes the Higgs Boson with mass M_H. In addition, the potential V gives rise to triple and quartic self-interactions that are proportional to M_H^2. The first term in the Higgs Lagrangian, see equation 2.22, induces the coupling of the Higgs boson to the gauge boson, the two trilinear vertices HWW and HZZ as well as the two quadrilinear vertices $HHWW$ and $HHZZ$.

Finally, to yield the masses of the fermions, Yukawa interactions between the Higgs and the fermion fields are introduced. Individual Yukawa couplings G_f are necessary for all massive fermions that relate the fermion mass with the Higgs vacuum expectation value,

$$m_f = G_f\frac{v}{\sqrt{2}}. \tag{2.31}$$

In the unitary gauge and for one generation of fermions, the Yukawa Lagrangian is given by

$$\mathcal{L}_Y = -\sum_f m_f\bar{\Psi}_f\Psi_f - \sum_f \frac{m_f}{v}\bar{\Psi}_f\Psi_f H. \tag{2.32}$$

Thereby, the fermions acquire mass, and an additional coupling between the Higgs field and the fermions is introduced that is proportional to the fermion mass. For three generations of fermions, the Lagrangian becomes more complicated as flavour mixing between the different quark and lepton generations needs to be taken into account. In the Standard Model, i.e. with massless neutrinos, there is no flavour mixing in the lepton sector. In the quark sector, the Yukawa couplings G_f are generalised to matrices for up- and down-type quarks, $G_u = (G^u_{ij})$ and $G_d = (G^u_{ij})$. One can now diagonalise the Yukawa couplings of the quarks using four unitary matrices $V^q_{L,R}$, with $q = u, d$. This does not change the structure of the interactions of the quarks with the Higgs boson and with the neutral gauge bosons, and of the Yukawa interaction in terms of the quark masses. It does however introduce flavour-changing quark interactions with the charged bosons. When the quark mass eigenstates are inserted in the Lagrangian describing the interactions of fermions with the gauge fields (equation 2.19), the unitary Cabibbo-Kobayashi-Maskawa (CKM) matrix is introduced by

$$V_{CKM} = V^u_L V^{d\dagger}_L = \begin{pmatrix} V_{ud} & V_{us} & V_{ub} \\ V_{cd} & V_{cs} & V_{cb} \\ V_{td} & V_{ts} & V_{tb} \end{pmatrix}. \tag{2.33}$$

It connects the down-type quarks d', s', b' and their mass eigenstates d, s, b by the relation

$$\begin{pmatrix} d' \\ s' \\ b' \end{pmatrix} = V_{CKM} \begin{pmatrix} d \\ s \\ b \end{pmatrix}. \tag{2.34}$$

Unitary requires that $V^\dagger V = 1$, from which follows that the matrix can be parametrised using three independent mixing angles and one phase, which is non-zero and responsible for CP violation in the standard model. The diagonal terms mediate the weak decay of quarks within a generation, while the off-diagonal terms of the CKM matrix allow for the transition of quark flavours between generations. The unitarity constraints also imply that the sum of the squares of the CKM matrix elements in each row and in each column is unity, meaning that the sum of the couplings for one up- or down-type quark is the same for all three generations.

Free Parameters

The Standard Model has 18 (or 19) free parameters in total that need to be determined by experiment, and seven additional ones if the non-zero neutrino masses are accommodated. The masses of the quarks and leptons give 9 free parameters (12 with neutrinos); they are summarised in table 2.3 that has been discussed above.

Four parameters are related to the CKM matrix. For non-zero neutrino masses, 4 equivalent parameters have to be added in the lepton sector. The current experimental values of the individual CKM matrix elements, including constraints from unitarity, are

$$V_{CKM} = \begin{pmatrix} 0.97428 & 0.0.2253 & 0.00347 \\ 0.2252 & 0.97345 & 0.0410 \\ 0.00862 & 0.0403 & 0.999152 \end{pmatrix}, \tag{2.35}$$

using a parametrisation introduced in reference [7]. The independent measurements of all 9 CKM matrix elements have shown that the CKM unitarity holds within current experimental and theoretical uncertainties.

There are two free parameters related to the strong interaction: the strong coupling constant $\alpha_s(M_Z^2) = 0.1184 \pm 0.0007$ [13], and the QCD vacuum angle Θ that would give rise to CP violation also in quantum chromodynamics, but which is very small ($\Theta < 10^{-9}$) as no CP violation has been observed in the strong interaction. In the electroweak sector, there are three free parameters that can be chosen as the fine structure constant $\alpha = 1/137.035999084(51)$, the Fermi constant $G_F = 1.166364(5) \cdot 10^{-5}$ GeV ^{2}, which is directly related to the weak coupling constant, and the Z boson mass of 91.1876 ± 0.0021 GeV. The last unknown parameter is the Higgs boson mass that is yet unknown. One can, however, exploit the fact that the experimental measurements overconstrain the list of parameters of the Standard Model and use the mass of the W boson, together with the mass of the top quark, to constrain the possible values for the Higgs boson mass, and combine this with information from direct searches for the Higgs boson [14].

2.2 The top quark at hadron colliders

2.2.1 Profile

The top quark is the heaviest elementary particle known to date with a mass of $m_{top} = 173.2 \pm 0.9$ GeV, measured at the Tevatron by the D0 and CDF collaborations [9]. It decays via the weak interaction to a W boson and a down-type quark. The relative fractions, given by the squares of the according CKM matrix elements, are $t \to Wb$ (99.8%), $t \to Ws$ (0.17%), and $t \to Wd$ (0.007%). Further decays are loop-suppressed and have not been observed yet. Unlike for the other quarks, the CKM-preferred top quark decay to a W boson and a b quark is kinematically allowed, leading to a large available phase space for the decay, i.e. a width of $\Lambda_{\text{top}} = 1.99^{+0.69}_{-0.55}$ GeV, corresponding to a lifetime of $\tau_{\text{top}} = 3.3^{+1.3}_{-0.9} \cdot 10^{-25}$ s [15]. Since the lifetime is smaller than the time scale of the strong interactions $\Lambda^{-1}_{\text{QCD}} \sim 10^{-23}$ s, the top quark decays before hadronisation as opposed to the other quarks. The top quark can hence be regarded as a quasi-free particle and imprints its spin information on the decay products.

Many details of top quark physics can be found in a number of comprehensive reviews, e.g. in references [16–19].

2.2.2 Proton-proton collision physics

Parton distribution functions and factorisation theorem

The LHC collides protons with protons, whereas the cross sections for physical amplitudes are calculated at parton level, i.e. for quarks and gluons in the initial state. Hence, the expected initial momenta and densities of the partons in the proton need to be known. The substructure

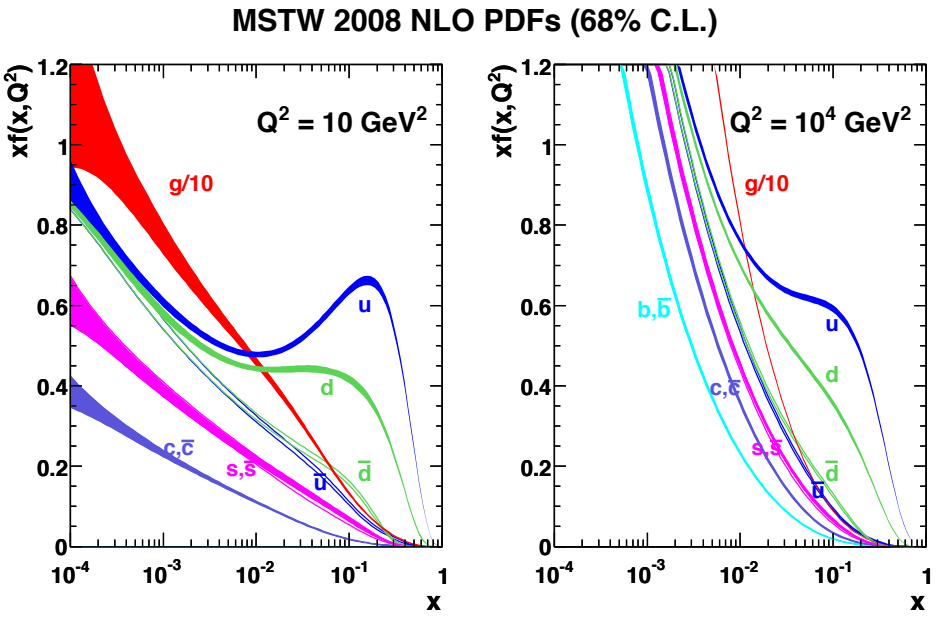

Figure 2.1: Distribution of x times the parton distribution functions, $x \cdot f(x, Q^2)$, for two values of the momentum transfer, $Q^2 = 10$ GeV^2 (left) and $Q^2 = 10^4$ GeV^2 (right), with the MSTW 2008 NLO PDF sets [20].

of hadrons has been investigated in deep inelastic lepton-hadron scattering experiments. In the experiment, the lepton has initial momentum k and final momentum k' after scattering. The scattering is mediated by a photon, a W boson, or a Z boson that transfers its four-momentum $q = k - k'$ to the hadron. Using the momentum transfer $Q^2 = -q^2$ and the fraction x of the hadron momentum that the interacting parton carries, one can directly measure the so-called structure function $F(x, Q^2)$ of a hadron. The structure functions are an incoherent sum over the quark and gluon distribution functions, the so-called *parton distribution functions* (PDFs), $f_i(x, Q^2)$ with $i = u, d, s, c, b, g$. They describe the probability that one finds a parton with momentum fraction x of the hadron momentum given a momentum transfer of Q^2. Figure 2.1 shows the distribution of the parton distribution functions for the gluon and the four light quarks and antiquarks as a function of x for two values of the momentum transfer Q^2. The distributions confirm the standard picture of the proton, which consists of three *valence* quarks (uud) with high probability to carry a significant fraction of the proton momentum, and a *sea* of gluons and quark-antiquark pairs $q\bar{q}$, for which the probability to carry a higher momentum fraction increases with the momentum transfer.

The total cross section for the production of a new particle X in pp collisions is given by the *factorisation theorem*,

$$\sigma(pp \to X) = \sum_{\text{partons } i,j} \int dx_1 dx_2 \; f_i(x_1, \mu_F^2) f_j(x_2, \mu_F^2) \; \sigma(ij \to X; x_1 x_2 s, \mu_F^2, \mu_R^2)), \quad (2.36)$$

with s being the squared centre-of-mass energy of the collision. The factorisation theorem separates the total cross section into two parts, the parton level cross section and the parton

distribution functions. At energies below the *factorisation scale* μ_F, the interactions between quarks and gluons are absorbed into the parton distribution functions; at higher energy scales, they are described by the parton level cross section $\sigma(ij \to X; x_1 x_2 s, \mu_F^2, \mu_R^2))$, which therefore depends on the choice of the factorisation scale μ_F.

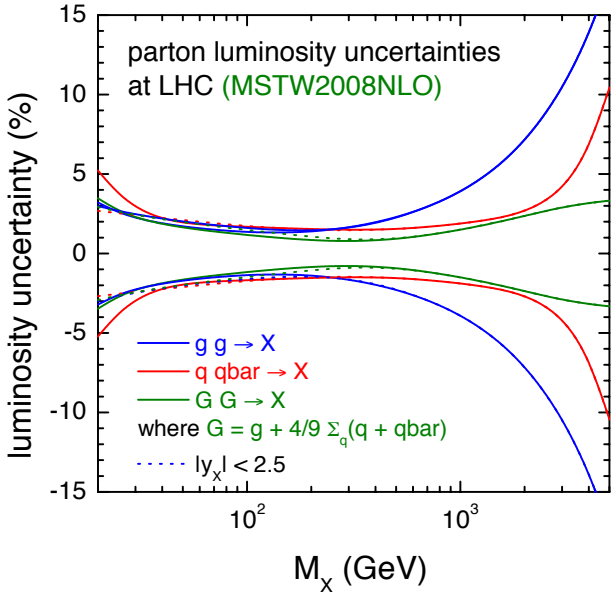

Figure 2.2: Uncertainty on parton luminosity at the LHC for gluon-gluon and quark-antiquark-initiated production of a particle X as function of the particle mass M_X with the MSTW 2008 NLO PDF sets [20].

The impact of the uncertainties due to parton distribution functions in the context of this analysis is studied with the help of the parton luminosity, which is proportional to the probability to yield an event with a given centre-of-mass energy in the parton-parton subsystem. Figure 2.2 shows the uncertainty on the parton luminosity for producing a new particle X as a function of the particle mass by gluon-gluon fusion, quark-antiquark annihilation, or a weighted combination of both. For quark-antiquark annihilation, the relative uncertainties are smaller than 2% for a particle mass between $2 \cdot m_{\mathrm{top}}$ and 1 TeV, and smaller than 3% for a particle mass up to 3 TeV. This implies that the production rates of new particles decaying to $\mathrm{t\bar{t}}$ that are produced by quark-antiquark annihilation are only subject to small uncertainties related to the parton distribution functions. For SM $\mathrm{t\bar{t}}$ production, of which a significant fraction is produced by gluon-gluon fusion as discussed below, the uncertainties are slightly higher due to the restricted knowledge of the gluon distribution function at higher x, especially for generated invariant masses of the top-antitop quark system in the TeV range, but the relative uncertainty is still smaller than 10% for $m_{\mathrm{t\bar{t}}} = 2$ TeV.

Parton shower approach and event generators

Perturbative calculations of QCD processes have two limitations. First, they can only be carried out to a given order in perturbation theory, depending on the complexity of the calculation. Second, the strong coupling constant α_S needs to be small for the perturbation series to converge.

To approximate the calculation of higher orders of α_S in the perturbation series, the splitting of a gluon or a light quark into two partons in the soft and collinear limit can be simulated with the *parton shower* approach. Given an ordering parameter, e.g. the p_{T} of the radiated gluon in the splitting $q \to qg$, the probability for such a splitting to occur can be calculated to all orders in α_S. This feature allows the straightforward inclusion of the parton shower approach in event generators based on the Monte Carlo (MC) method [21]. After each splitting that is performed on the basis of random sampling, the probability for the next splitting to occur can be calculated, and the procedure is repeated until an infrared cutoff scale is reached.

Perturbative cross section calculations and the parton shower approach can be combined in event generators by first producing the hard interaction according to a matrix element calculation and then using the parton shower approach to add additional splittings up to the infrared cutoff scale [21]. However, one needs to take into account that the showering approach and the matrix element calculations may have overlap, e.g. if hard, large-angle gluon radiation is produced in the parton shower. Therefore, matching methods are introduced that use cutoff scales to define whether an emission should be taken from the matrix element or the parton shower approach. Since the parton shower approach makes use of the soft and collinear limit, the transverse momentum of the emitted parton or the angle between two final state partons are typical cutoff variables. The cutoff scale will be referred to as *matching threshold* in the following, which is chosen to be in a regime where the parton shower is supposed to describe the emissions well.

The events are finally passed to the hadronisation step, which is carried out with the use of dedicated phenomenological models that are implemented in event generators [21]. In addition to the hard interaction, the event generators also need to take into account the coloured remnants of the two colliding protons, i.e. the *underlying event*. The additional partons are colour-connected to the hard interaction, which is generally also considered in the hadronisation process. Furthermore, more than one pair of partons may interact within the same proton-proton collision, leading to so-called *multiple parton-parton interactions*. Finally, *pile-up collisions* from additional proton-proton collisions may need to be simulated as well.

2.2.3 Top quark pair production at hadron colliders

In hadron collisions, top quark pairs are predominantly produced ($pp \to t\bar{t} + X$) by strong interaction processes. The production of the $\mathrm{t\bar{t}}$ pair is often accompanied by the production of additional jets, which will be implicitly assumed in the following when $\mathrm{t\bar{t}}$ appears in the final state. Top quark pairs can also be produced in association with a photon, a W or Z boson, a Higgs boson, or even an additional $\mathrm{t\bar{t}}$ pair. In the context of the search for new particles decaying to a $\mathrm{t\bar{t}}$ pair, the cross sections for these processes are negligible and will not be discussed in the following.

The two important subprocesses for $\mathrm{t\bar{t}}$ production are quark-antiquark annihilation, $q\bar{q} \to \mathrm{t\bar{t}}$, and gluon-gluon fusion, $gg \to \mathrm{t\bar{t}}$; the according Feynman diagrams are shown in figure 2.3. The production via quark-antiquark annihilation proceeds in the s channel, whereas the production via gluon-gluon fusion happens in the s, t, and u channels. At the LHC, which has a symmetric

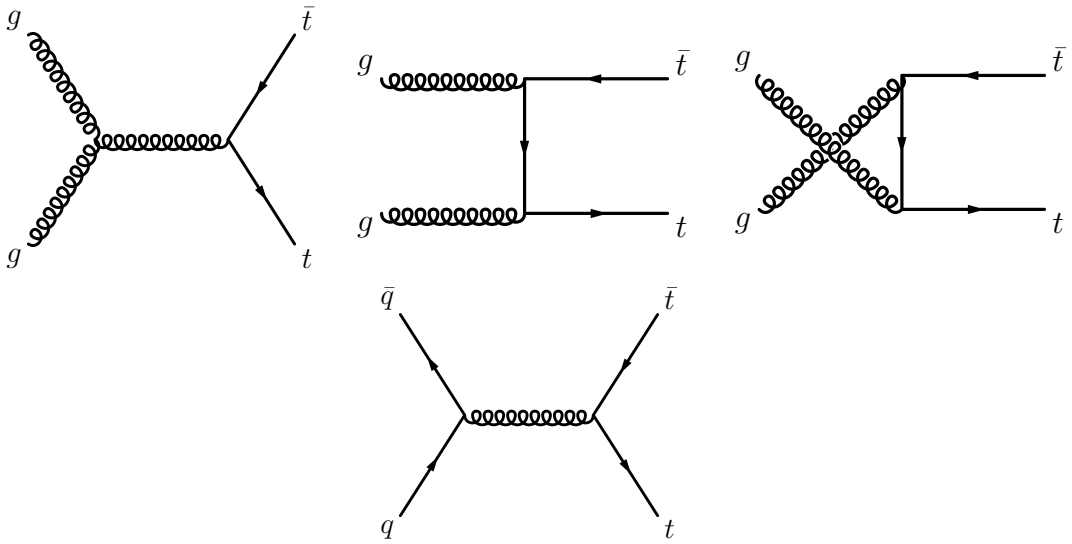

Figure 2.3: Feynman diagrams for top quark pair production in lowest order: $q\bar{q} \to t\bar{t}$ (bottom) and the three different $gg \to t\bar{t}$ channels (top).

initial state as it collides protons and protons, both production modes are also symmetric, as opposed to the Tevatron that collided protons and antiprotons. One should however note that in quark-antiquark annihilation in pp collisions, the quark in the initial state is typically a valence quark from one of the protons, whereas the anti-quark originates from the sea and therefore has smaller longitudinal momentum. This difference, which is not present in gluon-gluon fusion, can be used to test the Standard Model, e.g. to measure the top quark charge asymmetry, which would manifest as a difference in the rapidity distributions of top quarks and antitop quarks [22].

For the used setup of the LHC, i.e. pp collisions at a centre-of-mass energy of 7 TeV, the relative contributions to top quark pair production are

$$f(gg \to t\bar{t}) \sim 80\% \text{ and} \tag{2.37}$$
$$f(q\bar{q} \to t\bar{t}) \sim 20\%. \tag{2.38}$$

At present, the $\mathrm{t\bar{t}}$ production cross section at 7 TeV pp collisions is known from the theory side to full next-to-leading order accuracy. Parts of the next-to-next-to-leading order (NNLO) corrections have been calculated as well, with a summary given in reference [23] and a full calculation of the $q\bar{q} \to \mathrm{t\bar{t}}$ process at the Tevatron in reference [24]. Using a next-to-leading-log resummation technique, calculations of the approximate NNLO cross section for $\mathrm{t\bar{t}}$-plus-jets production have been obtained by a number of groups [25–28]. The results are as follows,

$$\sigma_{\mathrm{t\bar{t}}} = 158^{+18+15}_{-20-15}\ \mathrm{pb} \quad (\mathrm{NLO,\ MCFM}), \tag{2.39}$$
$$\sigma_{\mathrm{t\bar{t}}} = 156^{+8+8}_{-9-9}\ \mathrm{pb} \quad (\mathrm{Ahrens\ et\ al}), \tag{2.40}$$
$$\sigma_{\mathrm{t\bar{t}}} = 163^{+7+15}_{-8-15}\ \mathrm{pb} \quad (\mathrm{Beneke\ et\ al}), \tag{2.41}$$
$$\sigma_{\mathrm{t\bar{t}}} = 159^{+12+4}_{-14-4}\ \mathrm{pb} \quad (\mathrm{Cacciari\ et\ al}),\ \mathrm{and} \tag{2.42}$$
$$\sigma_{\mathrm{t\bar{t}}} = 163^{+7+9}_{-5-9}\ \mathrm{pb} \quad (\mathrm{Kidonakis\ et\ al}), \tag{2.43}$$

with the NLO results taken from reference [29]. The first uncertainty numbers denote the theory uncertainties (scale uncertainty, resummation, and related uncertainties), whereas the second numbers denote the uncertainties on the parton distribution functions and α_s. The calculations are carried out with slightly different values of the top quark mass, which ranges from $m_{\mathrm{top}} = 173.0$–173.3 GeV. The resulting differences in the cross section values are however well within the theory uncertainties.

An additional Standard Model process that yields two top quarks in the final state is the production of a Higgs boson with mass $m_H > 2 \cdot m_{\mathrm{top}}$. Due to the large Yukawa coupling of the top quark, the branching ratio of the Higgs boson decay to two top quarks is significant and has its maximum value of 20% at $m_H \sim 450$ GeV. One should however note that such high Higgs masses are indirectly excluded by electroweak precision measurements, and are also beginning to become excluded by direct searches for high mass Higgs bosons in the decay channels $H \to WW$ and $H \to ZZ$, with the excluded region ranging to $m_H = 600$ GeV at 95% confidence level [30].

2.2.4 Top quark pair decay channels

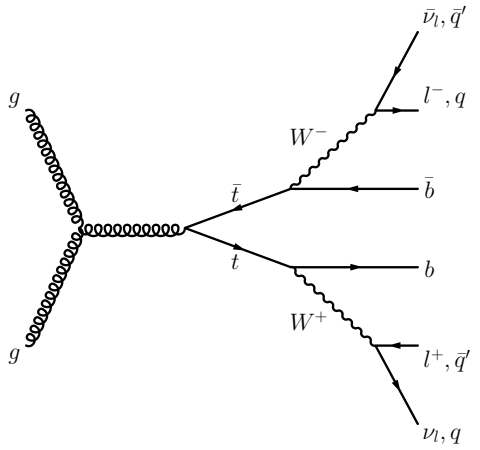

Figure 2.4: Generic decay chain of a $\mathrm{t\bar{t}}$ pair before hadronisation.

As the top quark always decays to a W boson and a down-type quark, in the following generically taken to be a b quark due to the dominant branching fraction, the signature of top quark pair production in the detector is governed by the decay channels of the two W bosons. Each W boson decays $10.80 \pm 0.09\%$ to a charged lepton and a neutrino, $W \to l\nu_l$, under the assumption of flavour universality [7]. The other $67.60 \pm 0.27\%$ of the decays are to pairs of quarks, either $W^+/W^- \to u\bar{d}/\bar{u}d$ or $W^+/W^- \to c\bar{s}/\bar{c}s$, with each of the two modes making up 50% of the hadronic decays. The quarks immediately hadronise and eventually form jets as which they are detected. The full decay chain without specification of the decays of the W bosons and before hadronisation is visualised in figure 2.4.

The decay chain is characterised according to the final state in the detector. The decay channels are

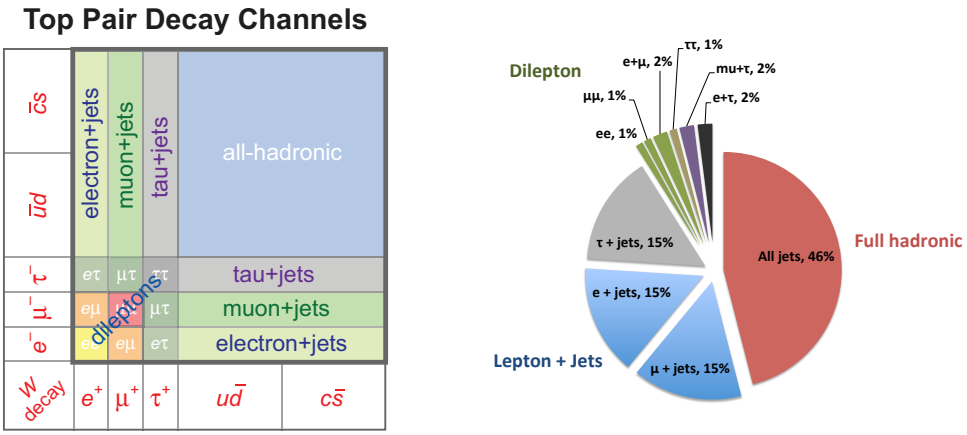

Figure 2.5: The different top quark pair decay channels resulting from the decay modes of the two W bosons in the $\mathrm{t\bar{t}}$ decay chain (left) [31] and resulting branching ratios for the different decay channels (right), with similar colours for final states that are usually considered within the same analysis.

- $t\bar{t} \rightarrow WWb\bar{b} \rightarrow 2l2\nu_l b\bar{b}$, dilepton or dileptonic channel with two leptons, two neutrinos, and two b quark jets in the final state;
- $t\bar{t} \rightarrow WWb\bar{b} \rightarrow l\nu_l 2qb\bar{b}$, lepton-plus-jets or semileptonic channel with one lepton, one neutrino, and four jets in the final state, of which two are b jets; and
- $t\bar{t} \rightarrow WWb\bar{b} \rightarrow 4qb\bar{b}$, all-jets or full hadronic channel, with 6 jets in the final state, of which two are b jets.

The label q denotes any light-flavoured quark (u, d, c, s), and the labels l and ν_l denote either of the three charged leptons and the according neutrino, respectively. As τ lepton decays lead to various final states that are generally harder to identify than electrons and muons, τ-plus-jets events are often not included in the semileptonic channel, and dileptonic channels with and without τ leptons are treated separately.

With the branching fractions of the decays of the two W bosons, the relative fractions of the different $\mathrm{t\bar{t}}$ decay channels can be calculated. The resulting fractions are shown in figure 2.5. The largest fraction of events of the top quark pair can be found in the full hadronic channel (46%). Each lepton-plus-jets channel contributes 14.6% of the total decays, summing up to 29.2% (43.8%) without (with) the τ-plus-jets channel. The dilepton channels make up 10.5% of the decays, with a fraction of 1.2% from each same-flavoured contribution ($\mu\mu$, ee, and $\tau\tau$) and 2.3% from each opposite-flavoured contribution ($e\mu$, $e\tau$, and $\mu\tau$).

In a hadron collision environment, events with charged leptons are a very clean signature with a comparably low rate of physical background processes; it is therefore easiest to detect $\mathrm{t\bar{t}}$ events in the dilepton channel, especially in the $e\mu$ channel. The dilepton channel does however have two disadvantages. First, the branching fraction is the smallest, making the channel less attractive for studies that are statistically limited like searches for rare phenomena. Second, the events contain two neutrinos of which only the sum of the transverse momentum components can be directly reconstructed, making a reconstruction of the full decay chain experimentally

challenging, which reduces the resolution of the reconstructed invariant mass of the $\mathrm{t\bar{t}}$ system. The full hadronic channel, on the other hand, has the highest branching fraction, but suffers from the huge background from multijet events produced via the strong interaction. Furthermore, the large number of possible permutations when associating jets to partons complicates the reconstruction of the full decay chain.

The lepton-plus-jets channel combines a high branching fraction with a clean signature, especially in the electron-plus-jets and muon-plus-jets channels that are considered in this analysis. The transverse momentum components of the one neutrino in the final state can be measured by means of the missing transverse energy in the reconstructed event. This allows the full reconstruction of the $\mathrm{t\bar{t}}$ decay chain, which is still subject to ambiguities due to the four jets in the decay and the reconstruction of the longitudinal component of the neutrino momentum. These ambiguities can be resolved with the help of the identification of b quark jets and the usage of information about the decay products.

Decays of B hadrons

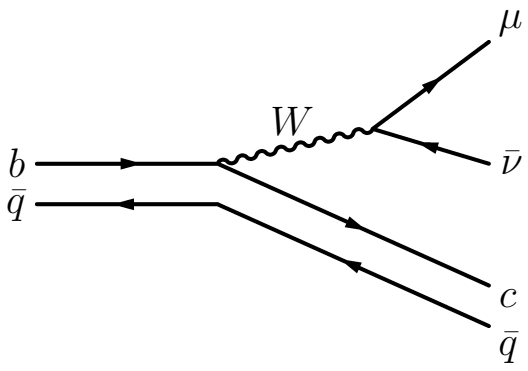

Figure 2.6: Exemplary Feynman diagram for the semileptonic decay of a B meson in the spectator model.

With two b quarks in the final state, b quark jets are of particular interest for analyses of $\mathrm{t\bar{t}}$ production. Due to the comparably long lifetime of the b quark, b quarks hadronise and form B hadrons. The median B hadron lifetime is of the order of $\tau_0 = 1.6 \cdot 10^{-12}$ s since b quarks only decay via the electroweak interactions [7]. As the b quark is lighter than its third-generation partner, the top quark, its decay amplitudes are given by off-diagonal CKM matrix elements and are hence suppressed.

In most B hadrons, the b quark is accompanied by light quarks (d, u, s), and the B hadron decays are well described by the decay of the b quark alone. The b quark predominantly decays via $b \to W^* c$, with the subsequent decay of the W boson to either a charged lepton and a neutrino or a $q\bar{q}'$ pair, which then hadronises. An example Feynman diagram for a semileptonic decay of a B meson in the so-called spectator model is shown in figure 2.6. In all cases, the c quark also hadronises and forms a charmed hadron or charmonium.

The comparably long lifetime of B hadrons means that it has a significant flight distance, which is given by $l_0 = c\frac{p}{m_B}\tau_0$. For a typical B hadron momentum of 100 GeV, this yields a flight distance of $l_0 \sim 1\ cm$. The trajectories of the decay products of the B hadron (or from the subsequent decay of a charmed hadron) hence originate at a displaced position from the primary interaction vertex. The reconstructed tracks of the charged decay products can be used to reconstruct a secondary decay vertex or to test how likely the track originates from the primary interaction vertex. This information is utilised to identify b quark jets.

2.2.5 Standard Model background processes relevant for top quark pair production

There are three categories of Standard Model processes that may enter in an event selection tailored for top quark pair production in the lepton-plus-jets channel:

- Events with a similar or the same final state, i.e. events with a charged lepton, a neutrino, and a number of jets (most importantly b jets).
- Events with a related final state where one object is missing or not identified as such, e.g. the production of a Z boson in association with jets where one of the two leptons from the Z boson is not reconstructed.
- Events that do not have the same final state, but are subject to misidentification, e.g. the production of multijet events with a secondary lepton from a B hadron decay that is wrongly identified as a prompt, isolated lepton.

The most important background processes belonging to the first category are the production of a W boson in association with jets and the production of single top quarks via the electroweak interactions. Further Standard Model processes with a similar final state, e.g. the production of two gauge bosons (WW, WZ, ZZ production), are typically not relevant as a background for top quark pair production due to their comparably low production cross sections; they are hence not discussed here.

Single top quarks are produced by three different mechanisms, s-channel, t-channel, and W-associated (or tW-channel) production. The according Feynman diagrams are shown in figure 2.7. Depending on the decay(s) of the final state W boson(s), all three production modes can lead to a final state with a charged lepton, a neutrino, at least one b quark jet, and at least one light-flavoured jet.

In leading order and considering b quarks in the proton (the so-called *5 flavour scheme*), single top quark production in the t channel has a b quark and a light up-type quark in the initial state. A spacelike W boson is exchanged, leading to a top quark and a down-type quark in the final state. Due to the up-type quark in the initial state, the production cross section for single top quark production is higher than for single antitop quark production in the t channel in pp collisions as u quarks are valence quarks in the proton. The calculated cross sections for top and antitop production in the t channel at approximate NNLO accuracy are given by

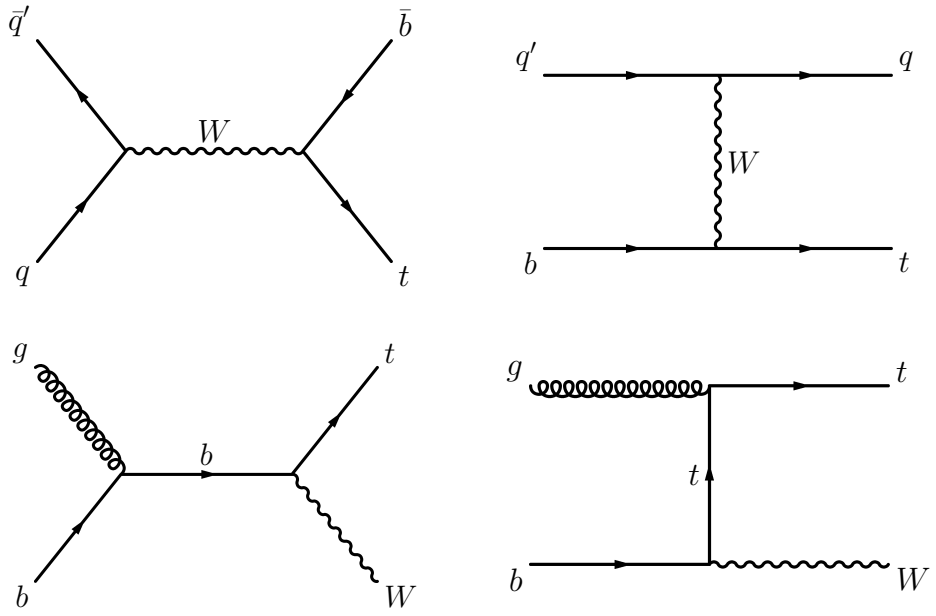

Figure 2.7: Leading order Feynman diagrams for the production of single top quarks in the s channel (top left), in the t channel (top right), and for the two production modes in association with a W boson (bottom).

$$\sigma_t^{\mathrm{t\ channel}} = 41.9^{+1.6+0.8}_{-0.2-0.8}\ \mathrm{pb} \quad \text{and} \tag{2.44}$$

$$\sigma_{\bar{t}}^{\mathrm{t\ channel}} = 22.7^{+0.5+0.7}_{-0.5-0.9}\ \mathrm{pb}, \tag{2.45}$$

with the first uncertainties denoting theory uncertainties and the second uncertainties denoting PDF uncertainties [32]. It turns out that the cross section for single top production is nearly twice as high as the cross section for antitop production, for the reasons given above.

The second most important production mode for single top quarks at the LHC is the tW channel. In both leading order diagrams, a gluon and a b quark in the initial state lead to a top quark and a W boson in the final state, $gb \to tW$. The first diagram proceeds via a b quark in the s channel, whereas the second diagram has a t channel exchange of a top quark. As the initial state neither contains u quarks nor d quarks, the cross sections for top and antitop production in the tW channel are the same, $\sigma^{\mathrm{tW\ channel}} = 15.7 \pm 0.4 \pm 1.1\ \mathrm{pb}$ at approximate NNLO accuracy, with the same conventions for the systematic uncertainties as before [33].

Single top production in the s channel is given by the process $q\bar{q}' \to W \to t\bar{b}$ with a timelike W boson. Like in the t channel, the production cross section for top quarks is higher than for antitop quarks as the two u valence quarks in the proton only appear in the diagram for top quark production. The cross section for s channel single top production is comparably small at the LHC and amounts to $\sigma^{\mathrm{s\ channel}} = 4.6 \pm 0.2\ \mathrm{pb}$ at approximate NNLO accuracy [34].

The production of a W boson in association with jets leads to a final state with a charged lepton, a neutrino, and a number of jets. Most important as background to $\mathrm{t\bar{t}}$ production are

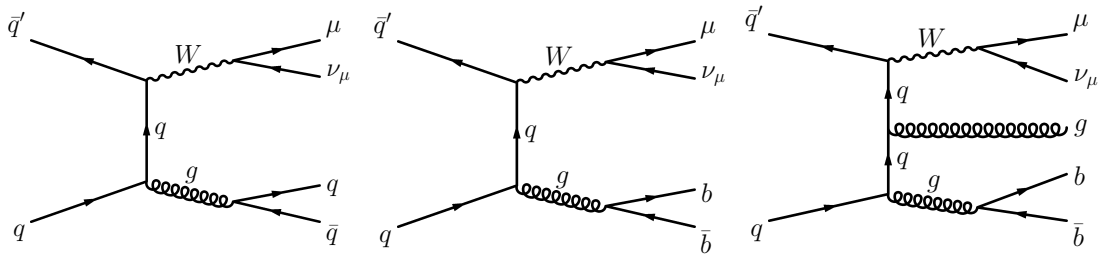

Figure 2.8: Exemplary Feynman diagrams for the production of a W boson in association with 2 jets (left), with two b jets (middle), and with 2 b jets and one additional jet (right).

events with at least 3 jets in the final state, especially if there are b quark or c quark jets among them. Figure 2.8 shows three Feynman diagrams as an example for the production of a W boson in association with either two light-flavoured jets, two b jets, or two b jets and one light-flavoured jet.

The inclusive cross section for W-plus-jets production is $\sigma_W = 31314 \pm 1558$ pb at NNLO accuracy [35]. However, the given uncertainty only reflects the uncertainty on the inclusive cross section and not the uncertainty on the production of a W boson with a higher number of jets that is relevant as a background process to $\mathrm{t\bar{t}}$ production. For a number of phase space cuts, most importantly a requirement of jet $p_\mathrm{T} > 25$ GeV, the W-plus-N-jet cross section is known at NLO accuracy for $N \leq 4$ [36]. Since the requirements on the phase space are different from the ones in this analysis, the calculated cross sections are not directly usable in this analysis, but they are recalculated by the used LO event generators. Nevertheless, the calculations show that the ratio $\sigma(W + (N+1)\text{-jets})/\sigma(W + (N)\text{-jets})$ is constant for $N \geq 2$, which is confirmed by a measurement of W-plus-jets production by the CMS experiment [37].

The production cross sections for W boson production in association with two heavy-flavoured jets have been calculated at NLO accuracy [38]. For $W + b\bar{b}$ production, the cross section is about a factor of two higher than the LO calculation. As the definition of b jets is dependent on the fiducial cuts for the jets, the results can however not directly be applied in this analysis. This implies that enhanced theoretical uncertainties need to be used, which are discussed below. Experimentally, the production cross section for W boson production in association with at least one b jet has been measured by the ATLAS collaboration [39]. The observed cross section exceeds the NLO prediction by about a factor of two, but is still compatible with the theory prediction within 1.5 standard deviations. On the other hand, the measurement of the production cross section of W boson production in association with a charm jet by the CMS collaboration yields a result that is fully consistent with NLO calculations [40].

A further background process that may lead to similar final states is the production of a Z boson in association with jets where the Z boson decays into two charged leptons. The inclusive production cross section for Z-plus-jets production is $\sigma_Z = 3048 \pm 132$ pb at NNLO accuracy, i.e. one order of magnitude smaller than for W-plus-jets production [35]. If the Z boson decays to two muons or electrons, events from Z boson production only appear as background if one of the leptons from the Z boson decay is not reconstructed, e.g. by being out of the detector acceptance, or not identified by the event selection criteria. In case the Z boson decays

to two τ leptons, one τ lepton may decay hadronically and the other one leptonically, with the hadronically decaying τ lepton reconstructed as a jet. The description of extra jet radiation is similar to the one for W boson production in association with jets, i.e. the ratios of the W- and Z-plus-N-jet cross sections only vary by a few per cent as a function of N for $N \geq 1$ [41].

The production cross section for multijet events is several orders of magnitude higher than for the other considered processes. However, they only contribute as background events to the analysis if either a charged lepton is produced inside a jet that passes the selection criteria for prompt leptons or if a jet is misidentified as a high quality lepton. Both cases are rare though still important due to the high initial cross section for multijet production; details on the estimation of these background processes are given below.

2.3 Extensions of the Standard Model

2.3.1 Limitations of the Standard Model

The Standard Model is a very successful and well-tested theory, and its predictions as well as the related calculational methods have been verified with high precision by a large number of experiments. There are, however, a number of limitations of the Standard Model that are listed in the following. On the one hand, these limitations give reason to find and to study theories that do not have these limitations; on the other hand, to search for phenomena that may indicate physics beyond the Standard Model (BSM physics).

Since the discovery of neutrino oscillations, it is known that the Standard Model in the form described above is not complete as it treats neutrinos as massless. There are two relatively straightforward ways to incorporate them into the Standard Model, and the presence of non-zero neutrino masses is hence no major drawback.

A more important shortcoming of the Standard Model is that it is no unified field theory of all known interactions. Most importantly, it does not include gravitation, and all attempts to derive a corresponding quantum field theory of gravitation have yet failed. At the Planck scale, $m_P = \sqrt{(\hbar c)/G} \sim 10^{19}$ GeV with Newton's constant G, gravitational effects are of similar strength as the forces in the Standard Model, and a quantum field theory including gravitation would be needed. Such a theory would have to address the hierarchy problem that stems from the Higgs mechanism in conjunction with the large difference between the electroweak scale and the Planck scale. In contrast to the other particles, the loop corrections to the Higgs boson mass are quadratically divergent. This means that the bare Higgs boson mass and the quantum corrections to it must nearly cancel to arrive at a Higgs boson mass of the order of 10^2 GeV that is needed for the electroweak theory. The procedure is also called *fine-tuning* and is not deemed *natural* as it involves a dimensionless parameter that is not of the order of unity. Another issue that is subject to fine-tuning in the Standard Model is the smallness of the QCD vacuum angle or the question why there is no CP violation in the strong interaction. This is also known as the *strong CP problem*.

Another feature of the Standard Model that may be unattractive from the theory point of view is its large number of free parameters. In addition, the masses of the fermions exhibit a

hierarchy; the top quark Yukawa coupling is of the order of one, whereas e.g. the up quark and electron Yukawa couplings are 5-6 orders of magnitude smaller. The hierarchy is even larger if one includes the non-zero neutrino masses. The Standard Model does not offer an explanation for the fermion mass hierarchy.

Finally, the Standard Model of cosmology predicts dark matter and dark energy. There is however no dark matter candidate in the Standard Model of particle physics. If one tries to reconcile the Standard Model with dark energy and interprets the vacuum energy, i.e. the cosmological constant, as dark energy, the resulting energy sum differs by about 100 orders of magnitudes from the measured value of the dark energy density. Hence, our current understanding of dark matter and of dark energy cannot be accommodated in the Standard Model.

2.3.2 General considerations

There are a number of extensions of the Standard Model that address some of the limitations discussed in the previous section. A prominent framework is characterised by an additional symmetry principle, *supersymmetry* (SUSY), which addresses the hierarchy problem by introducing superpartners to all particles by which the divergencies that arise in the calculation of the Higgs boson mass are cancelled. As the superpartners have not been observed in high-energy physics experiments, supersymmetry needs to be broken in all realistic SUSY models, for which a number of possible scenarios exist. An additional appealing feature is that, unlike in the Standard Model, the gauge couplings of the three Standard Model gauge symmetries unify at high energies in supersymmetric models [42]. If the so-called R parity is conserved, the superpartners may only be produced in pairs, thereby making the lightest superpartner a good dark matter candidate. This implies that most supersymmetric models, such as variants of the Minimal Supersymmetric Standard Model (MSSM), are not a natural candidate to produce single resonant particles that decay to top quark pairs (except for the supersymmetric Higgs bosons briefly discussed at the end of the following section). The same is true for models with similar symmetries, like T parity in certain little Higgs models.

In the following, various models are briefly introduced that predict new particles X that (preferentially) decay to top quark pairs, $X \to \mathrm{t\bar{t}}$, in the s channel.

2.3.3 Models for physics beyond the Standard Model predicting $\mathrm{t\bar{t}}$ resonances

In models with new strong dynamics, the elementary Higgs boson can be replaced by a fermion condensate that is coupled by a new strong interaction [43]. One simple model that introduces new strong dynamics is *Technicolour*. Technicolour adds a new interaction that is similar to QCD, but at a larger energy scale. New particles are introduced such as techniquarks, new vector mesons, and technipions. Depending on the couplings of the concrete Technicolour model, technipions can decay to top quark pairs, and this decay mode may be the dominant one.

Another instance of a model with new strong dynamics yet more relevant for top quark physics is *Topcolour*, in which the Higgs boson is a bound state composed of $\mathrm{t\bar{t}}$ [44]. Topcolour models predict neutral and charged top pions; there may also be topgluons that couple predominantly to third-generation quarks and hence decay to $\mathrm{t\bar{t}}$ and $b\bar{b}$ pairs. Certain models, like *Topcolour assisted Technicolour* that combines Topcolour with Technicolour [45], add a new U(1) gauge group that involves a new heavy Z' boson, which will again primarily decay to the third generation. Depending on the details of the model, the Z' boson may be visible as a narrow resonance decaying to $\mathrm{t\bar{t}}$ [46].

Little Higgs models try to explain the lightness of the Higgs boson by introducing new strong dynamics at a scale of $\sim$ 10 TeV that would make the Higgs boson a *Nambu-Goldstone* boson [47]. To make the loop contributions to the Higgs boson mass non-divergent, new particles at the TeV scale are introduced, typically gauge bosons and vector-like quarks (T quarks). The gauge bosons in these little Higgs models can show up as a vector resonance Z_H that may preferentially decay to fermions [48]. Such a resonance would be visible as an additional s channel contribution in top pair production; one should however note that the couplings to top quarks are not enhanced and the main discovery channel may rather be the decay to two charged leptons. The production of pairs of T quarks, which can decay via $T \to th$, $T \to tZ^0$, and $T \to bW^+$, gives rise to similar final states as top pair production, though it is no resonant contribution to the $m_{\mathrm{t\bar{t}}}$ spectrum.

By adding an extra dimension that is strongly warped, high energy scales on one particular slice (or brane) of this fifth dimension would rescale to a lower energy scale on another slice [49]. The wave functions of the Standard Model particles then need to describe how the particles are localised in the fifth dimension. By this principle, according *Randall-Sundrum* (RS) models can explain the hierarchy between the weak scale and the Planck scale. They predict heavy Kaluza-Klein (KK) partners of the Standard Model particles and/or a graviton that may be produced at LHC energies. Depending on the realisation of the RS model, KK gluons and/or KK gravitons may preferentially couple to top quarks and therefore decay to top quark pairs [50–52].

Models with at least two extra dimensions that are large compared to the weak scale also give a natural explanation for the weakness of gravity [53]. They may also give rise to gravitons that decay to top quark pairs; these gravitons are typically wider than the ones from warped extra dimensions. Even effects from string theory in a realisation with warped extra dimensions may be detectable in the form of string resonances decaying to top quark pairs [54].

Finally, one can consider a non-minimal Higgs sector, e.g. one with two Higgs doublets (2HDM) that appears in several extensions of the Standard Model [55,56]. In such a model, one of the neutral Higgs bosons may have reduced couplings to the gauge bosons and may hence primarily decay to top quark pairs.

2.3.4 Influence of new particles on $m_{\mathrm{t\bar{t}}}$ distribution

A phenomenological overview of different new particles that would appear as s-channel resonances in the $m_{\mathrm{t\bar{t}}}$ distribution is given in reference [57]. New particles with different spin (0,

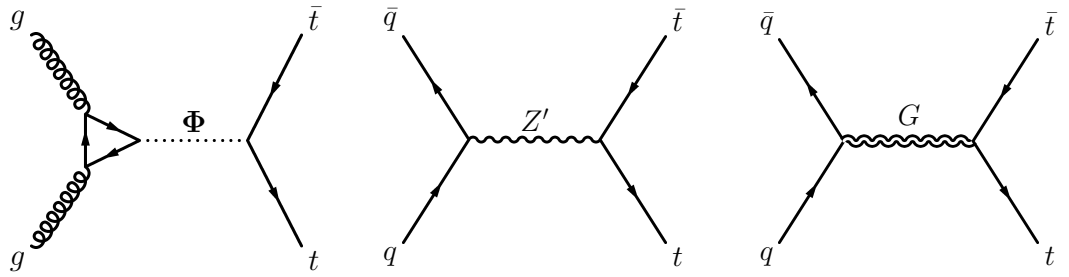

Figure 2.9: Selected BSM top quark pair production modes: Production of a neutral scalar $gg \to \Phi \to t\bar{t}$ via a fermion loop (left), of a heavy Z′ boson $q\bar{q} \to \mathrm{Z}' \to t\bar{t}$ (middle), and of a graviton $q\bar{q} \to G \to t\bar{t}$ (right).

1, 2), colour (colour singlet or colour octet), and parity (e.g. vector and axial vector couplings) are considered, and their effect on the $m_{\mathrm{t\bar{t}}}$ distribution as well as the interference with SM $\mathrm{t\bar{t}}$ production is calculated. Figure 2.9 shows Feynman diagrams for the production of three such resonances with different spin.

Besides the SM Higgs boson, spin 0 resonances that decay to $\mathrm{t\bar{t}}$ pairs appear e.g. in SUSY or 2HDM models. They generally have significant interference with SM $\mathrm{t\bar{t}}$ production, leading to a typical peak-dip structure in the $m_{\mathrm{t\bar{t}}}$ distribution for both the colour singlet and colour octet case. The exact structure of the peak-dip region depends on the width and on the colour structure of the particle, but is typically hard to resolve with the expected $m_{\mathrm{t\bar{t}}}$ resolution in experiments. Moreover, higher order corrections are expected to wash out the peak-dip structure [58]. Due to the loop in the production diagrams, the cross sections for spin 0 resonances are generally small, further complicating the discovery of a spin 0 resonance at the LHC.

A spin 1 resonance may either be a colour singlet or a colour octet and may also have vector and/or axial vector couplings. For a colour singlet particle, the interference with SM $\mathrm{t\bar{t}}$ production is negligible, and the resonance shows up as a peak in addition to the SM $m_{\mathrm{t\bar{t}}}$ distribution. The most prominent example of such a resonance is a topcolour Z′ [46]. The mass, width, and relative height of the peak for the topcolour Z′ as well as for the generic Z′ depend on the model. A specific leptophobic topcolour Z′ (also from reference [46]) serves as a benchmark model in this analysis. In this model, the branching ratio for the decay to $\mathrm{t\bar{t}}$ is 100%, yielding a high effective cross section. The cross sections have been updated for the 7 TeV LHC, including a correction of the calculation that yielded too high predicted cross sections in the previous analysis [59]. In this model, the cross section increases about linearly with the decay width. One should however note that there are similar models with lower branching ratio for the decay to $\mathrm{t\bar{t}}$ or with lower production cross sections.

For colour octet spin 1 resonances, interference with SM $\mathrm{t\bar{t}}$ production is still negligible for axial vector couplings, whereas a small level of interference is present in the case of vector couplings. There are a number of models for new physics that predict such spin 1 resonances. KK gluons appear in RS models and may preferentially decay to $\mathrm{t\bar{t}}$ pairs, depending on the RS model parameters. Detailed predictions are available for a number of models, of which one is taken as a reference model in this analysis [50]. The width and branching ratio for the decay to $\mathrm{t\bar{t}}$ pairs depends on the mass and RS model parameters. For the considered reference model

and a similar model implementation from reference [60], the KK gluon width is of the order of 20% of its mass and the branching ratio for the decay to $\mathrm{t\bar{t}}$ is $\sim 90\%$, making the search in the $m_{\mathrm{t\bar{t}}}$ spectrum the most prominent prospect for discovery.

Colour octet spin 1 particles with axial vector couplings can explain the top quark charge asymmetry measurements from the Tevatron; at the same time, such models are compatible with other measurements to date, e.g. searches for dijet resonances or the measurement of the top quark charge asymmetry at the LHC [61–63]. The considered masses for such axigluons are in the region above 1 TeV [64] as well as in the broader range from 700 GeV to 2.5 TeV. For higher masses, the axigluon models are disfavoured by searches for dijet resonances [65]. To explain the top quark charge asymmetry measurements at the Tevatron but to be compatible with constraints from other measurements, the gluons need to have enhanced couplings to top quarks and a significant production cross section relative to the SM $m_{\mathrm{t\bar{t}}}$ distribution, especially in the high $m_{\mathrm{t\bar{t}}}$ region. However, for light gluons in the mass range from 700 GeV to 1 TeV, the required cross sections may be as low as 1 pb [66].

The effect of spin 2 resonances, i.e. gravitons, on the $m_{\mathrm{t\bar{t}}}$ distribution depends on the model. In ADD models, the graviton can be highly degenerate in mass, with the sum of all KK states contributing to the $m_{\mathrm{t\bar{t}}}$ spectrum. The sum would be visible as an enhancement of the tail of the $m_{\mathrm{t\bar{t}}}$ distribution instead of resonant peaks. The ADD model could hence also lead to a measurable increase of the inclusive $\mathrm{t\bar{t}}$ cross section. The size of the additional contribution depends on the mass cutoff scale in the ADD model. In RS models, KK graviton modes appear that lead to a series of resonances in the $m_{\mathrm{t\bar{t}}}$ distribution [52,67]. With the mass of the first resonance given, the masses of the other resonances are fixed. The discovery of such a series of resonances would therefore distinguish between a RS model and other models with extra dimensions. The parameters of the RS model also affect the width and the height of the additional contributions to the $m_{\mathrm{t\bar{t}}}$ spectrum as well as the branching ratio for the decay to $\mathrm{t\bar{t}}$, which may be the dominant and hence the most important decay mode.

Finally, there are also models predicting non-resonant new physics that would affect the $m_{\mathrm{t\bar{t}}}$ distribution. However, since the contributions are non-resonant in the $m_{\mathrm{t\bar{t}}}$ distribution, they are not directly searched for in this analysis, and other observables like the top quark charge asymmetry or top quark spin correlations may be more sensitive for discovery, depending on the model. Such models may still show up in this analysis as deviations from the SM $m_{\mathrm{t\bar{t}}}$ distribution. A phenomenological analysis using an effective field theory approach is given in reference [68].

The analysis of the $m_{\mathrm{t\bar{t}}}$ distribution in reference [57] also includes an analysis of the theory uncertainties related to the $m_{\mathrm{t\bar{t}}}$ distribution. It is shown that the effects of scale and parton distribution function uncertainties on the shape of the $m_{\mathrm{t\bar{t}}}$ distribution are relatively small. The differences between NLO and LO calculations are however significant, especially in the high mass tail of the $m_{\mathrm{t\bar{t}}}$ distribution where the NLO distribution yields a higher event rate.

3 Experimental Setup

In this chapter, the experimental foundations of this work are described. The LHC is designed to provide proton-proton collisions at a centre-of-mass energy of 14 TeV and is operating at 8 TeV in 2012. In 2010 and 2011, it provided collisions at a centre-of-mass energy of 7 TeV. In addition to proton-proton collisions, the LHC can also provide collisions of lead ions.

As one of the two multipurpose detectors at the LHC, the CMS detector is designed to be able to provide detection of collision events for a number of purposes: the search for the Higgs boson in all relevant decay channels; searches for many different types of new particles, e.g. gravitons decaying to different types of particles that are present in theories with extra dimensions, undetectable particles in supersymmetric theories, new massive gauge bosons decaying to charged leptons; and various measurements in the context of Standard Model physics. Therefore, the CMS detector is laid out to provide precise measurements of muons, electrons, photons, charged particle tracks, jets, and missing transverse energy, combined with a large geometrical acceptance and good particle identification.

The experimental setup also includes the various software packages that are deployed for different purposes, e.g. the reconstruction of collision events, the analysis of the collision data, and the statistical inference. The two major software frameworks, the CMS software (CMSSW) and the Visual Physics Analysis (VISPA) framework, are described in more detail.

3.1 The Large Hadron Collider

The LHC is installed in the underground tunnel that was created between 1984 and 1989 for the Large Electron-Positron Collider (LEP) machine [70]. The underground tunnel is located at the border between France and Switzerland; it is between 45 m and 170 m below the surface and has a circumference of 27 km. For the LHC, new underground and surface structures were created at point 1 for ATLAS and at point 5 for CMS. The LEP structures at point 2 (for ALICE) and at point 8 (for LHCb) are reused. The LHC also reuses parts of the LEP pre-accelerator chain. An overview of the LHC collider together with the location of the experiments and the injector chain is shown in figure 3.1.

The design goal of the LHC is to provide highly energetic proton-proton collisions at a peak instantaneous luminosity of $\mathcal{L} = 10^{34}$ cm^{2}s^{-1}. The instantaneous luminosity $\mathcal{L}$ connects the production cross section σ_{event} for a certain type of event with the number of produced events N_{event},

$$\frac{dN_{\text{event}}}{dt} = \mathcal{L}\sigma_{\text{event}}. \tag{3.1}$$

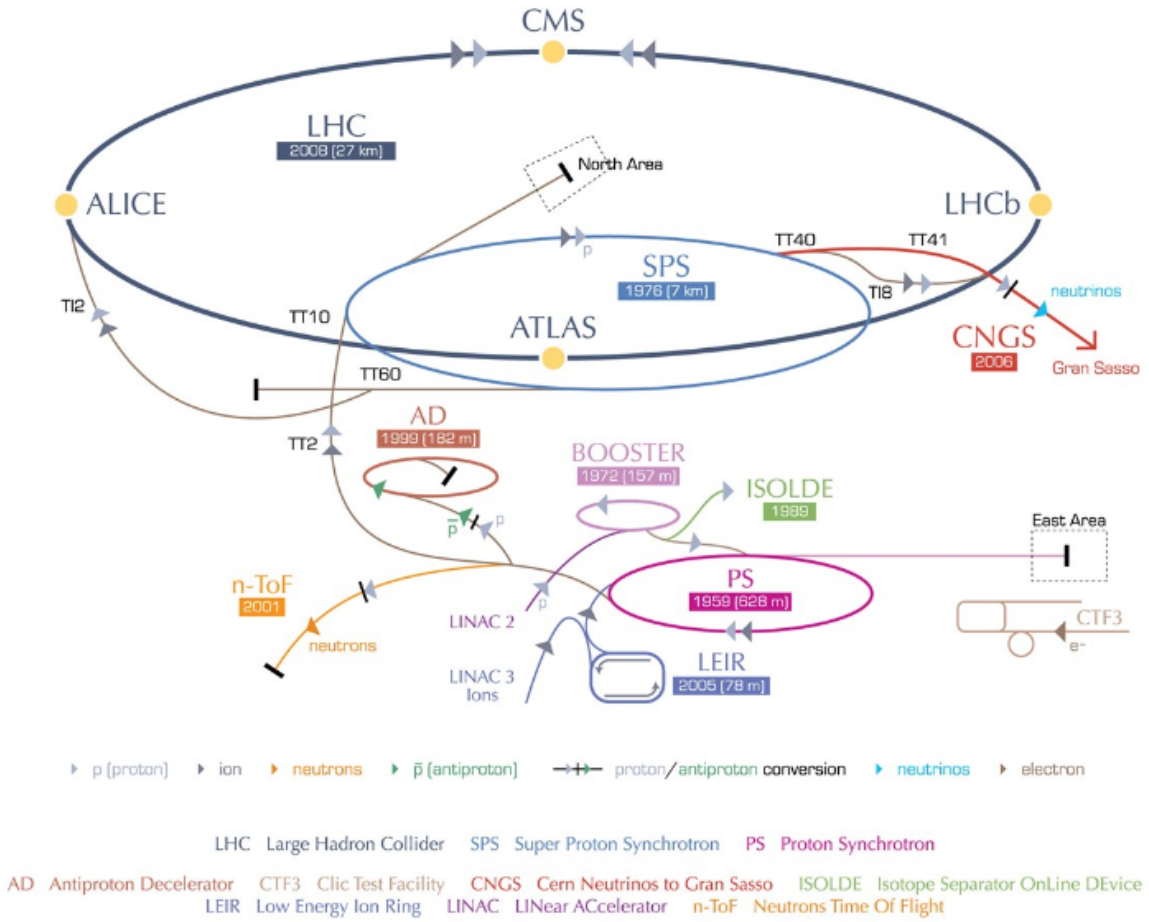

Figure 3.1: Overview of the LHC collider ring, the pre-accelerators and the LHC experiments [69].

Together with the production cross section, the amount of integrated luminosity $L = \int \mathcal{L} \mathrm{d}t$ yields the number of collisions events of a certain type that have been produced in total over time,

$$N_{\text{event}} = L\sigma_{\text{event}}. \tag{3.2}$$

In terms of collider quantities, the instantaneous luminosity can be expressed as

$$\mathcal{L} = \frac{N_b^2 n_b f_{\text{rev}} \gamma_r}{4\pi \varepsilon_n \beta^*} F, \tag{3.3}$$

with the number of particles per bunch N_b, the number of bunches per beam n_b, the revolution frequency f_{rev}, the relativistic gamma factor γ_r, the normalised transverse beam emittance ε_n, the beta function at the collision point β^*, and a geometric reduction factor F due to the non-zero crossing angle at the given interaction point.

A sufficient number of particles per bunch can only be achieved by colliding protons with protons, as opposed to the Tevatron, which collides protons with antiprotons. This implies that the LHC needs two rings to accelerate the protons in opposite directions. Due to the little space in the tunnel, a twin-bore magnet design is chosen in which the rings are magnetically coupled. To achieve the target centre-of-mass energy of 14 TeV, superconducting magnets made of NbTi Rutherford cables are deployed. The magnets have a maximum dipole field of 8.33 T to yield an energy of 7 TeV for the protons in each beam. To reach the field of more than 8 T, the magnets need to be cooled below 2 K with superfluid Helium. Magnets in previous accelerators operated at a maximum of ~ 5 T, only requiring a cooling temperature of ~ 4 K.

The goal of the injector chain (see figure 3.1) is to provide bunches of protons with an energy of 450 GeV and a low transverse beam emittance for injection into the LHC. The injector chain starts with the linear accelerator Linac2 that is fed by a hydrogen source. The Linac2 accelerates the protons to an energy of 50 MeV. Then three synchrotrons with increasing circumference are used. The Proton Synchrotron Booster increases the proton energy to 1.4 GeV; the Proton Synchrotron (PS) further raises the proton energy to 25 GeV; and the Super Proton Synchrotron (SPS) accelerates the protons to 450 GeV. The synchrotrons are also able to accelerate ions and to inject them into the LHC for lead ion operations. The proton bunches are then filled into the LHC ring, in which the energy is ramped up to 7 TeV (3.5 TeV for 2011 operations).

At design operations, the bunches are injected with a spacing of 25 ns, with each of the two proton beams consisting of 2 808 bunches at a centre-of-mass energy of 14 TeV. The operation of the collider at the design energy poses high requirements on the temperature of the magnets to avoid quenches. Such a quench occurred in 2008, leading to a delay of the LHC physics programme, with first collisions with a centre-of-mass energy of up to 2.36 TeV in 2009 and at 7 TeV in 2010. To guarantee stable operations, the LHC was then operated at 7 TeV in 2010 and 2011. At the end of the 2011 run, a maximum of 1 380 bunches per beam circulated in the LHC with a bunch spacing of 50 ns. At the same time, the bunch current was raised to over $1.4 \cdot 10^{11}$ protons per bunch, giving a peak instantaneous luminosity of $\mathcal{L} = 3.6 \cdot 10^{33}$ cm^{-2}s^{-1}.

The LHC provides collisions to four major detectors. The ATLAS and CMS detectors are multi-purpose detectors with the main focus on the analysis of proton-proton collisions. Both are delivered with the maximum possible amount of integrated luminosity to be able to find rare processes and to perform measurements with high precision. In 2010, the LHC provided an integrated luminosity of $L = 50$ pb^{-1} to both ATLAS and CMS. In 2011, the amount of integrated luminosity increased by more than two orders of magnitudes to $L = 6$ fb^{-1}. Both ATLAS and CMS also have dedicated heavy ion programmes.

The LHCb experiment focusses on physics processes containing B and D hadrons. Proton-proton collisions are delivered with a reduced instantaneous luminosity (more than 1 fb^{-1} in 2011) to the LHCb detector in order to avoid a too large number of multiple collisions. The ALICE experiment is exclusively designed for the analysis of heavy ion collisions.

3.2 The CMS detector

The CMS detector is 22 m long, has a diameter of 15 m, and weighs 14 000 tonnes. The name *Compact Muon Solenoid* hints at its relatively compact detector design, especially when com-

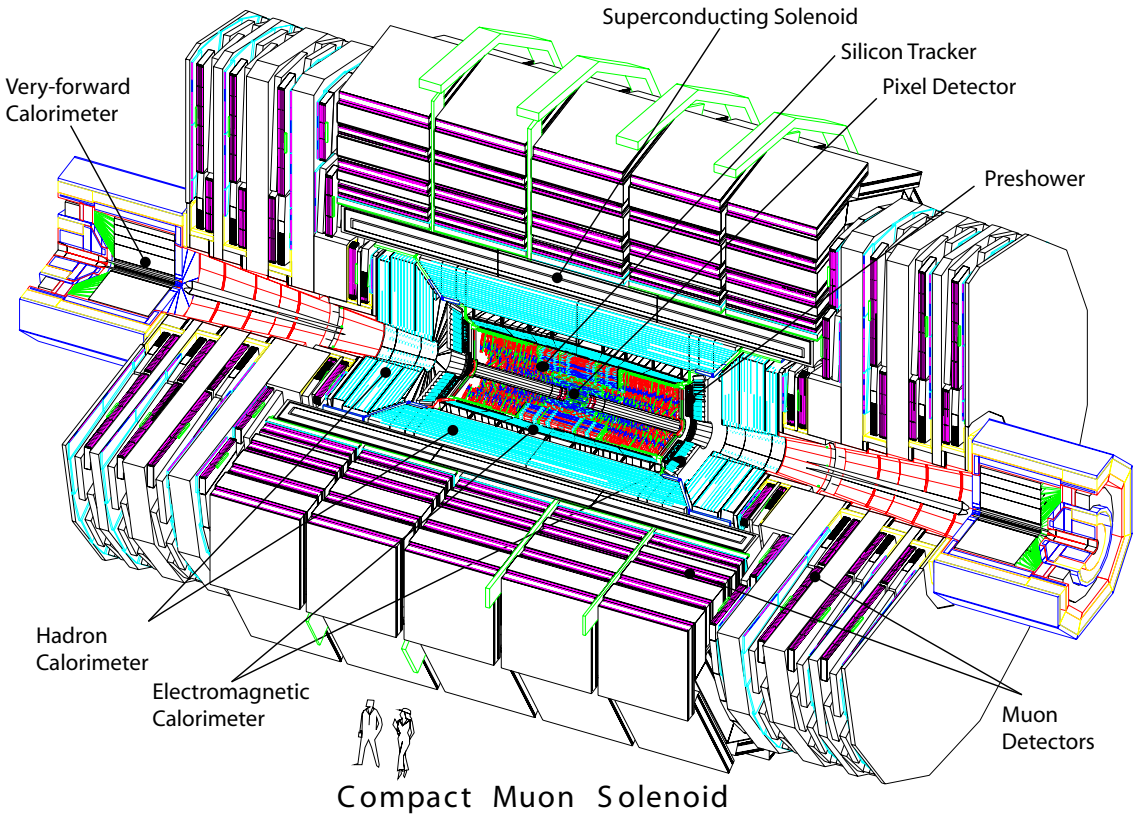

Figure 3.2: Overview of the CMS detector and its components [71].

pared to the ATLAS detector. A schematic view of the CMS detector is shown in figure 3.2 (a detailed description can be found in references [71] and [72]).

The compact design is reached by putting the solenoid magnet outside of the calorimeter systems. The CMS detector generally features barrel and endcap detectors, and in addition forward calorimetry systems. From the inside to the outside, there are silicon pixel and silicon strip tracking detectors, a lead-tungstate crystal electromagnetic calorimeter (ECAL), and a brass/scintillator hadron calorimeter (HCAL) within the magnetic field volume. The gas-ionisation muon detectors as well as an additional scintillator layer, the hadron outer (HO) that complements the HCAL, are located outside of the field volume.

The superconducting solenoid consists of an aluminium-stabilised niobium-titanium conductor, providing a magnetic field of up to 4 T (3.8 T in standard operations) at a stored energy of 2.7 GJ. It has a diameter of 6 m and is 13 m long. Outside of the cylindrical volume spanned by the solenoid, the magnetic field is returned by steel yokes that are interleaved with the muon systems. The steel yokes are arranged in five barrel wheels and three endcap disks at each end of the detector. From measurements with cosmic rays, the magnetic field strength is known to an accuracy of better than 0.1% in the tracker volume, to 3% in the central barrel wheels, and to 8% in the outermost barrel wheels [73].

The CMS coordinate system is defined as follows. The origin is the nominal collision point in the centre of the CMS detector. The x axis points radially towards the centre of the LHC ring;

the y axis points vertically upward; and, hence, the z axis goes along the direction of the beam that circulates anti-clockwise when looked at from above. There are two important angles, the azimuthal angle ϕ, measured in the x–y plane starting from the x axis, and the polar angle θ, measured starting from the z axis. As common in experimental particle physics, pseudorapidity is then given by $\eta = -\ln\tan(\theta/2)$.

The pseudorapidity is also used to distinguish the central, endcap, and forward regions of the CMS detector.

3.2.1 Tracking Detectors

The goal of the inner tracking detectors is to allow an efficient reconstruction of charged particle tracks with high purity and a precise determination of the track parameters. While a good determination of the curvature of the track leads to a precise measurement of the momentum and charge of the charged particles, it is also important to measure the spatial parameters with high accuracy to be able to differentiate tracks from primary interactions from long-lived particle tracks or tracks from non-primary collisions.

The inner tracking system consists of the following three subsystems:

- pixel detectors with size 100×150 μm^2 close to the interaction region,
- silicon microstrip detectors with strip size 10 cm$\times 150$ μm in the region 20 cm$< r <$ 55 cm,
- and silicon microstrip detectors with a larger size of 25 cm$\times 180$ μm for $r > 55$ cm.

The tracking systems consist of 66 million silicon pixels and 9.6 million silicon strips and provide coverage up to $|\eta| < 2.4$. At LHC design energy, the expected occupancy per pixel or per strip is of the order of 1% for the pixel detectors and 1-3% for the strip detectors, guaranteeing that high quality track reconstruction is possible with the given detector arrangement.

The layout of the pixel detectors is shown in figure 3.3. There are three barrel layers and 2 endcaps on either side. While the three barrel layers of hybrid pixel detectors are located at radii of 4.4 cm, 7.3 cm and 10.2 cm and have a length of 53 cm, the two end disks span a radius from 6 cm to 15 cm and are located at z distances of 34.5 cm and 46.6 cm from the centre of the detector. The total silicon area is approximately 1 m^2. The hybrid pixel design provides a spatial resolution of 20 μm for the z measurement and of 10 μm for the $r - \phi$ measurement.

The silicon strip detectors are divided into barrel and endcap detectors. In total, the silicon strip detector parts comprise 15 400 silicon strip modules that are mounted on a carbon-fibre structure and are operated at 20°C. The two barrel strip detectors are called TIB (Tracker Inner Barrel) and TOB (Tracker Outer Barrel); the two endcap detectors on either side of the detector are the TEC (Tracker End Cap) and the TID (Tracker Inner Discs). The total area of the silicon strip detectors amounts to ~ 200 m^2.

The inner part of the barrel detectors, the TIB, has 4 layers up to $|z| < 65$ cm. The outer part, the TOB, has 6 layers up to $|z| < 110$ cm. The first two layers of both the TIB and the TOB have

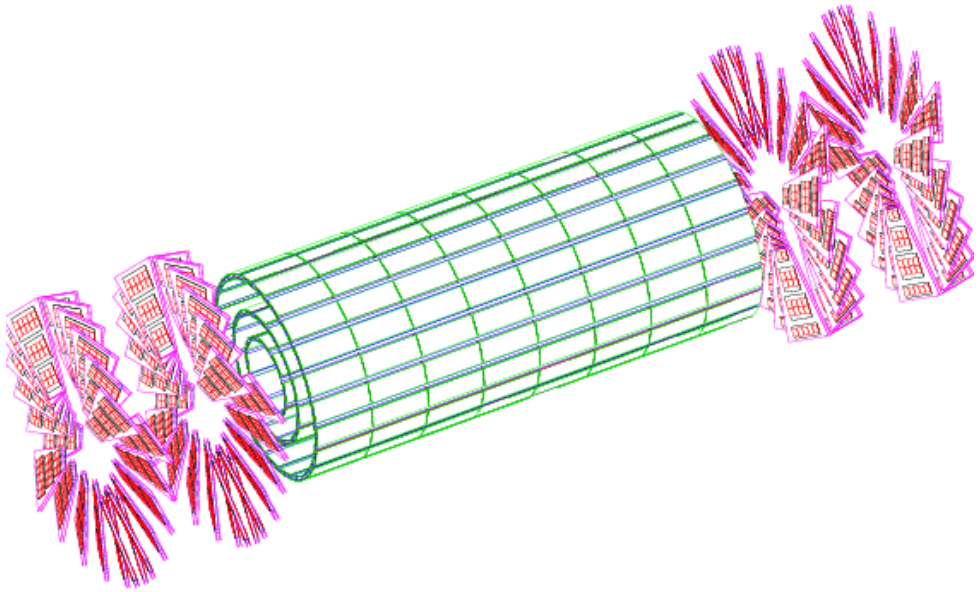

Figure 3.3: Three-dimensional view of the silicon pixel detectors [71].

so-called *stereo* modules with silicon strips mounted at an angle of 100 mrad. This arrangement provides measurements of both the r–ϕ and the r–z coordinates of individual tracker hits. The single point resolution is 23–34 μm in r–ϕ direction and $\sim$ 230 μm in r–z direction in the TIB, and 35–53 μm in r–ϕ direction and $\sim$ 530 μm in r–z direction in the TOB.

The two endcap strip detectors on each side of the detectors are made up of disks. In both the TEC and the TID, the modules are arranged in rings, with the strips pointing towards the beam line. Each TEC has 9 disks that range from $120\text{ cm} < |z| < 280\text{ cm}$, whereas each TID consists of 3 small disks between the two barrel strip detectors and the TEC. Similar to the barrel strip detectors, there are stereo modules in the first two TID and TEC rings as well as in the fifth TEC ring. The nominal single point resolution in r–ϕ direction varies from 28 to 53 μm depending on the strip pitch.

3.2.2 Electromagnetic Calorimeter

The electromagnetic calorimeter (ECAL) is designed to provide a precise energy measurement, most importantly for electrons and photons, together with a high granularity to support the identification of electrons and photons. The ECAL consists of a central barrel part and two endcaps that have additional preshower detectors, shown in figure 3.4. The central barrel part contains 61 200 scintillating crystals made of lead tungstate ($PbWO_4$), and each of the endcaps contains 7324 such crystals.

The crystals in the barrel have a front cross section of $\sim 22 \times 22$ mm^2 and have a length of 230 mm, corresponding to 25.8 radiation lengths. The endcap crystals have a slightly larger front cross section of 28.6×28.6 mm^2 and a slightly smaller length of 220 mm (24.7 radiation lengths). The small radiation length of lead tungstate crystals allows the ECAL to be compact. The relatively low light yield of the crystals however requires an amplified readout. Therefore,

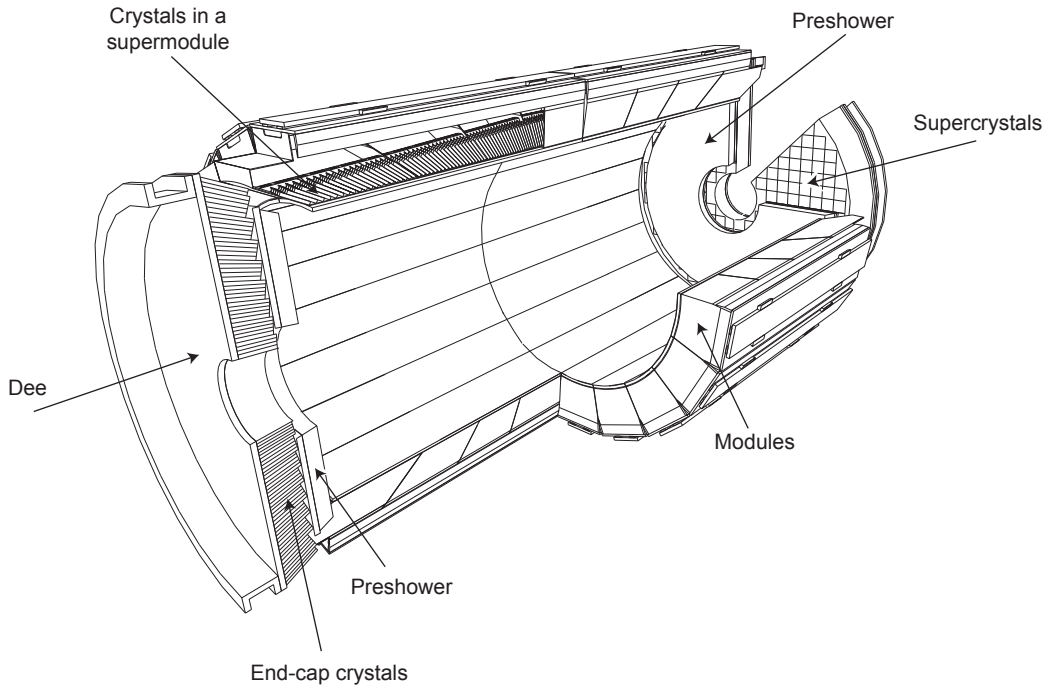

Figure 3.4: Layout of the electromagnetic calorimeter systems [74].

the scintillation light from the crystals is collected by avalanche photodiodes with an operating gain of 50 in the barrel part and by vacuum phototriodes with operating gains of 8-10 in the endcaps.

The ECAL barrel (EB) consists of 36 identical so-called *supermodules* with 1 700 crystals each that are placed at an inner radius of 129 cm. Each supermodule spans over a pseudorapidity range of $0 < |\eta| < 1.479$, i.e. half the length of the EB, and 20° in ϕ direction. In the barrel, each crystal covers 1° (0.0174 rad) in both η and ϕ direction.

The two ECAL preshower detectors (ES) in front of the ECAL endcaps consist of two planes of silicon strip detectors placed after two lead absorber plates with 2 and 3 radiation lengths, respectively. The preshower detectors cover the pseudorapidity range $1.653 < |\eta| < 2.6$ and support the separation of photons from pions.

Finally, the two ECAL endcaps (EE) are located at a distance of $|z| = 314$ cm from the centre of the detector. Each endcap is made of 2 semicircular half-disks in which the crystals are placed. The crystals are arranged in so-called *supercrystals*, 138 units of 5×5 crystals in the central part and 18 units with special shapes at the border of each half-disk.

The expected resolution of the energy measurement in the ECAL is given by

$$\left(\frac{\sigma_E}{E}\right)^2 = \left(\frac{2.8\%}{\sqrt{E/\,\text{GeV}}}\right)^2 + \left(\frac{12\%}{E/\,\text{GeV}}\right)^2 + (0.3\%)^2 \tag{3.4}$$

for energies below ~ 500 GeV, which was confirmed by test-beam data yielding a relative energy resolution of approximately 0.5% for 120 GeV electrons [72]. With 2011 LHC data,

this was reconfirmed in a measurement of the electron energy resolution as a function of the supercluster pseudorapidity using $Z \rightarrow ee$-events that showed good agreement between data and simulation [75].

3.2.3 Hadron Calorimeter

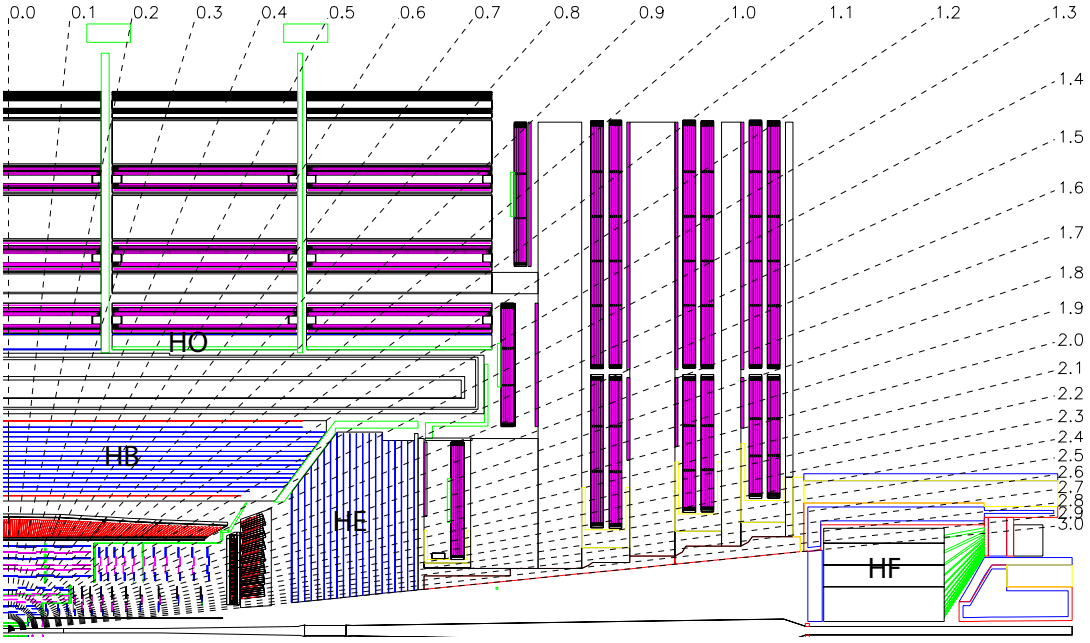

Figure 3.5: Layout of a quarter of the CMS detector with the positions of the hadron calorimeter systems, i.e. the hadron barrel (HB), hadron endcap (HE), hadron outer (HO), and hadron forward (HF) [72]. The dashed lines show the pseudorapidity with respect to the centre of the detector.

The hadron calorimeter (HCAL) encloses the ECAL and is located within the CMS magnet. To be able to provide a good measurement of the missing transverse energy, it is built as a hermetic system. The HCAL consists of brass as the absorber material and of plastic scintillators as the active medium. To maximise the number of radiation lengths the absorber material can provide, the plastic scintillators have a thickness of only 3.7 mm. The scintillators are read out via embedded wavelength-shifting fibres; these fibres are spliced to clear fibres that feed the light to the readout system. The HCAL is made of four parts, a barrel part, an endcap, a forward part, and the hadron outer outside of the magnet.

The hadron barrel (HB) is constructed in two half-barrels and has a length of 9 m at an outer diameter of 6 m, covering the pseudorapidity range $|\eta| < 1.4$. The HB is arranged in 2304 towers with a segmentation of $\Delta\eta \times \Delta\phi = 0.087 \times 0.087$. To assist in the identification of electrons and photons, the innermost scintillator plates have a higher thickness of 9 mm.

The two hadron endcaps (HE) cover the pseudorapidity region $1.3 < |\eta| < 3.0$ with a total number of 2304 towers. Unlike in the HB, the segmentation of the towers becomes coarser with

higher $|\eta|$, with the ϕ segmentation varying from 5°–10° and the η segmentation varying from 0.087–0.35.

The very forward region of $3.0 < |\eta| < 5.0$ is covered by the two hadron forward (HF) calorimeters. In contrast to the HB and the HE, the HF is a steel/quartz fibre calorimeter. Each HF has a depth of 1.65 m at a distance of 11.2 m from the interaction point. The segmentation of the 900 HF towers is $\Delta\eta \times \Delta\phi = 0.175 \times 20°$ except for the ones at lowest/highest $|\eta|$ with smaller/larger segmentation.

To be able to sample the energy from hadron showers traversing the other HCAL detectors, the hadron outer (HO) detector is placed beyond the muon systems, covering the pseudorapidity region $|\eta| < 1.26$. The scintillator detectors are arranged in 5 sections in line with the barrel muon system. The innermost ring has two scintillator layers after an iron absorber, whereas the other 4 rings have a single scintillator layer. The segmentation of the scintillators corresponds to the HCAL barrel tower segmentation.

The expected resolution of the HCAL energy measurement can be approximated by

$$\left(\frac{\sigma_E}{E}\right)^2 = \left(\frac{100\%}{\sqrt{E/\,\text{GeV}}}\right)^2 + (4.5\%)^2. \tag{3.5}$$

The estimated energy response in simulation was found to be in good agreement with first LHC collision data [76].

3.2.4 Muon Detectors

Besides neutrinos, muons with sufficient energy are the only particles that traverse the whole detector. Their signals are measured with a combination of tracking information and dedicated detectors in the muon system. The muon system comprises three types of gaseous detectors. The barrel region of $|\eta| < 1.2$ is equipped with drift tube chambers (DT), and the endcap region is covered with cathode strip chambers (CSC) up to $|\eta| < 2.4$. These two chamber types are complemented by resistive plate chambers (RPC) in both the barrel and the endcap regions up to $|\eta| < 1.6$. The DT and the CSC detectors provide a high position resolution; the RPC system, with a lower position resolution, has a better time resolution due to its fast response and is hence primarily used to supplement the triggering capabilities of the other two muon systems.

The layout of the muon detectors is shown in figure 3.6. In the barrel region of the detector, the DT and the central RPC detectors are interleaved with the magnet return yoke. They are mounted on 5 wheels along the beam line (labelled $YB-2$ to $YB+2$) and are structured in 4 stations at radii of 4.0, 4.9, 5.9 and 7.0 m from the beam axis. The 250 DT chambers are equally spread over the 5 wheels, with 12 chambers in each of the three inner layers of a wheel and 14 chambers in the outer layer of each wheel. To be able to measure high momentum muons at the boundaries of wheels, the positions of the DT chambers in the four stations are staggered such that a muon traverses at least three chambers. Each chamber in the three inner stations of a wheel consists of 12 planes of aluminium drift tubes, of which 8 planes are dedicated to coordinate measurements in the r–ϕ plane and 4 planes for measurements in the r–z plane. The

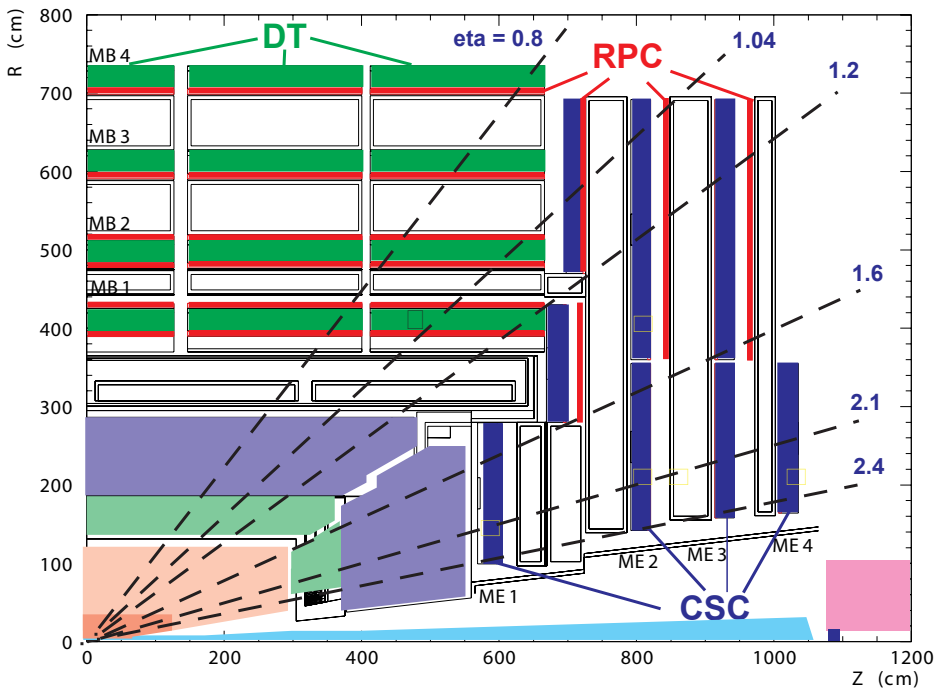

Figure 3.6: Schematic view of the muon systems in a quarter of the detector. The dashed lines indicate the pseudorapidity regions in which muons are measured by different combinations of subdetectors.

outermost chambers contain 8 planes for measurements in the r–ϕ plane only. Each plane is made up of chamber cells with a maximum drift length of 2.0 cm, with a single point resolution of $\sim$ 200 μm. In each muon station, the muon position can be measured with a ϕ coordinate resolution of $\sim$ 100 μm in position and 1 mrad in direction, leading to a good momentum resolution for high-momentum muons.

The two endcaps of the muon system contain 486 CSC detectors, arranged in 4 disks at a right angle to the beam pipe. The first disk comprises 3 rings of CSC detectors, the second and third disks comprise 2 rings, and the fourth disk comprises one ring. Each ring is made up of 36 or 18 CSC detectors (18 in the innermost rings of the second to fourth disks). The individual chambers are arranged such that there is no overlap in ϕ direction to avoid a loss of acceptance. Each CSC is made up of 6 gas gaps. The electron avalanche caused by the gas ionisation of a traversing particle results in a fast signal on the anode wire, which is accordingly used in the trigger system. A more precise measurement for the reconstruction of the muon is obtained by exploiting the charge distribution induced on the cathode strips. Each chamber provides a spatial resolution of the order of 200 μm (100 μm in the first disk) and an angular resolution in ϕ direction of $\sim$ 10 mrad.

3.2.5 Event Filter and Data Acquisition

At LHC design luminosity, there are $\sim 10^9$ interactions/sec in the CMS detector. However, only information about of the order of 10^2 events/sec can be permanently recorded, meaning that a

selection of interesting events has to take place. This is achieved by the data acquisition and event filter (most often called trigger) systems. There are 4 subsystems: detector electronics, hardware trigger processors (Level 1 trigger), a readout network, and a processor farm for event filtering (High Level Trigger).

There is a time window of 3.2 μs from the front-end detector electronics until the Level 1 trigger decision takes place. Meanwhile, the detector data is held in dedicated buffers. The Level 1 trigger algorithms run on custom hardware processors. Amongst other things, a reconstruction of photons, muons, electrons, and jets is performed, with the events being retained if the reconstructed objects pass certain p_{T} or E_{T} thresholds. Due to the limited time, the reconstruction leads to a coarser granularity and a lower resolution than the offline reconstruction. The output rate of the Level 1 trigger is around 100 kHz.

The data passing the Level 1 trigger criteria are then transferred to front-end readout buffers for further event filtering with the High Level Trigger (HLT). Each collision event has a storage size of $\sim$ 1.5 MB. In the HLT algorithms, various reconstruction techniques are performed that are very close to the offline reconstruction. To reduce the needed CPU time, events are discarded as soon as possible such that time-intensive algorithms only run when needed. For example, events may only be partially reconstructed in a certain detector region, or full tracking is only run if there are candidate objects fulfilling certain quality criteria. The output rate of the HLT is of the order of 100 Hz. The details of the HLT algorithms used for this analysis are briefly outlined below.

3.2.6 Luminosity Systems

The goal of the luminosity determination is to measure the amount of integrated luminosity with high precision in real time and for offline analysis [77,78]. In general, the monitoring of the luminosity relies on the measurement of physics processes with high cross sections such as the total pp cross section or the production of vector bosons. Measurements based on the total pp cross section have the advantage that they can yield a precision lower than the per cent level and that they only require simple hardware that does not rely on full operation of the CMS detector. Two techniques are deployed: The first one uses signals from the hadron forward calorimeter (HF), and the second one exploits the silicon pixel detector.

The luminosity measurement in the HF can be done with two methods. The first is a counting method: The mean number of interactions per bunch crossing can be deduced from counting the numbers of empty towers in the HF. The second method exploits the linear relationship between the luminosity and the average transverse energy deposit per tower.

The luminosity determination based on the pixel detector uses events triggered by a zero-bias trigger, i.e. a trigger that only uses the information that a bunch crossing takes place. In these events, the number of pixel clusters that are hit is counted, which is proportional to the instantaneous luminosity. Similar to the HF, one can also count events without any reconstructed vertex and deduce the number of expected vertices by assuming that the distribution of the number of vertices is distributed according to a Poisson distribution.

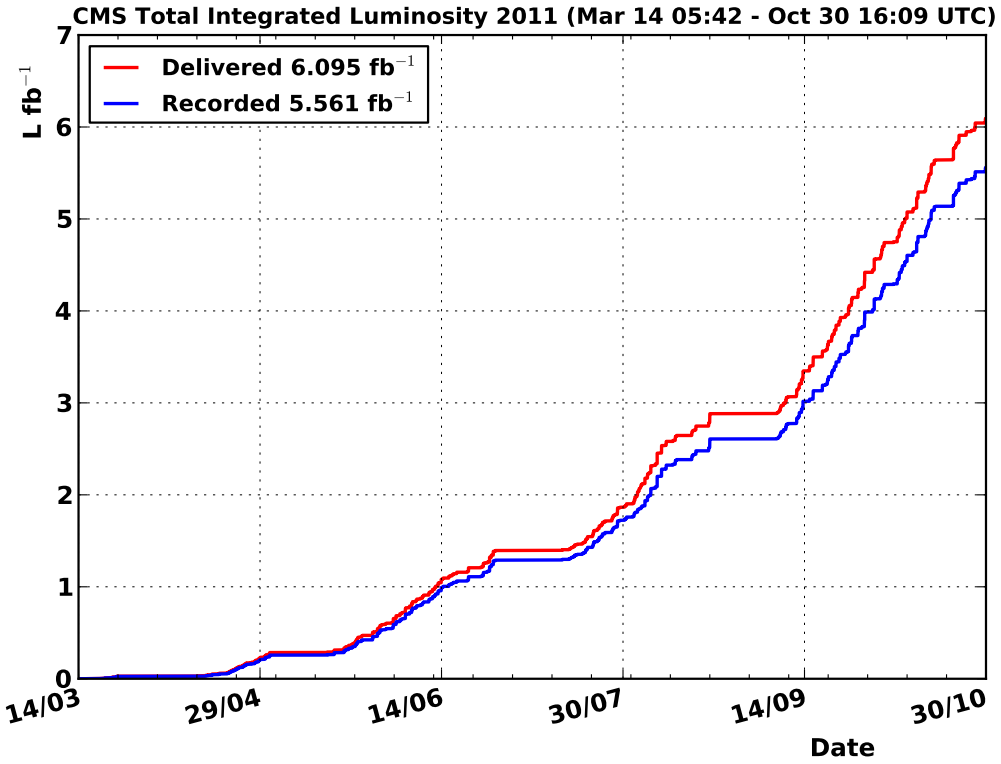

Figure 3.7: Integrated luminosity over time recorded with the CMS detector in 2011 [77].

An absolute calibration of the luminosity is achieved by so-called *Van der Meer scans* (VdM scan) [79]. In a VdM scan, the interaction rate is recorded as a function of transverse beam separation, yielding the transverse beam profile. The instantaneous luminosity in a bunch crossing can now be calculated from this transverse beam profile, the intensities of the two bunches, and the orbital frequency of the LHC. For the 2011 data-taking, VdM scans were used to determine the pixel cluster cross section, which is then used to calculate the integrated luminosity per recorded section of the data with the pixel cluster counting method [77].

Figure 3.7 shows the integrated luminosity over time in 2011. The LHC delivered an integrated luminosity of 6.1 fb^{-1} of which 5.6 fb^{-1} were recorded with the CMS detector. In 5.0 fb^{-1} of the recorded data, all subdetectors were operational and produced data with high quality as flagged by the CMS data quality group.

3.3 Software Setup

In general, physics data analysis requires a considerable amount of software, e.g. for the generation of simulated events, for the reconstruction of collision data, or to run algorithms for statistical inference. The pieces of software used in this work are based on two major frameworks,

the CMS software framework (CMSSW) and the Visual Physics Analysis framework (VISPA). CMSSW is the framework for most of the software deployed in the context of the CMS experiment, ranging from the simulation of the detector, event reconstruction, and implementation of the high level trigger to user data analysis [71]. VISPA is a visual development environment for physics analysis [80]. Both software frameworks are described in more details below.

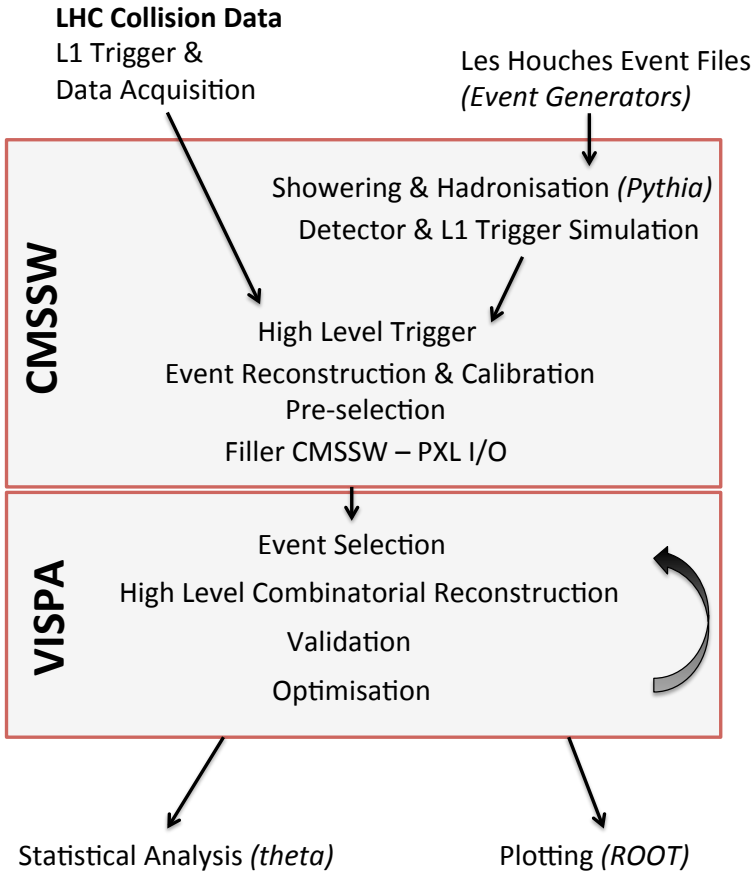

Figure 3.8: Overview of analysis flow. The analysis starts with either collision data or generated events at the top, which pass through several analysis steps in the CMSSW and VISPA frameworks.

The workflow of the analysis is shown in figure 3.8. The analysis begins with either collision data, as recorded by the data acquisition system, or simulated events, which are typically produced in the form of Les Houches Event (LHE) files, a common format for high-energy physics event files [81]. The subsequent steps are carried out within the CMSSW framework, using single events as the basic entity for the communication between different modules of the CMSSW framework. The events are then converted into the data format used in the VISPA framework, the so-called PXL I/O format [82]. The further analysis is carried out in the VISPA framework, including tasks such as the selection of events and the combinatorial reconstruction of composite objects. In contrast to the analysis steps in the CMSSW environment, the different parts of the analysis are typically repeated several times. This iterative workflow allows for a detailed optimisation and validation of the analysis. The results of the event-based analysis are then collected and passed to dedicated software frameworks for statistical inference or plotting.

3.3.1 Software in CMS

The CMS software provides the basic software architecture for several applications and domains: for tasks related to data-taking like the high level trigger, the reconstruction of events, the calibration and alignment of the detector necessary for the reconstruction, and the monitoring of the data quality; for tasks related to the production of simulated events, including the generation of events with event generators and the simulation of the CMS detector; and for tasks related to physics analysis like the visualisation of event data and high-level analysis requiring physics objects and analysis tools. To cope with the broad range of applications, CMSSW can be customised for a number of different computing environments.

CMSSW is based on individual modules written in C++. Events are processed by passing them through a sequence of modules with each module having access to the content of the current event. There are different types of modules, e.g. for data input and output, for filtering and analysing events, and for extending the event content by adding data products. The execution of the modules is steered by Python-based configuration files. The user can implement analysis logic by arranging the order in which modules are executed or by declaring when execution is stopped. Furthermore, configuration options can be set for each individual module. In addition to the modules, there are dedicated service and utility toolkits that can be used by the modules. There is no direct inter-module communication, allowing the reusability of modules and providing the possibility to test each module individually. Each module may however extend the content of the event. For the storage of data, CMSSW uses an I/O system based on the data analysis framework ROOT [83]. The reproducibility of results is guaranteed by using a provenance system that automatically records all necessary information.

The general structure of CMSSW described in the previous paragraph applies to all domains where CMSSW is used. In the following two paragraphs, the detector simulation and the physics analysis tools will be described in more detail.

The CMS detector is modelled with a full simulation of the detector structures and material [84]. The simulation is based on GEANT4 [85] and models the interaction of the particles produced in simulated events with the detector material. The software framework allows to combine simulation with real data to include measured detector noise or other instrumental effects. By comparing data with simulated events, both the modelling of the material budget in the simulation and the interaction of particles with matter in GEANT 4 have been improved.

The Physics Analysis Toolkit (PAT) provides physics objects, algorithms, and standard configuration files aimed at simplifying end user physics analysis [86]. In contrast to the output of the reconstruction, the PAT physics objects aggregate all relevant information in a single object. Each object can be extended with user-specific data in the form of either string-indexed real valued numbers or by generic complex objects. In this analysis, the pre-defined algorithms and standard configuration files are used as an input to the converter to the PXL I/O data format, which runs within the CMSSW framework.

3.3.2 VISPA and additional analysis software

While the reconstruction of physics objects is carried out within the CMSSW framework, the further analysis steps are performed with the help of the VISPA framework. The event data are

first transformed into the input-output format used by VISPA. VISPA is then deployed for the following analysis steps like the selection of collision events, the application of specific correction algorithms, and the reconstruction of composite objects. For plotting and the statistical analysis of the processed data, the ROOT and THETA [87] frameworks are used that are briefly introduced below.

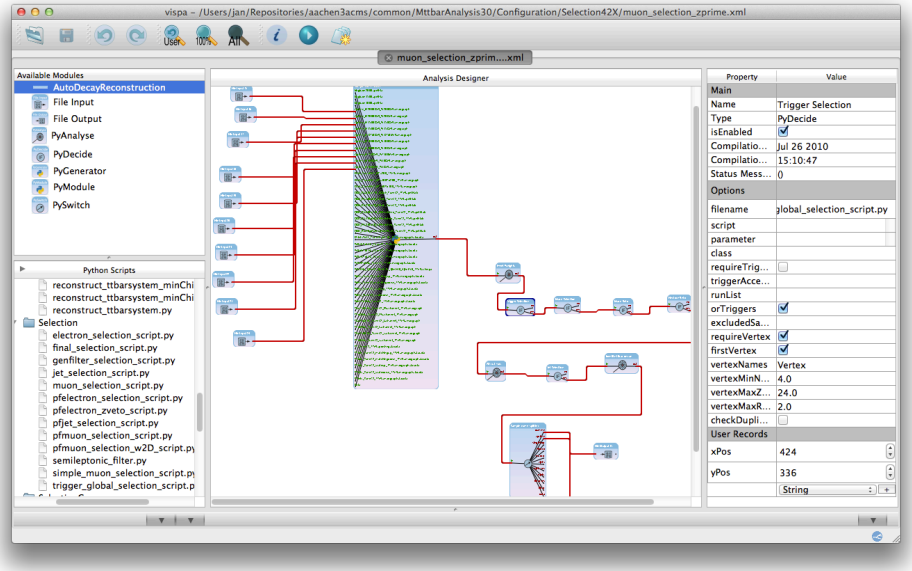

Figure 3.9: Screenshot of selection module in VISPA.

VISPA is a graphical development environment for physics analysis [80,88,89]. Based on a graphical framework (VISPA GUI), individual plug-ins offer the functionality needed for a modular physics analysis. The two key plug-ins for physics analysis, the *AnalysisDesigner* and the *DataBrowser*, rely on the object-oriented C++ toolkit PXL [82].

PXL provides the basic objects and algorithms for data analysis in high energy physics. Beyond objects like particles and vertices, PXL offers containers for these objects that may e.g. represent a complete collision event or a view of a collision event, an *EventView*. The *EventView* can be used as a separate container for generated and reconstructed events or to reconstruct an event under different reconstruction hypotheses. Most objects contain a dedicated object for user data, the *UserRecord*, which allows to store string-indexed simple data types in each object and thereby to arbitrarily extend the data content. To construct decay trees or to associate reconstructed and generated particles, relations may be built between particles and/or other objects. All objects are included in the dedicated PXL input-output (I/O) scheme. The I/O files are based on serial data chunks and are typically structured using individual collision events. Other basic functionalities include logging and exception handling.

In addition, PXL includes a module system to design modular physics analyses. In a modular physics analysis, events are either created from scratch or read from disk and then passed through a chain of modules. The module chain may implement analysis logic, e.g. by setting up modules for the selection of events, by adding or modifying data in order to reconstruct composite objects, or by running other algorithms on the data. All PXL objects are interfaced to

Python; all analysis modules can hence be written in C++ or Python, thereby providing means for both fast prototyping of analysis modules and for efficient handling of a large amount of data.

In the VISPA GUI, modular physics analyses are created with the *AnalysisDesigner* plug-in, the link between the GUI and the PXL module system. The *AnalysisDesigner* allows to create a physics analysis from scratch or to modify an existing one, e.g. by changing module options in the GUI, by selecting input files, or by adding additional modules. An example of a physics analysis step designed with VISPA used in this analysis is given in figure 3.9. The picture shows a screenshot of the event selection in the *AnalysisDesigner* with simulated Z' samples as input. The content of PXL I/O files can be visualised in the *DataBrowser*, which can e.g. show the relations between objects in a decay tree and the data content of each object. This visualisation is particularly useful for the verification of input data and algorithms.

A standalone version of the data analysis framework ROOT is used for the display of the results in the form of plots, to perform analytical fits, and as an efficient storage for unbinned data [83]. ROOT is an object-oriented framework written in C++, designed to handle large amounts of data. Similar to PXL, ROOT also provides an interface to PYTHON. In modular analyses in VISPA, ROOT objects and algorithms can hence directly be used in both C++ and Python analysis modules.

The statistical analysis is performed with the THETA framework, which implements algorithms for statistical modelling and inference [87]. A physical model can be constructed based on binned templates; it may depend on an arbitrary number of parameters. The model can be used to compare to data, to construct likelihood functions, and to efficiently produce a large number of pseudo-experiments. Furthermore, THETA includes algorithms to numerically solve integrals with the Metropolis-Hastings Markov chain Monte Carlo (MCMC) algorithm and deploys the MINUIT minimisation algorithms implemented in the ROOT package. With these ingredients, THETA provides various means to perform both frequentist and Bayesian statistical inference. Cross checks of the validity of the results calculated with THETA are obtained with the ROOT-based ROOSTATS package [90].

4 Reconstruction of Physics Objects

Events from top pair production in the lepton-plus-jets channel contain either an electron or a muon, a neutrino, and typically 4 jets, of which two are b quark jets. This chapter therefore describes how these objects are reconstructed; the details of the selection of events, which is based on these objects, are given in the next chapter. This analysis is based on an integrated reconstruction of the full event with the so-called *Particle Flow (PF)* algorithm, leading to improved resolutions of the jet energies and the missing transverse energy. Furthermore, the PF algorithm provides lepton identification and isolation techniques with a better performance compared to the sub-detector-based algorithms that are also used in CMS.

In this chapter, the PF algorithm is explained first, followed by the details of the reconstruction algorithms of the individual objects: muons, electrons, jets, b quark jets, and missing transverse energy.

4.1 The Particle Flow algorithm

The idea of the Particle Flow algorithm is to individually reconstruct all detectable particles in a collision event by exploiting and combining information from all relevant sub-detectors [91]. It is based on the fact that most stable particles, e.g. the constituents of particle jets, have rather low transverse momentum, and that an individual reconstruction of these particles, especially using information from the inner tracking detectors, can exploit special characteristics of these particles. Since the individual particles can be measured with relatively high precision, this also leads to high-precision measurements of derived objects like jets and missing transverse energy.

The PF algorithm involves three steps. First, the information from all sub-detectors needs to be obtained. The key ingredients are charged particle tracks, calorimeter clusters, and muon tracks. They need to be delivered with high efficiency and accuracy, and the PF algorithm therefore partly deploys dedicated reconstruction algorithms. Second, the ingredients from different sub-detectors are combined by a link algorithm. Third, the individual particles are reconstructed. From all individual reconstructed particles, combined objects like jets and missing transverse energy can be created.

4.1.1 Reconstruction of tracks, calorimeter clusters, and tracks in the muon system

Charged tracks are reconstructed with an iterative tracking strategy [92,93]. The reconstruction starts from seeds that are reconstructed from hits in different layers and/or disks of the silicon

pixel or silicon strip detectors [94]. The seeds are either built from triplets of hits or from pairs of hits with an additional constraint from a reconstructed primary vertex or the beamspot, which is calculated run-wise from an averaging over the positions of reconstructed vertices.

Starting from the seeds, trajectory candidates are reconstructed with a combinatorial Kalman filter method by iteratively extrapolating the intermediate trajectory to additional layers until the boundary of the tracker is reached or until there are no additional compatible hits. In each layer, new trajectory candidates are created from all compatible additional hits, and the extrapolated trajectory candidate is retained to account for the possibility of a missing hit in the current layer. Additional hits are searched for by starting from the outermost hits and extrapolating to the inner regions. The trajectory parameters and uncertainties are updated whenever an additional hit is added. Finally, tracks are created by fitting the hits of each trajectory candidate.

The charged tracks are reconstructed in 6 iterations with progressively loosened track seeding criteria. Tracker hits that are assigned to a reconstructed track are removed after each iteration. Seeds in the first three iterations are reconstructed using pixel detector hits in a thin cylinder around the beam axis. To also be able to reconstruct tracks from long-lived particles or electrons from photon conversions, combinations of hits in the pixel and the strip layers are used in the following iteration, and only strip hits in the final two iterations.

The reconstruction of calorimeter clusters has several goals. Neutral particles can only be detected in the calorimeters, and they need to be separated from the calorimeter depositions of charged particles. Conversely, this separation helps improve the energy measurement of charged particles. The showers of electrons and photons, which may e.g. be bremsstrahlung photons from electrons, mainly lead to energy deposits in the ECAL. To exploit the granularity of each subdetector, the calorimeter clusters are reconstructed separately for the preshower detector, the ECAL, and the HCAL. Local energy maxima are used as seeds, and the energy of neighbouring calorimeter cells is added if it is above a certain threshold. In case a calorimeter cell belongs to more than one cluster, the energy is shared according to the cell-cluster distance, determined with an iterative algorithm.

Finally, standalone muon tracks are reconstructed in the muon system. The dedicated muon reconstruction will be explained in more detail below.

4.1.2 Link algorithm

The link algorithm combines the information from the tracks, the calorimeter clusters, and the information from the muon system. Tracks and calorimeter clusters are associated by distances in the (η, ϕ)-plane. If more than one track matches a calorimeter cluster or vice versa, all combinations are retained. Possible bremsstrahlung photons are combined with tracks if the position is compatible with the tangent of a charged track that is extrapolated to the ECAL surface. Muons are reconstructed using a *global* track fit, combining a track in the muon system and a compatible charged track. Here, the χ^2 of the fit is used as a criterion to decide which link is preferred.

4.1.3 Reconstruction of particles (Particle Flow algorithm)

Finally, individual particles are reconstructed by the so-called particle flow algorithm. The algorithm identifies particles step by step. In each step, the used building blocks are removed from the further processing.

Muons of high quality are identified first; the expected average energy deposits in the calorimeters are subtracted. Then electrons are reconstructed, using a combination of calorimetric and tracking variables for the identification. The next step is the association of tracks with calorimeter clusters, giving rise to charged hadrons. This association uses tighter track selection criteria and a dedicated calibration of the calorimetric energy. Ambiguities in the association are resolved by exploiting both the comparison of calorimetric energy with the track momentum and the geometric distance of the track and the calorimeter cluster. The energy of the reconstructed charged hadrons is either taken from the track momentum or, if the track momentum and the energy of the calorimeter cluster are compatible, from a combined fit of the track and cluster measurements. If the calorimetric energy is much lower than that of the associated tracks, additional muons may be reconstructed with looser quality criteria. Neutral hadrons or photons are reconstructed if the energy of the calorimeter cluster is significantly larger than that of the associated tracks; if the excess is due to a cluster in the ECAL, a photon is created, otherwise a neutral hadron. Similarly, calorimeter clusters that are not linked to any track are used to reconstruct photons (ECAL clusters) and neutral hadrons (HCAL clusters).

The performance of the algorithm has been verified with data taken in 2010 [95]. For example, the absolute photon energy calibration has been validated using the reconstructed π^0 mass distribution to 1% precision. The hadron energy calibration has also been validated and corrected for differences between data and simulation. Finally, the performance of leptons within the particle flow algorithm has been studied separately [96].

4.2 Muon reconstruction and identification

Muon tracks are reconstructed with a combination of the information from the inner tracking detectors, i.e. the silicon pixel and strip detectors, and from the dedicated muon detectors, the drift tube chambers in the central region ($|\eta| < 1.2$), the cathode strip chambers in the endcap region ($0.9 < |\eta| < 2.4$), and the resistive plate chambers in both regions ($|\eta| < 1.6$). In the so-called *global muon reconstruction*, the trajectory of standalone muon tracks reconstructed in the muon detectors is extrapolated to the inner tracking detectors. If a matching track reconstructed in the inner tracking detectors is found, a combined global track fit is performed using the corresponding hits in all detectors. Compared to the reconstruction from inner tracks only, the global track fit can improve the momentum resolution for high p_{T} muons ($p_{\mathrm{T}}^{\mu} \gtrsim 200$ GeV). For muons with transverse momentum $p_{\mathrm{T}} < 100$ GeV, the relative muon momentum resolution is between 1% and 2% [97]. It degrades to a resolution of $\sim 5\%$ for muon $p_{\mathrm{T}} \sim 500$ GeV [98].

The global muon reconstruction is complemented by the *tracker muon reconstruction*. Opposed to the global muon reconstruction, inner tracks are extrapolated to the muon detectors to look for compatible hits or track stubs that do not give rise to full muon detector tracks. This

reconstruction uses only the tracker information to determine the muon momentum; it increases the reconstruction efficiency at low muon momentum ($p_{\mathrm{T}}^{\mu} \lesssim 20$ GeV). Finally, about 1% of the muons produced in collisions do not yield a reconstructed inner track. If there is a track in the muon system with no matching inner track, it is also considered as a muon candidate, though suffering from a significantly increased background rate from cosmic muons compared to the other two reconstruction algorithms.

Muons from the global reconstruction already make up a very pure sample, but one can still exploit several characteristics of high quality muons to improve the selection for physics analyses. Such variables can be put into three categories: the compatibility of the fitted track with the hits in the muon system and with the deposited energy in the calorimeters; the compatibility of the reconstructed muon track with originating from the primary vertex; and the quality of the reconstructed track, using variables like the χ^2 of the track fit, the number of hits that are well compatible with the track ("good" hits), and the number of tracking detector layers where a hit is expected but not found.

The performance of the muon reconstruction and identification algorithms have been measured using collision data [99]. The reconstruction and trigger efficiencies are close to design expectations, with a good agreement between data and simulation. Similarly, the simulation describes the observables used for muon identification well, with small differences in the distribution of the number of associated hits in the muon system that are attributed to the alignment and calibration conditions during the considered data-taking periods.

4.3 Electron reconstruction and identification

The reconstruction of electrons has three major components: the reconstruction of the energy deposits in the electromagnetic calorimeter, the reconstruction of the electron track, and the matching of the track with the energy deposits. As the tracker has up to two radiation lengths of material at a pseudorapidity of $\eta = \pm 1.5$, the reconstruction is often further complicated due to significant emission of bremsstrahlung photons.

There are two reconstruction algorithms, one starting from energy deposits in the ECAL, and one from a reconstructed track. The first algorithm begins with looking for clusters of crystals in the ECAL with a significant energy deposit. Clusters are reconstructed from neighbouring ECAL crystal entries with energies above a certain threshold, starting with the crystals with the highest energies. In a very narrow η and a wider ϕ window, the difference being due to the bending of the electron tracks in the magnetic field, nearby clusters are combined into *superclusters*, beginning with the most energetic clusters. The superclusters are used as seeds for the electron reconstruction and are matched to track seeds, which are reconstructed from either pairs or triplets of tracker hits. Then a dedicated track reconstruction is performed, similar to the standard track reconstruction but using a dedicated modelling of the expected energy loss and radiation of electrons in the tracking system. The radiation may e.g. give rise to kinks, i.e. changes of the curvature of the tracks. The reconstructed electron candidates are retained for further analysis if they fulfil selection criteria based on the matching between the track and

the supercluster positions in η and ϕ. The additional electron identification that is necessary to select electrons of high quality for analysis is described in the next chapter.

The track-driven reconstruction copes with the inefficient seeding for low p_{T} electrons and electrons in jets. Here, the reconstruction starts with potential electron tracks that are extrapolated to the surface of the ECAL. If a matching ECAL supercluster is found, a dedicated multivariate selection is used to decide if the reconstructed electron is kept for further reconstruction [100].

The performance of the reconstruction of electrons in data was studied in detail with CMS data taken in 2010; the reconstruction and selection efficiencies were also measured using data-driven techniques, verifying the good agreement of data with the detector simulation [101]. The combined electron trigger and reconstruction efficiencies are $\sim 99\%$ for electrons in the barrel region of the detector and $\sim 96\%$ in the endcap region. For electrons with $p_{\mathrm{T}} > 20$ GeV, the electron energy is measured with a resolution of 3% or better [97]. The resolution at high electron p_{T} improves due to the high resolution of the energy measurement in the ECAL, which becomes better than $\sim 0.5\%$ for $p_{\mathrm{T}} > 100$ GeV.

4.4 Jets

All particles reconstructed by the particle flow algorithm that are neither identified as isolated muons nor as isolated electrons may be constituents of jets and are hence used as input for the jet clustering algorithms. Here, the *anti-kt* clustering algorithm is deployed using a clustering parameter of $R = \sqrt{\Delta\eta^2 + \Delta\phi^2} = 0.5$ [102]. The anti-kt algorithm belongs to a general class of sequential recombination algorithms that involve a parameter p that sets the relative importance of the geometrical distance R and the transverse momentum p_{T}. By setting $p = -1$, i.e. setting p such that the importance of the transverse momentum scale is high compared to the geometrical distance, the anti-kt algorithm leads to jets with desirable theoretical and experimental features compared to other algorithm used in high-energy physics. From the theory side, the algorithm is both infrared- and collinear-safe. An appealing experimental feature is that the reconstructed hard jets are conical, distinguishing the anti-kt algorithm from other infrared- and collinear-safe algorithms like the *kt*, the *SisCone*, and the *Cambridge-Aachen* algorithms.

By using the information from all particles, 90% of the jet energy is typically reconstructed, a significant improvement compared to calorimeter-based jets or calorimeter jets that are corrected for the momentum of associated tracks. The high fraction of reconstructed energy also leads to a highly reduced dependence of the reconstructed energy on the flavour of the parton that gives rise to the jet when compared to the other jet reconstruction algorithms. On average, the energy of the reconstructed jets consists of 65% charged particles, 25% photons, and 10% neutral hadrons [103]. The jet reconstruction efficiency is close to 100%.

The jet energy scale is corrected to match the energy of generator level jets that are clustered from visible generated particles [104]. Due to the different detector response in different detector regions, the corrections are derived as a function of the pseudorapidity and the transverse momentum of the reconstructed jets. In addition, the jets are corrected for differences between

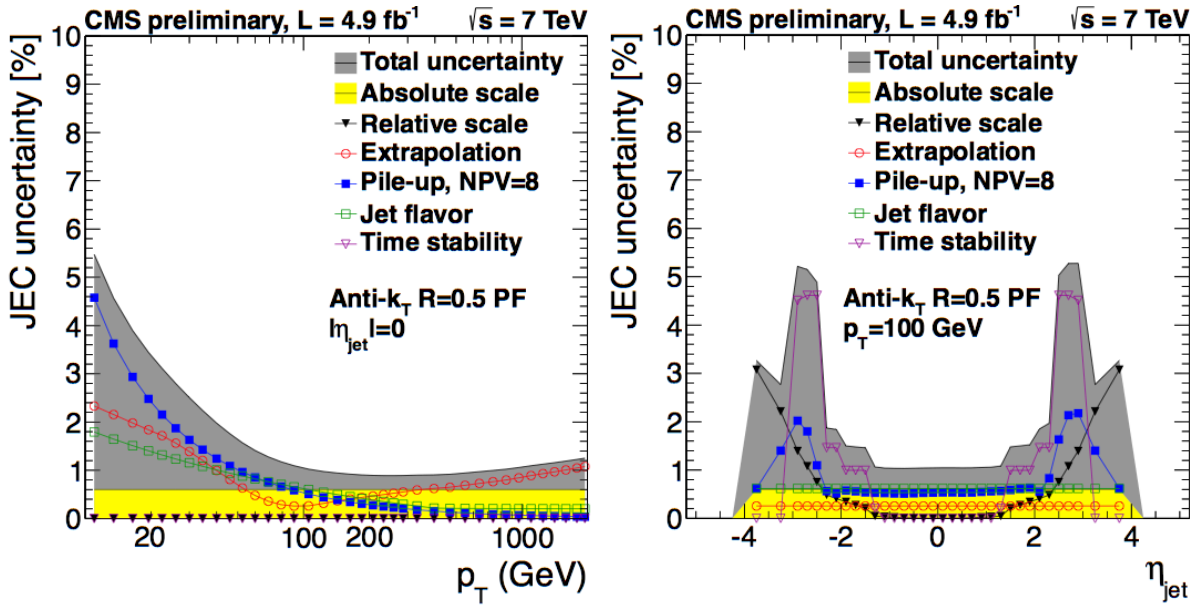

Figure 4.1: Combined uncertainties on the jet energy scale for particle-flow jets as a function of jet p_{T} (left) for jet $|\eta| = 0$ and as a function of jet η (right) for jet $p_{\mathrm{T}} = 100$ GeV derived with 2011 LHC data [103].

data and simulation. These residual corrections as well as the according jet energy scale uncertainties have been derived with LHC data taken in 2011 using different calibration methods. A summary of the absolute jet energy uncertainty as a function of jet transverse momentum is given in figure 4.1. For jets with transverse momentum $p_{\mathrm{T}} > 40$ GeV, the combined jet energy scale uncertainty is smaller than 2%. The most important sources of the jet energy scale uncertainty are due to the absolute scale of the jet energy, the dependence on the jet flavour, the modelling of pile-up interactions, and the extrapolation of the jet energy scale measurements in data to different regions of transverse momentum. For jets in the low transverse momentum region, i.e. with jet $p_{\mathrm{T}} < 100$ GeV, the uncertainties due to pile-up and the jet flavour are dominant. For jets with $100 < p_{\mathrm{T}} < 300$ GeV, the absolute energy scale is the most important source of uncertainty, with the total relative jet energy scale uncertainty being of the order of 1% only. For high p_{T} jets, the extrapolation uncertainty becomes dominant.

The resolution of the jet energy measurement is also highly improved by the particle flow algorithm, especially for low and medium jet energies. The jet energy resolution has been determined with LHC data [105]. For central jets in the pseudorapidity range $|\eta| < 0.5$, the relative jet p_{T} resolution is below 15% for jet $p_{\mathrm{T}} > 50$ GeV and below 10% for jet $p_{\mathrm{T}} > 80$ GeV. The measured resolution in data is found to be 5–29% worse than in simulation, depending on jet η, with a measurement uncertainty of 6–20%. The data-to-simulation scale factors are given by

- 1.05 ± 0.06 for $|\eta| < 0.5$,
- 1.06 ± 0.06 for $0.5 < |\eta| < 1.1$,
- 1.10 ± 0.06 for $1.1 < |\eta| < 1.7$,

- 1.13 ± 0.10 for $1.7 < |\eta| < 2.3$, and
- 1.29 ± 0.20 for $|\eta| > 2.3$.

Simulated jets are corrected for the difference in the resolution at analysis level. Each reconstructed jet in simulated events is matched to a particle jet on generator level, and the momenta of the reconstructed jets are changed by the uncertainty multiplied with the difference between the transverse momenta of the reconstructed and particle level jets.

4.5 Missing transverse energy

The only information that one can obtain about neutrinos (or other particles that do not interact with the CMS detector that appear in models for physics beyond the Standard Model) is the amount of undetected or *missing* energy. As only parts of the protons take part in the hard interaction, the determination of the longitudinal part of the missing energy involves high measurement uncertainties. The calculation of the transverse part of the missing energy relies on the fact that the interacting partons have insignificant transverse momentum. In the PF algorithm, the missing transverse energy is calculated by vectorially summing the transverse momenta of all reconstructed particles. The opposite of this vector is the missing transverse energy, $E_{\mathrm{T}}^{\mathrm{miss}}$.

Similar to jets, the inclusion of all single reconstructed particles significantly improves the resolution of the measured $E_{\mathrm{T}}^{\mathrm{miss}}$ compared to algorithms based on only calorimetric information or on calorimetric information corrected for all tracks in the event. In events from the production of a Z boson or a photon in association with jets, the $E_{\mathrm{T}}^{\mathrm{miss}}$ resolution can be measured by ignoring the two leptons from the decay of the Z boson or the photon in the reconstruction of the missing transverse energy and comparing the reconstructed missing transverse energy with the transverse momentum of the reconstructed Z boson or photon [106]. At low Z boson momentum, the $E_{\mathrm{T}}^{\mathrm{miss}}$ resolution is mostly affected by detector noise, the underlying event, and the number of simultaneous pp collisions. The resolution for both the $E_{\mathrm{T}}^{\mathrm{miss}}$ components parallel and perpendicular to the Z boson p_{T} is of the order of 10–20 GeV, depending on the number of simultaneous pp collisions [107]. The resolution of the $E_{\mathrm{T}}^{\mathrm{miss}}$ component perpendicular to the Z boson p_{T} remains at the level of 10–20 GeV as a function of Z boson p_{T}, whereas the resolution of the $E_{\mathrm{T}}^{\mathrm{miss}}$ component parallel to the Z boson p_{T} increases by about a factor of two when comparing low Z boson p_{T} with Z boson $p_{\mathrm{T}} \gtrsim 200$ GeV due to the recoiling jets.

The performance of the $E_{\mathrm{T}}^{\mathrm{miss}}$ reconstruction algorithm has also been checked in collision data using events from multijet production and from the production of a W boson decaying to a neutrino and either an electron or a muon [106,108,109]. In all cases, the agreement of data and simulation is good, and no dedicated corrections need to be applied to the simulation. Following the approach of reference [110], the uncertainty of the $E_{\mathrm{T}}^{\mathrm{miss}}$ estimation can be split into a number of uncertainty sources: the uncertainty of the jet energy scale and resolution for jets with high transverse momentum, the modelling of pile-up interactions, the uncertainty of the lepton energy scale, and the description of the remaining non-clustered energy. The relative uncertainty on the latter is determined to be 10%.

4.6 Identification of primary vertices and b quark jets

Primary vertices are used for three purposes: to reject events not coming from hard interactions; to associate tracks and particles to the primary hard interaction; and, in conjunction with the reconstruction of displaced vertices or tracks, to identify long-lived particles and to determine their flight distance.

The reconstruction of primary vertices uses an adaptive vertex fit [111]. In this fit, each track obtains a weight w_i between 0 and 1 that is a measure of the compatibility between the track and the primary vertex. The number of the degrees of freedom of this fit for n associated tracks is then given by $N_{dof} = 2\Sigma_{i=1}^{n} w_i - 3$.

The identification of b quark jets, denoted b-tagging in the following, is performed using an algorithm that exploits the long lifetime of b hadrons by reconstructing a secondary vertex from the tracks of the decay products. In comparison to other available algorithms based on the compatibility of tracks with originating from the primary interaction vertex, the algorithm based on the secondary vertex reconstruction is least sensitive to the presence of additional collisions in the CMS detector. Its performance has been measured not only in $b\bar{b}$ events but also in top quark pair production, i.e. in the same environment as this analysis [112–114].

Secondary vertices are reconstructed with a similar algorithm as primary vertices, i.e. with an adaptive vertex fit [115]. The adaptive vertex fit is performed using all tracks associated to one reconstructed jet. Only vertices with less than 65% of the tracks shared with the primary vertex are regarded as secondary vertices. To discriminate between secondary vertices from b jets and other jets, a measure of the compatibility of the position of the secondary vertex with the position of the primary vertex is used, the ratio of the three-dimensional flight distance and its uncertainty, $d = l/\sigma_l$, called flight distance significance. The flight distance significance can only be calculated if a secondary vertex is present, and the efficiency of the b-tagging is hence limited by the secondary vertex reconstruction efficiency for b jets of around 60-70%.

Two b-tagging working points are defined based on the target misidentification fraction of light-flavoured jets, *medium* with a fraction of 1% and *tight* with a fraction of 0.1%. The medium working point, which is used in this analysis, corresponds to a minimum discriminator value of $d > 1.74$. For b-flavoured jets with transverse momentum in the range 50 GeV $< p_{\mathrm{T}} <$ 80 GeV, the corresponding b-tag efficiency is $\sim 60\%$, whereas the efficiency for light-flavoured jet in the same p_{T} range to be identified as a b jet is $\sim 1.4\%$.

The b-tagging efficiencies have been measured in data with three methods, with the results being combined. The first method is based on semileptonic decays of b hadrons (called *PtRel*), the second method on different sets of control samples (called *System8*), and the third method on a reference b-tag algorithm that is calibrated in data events (called *Jet Probability*). The results of these b-tag efficiency measurements using collision data are compared to the nominal b-tag efficiencies in simulated events [114,116]. For jets with transverse momentum 80 GeV $< p_{\mathrm{T}} <$ 120 GeV (160 GeV $< p_{\mathrm{T}} <$ 320 GeV), the measurements can be summarised in a data-to-simulation correction factor of the b-tag efficiency for the secondary vertex algorithm of $SF_b = 0.95 \pm 0.02$ ($SF_b = 0.98 \pm 0.04$) for b quark jets. Figure 4.2 shows the corresponding measurements of the b-tag efficiency in data and simulation as a function of the

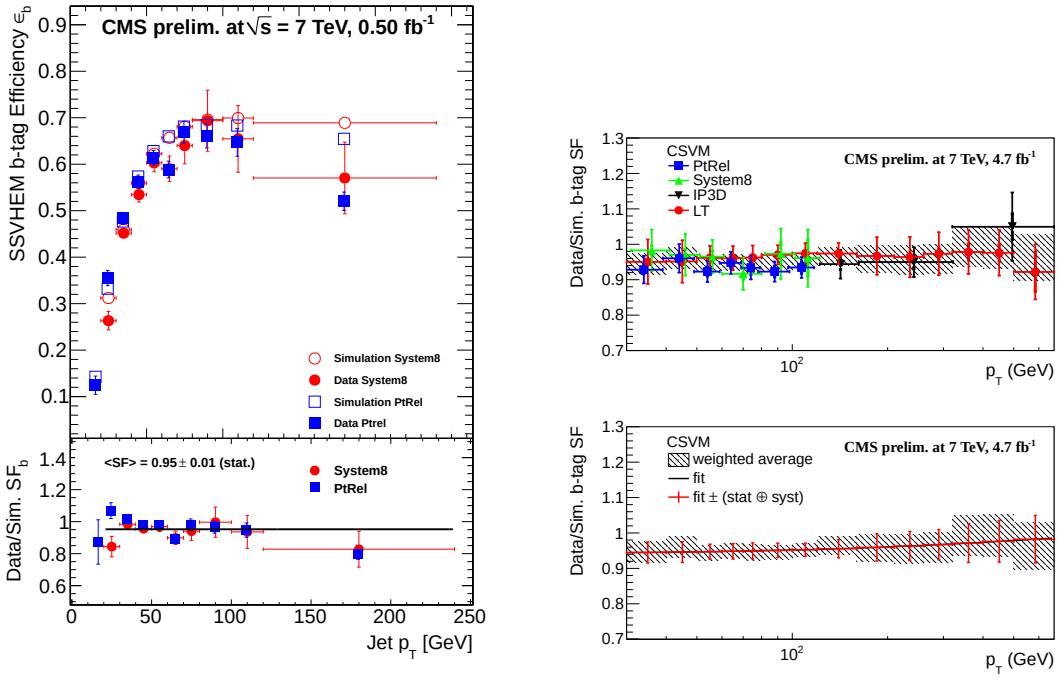

Figure 4.2: Measured b-tag efficiencies for b-flavoured jets in data and simulation as function of jet p_{T}. The efficiencies are shown for the simple secondary vertex tagger at working point medium as function of jet transverse momentum, determined with two different methods as given in the legend and derived with 0.5 fb^{-1} of collision data (left) [116], and for a combined secondary vertex tagger at working point medium using 4.7 fb^{-1} of data (right) [114]. The uncertainties for the combined secondary vertex algorithm are of similar size compared to the corresponding measurements for the simple secondary vertex tagger using 4.7 fb^{-1} that are used in the further analysis. The lower parts of the figures show the data-to-simulation scale factors that are applied for further data analysis based on simulated event samples.

transverse momentum of b-flavoured jets. Using the scale factor, events in simulated samples are reweighted to match the b-tagging efficiencies in data. This reweighting translates the measured efficiencies that are applicable per jet into event weights; more details on the technical implementation are given below.

The estimation of the rate of mistakenly b-tagging light-flavoured jets, called *mistag* rate in the following, has been carried out using multijet event samples from data and simulation. To determine the rate, reconstructed secondary vertices are used that have a distance to the primary vertex that is in the opposite direction of the jet under study, i.e. secondary vertices which yield a flight distance that has the opposite sign of the direction of the associated jet. The mistag rate is measured for several regions of the transverse momentum and the pseudorapidity of jets. In general, all measured data-to-simulation scale factors are consistent with unity, i.e. data and simulation agree well. The corresponding uncertainty amounts to less than 10% for jet $p_{\mathrm{T}} < 300$ GeV and less than 20% for jet $p_{\mathrm{T}} < 670$ GeV for the secondary vertex algorithm at working point medium. The measured scale factors range from $SF \sim 0.9$ at jet $p_{\mathrm{T}} = 30$ GeV

over $SF \sim 0.95$ for jets with $p_{\mathrm{T}} \sim 250$ GeV to values of $SF \sim 0.8$ at jet $p_{\mathrm{T}} \sim 650$ GeV [114].

5 Event Selection

This analysis focusses on the decay channel of the top quark pair with one charged lepton (either a muon or an electron), a neutrino and four jets, commonly denoted as lepton-plus-jets channel. In this chapter, the selection of these events will be described. After a discussion of the general selection strategy, an overview of the used simulated and measured datasets is given, followed by a description of the details of the event selection. Then, results of the application of the selection in data and simulation are described. Finally, efficiency corrections are detailed that are specific to the selected event sample.

5.1 Selection Strategy

The selection of events in a search for a new physics process is adapted to the goal of the search: to reach a high statistical significance for the possible discovery of the signal. To achieve this, the selection needs to reconcile two conflicting goals. On the one hand, as many signal events as possible should pass the selection. This typically implies requiring the presence of (at least a subset of) the final state objects predicted by the new physics process to be able to identify or reconstruct the process. On the other hand, the selected event sample should contain a high fraction of signal events. The latter is achieved by exploiting the different final states of signal and background events in terms of both particle content and kinematic properties.

Furthermore, the selection requirements should limit the influence of systematic uncertainties. This has two implications. First, the selection needs to rely on well-understood and commissioned physics objects. Second, the level of knowledge of the different background processes should guide the decision how restrictive the selection requirements are. It may thus be desirable to reduce the influence of a less well-known background process by tightening the selection requirements.

To reduce the impact of the choice between tightening the selection requirements and suffering from a high background rate, the selected events are put into different categories according to the numbers of jets and b-tagged jets for the statistical evaluation. This approach exploits the different signal-to-background ratios in the different categories. A further positive implication is that this categorisation helps to constrain the effect of systematic uncertainties when properly included in the statistical evaluation. Here, for example, the division of events according to the number of b-tagged jets constrains the uncertainty of the b-tag efficiency due to the knowledge of the b quark jet content of top quark events.

The used categories are events with

- 1 muon and 3 jets of which at least one is b-tagged (μ 3j1t);
- 1 muon and at least 4 jets of which none is b-tagged (μ 4j0t);
- 1 muon and at least 4 jets of which exactly one is b-tagged (μ 4j1t);
- 1 muon and at least 4 jets of which at least two are b-tagged (μ 4j2t);
- 1 electron and 3 jets of which at least one is b-tagged (e 3j1t);
- 1 electron and at least 4 jets of which none is b-tagged (e 4j0t);
- 1 electron and at least 4 jets of which exactly one is b-tagged (e 4j1t); and
- 1 electron and at least 4 jets of which at least two are b-tagged (e 4j2t).

The reasons for the choice of the categories are as follows. The number of categories should be kept at a manageable level, e.g. to have enough data events in each category to estimate the contribution from background events and to reduce the computing time for the statistical evaluation. Therefore, there are no additional categories for events with at least 5 jets or separate categories for events with 3 jets and either one or two b-tagged jets. In addition, the used categories need to contain a significant fraction of signal events to contribute significantly, and hence events with less than three jets or with three jets of which none is b-tagged are also disregarded. As explained below, the choice of only regarding events with at least three jets also allows for the usage of trigger paths that require at least three jets.

In this chapter, the event selection is described up to the selection of the lepton and either 3 or at least 4 jets; the details about the event numbers in the different categories will be given after the background estimation that is outlined in the next chapter.

5.2 Data event samples

The data-taking of the CMS detector underwent two periods in 2011, before and after a technical stop of the LHC in the beginning of September. These periods are called *Run 2011A* and *Run 2011B*. The events are split into different primary datasets during data-taking according to primary and secondary trigger objects. Part of the data events have been reprocessed in the so-called *May 10 re-reconstruction* or in the *August 05 re-reconstruction* to make use of updated reconstruction software and to deploy an updated ECAL calibration, respectively. Only "good" data events are used in this analysis, i.e. events of high data quality from periods of data-taking in which all subdetectors were fully operational.

A summary of the used datasets with the run period, the amount of integrated luminosity and the corresponding run numbers is given in table 5.1. The tiny differences in the integrated luminosities between the electron and the muon channel arise from runs in which the signal trigger was accidentally pre-scaled or from missing reconstruction jobs.

The sum of the integrated luminosities in the single datasets amounts to

- $L = 4.976$ fb^{-1} for the muon-plus-jets selection, and
- $L = 4.980$ fb^{-1} for the electron-plus-jets selection.

For simplicity, the integrated luminosity will be referred to as $L = 5.0$ fb^{-1} in the following.

Table 5.1: Datasets by run period with corresponding integrated luminosities (L_{int}) and run numbers.

Dataset name	Run period	L_{int} / pb^{-1}	Runs
ElectronHad May 10 ReReco	2011A	215	160404–163869
ElectronHad PromptReco v4	2011A	955	165071–167913
ElectronHad Aug 05 ReReco	2011A	390	170249–172619
ElectronHad PromptReco v6	2011A	707	172620–173692
ElectronHad PromptReco v1	2011B	2713	175860–180252
SingleMu May 10 ReReco	2011A	211	160404–163869
SingleMu PromptReco v4	2011A	955	165071–167913
MuHad Aug 05 ReReco	2011A	390	170249–172619
MuHad PromptReco v6	2011A	707	172620–173692
MuHad PromptReco v1	2011B	2714	175860–180252

5.3 Simulated event samples

The simulated event samples are generated with either MADGRAPH [117], PYTHIA [118], or POWHEG [119–121]. Generated events from MADGRAPH and POWHEG are subjected to the parton shower and hadronisation programs of PYTHIA 6 [122].

Table 5.2 lists the simulated datasets that are used as signal samples (Z′ and KK gluon with different generated masses and widths) or as default background samples. The second column contains the names of the used Monte Carlo generator programs, and the third column shows the labels that are used in the plot legends.

For reasons of computing time and availability of disk space, several samples are produced with additional requirements on generator level to reduce the numbers of events to be generated. Top pair events, Z′ events, and single top events are generated inclusively. W-plus-jets events only consider leptonic decays of the W boson. Similarly, in Z/γ^*-plus-jets events, only leptonic decays of the Z boson (or γ^*) are allowed. In addition, the invariant mass of the lepton pair must be greater than 50 GeV to remove the contribution from γ^* production with low-p_{T} leptons. The expected fraction of events passing the full event selection with a lepton pair mass of less then 50 GeV is negligible.

Table 5.2: Description of simulation datasets with phase-space cuts, according generator names, and plot labels.

Process	Event generator	Label
Signal datasets		
Z′ 500 GeV ($\Gamma/m_{Z'} = 1\%$)	MADGRAPH	Z′ 0.5 TeV
Z′ 500 GeV ($\Gamma/m_{Z'} = 10\%$)	MADGRAPH	
Z′ 750 GeV ($\Gamma/m_{Z'} = 1\%$)	MADGRAPH	Z′ 0.75 TeV
Z′ 1000 GeV ($\Gamma/m_{Z'} = 1\%$)	MADGRAPH	Z′ 1 TeV
Z′ 1000 GeV ($\Gamma/m_{Z'} = 10\%$)	MADGRAPH	
Z′ 1250 GeV ($\Gamma/m_{Z'} = 1\%$)	MADGRAPH	Z′ 1.25 TeV
Z′ 1500 GeV ($\Gamma/m_{Z'} = 1\%$)	MADGRAPH	Z′ 1.5 TeV
Z′ 1500 GeV ($\Gamma/m_{Z'} = 10\%$)	MADGRAPH	
Z′ 2000 GeV ($\Gamma/m_{Z'} = 1\%$)	MADGRAPH	Z′ 2 TeV
Z′ 2000 GeV ($\Gamma/m_{Z'} = 10\%$)	MADGRAPH	
KK gluon 1000 GeV	PYTHIA 8	
KK gluon 1500 GeV	PYTHIA 8	
KK gluon 2000 GeV	PYTHIA 8	
Background datasets		
$t\bar{t}$	MADGRAPH	$t\bar{t}$
W ($\rightarrow l\nu$) + jets	MADGRAPH	W$\rightarrow$lν [c]
Z/γ^* ($\rightarrow l^+l^-$) + jets ($m(l^+l^-) > 50$ GeV)	MADGRAPH	Z/$\gamma \rightarrow$ l$^+$l$^-$ [c]
Single top t-channel ($W \rightarrow l\nu$)	POWHEG [120]	Single-top
Single top s-channel ($W \rightarrow l\nu$)	POWHEG [120]	Single-top
Single top tW-channel ($W \rightarrow l\nu$)	POWHEG [121]	Single-top
Multijet μ enriched ($p_{\mathrm{T}}^{\mu} > 15$ GeV, $\hat{p_{\mathrm{T}}} > 20$ GeV)	PYTHIA 6	Multijet
Multijet $B/C \rightarrow e^a$ ($\hat{p_{\mathrm{T}}}$ 20-30 GeV)	PYTHIA 6	Multijet
Multijet $B/C \rightarrow e^a$ ($\hat{p_{\mathrm{T}}}$ 30-80 GeV)	PYTHIA 6	Multijet
Multijet $B/C \rightarrow e^a$ ($\hat{p_{\mathrm{T}}}$ 80-170 GeV)	PYTHIA 6	Multijet
Multijet EM enriched[b] ($\hat{p_{\mathrm{T}}}$ 20-30 GeV)	PYTHIA 6	Multijet
Multijet EM enriched[b] ($\hat{p_{\mathrm{T}}}$ 30-80 GeV)	PYTHIA 6	Multijet
Multijet EM enriched[b] ($\hat{p_{\mathrm{T}}}$ 80-170 GeV)	PYTHIA 6	Multijet

Samples generated inclusively if not marked otherwise. All p_{T} cut values are given in GeV. l denotes all leptonic decays, i.e. $l = e, \mu, \tau$.

a: Generator cut on in-flight-decays of b and c hadrons.

b: Enriched in conversion electrons.

c: The plot labels depend on the heavy flavour content as outlined in the text.

Table 5.3: Simulated datasets to study the effect of systematic uncertainties.

Process/Dataset	Event generator
$\mathrm{t\bar{t}}$ Q^2 scale up	MADGRAPH
$\mathrm{t\bar{t}}$ Q^2 scale down	MADGRAPH
$\mathrm{t\bar{t}}$ matching threshold up	MADGRAPH
$\mathrm{t\bar{t}}$ matching threshold down	MADGRAPH
$\mathrm{t\bar{t}}$ NLO generator	POWHEG [119]
W + jets Q^2 scale up	MADGRAPH
W + jets Q^2 scale down	MADGRAPH

Table 5.3 contains the details of the simulated datasets that are used to model the effects of systematic uncertainties related to the generation of events.

Table 5.4: Settings for systematic variations of MC simulation samples.

Process	Matching threshold	Variation up	Variation down
$\mathrm{t\bar{t}}$	20 GeV	40 GeV	10 GeV
$W/Z/\gamma^*$ + jets	10 GeV	20 GeV	5 GeV
Factorisation/renormalisation scale			
$\mathrm{t\bar{t}}$	$Q^2 = m_t^2 + \Sigma p_{\mathrm{T}}(\mathrm{jet})^2$	$\times 4$	$\div 4$
$W/Z/\gamma^*$ + jets	$Q^2 = m_{W/Z}^2 + \Sigma p_{\mathrm{T}}(\mathrm{jet})^2$	$\times 4$	$\div 4$

A summary of the settings used for the evaluation of generator systematic uncertainties is given in table 5.4. The first section in the table shows the default values and the variations of the matching threshold, the scale below which the description of jets is given from the matrix element simulation to the parton shower in PYTHIA, with different settings for $\mathrm{t\bar{t}}$ and $W/Z/\gamma^*$-plus-jets samples. The next section lists the values used for the variation of the factorisation and renormalisation scales (denoted as Q^2 scales), which are varied simultaneously. The scales are varied by a factor of 2 and $1/2$, corresponding to a variation of the Q^2 by respective factors of 4 and $1/4$. Details of the choice of the varied settings are given in reference [123].

Table 5.5 summarises the production cross sections of the considered background processes. In addition, the order in perturbation theory in which they are calculated is given and either the code with which they were calculated (MCFM, PYTHIA 6, MADGRAPH) or the according publication for the inclusive calculation.

5.4 Event Selection

5.4.1 Triggers

The general strategy to trigger events is to use as simple and stable trigger definitions as possible. Trigger requirements are applied to both data and simulated events. For simulated events

Table 5.5: Cross sections for SM background samples.

Process	Cross section [pb]
$\mathrm{t\bar{t}}$	157.5^{+23}_{-24} (NLO) [124]
Single top t ($W \to l\nu$)	64.57 $\pm$ 2.58 (approx. NNLO) [32]
Single top s ($W \to l\nu$)	4.63 $\pm$ 0.20 (approx. NNLO) [34]
Single top tW ($W \to l\nu$)	15.74 $\pm$ 1.21 (approx. NNLO) [33]
W ($\to l\nu$) + jets	31314 $\pm$ 1558 (NNLO) [35]
Z/γ^* ($\to l^+l^-$) + jets ($m(l^+l^-) > 50$ GeV)	3048 $\pm$ 132 (NNLO) [35]
Multijet μ enriched ($p_{\mathrm{T}}^{\mu} > 15$ GeV, $\hat{p_{\mathrm{T}}} > 20$ GeV)	84679 (LO) [117]
Multijet B/C$\to$E ($\hat{p_{\mathrm{T}}}$ 20-30 GeV)	132160, PYTHIA 6
Multijet B/C$\to$E ($\hat{p_{\mathrm{T}}}$ 30-80 GeV)	136804, PYTHIA 6
Multijet B/C$\to$E ($\hat{p_{\mathrm{T}}}$ 80-170 GeV)	9360, PYTHIA 6
Multijet EM enriched ($\hat{p_{\mathrm{T}}}$ 20-30 GeV)	2454400, PYTHIA 6
Multijet EM enriched ($\hat{p_{\mathrm{T}}}$ 30-80 GeV)	3866200, PYTHIA 6
Multijet EM enriched ($\hat{p_{\mathrm{T}}}$ 80-170 GeV)	139500, PYTHIA 6

in both the electron and the muon channel, trigger efficiency corrections are applied that were derived on 2011 data as outlined below.

To select top-pair events with muons, different types of trigger criteria are used for the different run ranges. This follows from the requirement that the trigger elements need to be unprescaled over the regarded run ranges, i.e. each recorded collision event needs to be considered for triggering. For the first ~ 1 fb^{-1} of data, a trigger criterion is applied that requires a single isolated muon. The muon reconstructed in the trigger sequence has to fulfil $p_T > 17$ GeV and pass an isolation criterion based on the transverse momenta of tracks in a cone around the muon axis, $trk_{iso} < trk_{iso}^{max}$. The threshold for the isolation criterion varies with the muon pseudorapidity. The details of the muon reconstruction and isolation requirements were adapted over time; they manifest in the version number of the trigger.

For later runs, a similar isolated muon trigger with the additional requirement of the presence of at least two or three jets with a threshold of $p_{\mathrm{T}}^{\mathrm{jet}} > 30$ GeV is used. The deployment of these muon-plus-jets triggers allows to keep events with relatively low muon p_{T}, as the p_{T} criteria for single isolated muon triggers were increased during the 2011 data-taking to cope with the increase of the instantaneous luminosity over time. In principal, a supplemental trigger with a non-isolated muon trigger definition with a higher p_{T} threshold would yield a slightly increased trigger efficiency for signal events, but this would imply the mixing of different primary datasets and is therefore not used for the sake of simplicity. While the usage of single muon triggers would avoid the complication of using trigger criteria involving jets, increasing the muon p_{T} threshold would lead to a sizeable loss of signal efficiency for all signal masses.

The complete list of muon-plus-jets triggers that are used is given in the following list together with the maximum run number for which the trigger requirement is applied. Note that the runs where single muon triggers are used are taken from the *SingleMu* datasets, whereas events with cross-trigger requirements are taken from the *MuHad* datasets.

- HLT_IsoMu17_v5 ($\leq$ 163269)
- HLT_IsoMu17_v6 ($\leq$ 163870)
- HLT_IsoMu17_v8 ($\leq$ 165969)
- HLT_IsoMu17_v9 ($\leq$ 166345)
- HLT_IsoMu17_v10 ($\leq$ 166373)
- HLT_IsoMu17_v9 ($\leq$ 167077)
- HLT_IsoMu17_v11 ($\leq$ 167914)
- HLT_IsoMu17_TriCentralJet30_v5 ($\leq$ 172619)
- HLT_IsoMu17_DiCentralJet30_v5 ($\leq$ 173198)
- HLT_IsoMu17_eta2p1_TriCentralJet30_v1 ($\leq$ 173656)
- HLT_IsoMu17_eta2p1_DiCentralJet30_v1 ($\leq$ 173692)
- HLT_IsoMu17_eta2p1_TriCentralJet30_v1 ($\leq$ 178419)
- HLT_IsoMu17_eta2p1_TriCentralPFJet30_v2 ($\leq$ 179958)
- HLT_IsoMu17_eta2p1_TriCentralPFJet30_v3 ($\leq$ 180252)

In summary, 24% of the data events are taken with the single muon trigger; 11% with the muon-plus-two-jet trigger; and the remaining 64% with muon-plus-three-jet triggers, where for the last 16% the jet definition in the trigger was switched to PF jets.

To emulate the data triggers in simulated events, the events are weighted according to a mixture of the three different trigger criteria. For simulated samples from the Summer 11 production campaign, the isolation part is always taken from the single isolated muon trigger (HLT_IsoMu17_v5). For simulated samples from the Fall 11 campaign, the trigger elements correspond to the cross triggers with restricted η range for the muon trigger (HLT_IsoMu17_eta2p1_TriCentralJet30_v1, HLT_IsoMu17_eta2p1_DiCentralJet30_v1) and a higher version for the single isolated muon trigger with additional quality criteria (HLT_IsoMu17_v14). These quality criteria induce a difference in efficiency between the different trigger versions. A correction for the difference between the two triggers is applied to simulated samples from the Summer 11 campaign. The PF-based jet triggers have not been simulated in the used simulated samples, and the efficiency is therefore derived from collision data.

In the electron channel, a cross trigger is used that requires an electron and three central jets with a minimum p_{T} of 30 GeV. Furthermore, the electron has to have a transverse momentum $p_{\mathrm{T}} > 25$ GeV and has to pass a set of electron identification cuts. For later runs, additional isolation criteria have been added to keep the trigger rates at a manageable value. The complete list of electron-plus-jets triggers is given in the following list:

- HLT_Ele25_CaloIdVT_TrkIdT_CentralTriJet30_v1 ($\leq$ 161216)
- HLT_Ele25_CaloIdVT_TrkIdT_CentralTriJet30_v2 ($\leq$ 163269)

- HLT_Ele25_CaloIdVT_TrkIdT_TriCentralJet30_v3 ($\leq$ 165969)
- HLT_Ele25_CaloIdVT_CaloIsoT_TrkIdT_TrkIsoT_TriCentralJet30_v1 ($\leq$ 166967)
- HLT_Ele25_CaloIdVT_CaloIsoT_TrkIdT_TrkIsoT_TriCentralJet30_v2 ($\leq$ 167913)
- HLT_Ele25_CaloIdVT_CaloIsoT_TrkIdT_TrkIsoT_TriCentralJet30_v4 ($\leq$ 173235)
- HLT_Ele25_CaloIdVT_CaloIsoT_TrkIdT_TrkIsoT_TriCentralJet30_v5 ($\leq$ 178380)
- HLT_Ele25_CaloIdVT_CaloIsoT_TrkIdT_TrkIsoT_TriCentralPFJet30_v2 ($\leq$ 179889)
- HLT_Ele25_CaloIdVT_CaloIsoT_TrkIdT_TrkIsoT_TriCentralPFJet30_v3 ($\leq$ 180252)

In 7.6% of the total data, the non-isolated electron trigger part is used, and in the last 16% of the data, jets in the trigger are reconstructed with the PF algorithm. In simulated events from the Summer 11 campaign, a non-isolated electron-plus-three-jet trigger is required. In addition, a single isolated electron trigger with the same ID and isolation definition is required with a weight corresponding to the fraction of the data where isolated electron-plus-jets triggers were used. In simulated events from the Fall 11 production, trigger elements corresponding to the trigger elements in data are used (HLT_Ele25_CaloIdVT_CaloIsoT_TrkIdT_TrkIsoT_TriCentral-Jet30_v5 and HLT_Ele25_CaloIdVT_TrkIdT_TriCentralJet30_v8). In contrast to the muon part of the muon-plus-jets triggers, the electron efficiency in simulated events is compatible between Summer 11 and Fall 11 samples.

5.4.2 Primary interaction vertex and selection of good collision events

The primary interaction vertex with the highest sum of the transverse momenta of the associated tracks needs to fulfil a number of criteria to classify the event as a pp collision event. First, the number of degrees of freedom of the adaptive vertex fit must be higher than 4, $N_{dof} > 4$. Then, the compatibility with originating from central pp collisions is tested with two criteria. The longitudinal distance to the origin needs to be smaller than $z = 24$ cm and the radial distance smaller than $\rho = 2$ cm. The reconstructed vertices are also used for the association of particle flow objects; only particles associated to the primary interaction vertex are used for the further reconstruction.

Events are rejected if they are affected by anomalous noise in the hadronic calorimeters, as tested by dedicated filters, or by so-called *beam scraping*. Beam scraping is induced by collisions of one of the proton beams with parts of the detector structures or the beam pipe, leading to a high occupancy of the inner tracking detectors. Both anomalous noise and beam scraping occur only rarely and do hence not lead to a significant reduction of the event rate.

5.4.3 Muons

For the muon selection, reconstructed particles are used as input that are classified as muons by the particle flow reconstruction. In the particle flow algorithm, an explicit criterion is used to choose whether muons are regarded as prompt (or isolated), i.e. coming from the primary interaction vertex, e.g. from the decay of a W boson, or whether these are secondary (or non-isolated), e.g. coming from a decay of a hadron in a jet. For this, an isolation variable is constructed that takes as input the reconstructed muon (μ) and the objects from the particle flow algorithm in a cone with size $R = 0.4$ around the muon, charged hadrons (ch), neutral hadrons (nh), and photons (γ). The so-called *relative isolation* is then defined as the ratio of the isolation deposits in a given cone around the muon direction and the muon p_T,

$$r_\mathrm{iso} = \frac{p_\mathrm{T}^\mathrm{ch} + E_T^\mathrm{nh} + E_T^\gamma}{p_\mathrm{T}^\mu}. \tag{5.1}$$

Muons with $r_\mathrm{iso} < 0.15$ and $p_\mathrm{T} > 10$ GeV are regarded as isolated; all other muons associated with the primary interaction vertex are direct input for the jet clustering algorithms. The collection of non-isolated muons is still retained for further analysis, most importantly to study the properties of multijet events.

Further requirements are made to identify good muons from decays of W bosons. The muon must be reconstructed with two algorithms, the tracker-only and the global reconstruction, the latter with at least two matched segments in the muon stations to match the trigger conditions. The global track fit needs to have good quality as expressed by the χ^2 divided by the number of the degrees of freedom, $\chi^2/N_\mathrm{dof} > 10$, and the track must be reconstructed from at least one hit in the muon detectors and from more than 10 hits in the silicon trackers of which at least one must be in the pixel detector. To reject badly reconstructed muons, cosmic muons, or muons from additional pp collisions, the longitudinal distance to the primary vertex must fulfil $|\Delta z| < 1$ cm. Similarly, the distance of closest approach of the muon to the beam spot in the transverse plane is used to reject muons from secondary decays, $d_{xy} < 0.02$ cm. All selection criteria described so far have a very high signal efficiency, $\varepsilon \lesssim 100\%$.

Then, muons are required to be in the fiducial region of the muon trigger, $|\eta| < 2.1$, and to have a transverse momentum $p_\mathrm{T} > 20$ GeV. Though the muon system extends to $|\eta| = 2.4$, the trigger and reconstruction efficiencies are reduced beyond $|\eta| = 2.1$. Furthermore, muons from $\mathrm{t\bar{t}}$ production (and even more so from heavy resonances) are central due to the high scale of the process. The p_T criterion needs to be beyond the p_T threshold of the muon trigger (17 GeV) to avoid a dependence on the modelling of the turn-on characteristics of the trigger that would introduce additional systematic uncertainties. In addition, the p_T criterion provides additional rejection of multijet and W-plus-jets events.

Figure 5.1 shows a comparison of the p_T and η distributions of the muon for different simulated samples. The p_T distribution has a similar shape for all background events, whereas it is slightly harder for the shown Z′ events for $m'_\mathrm{Z} = 1$ TeV. The p_T distribution for Z′ events is still falling from the trigger-induced threshold of 20 GeV. While increasing the muon p_T threshold to e.g. 30 GeV would reject $\sim 15\%$ of the background events, it would also reject 10% of the

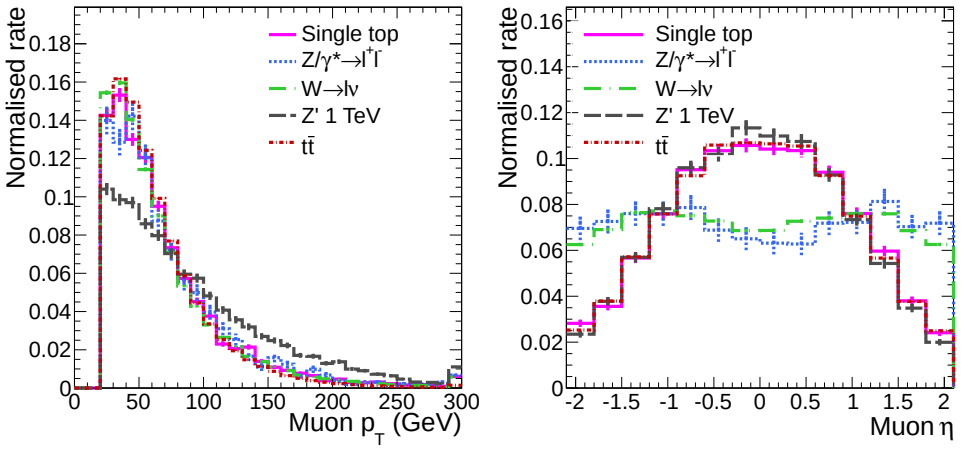

Figure 5.1: Comparison of the muon p_{T} distribution (left) and the muon η distribution (right) in muon-plus-jets events with at least 4 selected jets for different simulated samples.

signal events for $m'_{\mathrm{Z}} = 1$ TeV and would hence lead to a reduction of the sensitivity. Most of the muons can be found in the central detector region for $\mathrm{t\bar{t}}$, single top and Z′ events. Restricting the η range to $|\eta| < 2.1$ does therefore not significantly reduce the selection efficiency. For W- and Z-plus-jets events, the muon η distribution is approximately flat for the considered η range, with a preferred value of $\eta \sim 1.2$. One could improve the rejection of these background events by only selecting events with central muons, but the relative loss of signal events would not outweigh the suppression of W- and Z-plus-jets events, which are sub-dominant background processes.

Finally, the muons are required to fulfil a relative isolation criterion to reduce the background from multijet events, $r_{\mathrm{iso}} < 0.125$. Other commonly deployed isolation criteria are based on the sum of energies or momenta in a cone around the muon direction (e.g. the numerator in equation 5.1), which are however less efficient at high muon p_{T}. Since the muon p_{T} spectrum in multijet events is rapidly falling compared to $\mathrm{t\bar{t}}$ events or, more importantly, signal events at high invariant mass, relative isolation criteria improve the search sensitivity by increasing the signal efficiency at a similar background rejection. The relative isolation variable is based on information from the PF algorithm. This proves to be more optimal than using subdetector-based energy deposits or tracks, for which the signal efficiency is reduced at a given level of multijet background rejection. Furthermore, subdetector-based isolation criteria suffer from an increased dependence on pile-up interactions. The exact relative isolation value has not been optimised for this analysis, but is based on a common selection for top quark analyses in CMS. It has however been studied that changing the value has insignificant impact on the statistical sensitivity of this analysis.

5.4.4 Electrons

Particles classified as isolated electrons in the particle flow algorithm are used as input for the electron selection; all others are directly clustered into jets. Electrons need to pass a loose selection criterion used in the particle flow electron reconstruction and have a transverse momentum

$p_{\mathrm{T}} > 10$ GeV. In addition, a relative isolation variable is defined in the same way as in the muon case,

$$r_{\mathrm{iso}} = \frac{p_{\mathrm{T}}^{\mathrm{ch}} + E_T^{\mathrm{nh}} + E_T^{\mathrm{ph}}}{p_{\mathrm{T}}^{e}}, \tag{5.2}$$

where the transverse energies or transverse momenta of the charged and neutral hadrons as well as the photons are again summed in a cone of $R = 0.4$. Electrons with $r_{\mathrm{iso}} < 0.15$ are regarded as isolated in the particle flow algorithm.

Further requirements are made to obtain a sample of well-identified and isolated electrons. They need to have a transverse momentum $p_{\mathrm{T}} > 30$ GeV and be within the tracker acceptance, $|\eta| < 2.5$, but not within the overlap region between the EB and the EE, i.e. the pseudorapidity of the associated supercluster must lie outside the region $1.4442 < |\eta| < 1.5660$. The requirement on the transverse momentum is tighter than for muons due the higher trigger p_{T} threshold of 25 GeV. It also improves the rejection of multijet events, which constitute a more important background in the electron-plus-jets channel. Prompt electrons are selected by requiring that the transverse distance to the primary vertex fulfils $d_{xy} < 0.02$ cm and that the longitudinal distance to the primary vertex is small, $|\Delta z| < 1$ cm.

The identification of electrons is based on categories based on the electron quality for which variables are defined that distinguish electrons from background, e.g. from hadronic jets, photons, or hadrons [101]. The discriminating variables are based on the shower shape of the electron (spread of ECAL shower in η; amount of energy deposited in HCAL compared to energy deposited in ECAL in the direction of the electron) and on the compatibility of the electron track with the reconstructed ECAL cluster (distance of track and cluster in ϕ and η direction; ratio of energy deposited in ECAL cluster and track momentum E/p). Due to the different properties of the tracker and ECAL in the barrel and endcap regions and due to the high amount of tracker material, the application of selection criteria with different numerical values in different categories increases the separation of electrons from background.

The electrons are categorised by either being in the barrel or in the endcap, by the amount of bremsstrahlung, and by the ratio of energy deposited in the ECAL cluster and the track momentum E/p. The amount of bremsstrahlung is determined by summing up the energy from the radiated photons in the electron reconstruction. A particle with a large amount of radiation is e.g. much more likely an electron than a non-radiating particle; hence looser identification criteria are possible at the same level of background rejection. In addition, the criteria are determined continuously as a function of electron p_{T}. Several sets of the numerical values are obtained by individual optimisation at fixed signal-to-background ratios. Here, the set labelled "HyperTight" is used, which combines a high background rejection of the order of 10^{-2} with a signal efficiency of up to 90% at high electron p_{T}.

Additional criteria are necessary to reject non-prompt electrons due to photons converting into an electron-positron pair. First, electron tracks are required to have no missing hit in the innermost layer of the pixel detector, providing rejection against photon conversions in the tracker volume. Second, there may not be a reconstructed track which passes both of the following requirements: the distance of closest approach in the transverse plane to the primary vertex fulfils

$d_{xy} < 0.02$ cm, and the cotangent of the angle between this reconstructed track and the electron track passes the requirement $\Delta cot(\theta) < 0.02$. These criteria exploit that an electron-positron pair from a photon conversion originates from the same vertex, with the tracks being bent in opposite directions by the magnetic field.

Additional rejection of multijet background events is obtained by requiring that the electrons are well isolated, $r_{\text{iso}} < 0.1$. The definition of relative isolation and the motivation for using a relative isolation criterion instead of an absolute criterion or a subdetector-based one are the same as for muons. The numerical value is again chosen to be in line with standards defined in CMS analyses of top quark pair production.

5.4.5 Vetoes on events with additional isolated leptons

Events with additional isolated leptons are removed to reduce the amount of background from either Z-plus-jets events or dileptonic $\mathrm{t\bar{t}}$ events. $\mathrm{Z'} \to \mathrm{t\bar{t}}$ events with dileptonic $\mathrm{t\bar{t}}$ decay are not necessarily background; however, there exist dedicated analyses carried out by the CMS collaboration that are optimised for this final state. The rejection of second leptons leads to a very small reduction of the signal efficiency for lepton-plus-jets events, $\varepsilon < 1\%$, but leads to a significant reduction of the number of Z-plus-jets events.

In both the electron-plus-jets and muon-plus-jets selections, events with a muon (an additional one in the muon channel) fulfilling looser identification and selection requirements are rejected. This muon is defined by requiring that it originates from the global reconstruction and that it satisfies $p_{\mathrm{T}} > 10$ GeV, $|\eta| < 2.5$, and $r_{\text{iso}} < 0.2$.

In the muon-plus-jet channel, events with electrons passing the requirements $p_{\mathrm{T}} > 15$ GeV, $|\eta| < 2.5$ and $r_{\text{iso}} < 0.2$ are vetoed. Electron-plus-jet events are disregarded if they contain either a second isolated electron as defined above, or a secondary electron that, combined with the first electron candidate, yields a reconstructed Z boson with a mass close to the nominal Z boson mass, 76 GeV $< m_Z < 106$ GeV. The secondary electron is required to have $p_{\mathrm{T}} > 20$ GeV, $|\eta| < 2.5$, not to lie in the transition region between the ECAL barrel and the ECAL endcap, and to fulfil a loose relative isolation criterion, $r_{\text{iso}} < 1.0$.

5.4.6 Jets

Top quark pair events in the lepton-plus-jets channel contain four jets from the $\mathrm{t\bar{t}}$ decay, which are mostly central: two light-flavoured jets and one b jet from the hadronically decaying top quark, and one b jet from the leptonically decaying top quark. Jets are reconstructed with the anti-kt clustering algorithm using a cone size of $R = 0.5$ [102]. The algorithm takes all particles from the particle flow reconstruction attached to the primary vertex and not flagged as isolated leptons into account for the clustering. As common in top quark analyses at CMS, the jets must have a minimum transverse momentum of $p_{\mathrm{T}} > 30$ GeV and must be within the tracker acceptance, i.e. $|\eta| < 2.4$. On the one hand, these requirements ensure that only well-measured jets are considered for the analysis, that the influence of the jet energy scale and

resolution uncertainties are reduced (which are higher for jets at low transverse momentum or in the forward region), and that jets due to higher order matrix elements ($\mathrm{t\bar{t}}$ plus jets production) or from initial and final state radiation are suppressed. On the other hand, in a significant fraction of events, only three of the four jets from the $\mathrm{t\bar{t}}$ decay pass these selection criteria.

In the lepton-plus-jets trigger algorithms, jets are accepted if they have a transverse momentum $p_{\mathrm{T}} > 30$ GeV. The lepton-plus-jet triggers deploy a calorimeter-based jet clustering algorithm, whereas the offline jet reconstruction is performed using the PF algorithm. To avoid a dependence on the correct modelling of the correlation between calorimeter-based jets in the trigger and PF-based jets at analysis level, tight requirements need to be placed on the jets such that potential resolution and modelling effects are reduced. Therefore, the leading three jets need to pass $p_{\mathrm{T}} > 50$ GeV. All other jets, which are needed for the event reconstruction and the counting of the number of jets, need to fulfil $p_{\mathrm{T}} > 30$ GeV. To enhance the reduction of W-plus-jets events, the p_{T} criterion for the first jet is raised to a higher transverse momentum of $p_{\mathrm{T}} > 70$ GeV. After the statistical evaluation, this requirement was found to yield an optimal expected sensitivity for a broad range of considered Z' signal masses. Generally, varying the p_{T} requirements on the three leading jets only weakly affects the estimated sensitivity, whereas an increase of the p_{T} threshold for the fourth leading jet would lead to a reduced sensitivity.

In addition to the basic acceptance criteria, jets need to fulfil the following jet identification requirements to exclude jets from detector noise or other non-physical sources. The jets must consist of more than one particle flow object and have a non-zero charged hadron energy fraction, $f_{\mathrm{CH}} > 0$. They may neither be clustered from only photons, charged hadrons, or neutral hadrons. This is enforced by requiring that the fractions of charged electromagnetic energy f_{CE}, of neutral hadron energy f_{NH}, and of neutral electromagnetic energy f_{NE} are at most 99%, $f_{\mathrm{CE}} < 0.99, f_{\mathrm{NH}} < 0.99$, and $f_{\mathrm{NE}} < 0.99$. The efficiency of the jet identification criteria is higher than 99% per jet.

Due to the particle flow reconstruction, no dedicated disambiguation of jets and isolated leptons is necessary as all objects are identified in a coherent way.

5.4.7 Missing transverse energy

To further enhance the rejection of multijet and Z-plus-jets events, a requirement of a minimum amount of the missing transverse energy, $E_{\mathrm{T}}^{\mathrm{miss}} > 20$ GeV, is applied. Due to the neutrino, only a small fraction of signal and $\mathrm{t\bar{t}}$ events has a missing transverse energy of less than 20 GeV, while most of the multijet events have low $E_{\mathrm{T}}^{\mathrm{miss}}$ as no primary neutrinos or other undetectable particles are produced in the hard interaction. Besides suppressing background events that are subject to considerable systematic uncertainties, the low $E_{\mathrm{T}}^{\mathrm{miss}}$ region $E_{\mathrm{T}}^{\mathrm{miss}} < 20$ GeV is used as a control region to estimate the amount of multijet background.

Figure 5.2 shows the $E_{\mathrm{T}}^{\mathrm{miss}}$ distributions for different simulated samples in muon-plus-jets events with 3 or at least 4 selected jets. More than half of the multijet events and $\sim 40\%$ of the Z-plus jets events have $E_{\mathrm{T}}^{\mathrm{miss}} < 20$ GeV, whereas Z' events ($m'_{\mathrm{Z}} = 1$ TeV) have a significantly harder $E_{\mathrm{T}}^{\mathrm{miss}}$ distribution with less than 5% of the events failing the $E_{\mathrm{T}}^{\mathrm{miss}}$ criterion. W-plus-jets and $\mathrm{t\bar{t}}$ events have similar $E_{\mathrm{T}}^{\mathrm{miss}}$ distributions. Due to the hard neutrino, the $E_{\mathrm{T}}^{\mathrm{miss}}$ spectrum is

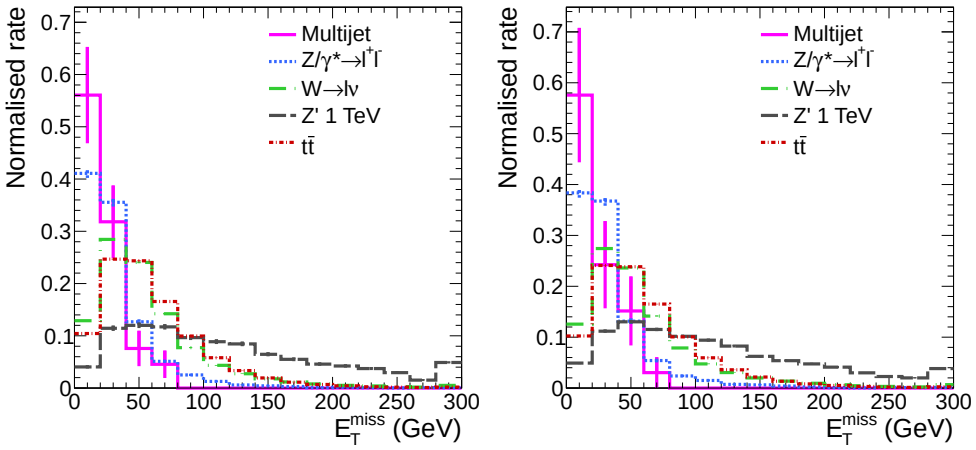

Figure 5.2: Comparison of the $E_{\mathrm{T}}^{\mathrm{miss}}$ distribution in muon-plus-jets events with 3 selected jets (left) and at least 4 selected jets (right) for different simulated samples.

significantly harder than for Z-plus-jets and multijet events. Though the $E_{\mathrm{T}}^{\mathrm{miss}}$ distribution is much broader for Z′ events with high Z′ masses, the most probable value is $E_{\mathrm{T}}^{\mathrm{miss}} \sim 50$ GeV for all events with a real W boson (Z′, $\mathrm{t\bar{t}}$, W-plus-jets). Therefore, a tighter $E_{\mathrm{T}}^{\mathrm{miss}}$ requirement would lead to a significant reduction of the signal efficiency.

5.4.8 Identification of b quark jets

Events from top quark pair production yield two b jets, whereas most background processes have no b quark content. Therefore, b-tagging is used to increase the statistical sensitivity by requiring at least one jet to be b-tagged in three-jet events, and by categorising events according to the number of b-tagged jets (0, 1, and at least 2 b-tagged jets) in events with at least four jets. Jets coming from b quarks are identified with the "Simple Secondary Vertex" algorithm described in the *Reconstruction* chapter, using the working point "Medium" that is defined by a nominal misidentification rate of 1% for light-flavoured jets.

A comparison of the distribution of the number of b-tagged jets for different simulated samples is shown in figure 5.3 for muon-plus-jets events with 3 and at least 4 selected jets. The comparison clearly shows the good separation between processes with top quarks ($\mathrm{t\bar{t}}$, single top, and Z′ production) and processes with small contributions from b jets (W-plus-jets and Z-plus-jets production). About 50% of the events with top quarks have exactly one b-tagged jet, and more than 30% of the three-jet events and more than 35% of the four-jet events from $\mathrm{t\bar{t}}$ and Z′ production contain at least two b-tagged jets. For single top events, the probability of having two b-tagged jets is slightly smaller than for $\mathrm{t\bar{t}}$ events since there may only be one b quark jet, depending on the production process.

5.4.9 Summary of acceptance criteria.

A summary of the acceptance criteria is given in table 5.6. Events are selected if they contain either a well-identified and isolated muon or electron, at least 3 central jets, and a certain amount

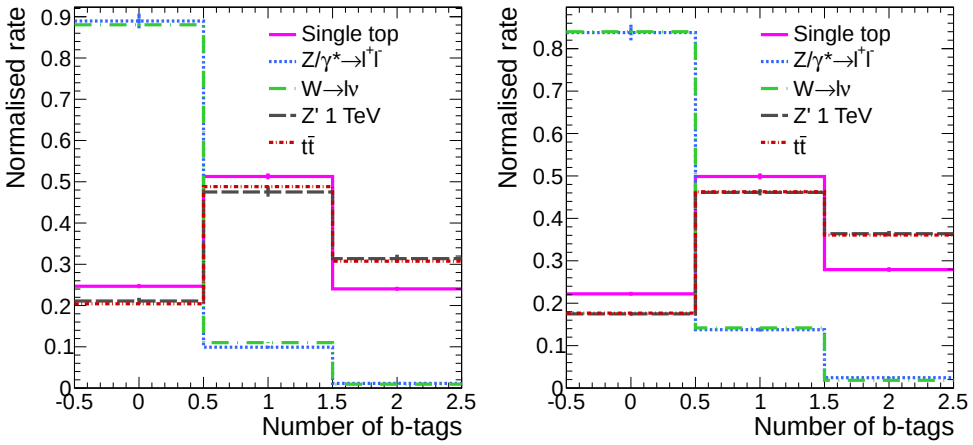

Figure 5.3: Comparison of the distribution of the number of b-tagged jets in muon-plus-jets events with 3 selected jets (left) and at least 4 selected jets (right) for different simulated samples.

Table 5.6: Summary of acceptance criteria.

Criterion	**Muon**	**Electron**	**Jets**	$\boldsymbol{E_{\mathrm{T}}^{\mathrm{miss}}}$
Minimum p_{T}	20 GeV	30 GeV	70/50/50/(30) GeV	20 GeV
Maximum $\lvert\eta\rvert$	2.1	2.5	2.4	-
Number	1 muon or 1 electron		3 or ≥ 4	-
Feature	$r_{\mathrm{iso}} < 0.125$	$r_{\mathrm{iso}} < 0.1$	$(0), 1, \geq 2$ b-tags	-

of missing transverse energy. For events with 3 jets, at least one of the jets needs to be identified as a b quark jet.

5.5 Selection Results

In the following, the results of the event selection will be shown for simulated and data events with the aim to show how background events are rejected by the different selection criteria. In addition, this gives a broad idea of the agreement between data and simulation "out of the box", i.e. tuned with collision data from 2010 and approximate detector conditions from 2011. A full account of the compatibility between data and simulation can only be made after additional efficiency corrections are applied and after background events are studied in more detail. The results of the event selection in the different categories mentioned above will hence only be discussed in a subsequent chapter.

5.5.1 Expected and observed event yields in the muon channel

Table 5.7 shows the expected and observed event yields at several stages of the muon-plus-jets selection. The individual rows contain the yields after the following selection criteria, which

Table 5.7: Expected and observed event yields at several stages of the muon-plus-jets selection. The last column shows the sum of all background (BG) contributions. The last row shows the impact of the hadronic part of the trigger on events with 3 selected jets passing the $E_{\mathrm{T}}^{\mathrm{miss}}$ requirement.

Event yield	**Data**	**$\mathrm{t\bar{t}}$**	**W + Jets**	**Z + Jets**	**Single t**	**Multijet**	**Sum BG**
Data trigger	10362063	–	–	–	–	–	–
Simulated	–	784000	$156 \cdot 10^6$	$15 \cdot 10^6$	423000	$421 \cdot 10^6$	–
μ trigger	–	100729	6635002	1429285	24513	2292760	10482289
Muon	2439109	86317	5357505	1194712	20944	641068	7300545
μ veto	2212694	80797	5357444	655528	20380	638296	6752445
e veto	2205005	74666	5356207	654320	19752	638229	6743173
1 jet	379796	59551	643963	66450	10472	18544	798981
2 jets	180298	48813	167044	19717	6151	4989	246713
3 jets	57449	25778	24809	3493	1738	470	56288
$E_{\mathrm{T}}^{\mathrm{miss}}$	49488	23147	21691	2078	1561	218	48695
4 jets	27080	16351	8605	933	830	50	26769
Jet trigger	–	22828	21241	1951	1539	218	47777

are applied sequentially:

- Simulated: Total number of expected events given the theoretical cross section and the integrated luminosity.
- Data trigger: Presence of a 10 GeV muon or 20 GeV electron and primary vertex selection plus event filters. Requirement of run-dependent triggers for data.
- μ trigger: Presence of a 10 GeV muon or 20 GeV electron and primary vertex selection plus event filters. Requirement of isolated muon trigger for simulated samples.
- Muon: Complete muon selection including identification and isolation ($p_{\mathrm{T}} > 20$ GeV).
- μ veto: Veto of additional isolated muon.
- e veto: Veto of isolated electron.
- 1 jet: Requirement of at least 1 jet (leading jet $p_{\mathrm{T}} > 70$ GeV).
- 2 jets: Requirement of at least 2 jets (2nd leading jet $p_{\mathrm{T}} > 50$ GeV).
- 3 jets: Requirement of at least 3 jets (3rd leading jet $p_{\mathrm{T}} > 50$ GeV).
- $E_{\mathrm{T}}^{\mathrm{miss}}$: Requirement of minimum amount of $E_{\mathrm{T}}^{\mathrm{miss}}$ ($E_{\mathrm{T}}^{\mathrm{miss}} > 20$ GeV).
- 4 jets: Requirement of at least 4 jets (4th leading jet $p_{\mathrm{T}} > 30$ GeV)
- Jet trigger: Presence of muon-plus-three-jet trigger in simulated events, shown with respect to events with at least 3 jets and passing the $E_{\mathrm{T}}^{\mathrm{miss}}$ requirement.

When comparing the numbers of data events and the sum of the simulated events for the different minimum numbers of jets, one needs to take into account that simulated events and data have different trigger requirements applied. The data are taken with a mixture of trigger requirements (isolated muon, isolated muon plus 2 jets, isolated muon plus 3 jets), whereas only the isolated muon trigger part is required in simulated events. The total event numbers for data and simulation are therefore expected to differ up to the selection of at least 3 jets, for which the requirements have been chosen to be in the plateau region of the jet trigger part. The table is nevertheless presented in the given format to be able to follow the relative selection efficiencies for each step using simulated events.

The first and second rows show the event numbers after the requirement of the triggers in data or in the simulation. In simulated events, the isolation requirement in the muon trigger part adds an irreducible inefficiency of more than 10%. To circumvent this, one could either use non-isolated muon trigger parts, but this would induce a yet more significant inefficiency due to the then necessary increase of the muon p_{T} thresholds; or one applies different triggers for different muon p_{T} ranges. With the 2011 trigger menu, the latter would require a mixture of different primary datasets, as the *MuHad* datasets only contain isolated lepton-plus-jets cross triggers, and is hence non-practical. The main reduction of the event numbers in the muon selection is due to the acceptance criteria.

The vetoes of events with additional isolated leptons only lead to a significant reduction of the number of events for physics processes that produce additional isolated leptons. The requirement of no additional isolated muon reduces the number of Z-plus-jets events by $\sim 45\%$; it also reduces the number of $\mathrm{t\bar{t}}$ events by $\sim 6\%$. Except for a very small contribution from $Z \to \tau\tau$ events, isolated electrons are only expected in dileptonically decaying events from $\mathrm{t\bar{t}}$ or tW-channel single top production. The numbers of selected events show that the veto of events with an isolated electron indeed only reduce events from these sources, more precisely by $\sim 8\%$ for $\mathrm{t\bar{t}}$ production and by $\sim 3\%$ for single top production.

The requirement of at least one jet with $p_{\mathrm{T}} > 70$ GeV reduces the number of $\mathrm{t\bar{t}}$ events by about 20%. The contributions from the other background processes decrease significantly: Only $\sim 3\%$ of the multijet, $\sim 12\%$ of W- and Z-plus-jets events, and $\sim 50\%$ of the single top events are expected to pass the leading jet requirement. About 82% and 53% of the $\mathrm{t\bar{t}}$ events fulfil the selection criteria for the second and third leading jets, respectively. The requirement on the third leading jet p_{T}, which has its origin in the usage of jets in the muon-plus-jets trigger, therefore leads to a significant reduction of the selection efficiency for $\mathrm{t\bar{t}}$ events, but it does not reduce the statistical sensitivity of the analysis owing to its more significant impact on other background events. The number of W- and Z-plus-jets events is reduced to $\sim 5\%$ with respect to events fulfilling the leading jet requirement, the number of multijet events to $\sim 2.5\%$, and the number of single top events to $\sim 17\%$.

After the selection of at least 3 jets, the dominant expected contributions are from $\mathrm{t\bar{t}}$ and W-plus-jest events, with about 25 000 each compared to a total of $\sim 56\,000$ events expected from all simulated background samples. The number of data events is within a few per cent of the expected contribution from simulated events and therefore already shows good agreement prior to the efficiency corrections and multijet background estimation discussed below. The requirement of a certain amount of $E_{\mathrm{T}}^{\mathrm{miss}}$ reduces the contributions from events with a real

Table 5.8: Fraction of selected events at several stages of the muon-plus-jets selection for three benchmark Z' simulation samples. For comparison, the fraction of events in the muon-plus-jets decay channel is 15%.

Event yield [%]	**Z′ 0.75 TeV**	**Z′ 1 TeV**	**Z′ 1.5 TeV**	**Z′ 2 TeV**
μ trigger	12.5	11.9	9.7	7.4
Muon	10.8	10.4	8.4	6.3
μ veto	10.1	9.7	8.0	6.1
e veto	9.4	9.0	7.4	5.7
1 jet	8.9	8.8	7.3	5.6
2 jets	8.2	8.3	6.9	5.3
3 jets	5.5	5.9	4.8	3.7
$E_{\mathrm{T}}^{\mathrm{miss}}$	5.1	5.7	4.6	3.6
4 jets	3.5	4.0	3.2	2.5
Jet trigger	5.0	5.6	4.5	3.5

neutrino, i.e. $\mathrm{t\bar{t}}$, W-plus-jets and single top events, by $\sim 10\%$, but reduces the number of events from multijet and Z-plus-jets production by up to 50%. Finally, the requirement of a fourth leading jet with $p_{\mathrm{T}} > 30$ GeV further increases the purity of $\mathrm{t\bar{t}}$ events, reducing the number of W-plus-jets events by $\sim 60\%$ and the number of $\mathrm{t\bar{t}}$ events by only $\sim 30\%$.

The last row shows to what extent the jet trigger requirements, which are required in $\sim 80\%$ of the data events, are expected to reduce the event numbers for the given offline selection. Relative to 3-jet-events passing the $E_{\mathrm{T}}^{\mathrm{miss}}$ criterion, the muon-plus-jets trigger reduces the overall event numbers by $\sim 2\%$ and the rate of $\mathrm{t\bar{t}}$ events by only $\sim 1\%$.

It is notable that the expected fraction of multijet events predicted from simulation is already below the 1% level for events with at least four jets and at the 2% level for events with at least three jets. Due to the insufficient number of simulated events, the simulated samples will be replaced by events from a control region in data.

Table 5.8 shows the fractions of selected events from three simulated Z' samples at the same event selection stages. The relative selection efficiencies are calculated with respect to the full Z' event samples with inclusive $\mathrm{t\bar{t}}$ decays. However, only 15% of the events lead to the muon-plus-jets final state. Without considering the τ-plus-jets channel with possible decay of the τ lepton into a muon, the relative fraction of muon-plus-jets decays in the selected Z' event sample is already more than 90%. Therefore, comparing the fraction of selected events with a total fraction of 15% gives a good indication of the relative fraction of selected events from the muon-plus-jets decay channel.

The selection efficiencies are generally similar to those of SM $\mathrm{t\bar{t}}$ events. A significant reduction of the event selection efficiency is due to the isolation requirement in the muon trigger, leading to a decrease of the fraction of selected events by up to 40% for $m_{\mathrm{Z}'} \sim 2$ TeV. On the other hand, events from Z' production with $m_{\mathrm{Z}'}$ in the TeV region tend to have jets with high p_{T} such that the requirements on the two leading jets only lead to a reduction of the number of events of $\sim 13\%$ for $m_{\mathrm{Z}'} = 0.75$ TeV and $\sim 7\%$ for $m_{\mathrm{Z}'} \gtrsim 1.5$ TeV, whereas about

Table 5.9: Expected and observed event yields at several stages of the electron-plus-jets selection.

Event yield	Data	$t\bar{t}$	W + Jets	Z + Jets	Single t	Multijet	Sum MC
Simulated	–	784000	$156 \cdot 10^6$	$15 \cdot 10^6$	423000	$33 \cdot 10^9$	–
e+jet trigger	2006198	93822	853357	317883	13608	5829776	7108446
1 jet	1062402	78210	207013	81242	9448	1837625	2213538
2 jets	818863	68102	117211	40856	7227	1333023	1566420
3 jets	353432	40787	35166	9580	3147	411486	500165
Electron	56350	22251	20585	5925	1677	3489	53927
e veto	54889	22005	20583	4872	1670	3489	52620
Z veto	53087	21718	20543	3323	1656	3489	50730
Muon veto	52282	20978	20541	3309	1633	3489	49951
$E_{\mathrm{T}}^{\mathrm{miss}}$	42354	18629	17562	1807	1440	1354	40792
4 jets	22893	13261	7191	818	751	371	22393
e trigger	–	13230	7172	815	750	371	22337

35% of SM $t\bar{t}$ events are rejected. For the third leading jet, the efficiency of Z' events for 0.75 TeV $< m_{Z'} < 2$ TeV is $\sim 70\%$, but only $\sim 50\%$ for SM $t\bar{t}$ production. Independent of the Z' mass, about 70% of the Z' events with at least three selected jets have an additional jet passing the requirement for the fourth jet. This fraction is similar to SM $t\bar{t}$ production.

The maximum total event selection efficiency is reached for $m_{Z'} \sim 1$ TeV. With respect to the branching fraction for muon-plus-jets decays of $\sim 15\%$, up to 40% of the events pass the selection criteria until the selection of 3 jets. Dependent on the Z' mass, 3.6–5.7% of the Z' events are expected to fulfil the requirement of 3 selected jets, and about 2.5-4% the requirement of at least 4 selected jets.

5.5.2 Expected and observed event yields in the electron channel

Table 5.9 shows the expected and recorded numbers of events at each step of the electron-plus-jets selection for various simulated samples and the full 5.0 fb^{-1} dataset. As in the muon-plus-jets selection, a skimming criterion is applied before the first event selection step that requires the presence of at least one lepton with $p_{\mathrm{T}} > 10$ GeV or $p_{\mathrm{T}} > 20$ GeV lepton (muon or electron, respectively). The individual columns show the following selection stages:

- e+jet trigger: Presence of a 10 GeV muon or 20 GeV electron, primary vertex selection, and requirement of trigger needing an electron (25 GeV) and three jets (30 GeV). The electron part of the trigger has no isolation requirements applied in simulated events; a mixture of non-isolated and isolated electron triggers is used in data.
- 1 jet: Requirement of at least 1 jet (leading jet $p_{\mathrm{T}} > 70$ GeV).
- 2 jets: Requirement of at least 2 jets (2nd leading jet $p_{\mathrm{T}} > 50$ GeV).

- 3 jets: Requirement of at least 3 jets (3rd leading jet $p_{\mathrm{T}} > 50$ GeV).
- Electron: Complete isolated electron selection.
- e veto: Veto of 2nd isolated electron.
- Z veto: Veto of 2nd electron that yields a reconstructed Z boson close to the Z mass.
- Muon veto: Veto of loose isolated muon.
- 4 jets: Requirement of at least 4 jets (4th leading jet $p_{\mathrm{T}} > 30$ GeV)
- e trigger: Presence of electron-plus-three-jets trigger with electron isolation requirement in simulated events.

The numbers of selected events at the different event selection steps are in general similar to the muon-plus-jets selection, and the relative selection efficiencies of the identical requirements on the leading three jets and $E_{\mathrm{T}}^{\mathrm{miss}}$ are therefore not discussed here. Starting from the requirement of an isolated electron, there is overall a reasonable agreement between data and simulation.

The vetoes of events with additional leptons are different than in the muon-plus-jets channel. The requirement of no additional isolated electron with $p_{\mathrm{T}} > 30$ GeV reduces the number of selected $\mathrm{t\bar{t}}$ events by $\sim 1\%$ and the number of Z-plus-jets events by $\sim 18\%$, while it has negligible effects for the other samples. The Z boson veto further reduces the number of Z-plus-jets events by $\sim 32\%$, while only reducing the number of events from the other background processes that can produce two isolated electrons, $\mathrm{t\bar{t}}$ and single top, by about 1.5%. Finally, the veto of events with a loosely isolated muon only has notable effects for $\mathrm{t\bar{t}}$ and single top events and leads to a decrease of the number of selected events of $\sim 3\%$ for $\mathrm{t\bar{t}}$ and $\sim 1.5\%$ for single top production. Like in the muon case, the total inefficiency of the vetoes of additional leptons is well below 1% for events with no expected second isolated leptons.

After the requirement of $E_{\mathrm{T}}^{\mathrm{miss}} > 20$ GeV, which has similar effects as in the muon channel, there are about 4% more events selected in data than predicted by the sum of the background processes. The agreement between the numbers is very good, especially if taking into account that the number of multijet events is subject to considerable uncertainties and that the efficiency corrections outlined below are not yet applied. With the additional requirement of at least 4 selected jets, there are about 2% more data events than predicted by the simulation.

The last row shows the effect of the additional isolation requirement in the electron-plus-three jets trigger that is used for the majority of the data-taking periods. In contrast to the isolation requirement in the muon trigger, the isolation requirement here only contributes a small inefficiency of well below 1%.

Table 5.10 shows the efficiency of the electron-plus-jets selection for Z′ events with three different Z′ masses. The relative selection efficiencies are similar to the muon channel. Two general differences can be observed: Due to the higher p_{T} threshold for electrons, the event selection efficiency is higher for muon-plus-jets events at lower Z′ masses, especially for masses well below 1 TeV. On the other hand, the selection efficiency at trigger level for $m_{Z'} \sim 2$ TeV is higher for electron-plus-jets events because the isolation criterion in the trigger is less restrictive.

Table 5.10: Fraction of selected events at several stages of the electron-plus-jets selection for three benchmark Z′ simulation samples.

Event yield [%]	**Z′ 0.75 TeV**	**Z′ 1 TeV**	**Z′ 1.5 TeV**	**Z′ 2 TeV**
e+jet trigger	12.1	13.3	12.3	10.8
1 jet	11.7	13.0	12.2	10.7
2 jets	11.0	12.5	11.8	10.4
3 jets	7.9	9.6	9.0	7.9
Electron	4.8	5.8	5.0	4.0
Electron veto	4.7	5.7	4.9	3.9
Z veto	4.7	5.7	4.9	3.9
Muon veto	4.6	5.5	4.7	3.7
$E_{\mathrm{T}}^{\mathrm{miss}}$	4.2	5.2	4.5	3.6
4 jets	2.9	3.7	3.1	2.6
e trigger	2.9	3.7	3.1	2.6

In summary, the overall selection efficiency in the semileptonic channel is up to 36% for the electron- and muon-plus-jets channels. When including all $\mathrm{t\bar{t}}$ decay channels, this translates to a total selection efficiency for Z′ events of the order of 7–11%. The additional exclusion of events with 3 jets and no b-tag in the statistical evaluation reduces this number by an absolute fraction of at most 1% for high Z′ masses.

5.6 Corrections applied to simulated events

In the following, several efficiency calculations and other corrections will be detailed that are specific to the considered final state, selection, and/or datasets. For both muon-plus-jets and electron-plus-jets events, data-to-simulation scale factors are derived to correct simulated events for the differences between data and simulation. The general assumption is made that all corrections factorise, e.g. that the trigger efficiency corrections for lepton-plus-jets triggers can be split into a hadronic and a leptonic part,

$$\varepsilon_{\mathrm{trigger}} = \varepsilon_{\mathrm{hadronic}} \cdot \varepsilon_{\mathrm{lepton}}, \tag{5.3}$$

and that the total lepton efficiency can be subdivided into reconstruction, trigger, and identification plus isolation efficiencies,

$$\varepsilon_{\mathrm{lepton}} = \varepsilon_{\mathrm{reconstruction}} \cdot \varepsilon_{\mathrm{trigger}} \cdot \varepsilon_{\mathrm{ID+isolation}}. \tag{5.4}$$

To minimise the dependence on this assumption, all corrections are applied in the form of data-to-simulation scale factors, i.e. the same selection criteria are applied to both data and simulated events, and the simulated events are corrected for the differences.

5.6.1 Trigger and lepton identification efficiencies

For the lepton-plus-jets triggers, the trigger efficiency is measured separately for the hadronic part and the leptonic part of the trigger. The efficiency for the leptonic part in both the electron and the muon channel is determined with the so-called *tag-and-probe* technique. The concept of the tag-and-probe technique is to select Z-plus jets events where the Z boson decays to two leptons that yield the Z boson mass when added vectorially, $m(l^+l^-) \sim m_Z$. If one of the two leptons from the Z boson decay fulfils a given set of tight selection criteria, it is considered as the *tag* lepton, and the other lepton is considered as the *probe*. It is then tested if the probe lepton passes the selection criteria under study, e.g. if it passes the trigger requirement. The fraction of probe leptons that pass the selection criteria is equivalent to the efficiency for passing the selection criteria. To correctly estimate the efficiency with the tag-and-probe method, one needs to take into account that both leptons can serve as a tag. Furthermore, it needs to be ensured that the selection of the tag as well as the criterion of the compatibility with the Z boson mass yield a pure sample of Z-plus-jets events. If it is not the case, background contributions from events with no or only one prompt lepton need to be subtracted for the efficiency estimation, and relevant systematic uncertainties need to be estimated.

For all results in the following, a Z mass window of $80\ \text{GeV} < m_{l^+l^-} < 100\ \text{GeV}$ is used, and the efficiencies are determined by dividing the numbers of events with a probe lepton passing the criterion under investigation by the number of all events with a probe lepton. To estimate the contribution from background, the Z mass window is varied and it is checked by which amount the scale factor varies. In addition, fits of parametric signal and background distributions to the $m_{l^+l^-}$ distribution are performed, and the resulting scale factors are compared to the ones from the direct counting. The differences are briefly discussed below and are taken into account as systematic uncertainties.

In the single muon and the muon-plus-jets triggers, a so-called trigger element is created if an object, in this case a muon, passes the relevant trigger criteria. Since the reconstruction algorithms at trigger level are different from the offline reconstruction, this trigger element needs to be matched to the reconstructed object, i.e. the muon, to test whether it passes the trigger requirements. The matching of the trigger element and the reconstructed object is performed with a geometric criterion based on the ΔR distance. Both tag and probe muons need to pass all muon selection criteria outlined in the event selection. In addition, a tag muon must be matched to a muon trigger element that is deployed in one of the used triggers depending on the run range. If the probe muon is matched to an according muon trigger element, it qualifies as a muon that fulfils the trigger criteria.

The measurement of the muon trigger efficiency is carried out in events with at least two jets to be in a kinematic region similar to the selected events and to have a sufficient number of events for the calculation of the efficiency. The efficiency is measured for both data and simulated events. The quotient of the trigger efficiencies in data $\varepsilon_{\text{data}}(x)$ and simulation $\varepsilon_{\text{sim}}(x)$ defines the data-to-simulation scale factor $f(x) = \frac{\varepsilon_{\text{data}}(x)}{\varepsilon_{\text{sim}}(x)}$. The scale factor $f(x)$ can be determined as a function of a certain variable x to check for dependencies of the scale factor on the kinematic properties of the muon or on general event properties. The measured scale factor is shown as a function of muon η in figure 5.4 for the two run periods 2011A and 2011B. While

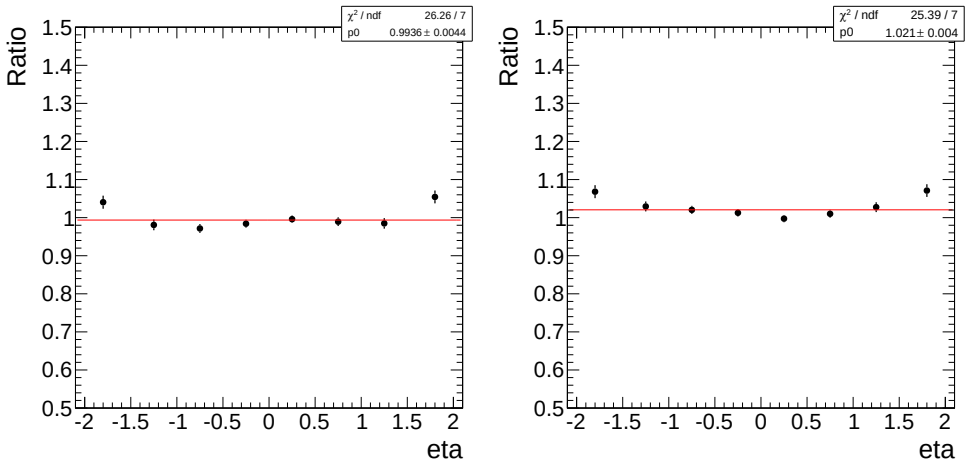

Figure 5.4: Data-to-simulation scale factor for the isolated muon trigger efficiency as a function of muon η for the run periods 2011A (left) and 2011B (right).

the scale factor is relatively flat in the central detector region, it is ~ 1.05 for $1.8 < |\eta| < 2.1$ and hence significantly above 1. Due to the low contribution of muons in this η region, a flat scale factor is assumed for the trigger efficiency, and the difference for high η muons is absorbed in the systematic uncertainty of the scale factor. The average scale factor is $\sim 1\%$ above unity.

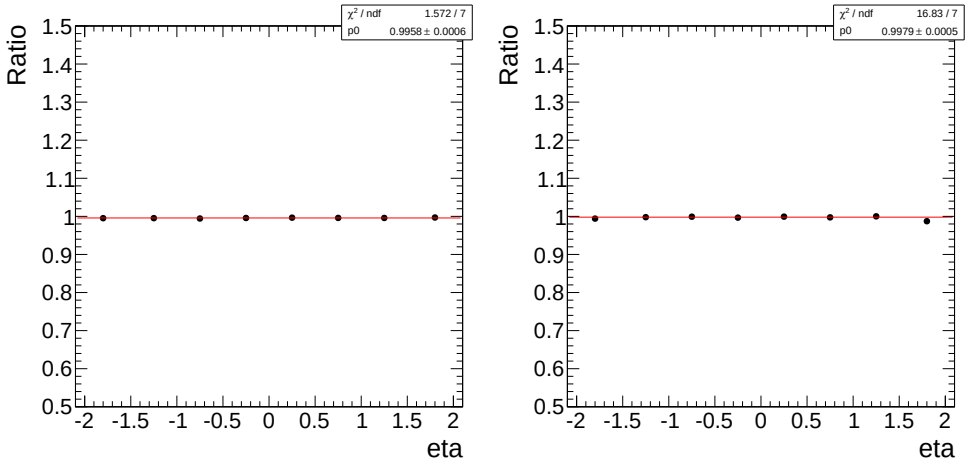

Figure 5.5: Data-to-simulation scale factor for the isolated electron trigger efficiency as a function of electron η for the run periods 2011A (left) and 2011B (right).

The electron trigger efficiency in electron-plus-jets events is measured with the same technique. Both the tag and the probe electrons are required to pass the electron selection criteria used in this analysis. The match to a run-dependent trigger element defines whether the electron has initiated the electron part of the electron-plus-three-jets trigger. As above, the tag electron must be matched to an electron on trigger level. For the same reasons as above, the measurement is carried out in events with at least two jets. The resulting data-to-simulation scale factors as a function of electron pseudorapidity are shown in figure 5.5, again for the two run periods 2011A and 2011B. The average scale factor is slightly lower than one, but compatible with unity within half a per cent.

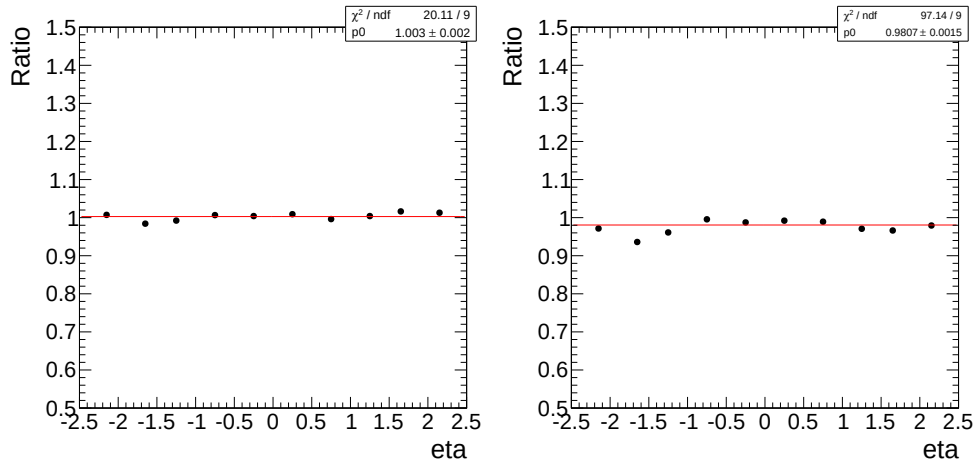

Figure 5.6: Data-to-simulation scale factor for the muon identification and isolation efficiency as a function of muon η for the run periods 2011A (left) and 2011B (right).

For the measurement of the muon identification and isolation efficiency, the tag-and-probe technique is used as well, but different requirements are posed to the tag and probe muons. The tag muon needs to fulfil all standard event selection criteria including muon identification and isolation; in contrast to the measurement of the trigger efficiencies, the muon does not need to match to a muon trigger element. To qualify as a probe muon, a muon must pass all event selection criteria except for identification and isolation, i.e. it must be a reconstructed PF muon with $p_{\mathrm{T}} > 20$ GeV and $|\eta| < 2.1$. The resulting data-to-simulation scale factors are shown in figure 5.6, again as a function of muon η. For the run period 2011A, the scale factor is close to unity, with deviations as a function of muon η of the order of 1%. The scale factor for the run period 2011B is on average below one, $f \sim 0.98$, and varies by a few per cent as a function of muon η, with the scale factor being closer to one for central muons.

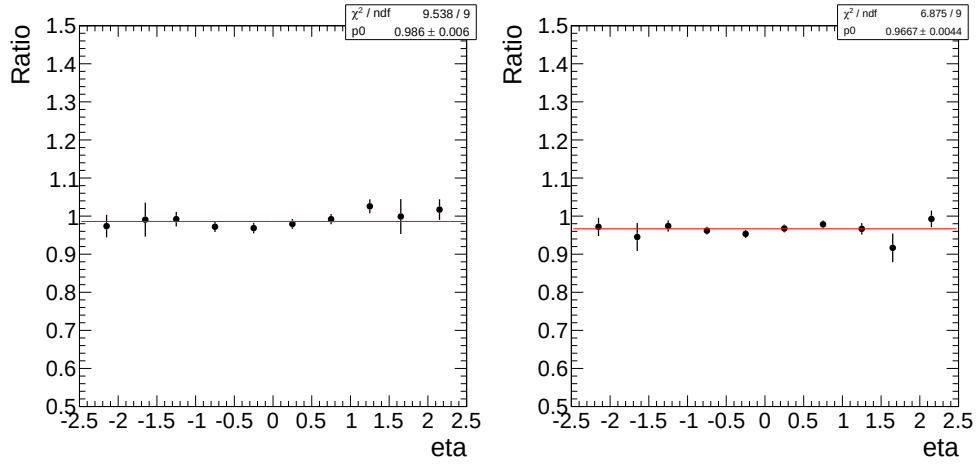

Figure 5.7: Data-to-simulation scale factor for the electron identification and isolation efficiency as a function of electron η for the run periods 2011A (left) and 2011B (right).

For the measurement of the efficiency for electrons to be identified and isolated, the following requirements are made for the tag and the probe electrons. An electron must pass all selection

criteria including acceptance, identification, and isolation to be a tag electron; a reconstructed electron only needs to fulfil the acceptance criteria to be a probe electron. The efficiency for a probe electron to pass the identification and isolation criteria is again measured in data and simulation. The data-to-simulation scale factors, shown in figure 5.7, are flat as a function of electron η within statistical uncertainties. The mean value of the scale factor is $f \sim 0.99$ for the run period 2011A and $f \sim 0.97$ for the run period 2011B, i.e. the identification and isolation efficiency is overestimated by a few per cent in the simulation.

The efficiency of the hadronic part of both the muon-plus-jets and the electron-plus jets triggers is determined with collision data. Compared to the efficiencies for the single lepton triggers, a different technique needs to be deployed as there are no relevant physics processes that would allow a tag-and-probe technique. There are two different strategies for the determination of the efficiency. First, the efficiency can be further factorised into the efficiency for a reconstructed jet to induce the single jet trigger with p_{T} threshold of 30 GeV by matching the relevant trigger element to the reconstructed jet, similar to the leptons as discussed above. The single jet efficiencies are then multiplied to obtain the efficiency for the two-jet or three-jet trigger. In the jet p_{T} range of interest, this technique can only be applied to few of the first runs from the 2011 data-taking; the necessary information to determine the jet trigger efficiencies in later runs is not saved for technical reasons. For the runs under consideration, data and simulation agree well, and the efficiency becomes close to 100% for reconstructed jets with $p_{\mathrm{T}} > 50$ GeV.

The second way of determining the efficiency is to require looser triggers, e.g. a muon-plus-one-jet trigger to measure the efficiency of the muon-plus-two-jets trigger, or requiring a single muon trigger to measure the muon-plus-three-jets trigger efficiency with respect to the offline selection. With this technique, data-to-simulation scale factors have been obtained as a function of a number of event properties, e.g. the p_{T} of the third leading jet. However, the measurements suffer from relatively high statistical uncertainties due to the high pre-scales for the control triggers, and systematic differences between $\mathrm{t\bar{t}}$ events and W-plus-jets events are observed in the turn-on region of the trigger, i.e. for jet $p_{\mathrm{T}} < 50$ GeV, which is therefore excluded by the event selection.

For jets with $p_{\mathrm{T}} > 50$ GeV, the measurements from both techniques show that the data-to-simulation scale factor is flat as a function of jet p_{T} and η and that it is compatible with one both for the run ranges in which a calorimeter-based and a PF-based jet reconstruction was applied. Hence, no efficiency corrections need to be applied.

In summary, data-to-simulation scale factors are applied to simulated events in both the muon-plus-jets and the electron-plus-jets channel. The scale factors combine information about the differences between data and simulation in the reconstruction, trigger, identification, and isolation of leptons. In the muon channel, the combined scale factor amounts to $f_{\mathrm{muon}} = 0.995$; in the electron channel, the combined scale factor is given by $f_{\mathrm{electron}} = 0.976$.

5.6.2 Pile-up interactions

Besides the hard collision under investigation, additional interactions can occur when two bunches are brought to collision in the CMS detector. The number of interactions generally

depends on the instantaneous luminosity, on the number of colliding bunches, and on the total inelastic cross section for pp collisions at 7 TeV. Furthermore, due to the bunch spacing of $\Delta t = 50$ ns, additional collisions occur during the previous and following bunch crossings that affect the detector readout. The additional collisions in the same bunch crossing are generally referred to as *in-time pile-up*, and the collisions at ± 50 ns as *out-of-time pile-up*.

In simulated events, in-time and out-of-time pile-up interactions are generated with the PYTHIA event generator. Since the instantaneous luminosity profile of the collision data was not known at the time of the generation of the events, a certain profile was assumed that was supposed to reflect the expected number of pile-up interactions in the data, with some contingency for higher and lower number of pile-up interactions. The distributions of pile-up interactions in data and simulated events do not match, hence simulated events are reweighted to reflect the number of pile-up interactions as observed in data. Technically, simulated events are reweighted such that the observed numbers of in-time and out-of-time pile-up interactions match the distribution of the observed number of pile-up interactions in data.

In the calculation of the weights, the inelastic pp cross section is assumed to be

$$\sigma_{\text{inel}}^{pp} = 68.0 \pm 2.0(\text{sys}) \pm 2.4(\text{lumi}) \pm 4.0(\text{extrapolation}) \text{ mb}, \tag{5.5}$$

as measured by the CMS collaboration [125]. The TOTEM experiment measured an inelastic pp cross section [126] of

$$\sigma_{\text{inel}}^{pp} = 73.5 \pm 0.6(\text{stat})^{+1.8}_{-1.3}(\text{sys}) \text{ mb}. \tag{5.6}$$

To account for the difference between the CMS and TOTEM measurements, the estimations for the numbers of pile-up interactions in data are repeated with $\pm 8\%$ variations of the inelastic cross section. This uncertainty is also considered to reflect possible differences of the tracking efficiency in data and simulation as well as modelling uncertainties of the simulated pile-up interactions.

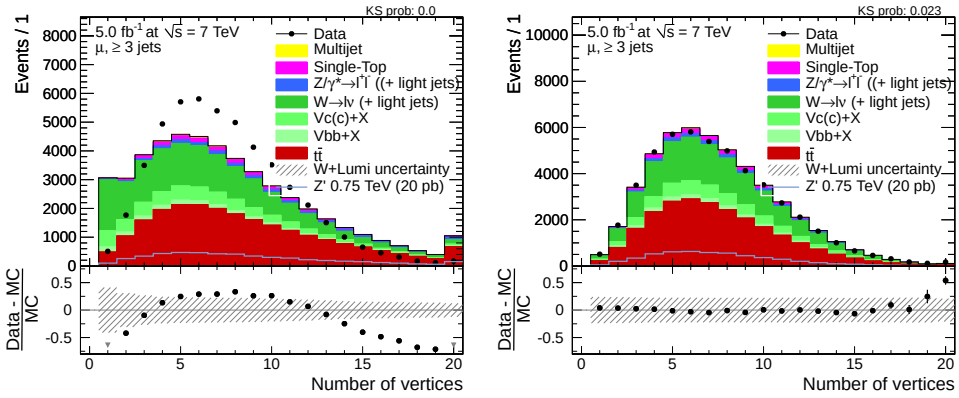

Figure 5.8: Number of reconstructed vertices in muon-plus-jets events with at least 3 jets before (left) and after (right) reweighting for the estimated number of pile-up interactions in data.

The number of reconstructed vertices can be used as a measure for the number of pile-up interactions as inelastic pp collisions produce charged particles that are reconstructed as tracks from a common vertex. Figure 5.8 shows a comparison of the distributions of the number of reconstructed vertices in data and simulation before and after the reweighting for the observed number of pile-up interactions in data. Whereas there is a clear discrepancy between simulation and data before reweighting, the distributions agree well after the reweighting procedure. The good agreement confirms the correct estimation of the number of pile-up interactions in data as well as the sufficient quality of the simulation of pile-up events with PYTHIA.

5.6.3 b-tag efficiency

As outlined in the previous chapter, the measured b-tag efficiency in data differs from the b-tag efficiency in simulation, and simulated events need to be corrected for this difference. The differences of the b-tag efficiency in data and simulation are provided in the form of p_{T}- and η-dependent data-to-simulation scale factors f_{b}. From these scale factors, weights are calculated that are multiplied with the weight of each simulated event. Without a requirement on the number of b-tagged jets, the application of these additional event weights does not change the expected number of simulated events from a given process. The weights for an event to contain 0, 1, or 2 b-tagged jets are calculated with only those simulated jets that are b-tagged,

$$w(0\ b-\mathrm{tags}) = \prod_{i=1}^{N_{b\ \mathrm{jets}}} (1 - f_{\mathrm{b}}), \tag{5.7}$$

$$w(1\ b-\mathrm{tag}) = \sum_{j=1}^{N_{b\ \mathrm{jets}}} f_{\mathrm{b}} \prod_{i\neq j}^{N_{b\ \mathrm{jets}}} (1 - f_{\mathrm{b}}), \tag{5.8}$$

$$w(2\ b-\mathrm{tags}) = \sum_{j=1}^{N_{b\ \mathrm{jets}}} f_{\mathrm{b}} \sum_{k=1}^{N_{b\ \mathrm{jets}}} f_{\mathrm{b}} \prod_{i\neq j, i\neq k}^{N_{b\ \mathrm{jets}}} (1 - f_{\mathrm{b}}), \tag{5.9}$$

and accordingly for higher b-tag multiplicities. The products or sums with the label $N_{b\ \mathrm{jets}}$ only include jets that are b-tagged in simulation, regardless of the jet flavour. For scale factors $f_{\mathrm{b}} > 1$, the event weights can become negative, and it needs to be ensured that the sum of all background events in each bin of the observable is positive for the statistical evaluation. Compared to alternative methods to apply the b-tag scale factors that are based on a parametrisation of the b-tag probability as a function of a certain number of jet and event properties, the given procedure has the advantage that the dependency of the b-tag efficiency on the jet kinematics and on the final state is automatically included by directly using the b-tag information in the simulation.

6 Reconstruction of $m_{\mathrm{t\bar{t}}}$

The reconstruction of the invariant mass of the top-antitop quark system ($m_{\mathrm{t\bar{t}}}$) aims at reconstructing the mass of a new particle as precisely as possible. In the search for a narrow resonance in addition to the falling $m_{\mathrm{t\bar{t}}}$ spectrum, which is mostly due to SM $\mathrm{t\bar{t}}$ production, a smaller reconstructed width of $m_{\mathrm{t\bar{t}}}$ provides a higher signal-to-background ratio and therefore leads to a higher significance in the statistical evaluation. Improving the reconstruction of $m_{\mathrm{t\bar{t}}}$ to yield a good resolution is therefore the most important goal of the reconstruction.

The invariant top quark pair mass is given by the invariant four-vector sum of the final state objects, i.e. the charged lepton, the reconstructed neutrino, and four jets. There are a few complications that evolve from this final state. First, only the transverse component of the neutrino is given by the missing transverse energy, and the longitudinal component needs to be deduced from the presence of a W boson in the $\mathrm{t\bar{t}}$ decay chain. Second, more than four jets may be selected, e.g. due to initial state radiation. In this case, the four jets originating from the $\mathrm{t\bar{t}}$ decay need to be selected to correctly reconstruct $m_{\mathrm{t\bar{t}}}$. Third, a quark from the $\mathrm{t\bar{t}}$ decay chain may have too low transverse momentum to produce a jet that passes the event selection, leading either to a final state of only three selected jets or to a final state with four or more selected jets of which at most three originate from the $\mathrm{t\bar{t}}$ decay. Finally, two or more quarks from the $\mathrm{t\bar{t}}$ decay chain may be reconstructed as only one jet. This may happen if the angular distance between two quarks is small compared to the size of the jet cone.

The distribution of the difference between reconstructed and generated $m_{\mathrm{t\bar{t}}}$, $m_{\mathrm{t\bar{t}}}^{\mathrm{rec}} - m_{\mathrm{t\bar{t}}}^{\mathrm{gen}}$, is used to study the resolution of the reconstructed $m_{\mathrm{t\bar{t}}}$. It typically exhibits two components, a Gaussian core in which $m_{\mathrm{t\bar{t}}}$ is reconstructed with a resolution given by the resolution of the objects that enter the $m_{\mathrm{t\bar{t}}}$ reconstruction, and tails towards higher or lower $m_{\mathrm{t\bar{t}}}$ due to one of the reasons given above, e.g. the inclusion of a jet not coming from the $\mathrm{t\bar{t}}$ decay in the $m_{\mathrm{t\bar{t}}}$ reconstruction. The distribution of $m_{\mathrm{t\bar{t}}}$ from SM $\mathrm{t\bar{t}}$ production is steeply falling beyond the region of the production threshold of $m_{\mathrm{t\bar{t}}} \gtrsim 2 \cdot m_{\mathrm{top}}$. Hence, a tail in the $m_{\mathrm{t\bar{t}}}$ resolution towards high values is to be avoided as it increases the background to new particles with high mass. An important aspect of the $m_{\mathrm{t\bar{t}}}$ reconstruction is therefore to identify the jets that are due to the $\mathrm{t\bar{t}}$ decay products.

The first part of this chapter will be devoted to the topology of $\mathrm{t\bar{t}}$ production in the semileptonic decay channel. The remaining part of the chapter describes the strategy for the reconstruction of $m_{\mathrm{t\bar{t}}}$, which involves three steps. First, a W boson is reconstructed from the charged lepton and the missing transverse energy by using a W boson mass constraint. Then, reconstructed jets are selected that most likely originate from the $\mathrm{t\bar{t}}$ decay chain. Finally, the mass of the four-vector sum of all selected objects is used as an estimator for the invariant top quark pair mass. The association of jets to partons and the discussion of the quality of the reconstruction

will be detailed in separate sections for events with at least four jets and for events with three selected jets.

6.1 Topology

More than 90% of the $\mathrm{t\bar{t}}$ or Z′ events that pass the event selection are from semileptonic $\mathrm{t\bar{t}}$ decays. In the following, the topology of the selected events will be described. As mentioned above, the goal of the $m_{\mathrm{t\bar{t}}}$ reconstruction is to be able to measure the complete $m_{\mathrm{t\bar{t}}}$ spectrum, to compare to SM $\mathrm{t\bar{t}}$ production, and to search for new particles in this regime. With increasing $m_{\mathrm{t\bar{t}}}$, it becomes more likely that two or more quarks are associated to the same jet, called "jet merging" in the following. To cope with jet merging, events with only three selected jets are retained to recover events in which either two jets merge or a jet fails the p_{T} threshold. In the limit of very high $m_{\mathrm{t\bar{t}}}$ ($m_{\mathrm{t\bar{t}}} \gg 2$ TeV), jet merging occurs in most events, and the fraction of events with only two jets further increases; there are also additional complications with the event selection and reconstruction that are briefly mentioned below. This topology is therefore tackled by dedicated analyses that optimise the reconstruction in the regime of high $m_{\mathrm{t\bar{t}}}$, but which are not able to measure the distribution of $m_{\mathrm{t\bar{t}}}$ in the full possible mass range starting from $m_{\mathrm{t\bar{t}}} \sim 2 \cdot m_{\mathrm{top}}$.

The decay topology generally depends on the generated $m_{\mathrm{t\bar{t}}}$. For $m_{\mathrm{t\bar{t}}}$ in the threshold region, i.e. above the production threshold corresponding to $m_{\mathrm{t\bar{t}}} \gtrsim 345$ GeV, the top quarks have low p_{T} and tend to have well separated decay products. Two jets may still merge if they happen to point in the same direction. In the threshold region, the most frequent merges involve the b quark from the leptonically decaying top quark and one of the jets from the hadronically decaying top quark. For $m_{\mathrm{t\bar{t}}}$ around 600 GeV, i.e. an average top quark p_{T} of more than 100 GeV, merges of two jets both coming from the decay of the hadronically decaying top quark become dominant.

For $m_{\mathrm{t\bar{t}}}$ in the 1 TeV region and beyond, the top quarks start to have a significant transverse momentum compared to their mass. The top quarks are highly boosted, and the angular distance between the three decay products is therefore reduced. Since the top quarks propagate into opposite directions in the rest frame of the $\mathrm{t\bar{t}}$ system, the decay products of the top quarks also tend to be contained in two separate hemispheres with increasing $m_{\mathrm{t\bar{t}}}$. If the angular distance between two (or three) quarks becomes smaller than $\Delta R = 0.5$, the corresponding jets may merge. Whether two or three jets merge depends on the p_{T} of the top quark. For very high p_{T}, $p_{\mathrm{T}} \gtrsim 1$ TeV, the angular distances become yet smaller, and it becomes more likely that the three quarks lead to only one reconstructed jet, a so-called "top jet". For intermediate or high p_{T}, it is about equally likely that the two jets from the decay of the W boson merge or that one of the jets from the W boson decay merges with the b jet. To cope with jet merging, dedicated algorithms have been developed that make use of the jet substructure to discriminate between standard quark jets and merged jets [127,128].

The leptonically decaying top quark leads to a b jet, a neutrino, and a charged lepton and does therefore not suffer from jet merging. However, the charged lepton and the b jet become closer in ΔR, and the charged lepton may become less well isolated. This induces a reduction of the isolation efficiency for high $m_{\mathrm{t\bar{t}}}$ that is briefly discussed in the previous chapter. For this

topology, dedicated analyses are carried out within the CMS collaboration that rely on different trigger paths to avoid a dependence on lepton isolation [129,130].

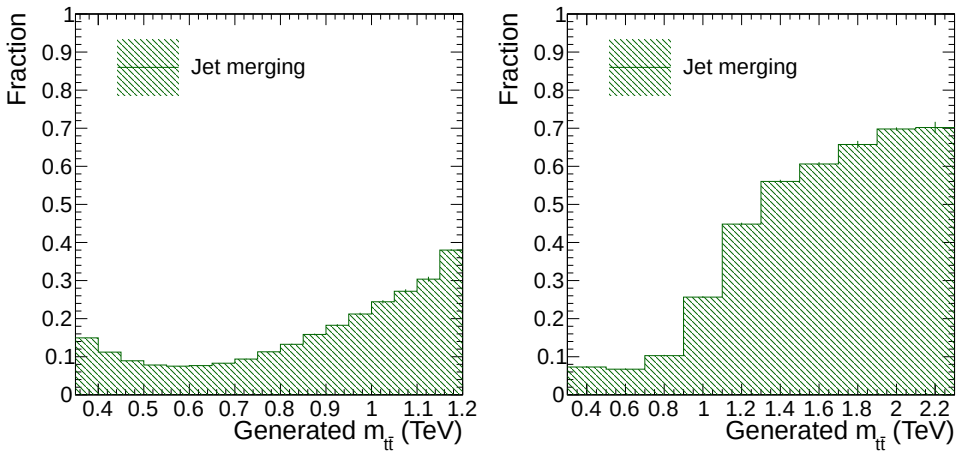

Figure 6.1: Fraction of events where at least two quark jets from the $\mathrm{t\bar{t}}$ decay chain merge, i.e. where the quarks are both within $\Delta R < 0.5$ of the same reconstructed jet, for simulated events from SM $\mathrm{t\bar{t}}$ production (left) and from Z' production (right).

Using simulated events, the fraction of events with merged jets is studied. Reconstructed jets are associated to generated partons by requiring that the angular distance between a jet and a parton fulfils $\Delta R < 0.5$. The value of $R = 0.5$ is chosen to correspond to the jet radius in the anti-kt algorithm. In rare cases, a parton is associated to two reconstructed jets. Then only the association with the closest jet in ΔR is kept. If two partons are associated to a single jet, the jet is called a merged jet, regardless of the p_{T} of the partons.

Figure 6.1 shows in which fraction of events at least two jets merge as a function of the generated $m_{\mathrm{t\bar{t}}}$. The fractions are shown separately for SM $\mathrm{t\bar{t}}$ production in the range 350 GeV $< m_{\mathrm{t\bar{t}}} < 1200$ GeV and for Z' production in the range 350 GeV $< m_{\mathrm{t\bar{t}}} < 2250$ GeV. The reasons are two-fold. On the hand, the number of simulated SM $\mathrm{t\bar{t}}$ events becomes small for high $m_{\mathrm{t\bar{t}}}$; on the other hand, SM $\mathrm{t\bar{t}}$ events have a mixture of gg- and $q\bar{q}$-induced initial states, whereas Z' events are exclusively $q\bar{q}$-induced. The $m_{\mathrm{t\bar{t}}}$ ranges and the separation of SM $\mathrm{t\bar{t}}$ and Z' events are therefore adapted for all similar plots in this chapter.

The fraction of events with merged jets is about 10% for $m_{\mathrm{t\bar{t}}}$ in the bulk region. Near the production threshold, the fraction of events with merged jets is slightly higher than for $m_{\mathrm{t\bar{t}}} \sim 600$ GeV as the top quarks are produced with low transverse momentum, which makes the merging of jets from the two different top quarks more likely. Above $m_{\mathrm{t\bar{t}}} = 700$ GeV, the fraction increases from about 20% at 1 TeV to 50 % at 1.5 TeV and 70% at 2 TeV, illustrating the transition from low-p_{T} top quarks with a low probability for jet merging to high-p_{T} top quarks with a high probability.

In the following, it will be discussed in which fraction of events all four jets from the top quark decay are present in the event, and in in which fraction of events three jets are present of which one jet is merged, i.e. events that still contain the full information about the $\mathrm{t\bar{t}}$ decay.

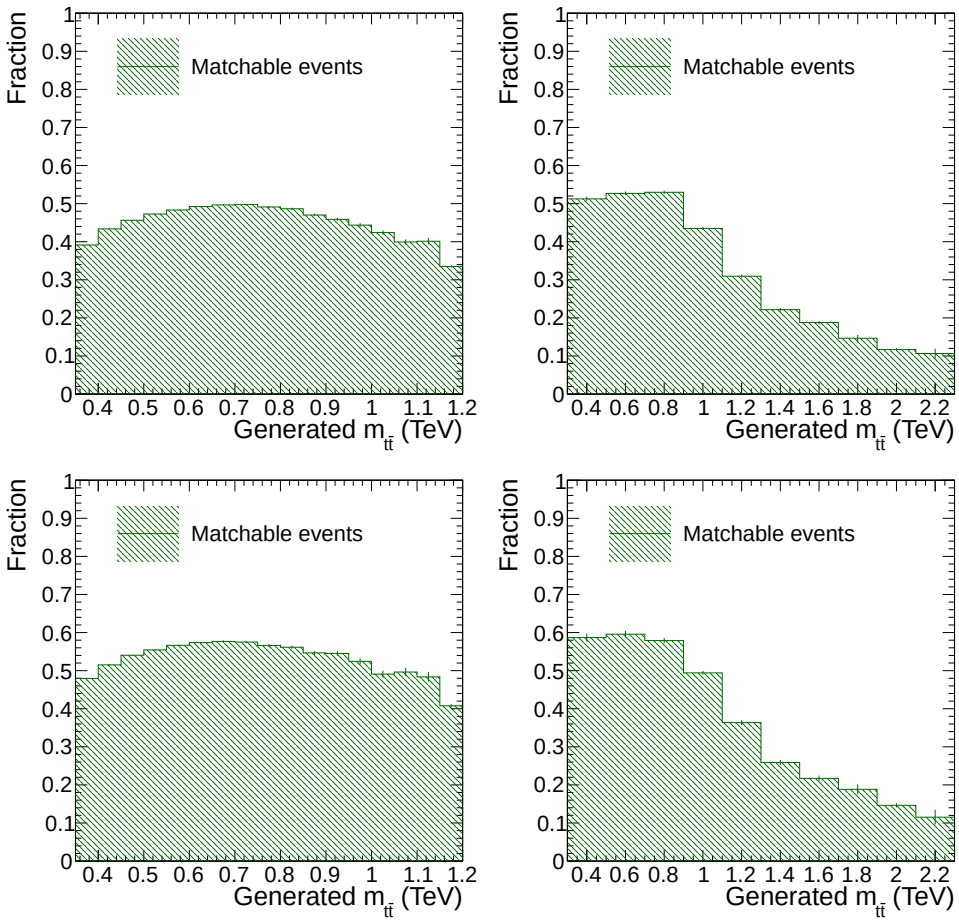

Figure 6.2: Fraction of events where each quark from the $\mathrm{t\bar{t}}$ decay is exclusively associated to one reconstructed jet for simulated events from SM $\mathrm{t\bar{t}}$ production (left) and from Z' production (right) and for either at least four selected jets (top) or at least five selected jets (bottom).

The fraction of events where each quark is associated to a unique jet is shown in figure 6.2. In addition to the jets, each event also contains a charged lepton and missing transverse energy due the neutrino. The charged lepton corresponds to the generated lepton in close to 100% of the events, and the requirement of an association of all four quarks to reconstructed jets is therefore sufficient to have a fully reconstructible event. The fraction of fully reconstructible events with at least four selected jets is 40–50% from the threshold region up to $m_{\mathrm{t\bar{t}}} \sim 1$ TeV, with the maximum around 700 GeV. Beyond 1 TeV, the fraction steadily declines down to a bit more than 10% at 2 TeV. The fraction of fully reconstructible events with at least five selected jets is, on average, 7% higher than for events with at least four jets. It is therefore important to develop a strategy to select the four jets from the $\mathrm{t\bar{t}}$ decay in these events.

To understand the production of additional jets in more detail, the fractions of events with a different number of selected jets not coming from the decay of the $\mathrm{t\bar{t}}$ pair are shown in figure 6.3 for events from $\mathrm{t\bar{t}}$ and Z' production. For $\mathrm{t\bar{t}}$ production, only about 40% of the events have no additional jet, about 40% have one extra jet, and about 20% of the events have at least two additional jets. The number of extra jets is slightly increasing with higher $m_{\mathrm{t\bar{t}}}$. At low Z' mass,

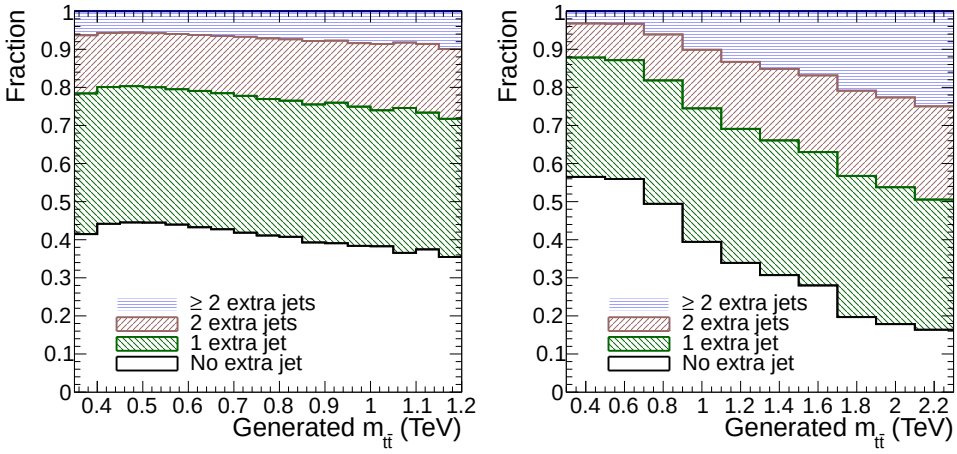

Figure 6.3: Number of selected jets not associated to a quark in the $\mathrm{t\bar{t}}$ decay chain in $\mathrm{t\bar{t}}$ events (left) and Z′ events (right) with semileptonic signature.

the fraction of events with no extra jet is more than 50% and hence higher than for $\mathrm{t\bar{t}}$ production, meaning that Z′ events at low mass are easier to reconstruct than $\mathrm{t\bar{t}}$ events. The reason for this is that $\mathrm{t\bar{t}}$ events mostly originate from gluon-gluon fusion, which implies a higher probability for initial state radiation, whereas Z′ events are only produced through $q\bar{q}$ annihilation. However, the number of extra jets significantly increases with Z′ mass. At a Z′ mass of 2 TeV, less than 20% of the events are expected to have no extra jets, owing to the high scale of the process.

The significant fraction of events with additional jets means that it is important to identify the jets from the $\mathrm{t\bar{t}}$ decay chain for the reconstruction of $m_{\mathrm{t\bar{t}}}$. Except for final state radiation, adding the additional jets to the reconstructed $m_{\mathrm{t\bar{t}}}$ would lead to an overestimation of $m_{\mathrm{t\bar{t}}}$ that is to avoid to improve the $m_{\mathrm{t\bar{t}}}$ resolution and to reduce the background from events with lower generated $m_{\mathrm{t\bar{t}}}$.

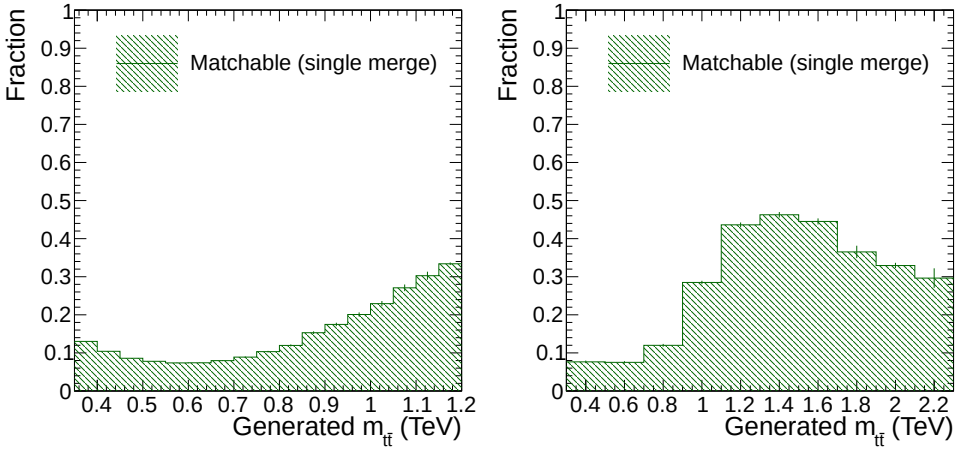

Figure 6.4: Fraction of events with three selected jets where all quarks from the $\mathrm{t\bar{t}}$ decay are associated to jets, amongst which needs to be a merged jet, for simulated events from SM $\mathrm{t\bar{t}}$ production (left) and from Z′ production (right).

Events with three selected jets are only reconstructable if one of the jets is a merged jet.

Figure 6.4 shows the fraction of events with three selected jets in which all four quarks are matched to the three jets among which must be exactly one merged jet. Just above the production threshold, the fraction is $\sim 13\%$, falling to $\lesssim 10\%$ around $m_{\mathrm{t\bar{t}}} = 600$ GeV, as indicated above by the higher total fraction of merged jets at production threshold compared to intermediate $m_{\mathrm{t\bar{t}}}$ values. Beyond 600 GeV, the fraction of reconstructable events steadily increases up to $m_{\mathrm{t\bar{t}}} \sim 1.4$ TeV with a fraction of close to 50%, showing that a reconstruction of $m_{\mathrm{t\bar{t}}}$ under the assumption of jet merging is worthwhile especially in this mass region. As seen above, the total fraction of merged events also rises for higher $m_{\mathrm{t\bar{t}}}$; the fraction of reconstructable events however falls again as it becomes more likely that all three jets on the hadronic side merge and that the third jet is an additional jet, as opposed to events at low $m_{\mathrm{t\bar{t}}}$ in which the events are not reconstructable because the fourth jet is not selected or reconstructed.

6.2 Reconstruction of the W boson

The leptonically decaying W boson cannot be reconstructed directly as the longitudinal momentum of the neutrino is not known. However, one can exploit the known mass of the W boson of $m_W = 80.4$ GeV to construct a quadratic equation for the longitudinal momentum of the neutrino, using the measured missing transverse energy and the lepton momentum [131]. The momentum of the reconstructed neutrino is then given by

$$\vec{p}^{\,\nu} = \begin{pmatrix} E_{\mathrm{x}}^{\mathrm{miss}} \\ E_{\mathrm{y}}^{\mathrm{miss}} \\ \frac{1}{2(p_{\mathrm{T}}^{\ell})^2}\left(A p_L^{\ell} \pm E^{\ell}\sqrt{A^2 - (2p_T^{\ell}E_{\mathrm{T}}^{\mathrm{miss}})^2}\right) \end{pmatrix} \tag{6.1}$$

with the constant

$$A = m_W^2 + 2\left(p_x^{\ell}E_{\mathrm{x}}^{\mathrm{miss}} + p_y^{\ell}E_{\mathrm{y}}^{\mathrm{miss}}\right), \tag{6.2}$$

using the momenta of the reconstructed lepton p^{ℓ} and the missing transverse energy $E_{\mathrm{T}}^{\mathrm{miss}}$ and its x and y components $E_{\mathrm{x}}^{\mathrm{miss}}$ and $E_{\mathrm{y}}^{\mathrm{miss}}$ as inputs. For $A^2 - (2p_T^{\ell}E_{\mathrm{T}}^{\mathrm{miss}})^2 > 0$, the quadratic equation has two real solutions; for $A^2 - (2p_T^{\ell}E_{\mathrm{T}}^{\mathrm{miss}})^2 = 0$, it has one real solution; and for $A^2 - (2p_T^{\ell}E_{\mathrm{T}}^{\mathrm{miss}})^2 < 0$, only imaginary solutions exist. If there are two real solutions and there are at least four jets, both are passed to the χ^2-based jet-parton association described in the next section, and the one giving the overall minimum χ^2 is chosen. The choice of the neutrino p_Z solution in events with three selected jets is described at the end of this chapter.

If the equation only has imaginary solutions, which happens in about 30% of the cases for $\mathrm{t\bar{t}}$ and Z' signal events, either the lepton momentum or the missing transverse energy have been mismeasured under the assumption that they come from the decay of a W boson. As the lepton momenta are measured with high precision, the most probable reason is a mismeasurement of $E_{\mathrm{T}}^{\mathrm{miss}}$. This knowledge can be exploited by modifying the individual $E_{\mathrm{T}}^{\mathrm{miss}}$ components in the transverse plane, $E_{\mathrm{x}}^{\mathrm{miss}}$ and $E_{\mathrm{y}}^{\mathrm{miss}}$, such that only one real solution remains, i.e. the term under the square root becomes zero. To arrive at a unique solution, it is required that the changes of

the measured values of $E_{\mathrm{x}}^{\mathrm{miss}}$ and $E_{\mathrm{y}}^{\mathrm{miss}}$ should be minimal. This leads to the requirement that the scalar sum of the changes of the x and the y component of $E_{\mathrm{T}}^{\mathrm{miss}}$, $\Delta E_{\mathrm{x}}^{\mathrm{miss}} + \Delta E_{\mathrm{y}}^{\mathrm{miss}}$, should be minimal. Both $E_{\mathrm{T}}^{\mathrm{miss}}$ components are treated in the same way due to the radial symmetry of the CMS detector. The requirement yields an equation of third order that can be solved either analytically or numerically (see reference [132] for the numerical derivation). Since both solutions are equivalent, the analytic approach is chosen here.

6.3 Association of jets to partons and reconstruction of $m_{\mathrm{t\bar{t}}}$ in events with at least four jets

The association of jets to partons has three goals. First, in events with more than four selected jets, the four jets that originate from the decay of the $\mathrm{t\bar{t}}$ pair need to be chosen for the reconstruction of $m_{\mathrm{t\bar{t}}}$. Second, the selected jets need to be associated to partons in the $\mathrm{t\bar{t}}$ decay chain to be able to reconstruct intermediary objects like the two top quarks, which are e.g. used to test the reconstruction. Third, finding a correct jet-parton association also involves finding the better solution for the longitudinal momentum of the neutrino in case of an ambiguity. The top-antitop quark pair system is then reconstructed by vectorially adding the four selected jets, the reconstructed neutrino, and the lepton, yielding the reconstructed invariant top-antitop quark mass $m_{\mathrm{t\bar{t}}}$.

For the association of jets to partons, all intermediate objects are reconstructed, i.e. the two top quarks and the two W bosons, and they are used to select the jets from the $\mathrm{t\bar{t}}$ decay in the following. Depending on the decay of the W boson, the mother top quarks are either called leptonically or hadronically decaying top quark. One jet needs to be associated to the b quark from the leptonically decaying top quark, and three jets to the hadronically decaying top quark. Of these, two form a W boson and are interchangeable, and a third jet must be associated with the b quark. If there are two solutions for the longitudinal momentum of the reconstructed neutrino, both are considered in the association.

In an event where N ($N \geq 4$) jets are reconstructed, there are $\binom{N}{N-4}$ subsets of four jets, and for each of them there are 12 possible combinations to assign the jets to generated quarks when considering the two light-flavoured jets from a W boson as indistinguishable, and 24 if an ambiguity is present for the longitudinal momentum of the neutrino. As discussed above, there is at least one additional jet in more than half of the events for both $\mathrm{t\bar{t}}$ and Z' production, which significantly increases the number of permutations to be considered.

To find the correct assignment, a χ^2 variable is defined and evaluated for all possible jet-parton associations, and the reconstruction version with the minimum χ^2 is chosen. In addition, information from the identification of b quark jets is exploited. When one or two b-tagged jets are present, they may only be associated to a b parton in the decay chain, thereby reducing the number of possible combinations. If three jets are b-tagged, two of them must be assigned to the b quarks.

The total χ^2 is defined as a sum over five χ^2 terms,

$$\chi^2 = \chi^2_{m(tlep)} + \chi^2_{m(thad)} + \chi^2_{m(whad)} + \chi^2_{HTfrac} + \chi^2_{pt(\mathrm{t\bar{t}})}. \tag{6.3}$$

The individual χ^2 terms have the form

$$\chi^2_x = (x_{\mathrm{meas}} - x_{\mathrm{MC}})^2 / \sigma^2_{\mathrm{MC}}, \tag{6.4}$$

with the measured value of the quantity x_{meas}, its expected value x_{MC}, and its resolution σ_{MC}. The expected value and the resolution are determined in simulated events.

The meaning of the individual terms is

- $\chi^2_{\mathrm{m(tlep)}}$: Mass of the leptonic top quark.
- $\chi^2_{\mathrm{m(thad)}}$: Mass of the hadronic top quark.
- $\chi^2_{\mathrm{m(whad)}}$: Mass of the hadronic W boson.
- $\chi^2_{pt(\mathrm{t\bar{t}})}$: Transverse momentum of the $\mathrm{t\bar{t}}$ system.
- χ^2_{HTfrac}: Fraction of Σp_{T} of selected jets compared to Σp_{T} of all jets, $\frac{\Sigma p_{\mathrm{T}}(\text{selected jets})}{\Sigma p_{\mathrm{T}}(\text{all jets})}$; called H_T fraction in the following.

The three mass terms make use of the well-known masses of the W boson and the top quarks in the decay chain and are therefore well-suited to associate the reconstructed jets to partons. The other two terms only have an effect in events with more than four jets, and their main purpose is to avoid the selection of jets that do not originate from the $\mathrm{t\bar{t}}$ decay chain but from additional jets or radiation. The first of the two exploits that the transverse momentum of the $\mathrm{t\bar{t}}$ system tends to be smaller for the correctly associated four jets, and the inclusion of the second quantity prefers jets with higher transverse momenta and thereby disfavours jets from additional radiation as they typically have lower transverse momenta.

Both the central values and the widths (σ_{MC}) are derived from simulated $\mathrm{t\bar{t}}$ events, see figure 6.5 for the corresponding distributions. A correct jet-parton association is defined by requiring that the 4 reconstructed jets are correctly matched to the two b quarks from the top quark decays and to the two light quarks from the W boson decay (which are indistinguishable for the purpose of the reconstruction of the $\mathrm{t\bar{t}}$ system). In addition, if there are two real solutions in the reconstruction of the longitudinal momentum of the neutrino, the reconstruction version needs to be identified that is closer in absolute value to the longitudinal momentum of the generated neutrino. For the correct jet-parton association, the most probable values at the expected values of the top quark mass and the W boson mass are clearly visible, whereas the distribution for all possible jet-parton associations is significantly broader, with a tail mostly towards higher reconstructed mass values. The transverse momentum of the $\mathrm{t\bar{t}}$ system only shows a modest discrimination between correct and all associations, with the correct association yielding slightly smaller transverse momenta. Apart from increasing the fraction of correct jet-parton associations, the inclusion of the $p_{\mathrm{T}}^{\mathrm{t\bar{t}}}$ variable also tends to prefer a reconstruction version for background events that reduces the numerical value of $m_{\mathrm{t\bar{t}}}$, which in turn reduces the fraction of background events in the region of high $m_{\mathrm{t\bar{t}}}$. The last input variable for the χ^2, the sum of the p_{T} of the jets used for the jet-parton association divided by the sum of p_{T} of all jets, is only different from one for events in which more than four jets are present. This quantity is added to the χ^2 definition as it significantly increases the fraction of correct associations in these events.

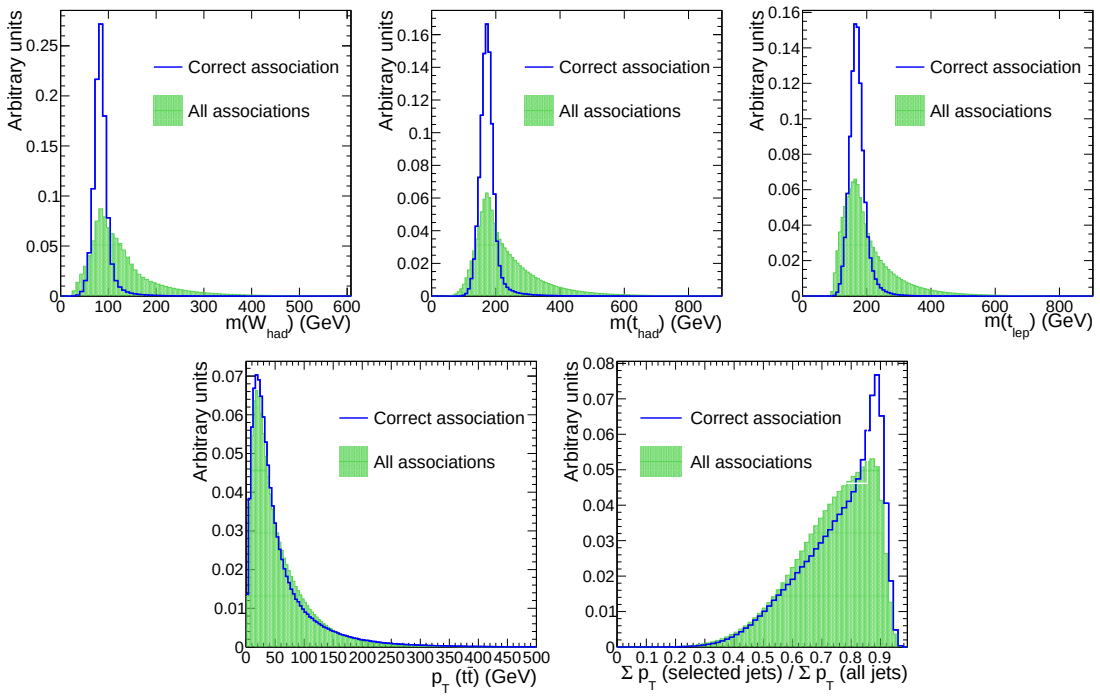

Figure 6.5: Distributions of the different quantities used for the χ^2-based jet-parton association in simulated $\mathrm{t\bar{t}}$ events: hadronic W boson mass (top left), hadronic top quark mass (top middle), leptonic top quark mass (top right), p_{T} ($\mathrm{t\bar{t}}$ system) (bottom left), and H_T fraction (bottom right, with the x axis adjusted to only include events with at least five jets). The green histograms show the distributions for all possible jet-parton associations; the blue lines show the distributions for the correct association.

The determined central values and widths are summarised in table 6.1. For the three mass terms, the values are obtained from fitting a Gaussian distribution to the mass distributions in simulated events with correct jet-parton association. As no flavour-specific jet energy scale corrections are applied, the observed small deviations from the generated values of the top quark and W boson masses are expected. Instead of taking fixed widths for the invariant top quark and W boson masses, it has also been studied to use the minimal χ^2 from a constrained kinematic fit to take p_{T}- and η-dependencies of the momentum resolutions into account. This does however not increase the fraction of correct solutions. For the two other terms, the resolutions are non-Gaussian; hence a heuristic approach to determine the inputs for the χ^2 calculation is chosen. The widths are determined from the root mean squares of the input distributions, and the central values are set to 0 GeV for the transverse momentum of the $\mathrm{t\bar{t}}$ system and to 1 for the H_T fraction to indicate the preference for low/high values of the respective quantity.

The values and widths of the χ^2 variables may also be determined in simulated Z′ events. For a mixture of all used Z′ samples with equal weights, the resulting numbers are very close to the ones from $\mathrm{t\bar{t}}$ production, see figure 6.6 for the corresponding distributions. Hence, the values determined in $\mathrm{t\bar{t}}$ events are used as they reflect the expected composition of $\mathrm{t\bar{t}}$ events in data.

Figure 6.7 shows the fraction of events with correct jet-parton association for three different reconstruction algorithms, the default χ^2 described in the text (χ^2 (with b-tag)), the same χ^2 but without usage of b-tag information (χ^2 (no b-tag)), and a simpler algorithm that takes the

Table 6.1: Quantities used in the χ^2 definition with reference values and widths.

Quantity x	**Reference value x_{MC}**	**Width σ_{MC}**
$m(t_{\mathrm{lep}})$	169.7 GeV	17.2 GeV
$m(t_{\mathrm{had}})$	171.6 GeV	17.4 GeV
$m(W_{\mathrm{had}})$	82.7 GeV	10.2 GeV
$p_T(\mathrm{t\bar{t}})$	0 GeV	57.1 GeV
H_T fraction	1.0	0.13

four leading jets and the smaller absolute value of the neutrino p_z solution (leading jets). The numbers are derived in events with at least four jets where an unambiguous association of jets to partons is possible. The leading jets algorithm leads to about 40% correct associations in $\mathrm{t\bar{t}}$ events, with a slow decrease towards higher generated $m_{\mathrm{t\bar{t}}}$ values. In Z′ events, where the numbers can be derived for higher values of $m_{\mathrm{t\bar{t}}}$, the decrease is stronger with only about 25% of the events being correctly reconstructed at $m_{\mathrm{t\bar{t}}} \sim 2$ TeV. The χ^2-based algorithms with and without use of b-tag information perform very similar, with a correct association in $\sim 50\%$ of the events for $m_{\mathrm{t\bar{t}}}$ in the threshold region rising to $\sim 70\%$ for high $m_{\mathrm{t\bar{t}}}$, i.e. $m_{\mathrm{t\bar{t}}} > 1$ TeV. The inclusion of b-tag information increases the fraction of correct associations by a few per cent, which is more visible in $\mathrm{t\bar{t}}$ events. At the same generated $m_{\mathrm{t\bar{t}}}$, the fraction of correct associations is a few per cent higher for Z′ production than for SM $\mathrm{t\bar{t}}$ production. This is due to the gluon-gluon induced fraction of $\mathrm{t\bar{t}}$ events where initial state radiation is more likely, thereby making the association of jets to partons more difficult.

The ultimate goal of the reconstruction is to reconstruct $m_{\mathrm{t\bar{t}}}$ as close as possible to the generated $m_{\mathrm{t\bar{t}}}$. Figure 6.8 shows the difference between reconstructed and generated $m_{\mathrm{t\bar{t}}}$, $m_{\mathrm{t\bar{t}}}^{\mathrm{rec}} - m_{\mathrm{t\bar{t}}}^{\mathrm{gen}}$, in four different $m_{\mathrm{t\bar{t}}}$ regions for events with at least four selected jets where an association of jets to partons is possible. Depending on the $m_{\mathrm{t\bar{t}}}$ region, the events are either taken from SM $\mathrm{t\bar{t}}$ production or from Z′ production. At a given $m_{\mathrm{t\bar{t}}}^{\mathrm{gen}}$, the distributions are hardly indistinguishable and are therefore not shown separately. For all regions of $m_{\mathrm{t\bar{t}}}$, the leading jets algorithm performs worst, whereas the χ^2-based algorithms have a resolution that is in between the one of the leading jets algorithm and the correct jet-parton association. For low $m_{\mathrm{t\bar{t}}}$, the leading jets algorithm has a tail towards too high reconstructed $m_{\mathrm{t\bar{t}}}$, which is significantly reduced with the χ^2-based algorithms. Beyond the threshold region, the $m_{\mathrm{t\bar{t}}}$ spectrum is falling for SM $\mathrm{t\bar{t}}$ production, and a tail towards too high reconstructed $m_{\mathrm{t\bar{t}}}$ values hence implies that the background to a Z′ signal increases as more events are shifted to higher $m_{\mathrm{t\bar{t}}}$ values than vice versa. The χ^2-based algorithms therefore not only improve the number of correct associations and the $m_{\mathrm{t\bar{t}}}$ resolution, but also reduce the background to a resonant signal beyond the threshold region.

Numerical values for the resolution are defined by fitting a Gaussian function to the $m_{\mathrm{t\bar{t}}}$ distributions in the range -250 GeV $< m_{\mathrm{t\bar{t}}}^{\mathrm{rec}} - m_{\mathrm{t\bar{t}}}^{\mathrm{gen}} < 250$ GeV. The width of the normal function is then taken as a measure of the resolution. Since the difference between reconstructed and generated $m_{\mathrm{t\bar{t}}}$ does not strictly follow a Gaussian distribution, this definition of resolution is only a useful approximation to study the characteristics of the resolution as a function of $m_{\mathrm{t\bar{t}}}$. The most optimal resolution depends on several factors, e.g. on how many events end up in the tail of the distribution of the resolution as discussed in the previous section. Figure 6.9 shows

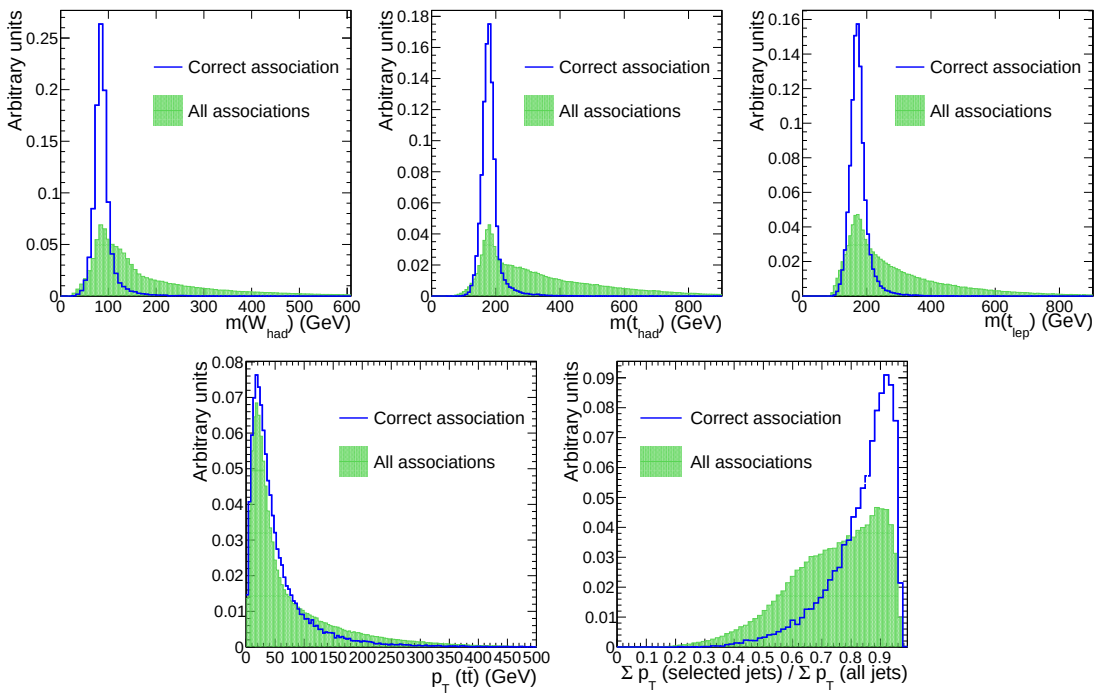

Figure 6.6: Distributions of the different quantities used for the χ^2-based jet-parton association in simulated Z′ events (for a range of masses from 0.5 TeV to 2 TeV): hadronic W boson mass (top left), hadronic top quark mass (top middle), leptonic top quark mass (top right), p_{T} ($\mathrm{t\bar{t}}$ system) (bottom left), and H_T fraction (bottom right). The green histograms show the input variables for all possible jet-parton associations; the blue lines show the distributions for the correct association.

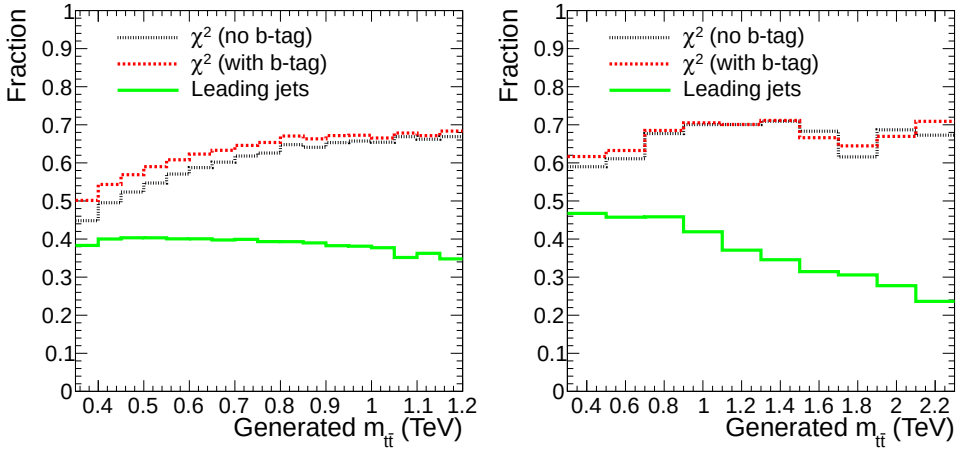

Figure 6.7: Fraction of events with correct jet-parton association using different reconstruction algorithms for events with at least four jets from SM $\mathrm{t\bar{t}}$ production (left) and from Z′ production (right).

the relative (defined by $(m_{\mathrm{t\bar{t}}}^{\mathrm{rec}} - m_{\mathrm{t\bar{t}}}^{\mathrm{gen}})/m_{\mathrm{t\bar{t}}}^{\mathrm{gen}}$) and absolute resolution as a function of generated $m_{\mathrm{t\bar{t}}}$. For the correct jet-parton association, the relative resolution is of the order of 8% for the whole $m_{\mathrm{t\bar{t}}}$ spectrum. The relative resolution for the χ^2-based association with and without

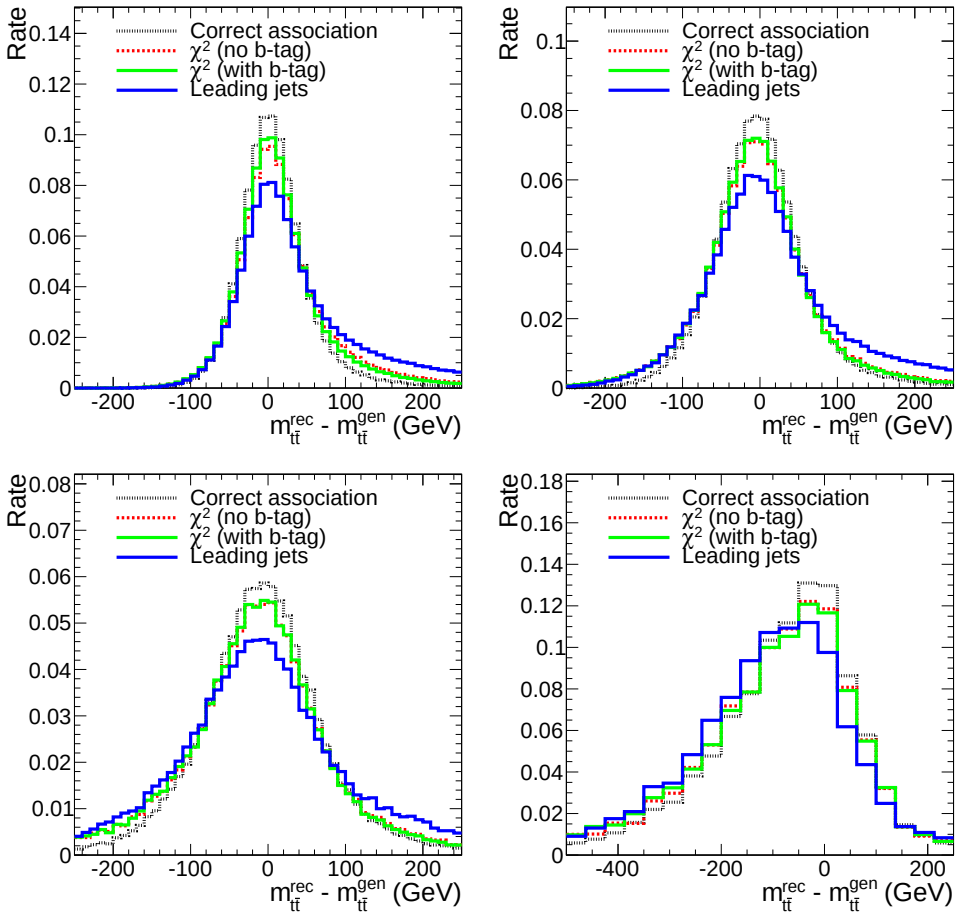

Figure 6.8: Difference between reconstructed and generated $m_{\mathrm{t\bar{t}}}$ for three different reconstruction algorithms and the correct association of jets to partons in four regions of generated $m_{\mathrm{t\bar{t}}}$: 300 GeV $< m_{\mathrm{t\bar{t}}}^{\mathrm{gen}} <$ 550 GeV (top left), 550 GeV $< m_{\mathrm{t\bar{t}}}^{\mathrm{gen}} <$ 800 GeV (top right), 800 GeV $< m_{\mathrm{t\bar{t}}}^{\mathrm{gen}} <$ 1200 GeV (bottom left), and 1200 GeV $< m_{\mathrm{t\bar{t}}}^{\mathrm{gen}} <$ 2200 GeV (bottom right). The distributions are shown for events with at least four selected jets where an association of partons to jets is possible. For $m_{\mathrm{t\bar{t}}}^{\mathrm{gen}} <$ 1200 GeV, the events are from SM $\mathrm{t\bar{t}}$ production, whereas for $m_{\mathrm{t\bar{t}}}^{\mathrm{gen}} >$ 1200 GeV, the events are from a mixture of Z′ samples with equal weight and Z′ masses of 1.25 TeV, 1.5 TeV, and 2 TeV.

inclusion of b-tag information yields a slightly worse resolution of $\sim 9\%$, also with no notable dependence on generated $m_{\mathrm{t\bar{t}}}$. The leading jets algorithm leads to a yet worse resolution of 10–11% for $\mathrm{t\bar{t}}$ events, with a slight increase as a function of generated $m_{\mathrm{t\bar{t}}}$, and of $\sim 10\%$ for Z′ production.

To summarise, the χ^2-based algorithm to associate jets to partons significantly improves the fraction of correct jet-parton associations as well as the resolution of the reconstructed $m_{\mathrm{t\bar{t}}}$ when compared to an $m_{\mathrm{t\bar{t}}}$ reconstruction that only takes the four leading jets into account. The inclusion of b-tagging in the χ^2-based association leads to an increase of the fraction of correct associations, but has no notable effect on the resolution itself. In the following, the χ^2-based algorithm with the inclusion of b-tagging are used to reconstruct $m_{\mathrm{t\bar{t}}}$ for events with at least

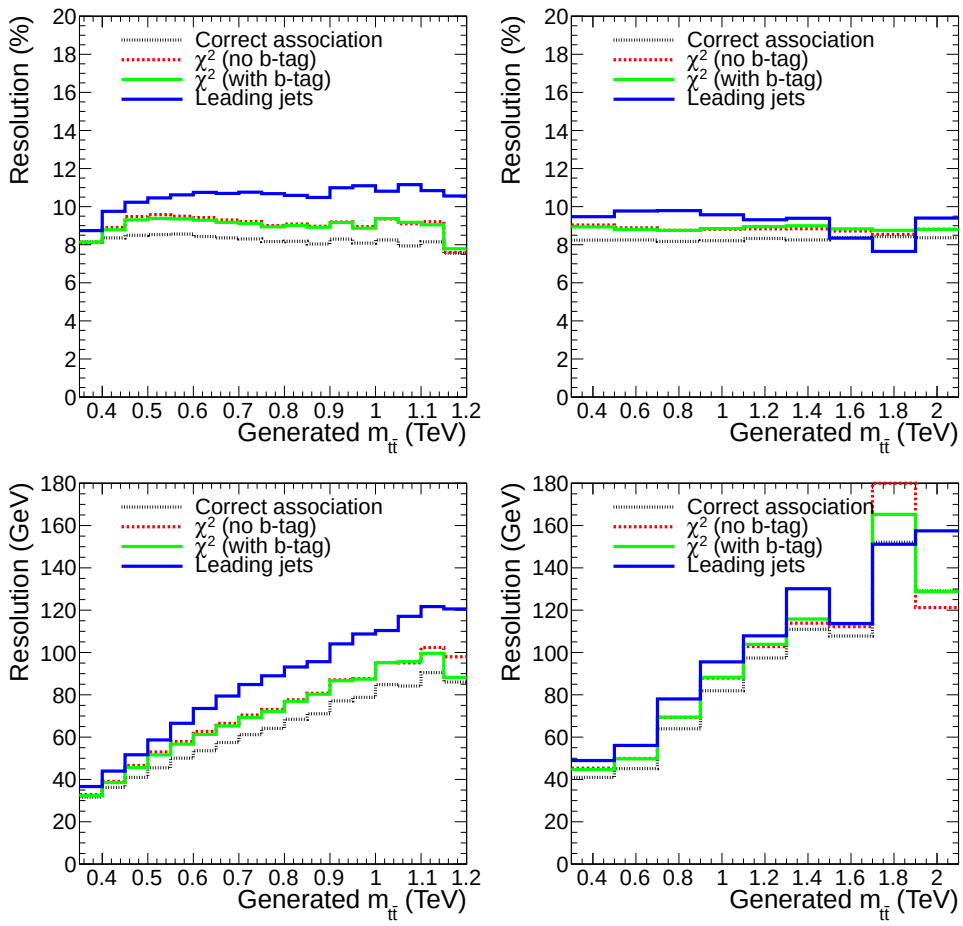

Figure 6.9: Relative (top) and absolute (bottom) resolution of reconstructed $m_{\mathrm{t\bar{t}}}$ for three different reconstruction algorithms and the correct association of jets to partons. The distributions are shown for events from SM $\mathrm{t\bar{t}}$ production (left) and from Z′ production (right) with at least four selected jets where an association of partons to jets is possible.

four jets.

A further improvement of the resolution for events with correct jet-parton association can be obtained by applying a constrained kinematic fit for each event, as e.g. applied in the predecessor of this analysis [133]. However, for events with non-correct jet-parton association, the constrained kinematic often even leads to a decrease of the resolution due to the unphysical constraints. The resulting impact of applying the kinematic on the search sensitivity was found to be negligible for the considered signal models. The kinematic fit is hence not applied for reasons of simplicity. To be sensitive to additional signal models that have strong interference with SM $\mathrm{t\bar{t}}$ production, the improvement of the resolution that the kinematic fit provides for events with correct jet-parton association may be necessary as e.g. peak-dip structures are otherwise washed out.

6.4 Reconstruction in events with exactly three selected jets

There are always four quarks in semileptonic $\mathrm{t\bar{t}}$ events on generator level. Events with only three selected jets may hence exist for two reasons: either a quark gives rise to a jet that does not pass the selection cuts, or two jets merge. As discussed above, the probability for the latter case increases with the p_{T} of the top quarks and therefore with the generated $m_{\mathrm{t\bar{t}}}$. The major reason for jets not passing the selection cuts is that they fail the requirement on the transverse momentum of $p_{\mathrm{T}} > 30$ GeV. There is also a small fraction of events where one of the jets points into the forward direction, i.e. $|\eta| > 2.4$, and an insignificant fraction where a jet fails the identification criteria. For top quark pair production in the Standard Model, the fraction of events with a jet failing the acceptance criteria is about 85%, and the fraction of events with jet merging is about 15%.

Due to the high fraction of events with a jet failing the acceptance criteria, no attempt is made to explicitly reconstruct all intermediate decay products in the $\mathrm{t\bar{t}}$ decay chain as opposed to events with 4 jets. Therefore, a simple reconstruction algorithm is performed. To reconstruct the $\mathrm{t\bar{t}}$ system, the three selected jets, the lepton and the neutrino are added vectorially. In case the solutions for the longitudinal momentum of the neutrino are real, the one is chosen that gives a reconstructed leptonic top quark mass closer to the expected top mass from table 6.1 when combined with either of the two jets and the lepton. One could in principal also use jets with lower transverse momentum for the reconstruction of the $\mathrm{t\bar{t}}$ system. This is however not done for two reasons: the knowledge of the jet energy scale is significantly reduced for jets with $p_{\mathrm{T}} < 30$ GeV, and $m_{\mathrm{t\bar{t}}}$ may be reconstructed too high in case of jet merging. In the following, the performance of the choice of the neutrino p_z solution will be compared to another common choice, the smaller numerical value of $|p_z|$.

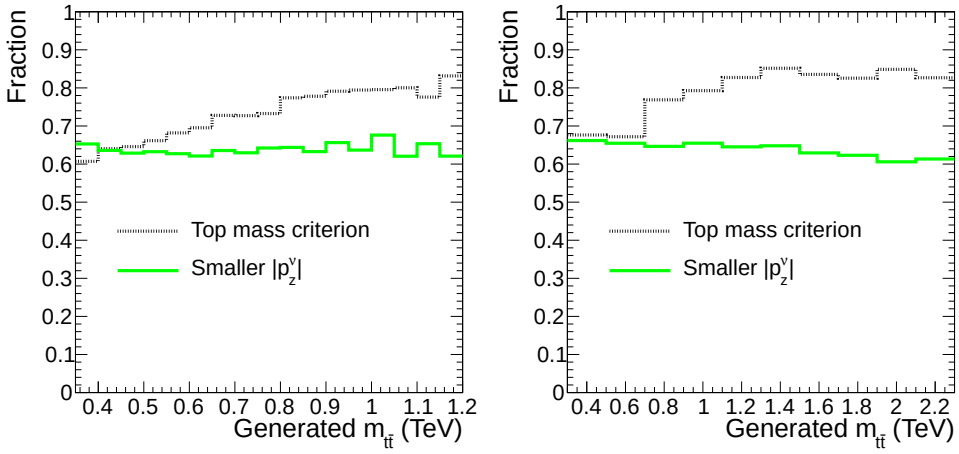

Figure 6.10: Fraction of events where the two reconstruction algorithms (top mass criterion, smaller longitudinal momentum of the neutrino) yield a reconstructed neutrino closer to the generated neutrino for simulated events from SM $\mathrm{t\bar{t}}$ production (left) and from Z′ production (right).

Figure 6.10 compares the fraction of events in which the selected neutrino p_z solution is closer in ΔR to the generated neutrino for the two mentioned reconstruction algorithms. The smaller numerical value of $|p_z|$ corresponds to the better solution in 60–67% of the events for both $\mathrm{t\bar{t}}$ and Z′ production. The fraction is relatively constant as a function generated $m_{\mathrm{t\bar{t}}}$, with a slight decrease towards high $m_{\mathrm{t\bar{t}}}$. In the threshold region, the top mass criterion performs similarly and finds the better solution in 60–67% of the events. In contrast to the first algorithm, the fraction of correct solutions increases with generated $m_{\mathrm{t\bar{t}}}$, and the top mass criterion chooses the correct solution in more than 80% of the events for $m_{\mathrm{t\bar{t}}} > 1$ TeV. Therefore, the top mass criterion is a significant improvement of the baseline algorithm, the smaller $|p_z|$ solution.

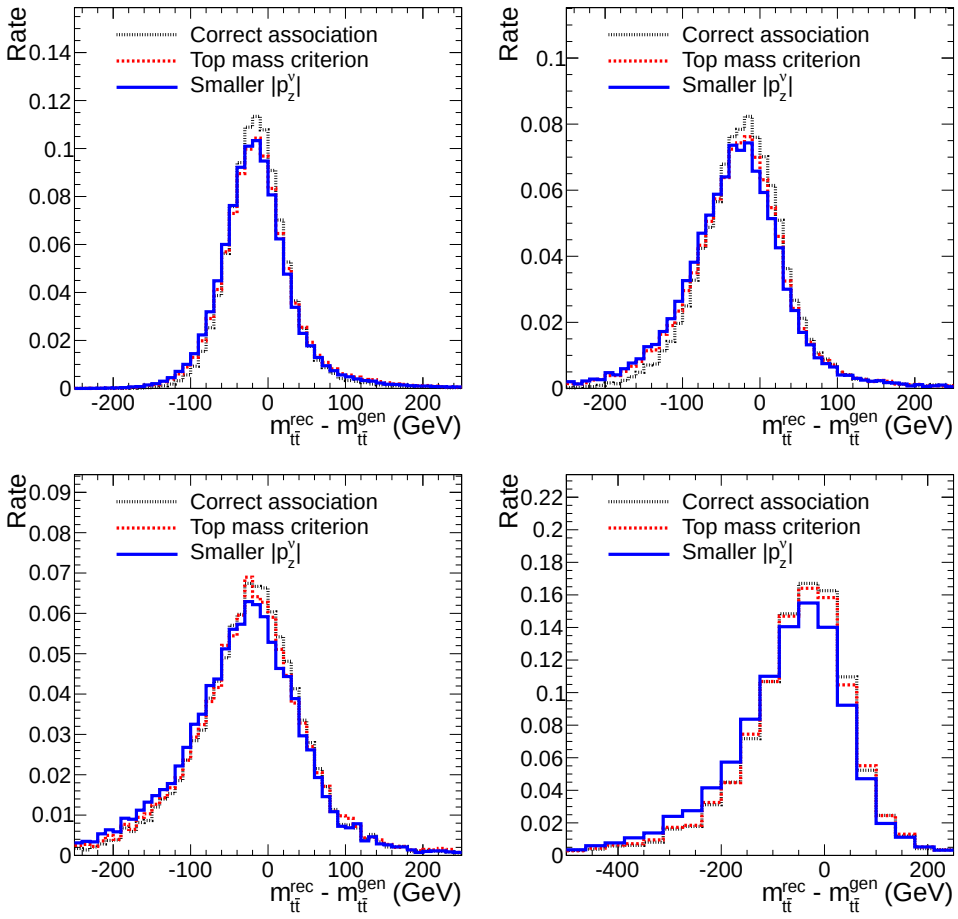

Figure 6.11: Difference between reconstructed and generated $m_{\mathrm{t\bar{t}}}$ for three different reconstruction algorithms and the correct association of jets to partons in four regions of generated $m_{\mathrm{t\bar{t}}}$: 300 GeV $< m_{\mathrm{t\bar{t}}}^{\mathrm{gen}} <$ 550 GeV (top left), 550 GeV $< m_{\mathrm{t\bar{t}}}^{\mathrm{gen}} <$ 800 GeV (top right), 800 GeV $< m_{\mathrm{t\bar{t}}}^{\mathrm{gen}} <$ 1200 GeV (bottom left), and 1200 GeV $< m_{\mathrm{t\bar{t}}}^{\mathrm{gen}} <$ 2200 GeV (bottom right). The distributions are shown for events with three selected jets where an association of partons to jets is possible. For $m_{\mathrm{t\bar{t}}}^{\mathrm{gen}} < 1200$ GeV, the events are from SM $\mathrm{t\bar{t}}$ production, whereas for $m_{\mathrm{t\bar{t}}}^{\mathrm{gen}} > 1200$ GeV, the events are from a mixture of Z′ samples with equal weight and Z′ masses of 1.25 TeV, 1.5 TeV, and 2 TeV.

The difference between reconstructed and generated $m_{\mathrm{t\bar{t}}}$ for the two reconstruction algorithms and the correct choice of the neutrino p_z solution is shown in figure 6.11 in four different

regions of generated $m_{t\bar{t}}$. The mean values for all reconstruction versions have a negative difference over the complete $m_{t\bar{t}}$ range, indicating that a certain amount of energy is lost in the reconstruction. The mean is slightly smaller and therefore shows a larger difference from zero for the smaller neutrino $|p_z|$ solution, and the top quark mass algorithm yields a mean closer to the one from the correct reconstruction version. There is no significant tail towards higher $m_{t\bar{t}}$ values, whereas a small tail towards too low reconstructed $m_{t\bar{t}}$ values emerges for $m_{t\bar{t}} > 1$ TeV, which is slightly more pronounced when taking the smaller neutrino $|p_z|$ value.

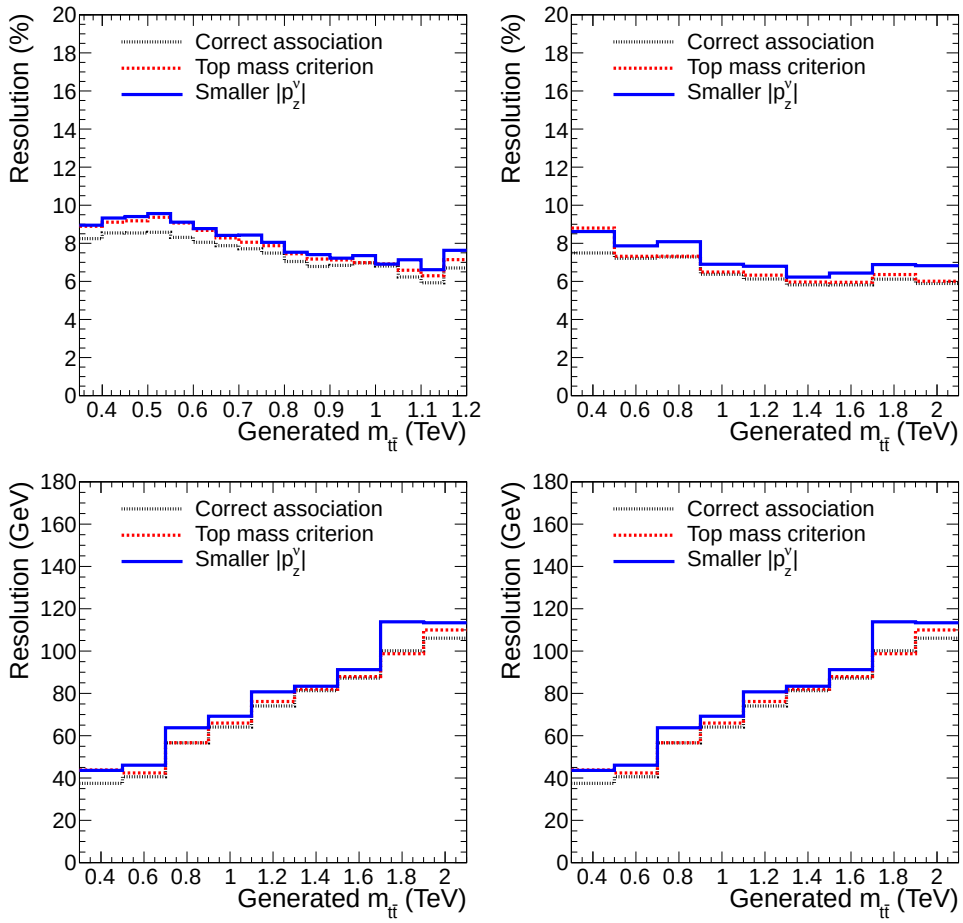

Figure 6.12: Relative (top) and absolute (bottom) resolution of reconstructed $m_{t\bar{t}}$ for two reconstruction algorithms and the correct association of jets to partons. The distributions are shown for events with three selected jets from SM $t\bar{t}$ production (left) and from Z' production (right) where an association of partons to jets is possible.

The relative and absolute resolutions of the $m_{t\bar{t}}$ reconstruction in reconstructable events with exactly three jets are shown in figure 6.12. Like for events with at least four jets, the numerical values of the resolution are determined by fitting a Gaussian function to the difference between reconstructed and generated $m_{t\bar{t}}$. The relative resolution is $\sim 8\%$ for the correct solution in the threshold region and constantly falls down to $\sim 6\%$ for $m_{t\bar{t}} \sim 2$ TeV. The two reconstruction algorithms yield a resolution that is typically 1% higher. For SM $t\bar{t}$ production in the bulk region, the two algorithms give a similar resolution. For Z' production, the top mass criterion improves the resolution compared to the smaller $|p_z|$ solution, and the obtained resolution is close to the one from the correct solution.

In summary, the top mass criterion improves both the fraction of correct solutions and the $m_{\mathrm{t\bar{t}}}$ resolution and is hence used to reconstruct $m_{\mathrm{t\bar{t}}}$ for events with three jets in the following. Compared to the resolution obtained in events with at least four jets, the $m_{\mathrm{t\bar{t}}}$ resolution in events with three jets is similar for $m_{\mathrm{t\bar{t}}}$ in the threshold region and slightly better for higher $m_{\mathrm{t\bar{t}}}$. One should however take into account that the $m_{\mathrm{t\bar{t}}}$ reconstruction in three-jet events tends to underestimate the generated $m_{\mathrm{t\bar{t}}}$, and the reconstruction quality can hence be considered as compatible.

7 Background Estimation

This chapter describes the estimation of the relevant background processes and compares the estimated distributions from simulated events with the data. The different background processes can be subdivided according to their similarity to the signal processes. Processes that have a similar final state are generally modelled by event generators, whereas the simulation of events that do not contain an isolated lepton from the decay of a W boson are regarded as instrumental background.

These events stem from multijet production and are typically not modelled well by event simulations. The event yields and shapes are hence estimated using techniques that make use of the special characteristics of according data events. There are a number of possible reasons why electrons and muons from multijet production may be measured as well-identified, isolated leptons, which will be outlined below. These measurement techniques, often called "data-driven", generally estimate the event yields and kinematic distributions of multijet events in the signal region by extrapolating from appropriate control regions. To verify that these extrapolations are sensible, and to determine systematic uncertainties of the estimation, simulated multijet event samples are used.

Events that mimic the signal final state, i.e. events that contain an isolated lepton, jets, amongst those possibly b jets, and missing transverse energy, are modelled with the help of event generators. Though it is in principle possible to reduce the number of non-$\mathrm{t\bar{t}}$ background events by imposing further or tighter event selection requirements, this also leads to a reduction of the signal efficiency. Instead of using further selection requirements, the categorisation of events increases the expected sensitivity of the analysis by maximising the signal efficiency, by exploiting different signal-to-background ratios in the different categories, and by using the data to constrain the uncertainties on the description of the background processes.

In the following, the estimation of multijet events in both the muon and the electron channel will be explained. Then, the treatment of events from all other background processes will be discussed. In the subsequent section, the modelling of the different background contributions is validated by comparing kinematic distributions from data and simulated events. Finally, it is discussed how well the simulation describes the observed kinematic distributions that are relevant for the reconstruction of the $\mathrm{t\bar{t}}$ system.

7.1 Multijet events with muons

In multijet events with a muon that passes the event selection criteria, most importantly the relative isolation criterion, the muon almost exclusively originates from decays of B hadrons

and kaons according to simulated multijet event samples. The contributions from events with non-real muons, e.g. from hadrons punching through the hadron calorimeters, are expected to be negligible. Due to the underground position of the CMS detector and the tight timing requirements in the muon reconstruction, the contribution from cosmic muons is also negligible. A possible influence of cosmic muons is excluded by verifying that the number of reconstructed muons that have a high distance in the longitudinal direction to the reconstructed primary vertex is negligible.

The muons from decays of B hadrons and kaons have two features in common. First, they come from hadrons that form jets, and they are hence close to a hadronic jet. Second, their mother hadrons have a non-negligible average lifetime, and the muons therefore originate from a displaced interaction vertex.

In addition, there are no hard primary neutrinos in multijet events as the only source of real missing energy is from partially leptonic decays of B hadrons, leading to a relatively small amount of missing transverse energy.

Estimation of event yields

The event yields for multijet production in the muon channel are estimated using two control regions, the region of low missing transverse energy as a multijet-enriched control region, and the region of high relative isolation as a model for kinematic distributions. In the low $E_{\mathrm{T}}^{\mathrm{miss}}$ control region, the yield of multijet events is determined by a template fit, and the determined yields are then extrapolated to the signal region. This estimation is performed separately in all four event categories in the muon channel.

The template fit makes use of the distribution of the transverse momentum of the vectorial sum of all selected jets. The vectorial sum of all selected jets is commonly denoted as *hadronic final state (HFS)*. The HFS p_{T} distributions from multijet production and from events with a real W boson exhibit significant shape differences for events with low missing transverse energy. Compared to other properties of reconstructed events that show a significant shape difference between multijet and other background events like the transverse W boson mass, the HFS p_{T} distribution leads to the estimation with the smallest uncertainty.

The number of simulated multijet events corresponds to an integrated luminosity of ~ 300 pb^{-1}, which is more than a factor of ten less than the used dataset. Only of the order of 10 of these simulated events pass the event selection prior to categorisation. Therefore, the number of simulated events is not sufficient to validate the presented methods in detail. The estimation therefore relies on estimations from control regions in data and on different analyses where the number of simulated events allows to validate the used methods [61,113].

The two sideband regions in data are illustrated in figure 7.1: events with low missing transverse energy ($E_{\mathrm{T}}^{\mathrm{miss}} < 20$ GeV), which are enriched in multijet events, and events with high relative isolation ($0.2 < r_{iso} < 0.5$), which are dominated by multijet events. The yield of the multijet contribution in the signal region is determined by first fitting templates of the multijet background and of all other backgrounds to the HFS p_{T} distribution in the low $E_{\mathrm{T}}^{\mathrm{miss}}$ and

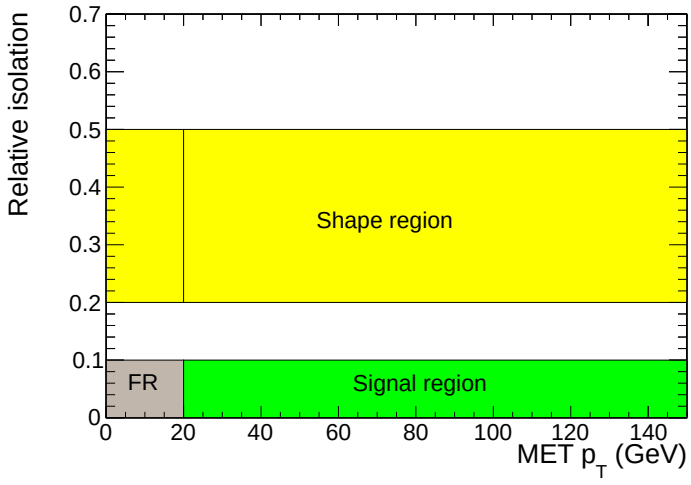

Figure 7.1: Illustration of the different sideband regions used for the estimation of multijet events. The regions are labelled according to their corresponding purpose: the fit region (*FR*) where the sideband fit is performed, the *Shape region* where the shape of kinematic distributions is derived (split by a line to indicate the division between the low $E_{\mathrm{T}}^{\mathrm{miss}}$ region used to derive the shape for the transverse W mass fit and the high $E_{\mathrm{T}}^{\mathrm{miss}}$ region used to derive the extrapolation factor), and the *signal region*.

isolated ($0.125 > r_{iso}$) region (FR); this estimation is then extrapolated to the signal region ($E_{\mathrm{T}}^{\mathrm{miss}} > 20$ GeV) using the ratio of events with high and low $E_{\mathrm{T}}^{\mathrm{miss}}$ in the non-isolated region.

One can also think of the method in a different way: The region of low $E_{\mathrm{T}}^{\mathrm{miss}}$ is used to derive a scale factor for the multijet background from the high relative isolation control region to the low relative isolation region. This scale factor can hence be regarded as a measure of the probability that a multijet event has low relative isolation. Then, the assumption is made that this scale factor is universal, i.e. that it applies for both the low and the high $E_{\mathrm{T}}^{\mathrm{miss}}$ region. To be able to compare the scale factors in the different categories, they are also given in table 7.1.

Estimation of kinematic distributions

In the following, the high relative isolation region is supposed to serve as a full model for multijet events. This means that, for the purpose of comparing data with background, the assumption is made that the events from the high relative isolation region describe all kinematic properties of multijet events in the signal region. Due to the low number of simulated multijet events, this assumption is verified in a sideband region with a higher number of predicted multijet events, which is defined by relaxing the requirement of at least three selected jets and by reducing the jet p_{T} thresholds.

For the fit in the low $E_{\mathrm{T}}^{\mathrm{miss}}$ region, multijet events are taken from the distribution in the region of high relative isolation and low $E_{\mathrm{T}}^{\mathrm{miss}}$ ($E_{\mathrm{T}}^{\mathrm{miss}} < 20$ GeV, $0.2 < r_{iso} < 0.5$). The extrapolation factor from the low $E_{\mathrm{T}}^{\mathrm{miss}}$ region ($E_{\mathrm{T}}^{\mathrm{miss}} < 20$ GeV) to the signal region ($E_{\mathrm{T}}^{\mathrm{miss}} > 20$ GeV) is determined in the full high relative isolation region ($0.2 < r_{iso} < 0.5$). The distributions from the other background processes (W/Z plus jets, $\mathrm{t\bar{t}}$, single top) are taken from simulated

events and are treated as one combined distribution since they all have compatible HFS p_{T} distributions. The same generally also holds for a possible contamination from Z′ or other signal events in the low $E_{\mathrm{T}}^{\mathrm{miss}}$ region, though the HFS p_{T} becomes harder at high Z′ mass. At high Z′ mass, the relevant signal cross sections are however relatively low, and a possible signal contamination in the low $E_{\mathrm{T}}^{\mathrm{miss}}$ region is hence negligible. According to the simulation, the high relative isolation region is dominated by multijet events with an expected purity of more than 98%. This implies that a possible contamination from other background processes or from signal events can be neglected.

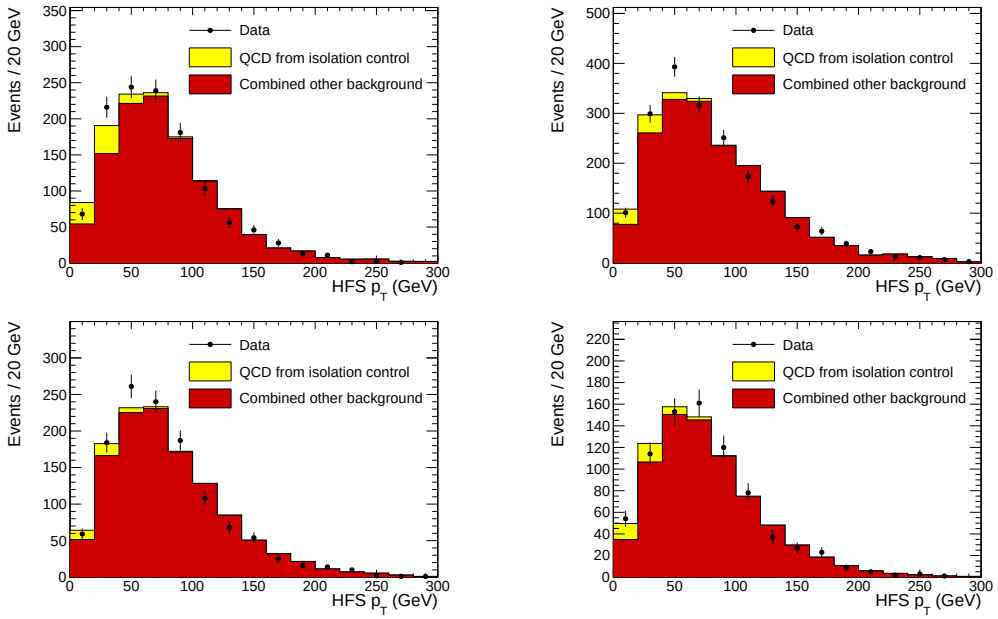

Figure 7.2: The fitted HFS p_{T} templates for the different jet/b-tag multiplicities in the $E_{\mathrm{T}}^{\mathrm{miss}}$ fit region ($E_{\mathrm{T}}^{\mathrm{miss}} < 20$ GeV) in the muon channel for events with 3 jets and at least one b-tag (top left); with 4 jets and no b-tags (top right), 1 b-tag (bottom left), and at least 2 b-tags (bottom right).

The two templates (multijet defined by $E_{\mathrm{T}}^{\mathrm{miss}} < 20$ GeV and $0.2 < r_{iso} < 0.5$ and the combined background from simulation with $E_{\mathrm{T}}^{\mathrm{miss}} < 20$ GeV and $r_{iso} < 0.1$) are fit to the data distribution obtained from events with $r_{iso} < 0.1$ and $E_{\mathrm{T}}^{\mathrm{miss}} < 20$ GeV. This fit is repeated in all four categories (3 jets with at least one b-tag, 4 jets with 0, 1, and at least 2 b-tags) and gives an estimate of the number of multijet events in the low $E_{\mathrm{T}}^{\mathrm{miss}}$ region. The yields are then separately extrapolated to the signal region for the four categories. The calculated yields in the signal region are summarised in table 7.1. They confirm that the contribution from multijet events is small compared to the total number of events in the signal region. The resulting HFS p_{T} distributions in the low $E_{\mathrm{T}}^{\mathrm{miss}}$ region can be found in figure 7.2, with the full background model showing good agreement with the data.

The statistical uncertainties of the calculated yields are of the order of 30-50%. Systematic uncertainties evolve from the extrapolation from low $E_{\mathrm{T}}^{\mathrm{miss}}$ to high $E_{\mathrm{T}}^{\mathrm{miss}}$ as well as from the composition and shape of the templates for the multijet and the other background processes. The uncertainties from the shapes of the other background processes are expected to be small

Table 7.1: Predicted yields in the signal region using the results from the template fit in the low $E_{\mathrm{T}}^{\mathrm{miss}}$ sideband ($E_{\mathrm{T}}^{\mathrm{miss}} < 20$ GeV) in the muon channel.

Region	$\boldsymbol{N_{\mathrm{est,\,QCD}}^{\mathrm{data}}}$	$\boldsymbol{sf_{\mathrm{QCD}}}$
3j0t	518 ± 70 (stat.) ± 148 (syst.)	0.36 ± 0.05
3j1t	163 ± 44 (stat.) ± 90 (syst.)	0.23 ± 0.06
4j0t	194 ± 62 (stat.) ± 73 (syst.)	0.07 ± 0.02
4j1t	104 ± 60 (stat.) ± 44 (syst.)	0.05 ± 0.03
4j2t	152 ± 64 (stat.) ± 80 (syst.)	0.15 ± 0.06

as the HFS p_{T} shapes are very similar. This is checked by replacing the combined background model with a model only using simulated $\mathrm{t\bar{t}}$ events. The resulting yields vary by up to 10% in the different categories, which induces a negligible uncertainty compared to the other sources of systematic uncertainties. The uncertainties from the $E_{\mathrm{T}}^{\mathrm{miss}}$ extrapolation and the shape of the multijet templates are estimated by varying the borders of the high relative isolation sideband. The definition of the sideband region is changed to $0.15 < r_{iso} < 0.4$ and $0.3 < r_{iso} < 0.6$. The two different variations give deviations with a similar absolute value. The higher deviation is used as the estimate of the systematic uncertainty and is quoted in table 7.1. It is also ensured that changing the $E_{\mathrm{T}}^{\mathrm{miss}}$ fit region to either 0 GeV $< E_{\mathrm{T}}^{\mathrm{miss}} < 15$ GeV or to 5 GeV $< E_{\mathrm{T}}^{\mathrm{miss}} < 20$ GeV does not have a sizeable impact on the estimated yields. The resulting changes are of the order of 10% and hence smaller than the statistical uncertainties. The combined systematic uncertainties are of the order of 15% to 60%, depending on the region, and are generally smaller than the statistical uncertainties. The statistical and systematic uncertainties are added in quadrature, and the combined uncertainties are used in the statistical evaluation.

The resulting inclusive $E_{\mathrm{T}}^{\mathrm{miss}}$ distributions using the estimated multijet background are displayed in figure 7.3. The general agreement of the $E_{\mathrm{T}}^{\mathrm{miss}}$ shapes is good (though not excellent as there is a small downward slope of the complete distribution for which the multijet background cannot account), indicating that the estimation of the multijet background performs well.

Table 7.2: Comparison of predicted scale factors from fits to the $E_{\mathrm{T}}^{\mathrm{miss}}$ distribution and from the default template fit in the low $E_{\mathrm{T}}^{\mathrm{miss}}$ region.

Region	**Scale factor** $\boldsymbol{E_{\mathrm{T}}^{\mathrm{miss}}}$	**Scale factor fit**
3j1t	0.16 ± 0.11	0.20 ± 0.06
4j0t	0.13 ± 0.5	0.08 ± 0.02
4j1t	0.10 ± 0.06	0.05 ± 0.03
4j2t	0.00 ± 0.05	0.15 ± 0.06

An additional cross check is performed with the help of the distribution of the missing transverse energy. Using the region of $0 < E_{\mathrm{T}}^{\mathrm{miss}} < 100$ GeV, the combined background and the multijet model from the anti-isolation region are fitted to the data, and scale factors for the extrapolation of events from the anti-isolation region to the signal region are derived. The results are listed in table 7.2, with the uncertainties denoting the statistical uncertainty as given by the

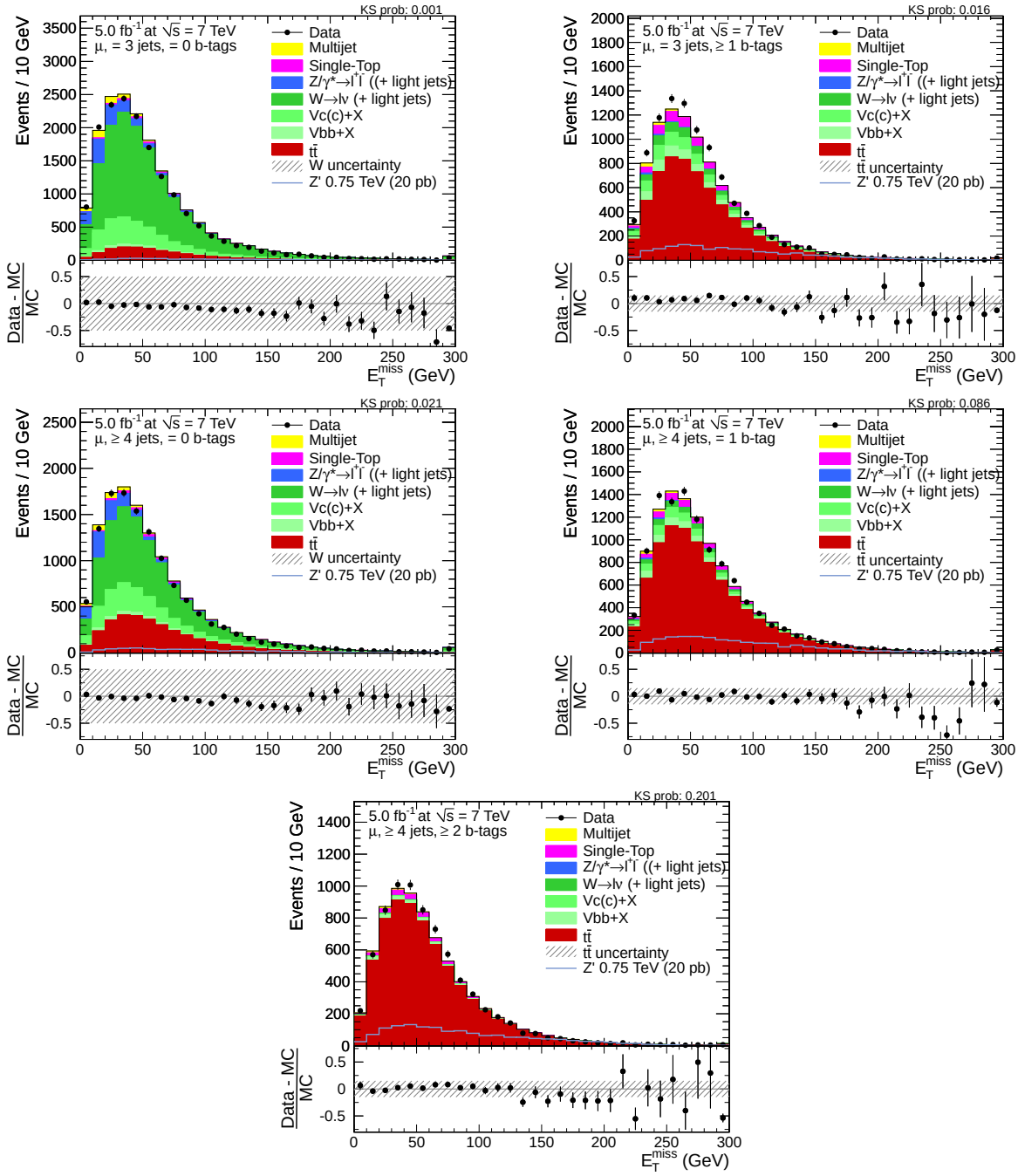

Figure 7.3: Distribution of $E_{\mathrm{T}}^{\mathrm{miss}}$ in muon-plus-jets events after scaling the multijet contribution to estimations from data-driven method for events with 3 jets and no b-tag (top left), 3 jets and at least 1 b-tag (top right), and with at least 4 jets and 0 b-tags (middle left), 1 b-tag (middle right), and 2 b-tags (bottom).

likelihood fit. The resulting scale factors are compared to the scale factors from the HFS p_{T} fits in the region of low $E_{\mathrm{T}}^{\mathrm{miss}}$. For events with 4 jets and at least two b-tags, the $E_{\mathrm{T}}^{\mathrm{miss}}$ fit gives a multijet yield of zero, resulting in an unreliable error estimation from the fit. The scale factor is however still compatible when taking systematic uncertainties into account. For all other categories, the scale factors agree well within the statistical uncertainties.

7.2 Multijet events with electrons

In the electron channel, the sources of multijet events are three-fold. First, electrons from the decays of B hadrons and other long-lived hadrons may be reconstructed as isolated and well-identified electrons, similar to the muon channel. Second, one of the electrons from a photon conversion (either inside a jet or from a prompt photon) can be highly energetic and well isolated. Third, a jet with at high fraction of electromagnetic energy may be misidentified as an electron. Simulated events show that the most important contribution is from photon conversions and the second most important from hadronic decays, whereas the fraction of misidentified jets is small.

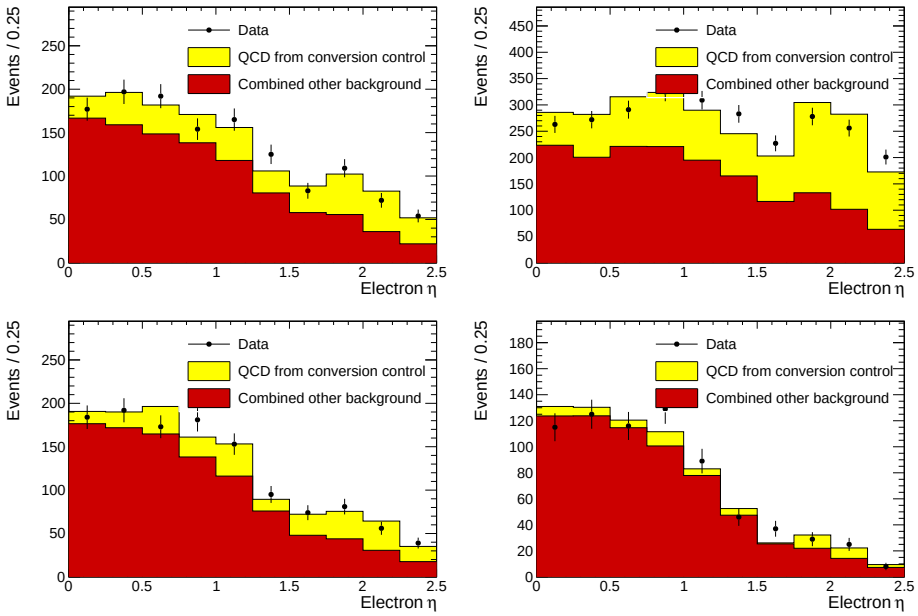

Figure 7.4: The fitted electron η templates for the different jet multiplicities in the $E_{\mathrm{T}}^{\mathrm{miss}}$ control region ($E_{\mathrm{T}}^{\mathrm{miss}} < 20$ GeV) in the electron channel. Shown are events with 3 jets and at least one b-tag (top left) and with 4 jets and either no b-tags (top right), 1 b-tag (bottom left), or at least 2 b-tags (bottom right).

The yield estimation is performed using the same technique as described above for muons, but with a different fitted distribution. In a $E_{\mathrm{T}}^{\mathrm{miss}}$ control region ($E_{\mathrm{T}}^{\mathrm{miss}} < 20$ GeV), a simultaneous fit to the observed electron pseudorapidity distribution is performed, using two components from either events with real W bosons or from multijet events that are modelled with a control region enriched in conversions. The conversion control region is defined by either the requirement

of at least one missing hit in the innermost layer of the pixel detector or by the presence of a partner track from a conversion partner matching algorithm. The fit to the pseudorapidity is used to determine a scale factor for events failing the conversion rejection algorithm, as outlined in the previous section. The resulting yields and the kinematic distributions from the conversion control region are used in the statistical evaluation and also for the plots shown throughout this thesis.

A different fit variable than in the muon channel is used due to the different sources of multijet events in the electron channel. The electron pseudorapidity distribution is chosen as it provides good separation of multijet events and events with a real W boson. At the same time, the results prove to be stable under systematic variations, e.g. compared to the distribution of the transverse W boson mass. The distribution of the HFS p_{T}, which is used in the muon channel, separates significantly less well between multijet events and events with a real W boson.

Table 7.3: Predicted yields in the signal region using the template fit method in the $E_{\mathrm{T}}^{\mathrm{miss}} < 20$ GeV control region in the electron channel.

Region	$\boldsymbol{N}^{\mathbf{data}}_{\mathbf{est,\,multijet}}$	$\boldsymbol{f}_{\mathbf{multijet}}$
3j0t	1528 ± 135 (stat.) ± 840 (syst.)	0.48 ± 0.04 (stat.)
3j1t	491 ± 76 (stat.) ± 195 (syst.)	0.67 ± 0.10 (stat.)
4j0t	1398 ± 118 (stat.) ± 866 (syst.)	0.61 ± 0.05 (stat.)
4j1t	504 ± 89 (stat.) ± 227 (syst.)	0.79 ± 0.09 (stat.)
4j2t	210 ± 93 (stat.) ± 91 (syst.)	0.73 ± 0.32 (stat.)

The resulting correction factors and predicted numbers of events are summarised in table 7.3. With numerical values of 0.48–0.79, the estimated scale factors appear to be relatively universal. They are slightly lower for three-jet events than for four-jet events, especially for events with no b-tagged jet. Figure 7.4 shows the templates scaled to the predicted yields from the fit. The statistical uncertainties are similar to the muon channel and are of the order of 5–50%. Systematic uncertainties are evaluated by using events from a control region with a high relative isolation of the electron, $0.2 < r_{iso} < 0.5$, which are enriched in electrons from the decay of hadrons. The deviation from the nominal estimation is quoted as a systematic uncertainty in table 7.3. Since the multijet events in the electron channel are expected to be from a mixture of heavy flavour decays and conversions, this uncertainty should give a conservative estimate of the maximum range of the yields. Additional systematic uncertainties are estimated in the same way as in the muon channel, i.e. by replacing the shape of the electron η distribution for the combined other background samples with the one from $\mathrm{t\bar{t}}$ events only, and by varying the borders of the $E_{\mathrm{T}}^{\mathrm{miss}}$ fit region. These result in relatively small uncertainties of sizes similar to the muon channel. The combined systematic uncertainties are slightly larger than in the muon channel and of the order of 40-60%. The combined statistical and systematic uncertainties are used in the statistical evaluation.

The $E_{\mathrm{T}}^{\mathrm{miss}}$ distributions including the results from the data-driven estimation of multijet events are shown in figure 7.5. The model falls slightly low in events with 3 jets and 0 b-tags in the region of low $E_{\mathrm{T}}^{\mathrm{miss}}$, though compatible within an underestimation of multijet events of 20%

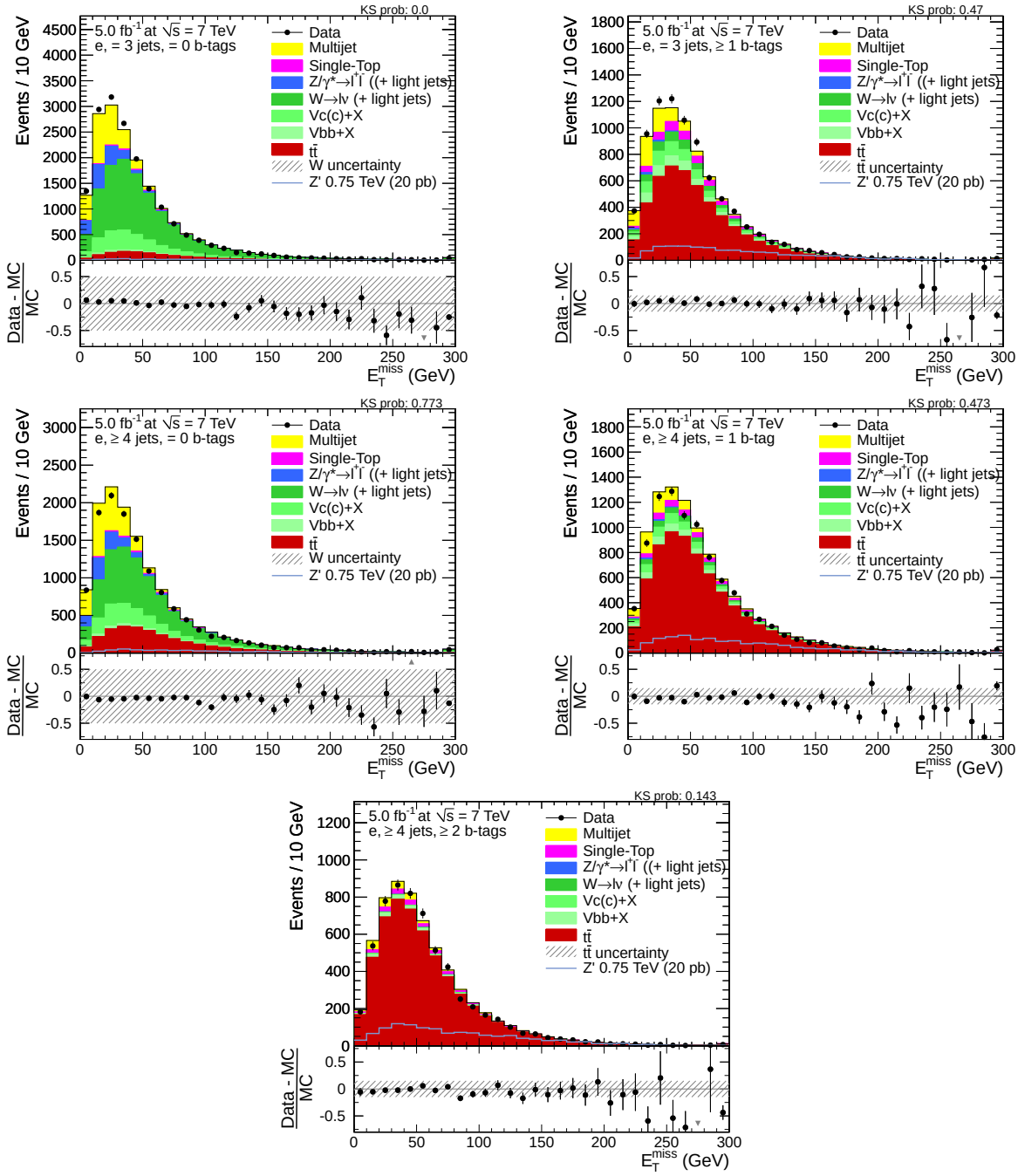

Figure 7.5: Distribution of $E_{\mathrm{T}}^{\mathrm{miss}}$ in inclusive range after scaling of electron multijet contribution to estimations from data-driven method for events with 3 jets and no b-tag (top left), 3 jets and at least 1 b-tag (top right), and with at least 4 jets and 0 b-tags (middle left), 1 b-tag (middle right), and 2 b-tags (bottom).

and therefore fully covered by the 50% relative uncertainty. This difference coincides with the smaller scale factor estimated above, underlining the universality of the scale factors. The other $E_{\mathrm{T}}^{\mathrm{miss}}$ distributions are well described by the prediction.

Table 7.4: Comparison of predicted scale factors from fits to the $E_{\mathrm{T}}^{\mathrm{miss}}$ distribution and from the default template fit in the low $E_{\mathrm{T}}^{\mathrm{miss}}$ region.

Region	**Scale factor $E_{\mathrm{T}}^{\mathrm{miss}}$ fit**	**Scale factor electron η fit**
3j1t	0.49 ± 0.12	0.63 ± 0.12
4j0t	0.57 ± 0.04	0.58 ± 0.05
4j1t	0.63 ± 0.08	0.65 ± 0.10
4j2t	0.44 ± 0.41	0.71 ± 0.32

Like in the muon channel, the results are cross-checked by comparing the resulting scale factors for events from the conversion-enriched control region with scale factors obtained in a fit to the $E_{\mathrm{T}}^{\mathrm{miss}}$ distribution. Table 7.4 summarises the scale factors in the four different event categories together with their statistical uncertainties. The scale factors from both methods turn out to be compatible within statistical uncertainties, confirming the validity of the estimated event yields.

7.3 Events with a W or Z boson and jets

The inclusive W- and Z-plus-jets cross sections in 7 TeV pp collisions have been calculated at NNLO accuracy and are thus known with high precision. However, the relative fractions of events with different jet multiplicities as well as the kinematic properties of W/Z-plus-jets events are only modelled by the used event generators and are hence subject to larger uncertainties. Both the inclusive W/Z-plus-jets cross section calculations as well as the validity of the simulation of the production in association with jets have been confirmed by measurements from the ATLAS and CMS collaborations [134,135].

7.3.1 General strategy

This section outlines a validation of the kinematic distribution of W-plus-jets events in event samples that are enriched in W boson production, and it is explained how W-plus-jets events are treated in this analysis.

The general strategy is as follows. With a loose constraint on the yield of W-plus-jets events of 50%, the template fit used in the statistical evaluation obtains a relatively precise value of the observed yield of W-plus-jets events, with an uncertainty of the order of 10%, by exploiting the high fraction of W-plus-jets events in events with 4 jets of which none is b-tagged. In other words, the W-plus-jets yield is fitted in situ to the data. As will be shown in the following, the yield of W-plus-jets events is well estimated in events with 3 and more than 4 jets when scaling to the inclusive NNLO cross section and using the default MADGRAPH simulation. Hence, no

prior corrections of the W-plus-jets yields are applied. In the next section, a comparison of the distribution of several kinematic quantities will be shown for data and simulated events with three jets of which none is b-tagged.

To be able to independently study samples enriched in heavy flavour jets and to be able to apply related systematic uncertainties, the W/Z-plus-jets event samples are split according to the flavour of the additional jet. Events with at least one selected jet with b flavour are combined to W+b+X, events with at least one c-flavoured jet but no b-flavoured jet to W+c+X, and the rest of the events to W+light flavour. For both the W+b+X and W+c+X samples, an increased yield uncertainty of 100% will be used to cope with the higher uncertainties on the modelling of the heavy flavour contribution in the regarded phase space. In the following, an additional validation of the rate of heavy-flavour-enriched W-plus-jets events is presented that makes use of the lepton charge asymmetry in W-plus-jets events, which is not present in $\mathrm{t\bar{t}}$ or signal events.

In addition to the yield uncertainty of 50%, systematic samples with varied renormalisation and factorisation scales are used. These variations have a high impact on the event yields. For an increased scale, the predicted yields are reduced by roughly a factor of 2; for a reduced scale, they are increased by more than a factor of 2. The yields from the varied samples are incompatible with the data, indicating that the default settings are a reasonable choice.

7.3.2 Kinematic distributions in events with 3 jets and no b-tags

About 80% of the events with 3 selected jets of which none is b-tagged are expected to stem from the production of a W boson in association with jets. The comparison of data and simulation in this event category therefore provides useful information about the description of the simulated event samples describing W-plus-jets production.

In the following, kinematic distributions will be compared between data and simulated events. The contributions from simulated events are shown as a stacked histogram except for simulated Z' events. The different simulated samples are represented by the different colours given in the legend, which is only drawn in a subset of the plots. At the bottom of each plot, the ratio of data and simulated events is shown in the form $(N_{\mathrm{data}} - N_{\mathrm{sim}})/N_{\mathrm{sim}}$ with the number of data events N_{data} and the number of expected events from simulation N_{sim} in each bin. The ratio is accompanied by an illustration of the assumed rate uncertainties for certain backgrounds, e.g. an uncertainty of 50% for the W-plus-jets yield in the following plots, to help judge the compatibility of the total event rates.

On top of each plot, the Kolmogorov-Smirnov (KS) probability is shown [136]. The KS probability is a measure of the statistical compatibility of the two histograms, i.e. the histograms representative of the sum of the backgrounds and the data. For unbinned data, the KS probability is uniformly distributed between 0 and 1 if the two datasets are due to the same underlying distribution. For binned data, the value of the KS probability for compatible distributions is shifted towards 1. The shift is however small if the number of bins is high and if the bin size is below the detector resolution. If the KS probability is very small, the two histograms under consideration are statistically not compatible, and it needs to be checked that the difference is covered by systematic uncertainties.

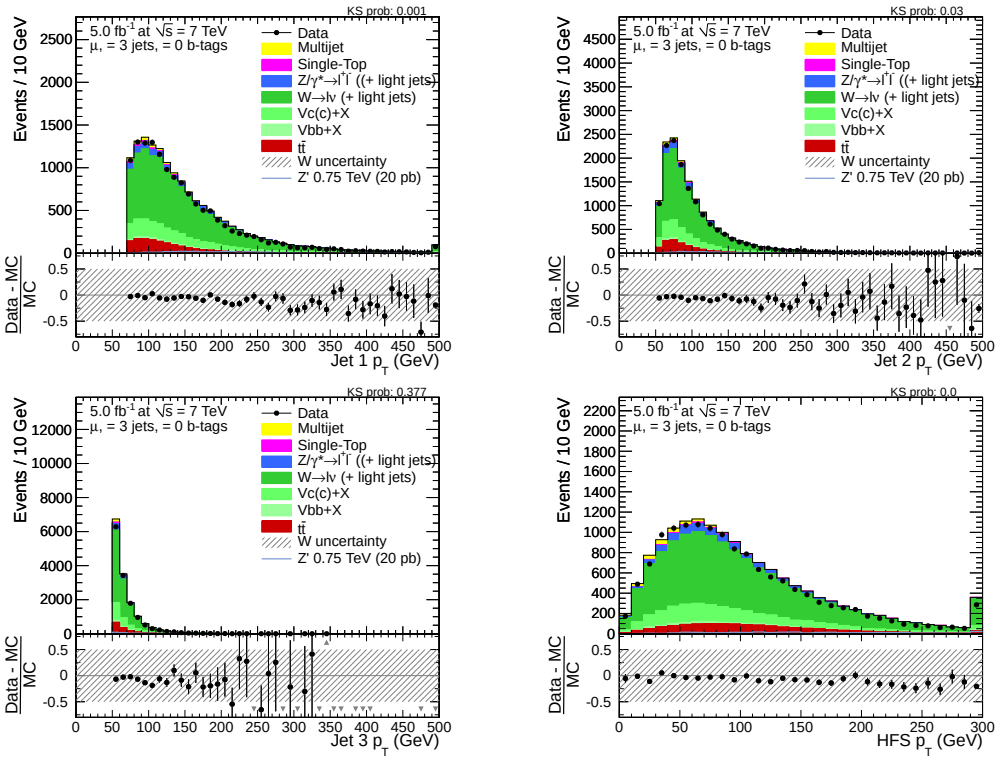

Figure 7.6: Distribution of jet p_{T} for the leading (top left), second leading (top right) and third leading (bottom) jet in muon-plus-jets events with three jets and no b-tag.

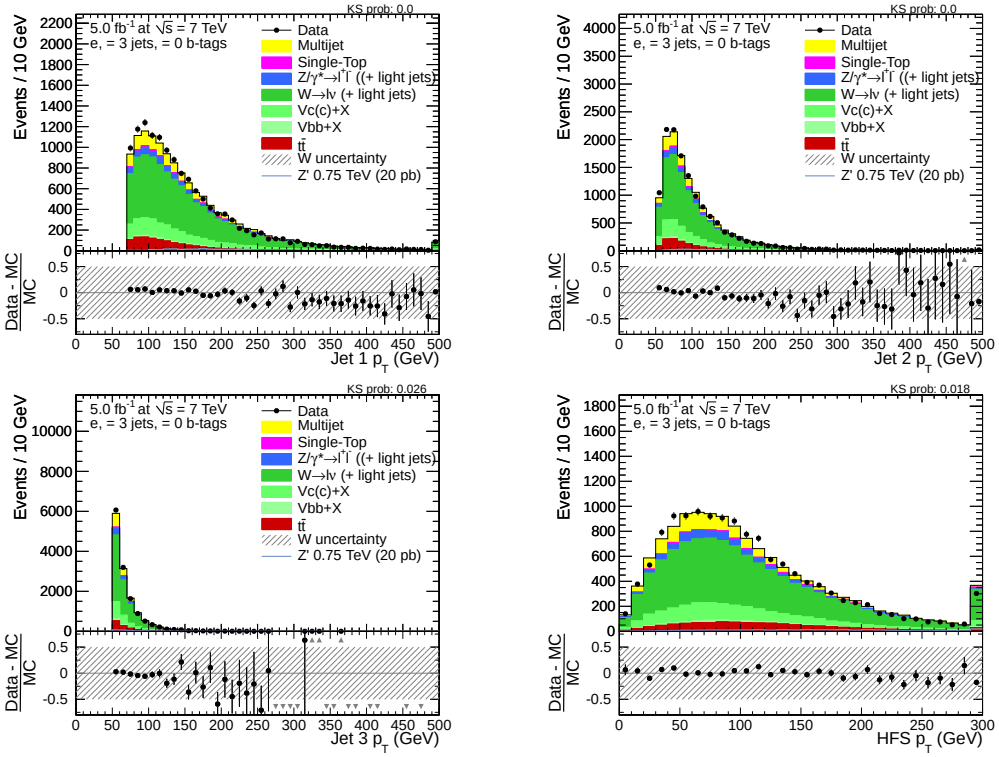

Figure 7.7: Distribution of jet p_{T} for the leading (top left), second leading (top right) and third leading (bottom) jet in electron-plus-jets events with three jets and no b-tag.

First, the modelling of jet properties is checked. Figures 7.6 and 7.7 show the distributions of the transverse momenta of the three leading jets and of the hadronic final state for muon- and electron-plus-jets events, respectively. The jet p_{T} and HFS p_{T} spectra in data are generally softer than in simulated events, but compatible within variations of the jet energy scale uncertainty. In addition to the jet energy scale uncertainty, the jet p_{T} spectra are also subject to modelling uncertainties due to variations of the renormalisation and factorisation scales as well as the matching threshold. Apart from the general small disagreement of the slope, the simulation well reproduces the general features of the jet p_{T} distributions. The leading jet p_{T} spectrum peaks at around 100 GeV, the second leading jet p_{T} spectrum at about 70 GeV, and the third leading jet p_{T} spectrum is constantly falling from the selection threshold of 50 GeV. The HFS p_{T} distribution reaches its maximum at ~ 70 GeV.

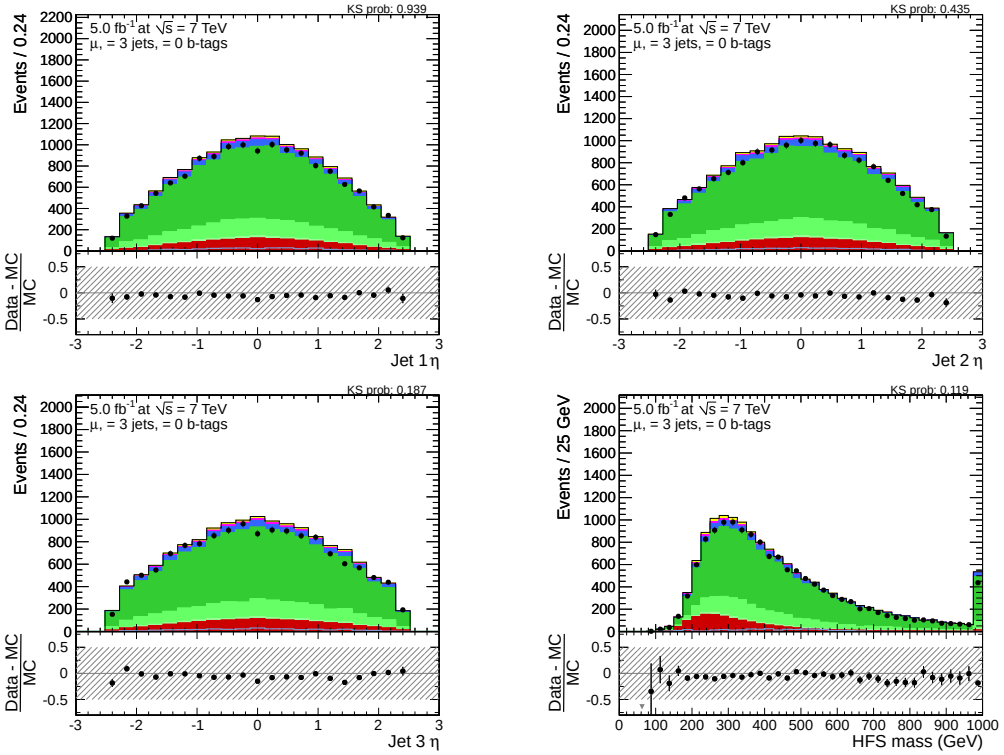

Figure 7.8: Distribution of jet η for the leading (top left), second leading (top right) and third leading (bottom) jet in muon-plus-jets events with three jets and no b-tag.

The distributions of the pseudorapidity of the leading three jets and the mass of the hadronic final state are displayed in figures 7.8 (muon channel) and 7.9 (electron channel). The jet η distributions peak at $\eta = 0$ for all background samples and become wider for the subleading jets. Since the jet η distributions are broader for W/Z-plus-jets production than for $\mathrm{t\bar{t}}$ production, the agreement of data and simulation gives a measure for the correct modelling of the composition of the data. All data distributions are well reproduced by the simulation. Similar to the jet momenta and HFS p_{T}, the distribution of the HFS mass is a handle on the simulation of the radiation of additional jets, in particular the angles between the jets. The comparison of data and simulation shows reasonable agreement, with the simulated events preferring slightly smaller masses in both the muon and the electron channel.

Figure 7.10 shows four distributions related to the simulation of the properties of the muon,

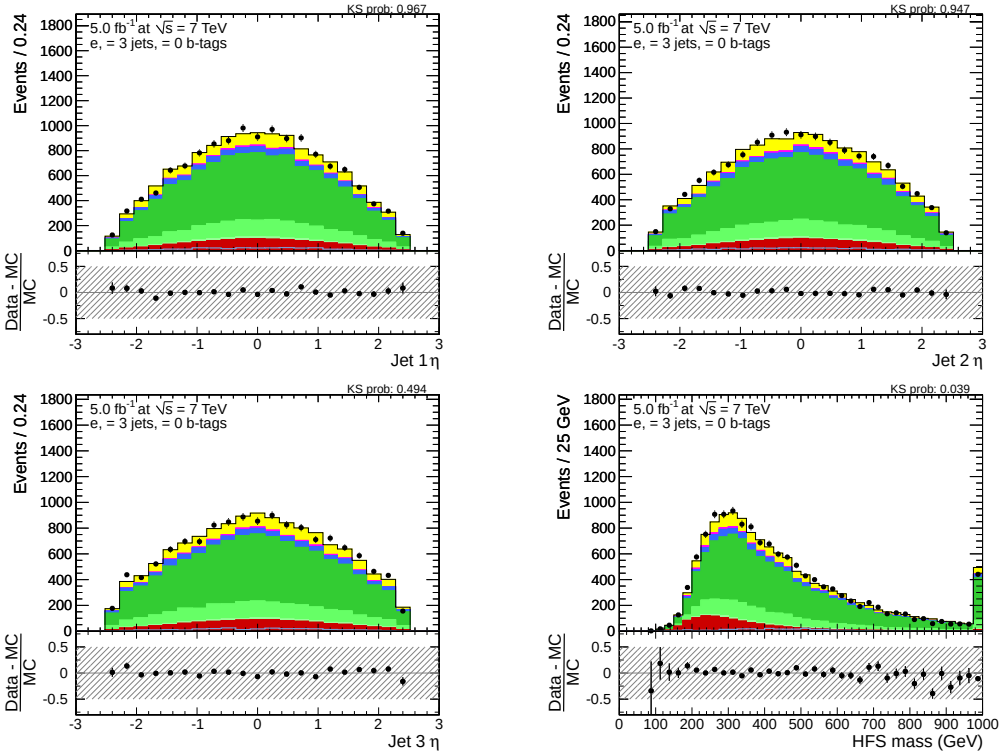

Figure 7.9: Distribution of jet η for the leading (top left), second leading (top right) and third leading (bottom) jet in electron-plus-jets events with three jets and no b-tag.

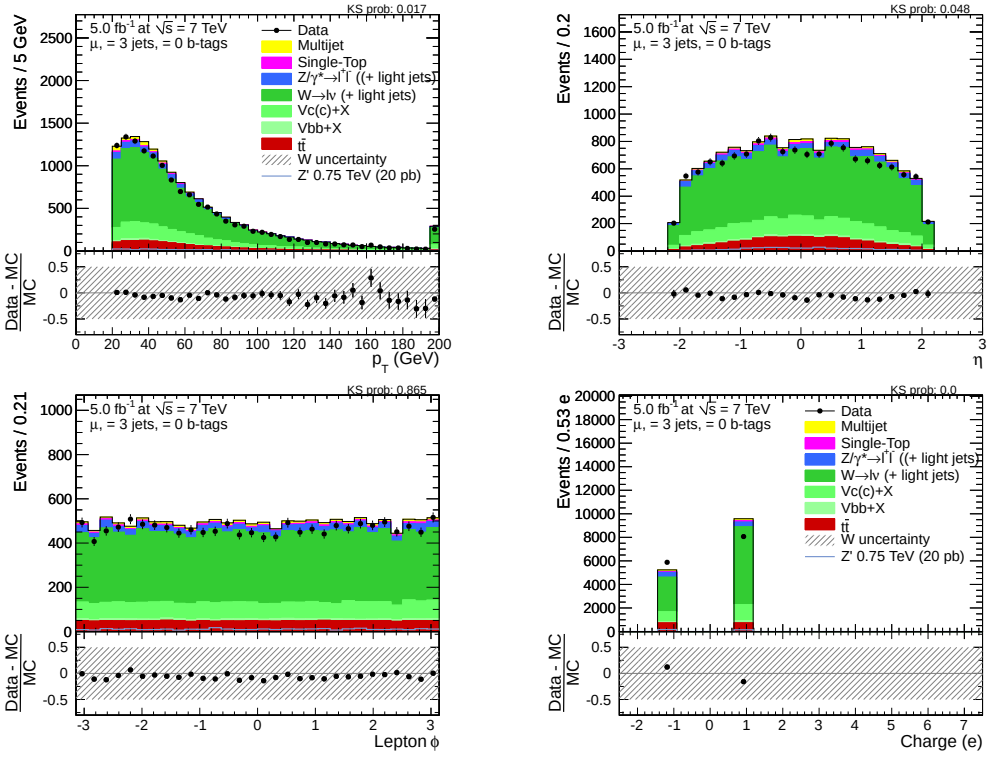

Figure 7.10: Distribution of muon p_{T} (top left), pseudorapidity η (top right), azimuth angle ϕ (bottom left) and charge (bottom right) in muon-plus-jets events with three jets and no b-tag.

the transverse momentum p_{T}, pseudorapidity η, azimuth angle ϕ, and charge. The simulation describes the muon p_{T} distribution reasonably well, with the data favouring slightly smaller values of muon p_{T}. The muon η distribution peaks in the central detector region for $\mathrm{t\bar{t}}$ events and falls off towards higher $|\eta|$ values, whereas it is almost flat for W-plus-jets events. The η distribution therefore provides a good indication of the modelling of the background composition. There is generally reasonable agreement between data and simulation, although there is a small deficit of data events in the pseudorapidity regions $\eta \sim 0$ and $|\eta| \sim 1$. As will be shown below, the data-simulation agreement of the muon η distributions improves in the $\mathrm{t\bar{t}}$-dominated phase space, indicating that the muon η distribution is not perfectly modelled by the W-plus-jets simulation, and possibly also by the multijet prediction.

The distribution of the azimuth angle ϕ is well described by the simulation, which shows that there are no unexpected detector inefficiencies as the ϕ distribution is expected to be flat for all background processes. The muon charge distribution shows a significant disagreement between data and simulation. The simulation predicts a higher number of positively charged muons compared to negatively charged ones than present in the data. However, the lepton charge asymmetry in inclusive W-plus-jets events was shown to be well reproduced by the simulation in a dedicated measurement [137]. The discrepancies may therefore arise from the modelling of the charge asymmetry in the presence of extra jets with MADGRAPH. As the lepton charge has no influence on the event reconstruction or selection, the difference between data and simulation has no effect on the $m_{\mathrm{t\bar{t}}}$ distribution or on other kinematic distributions.

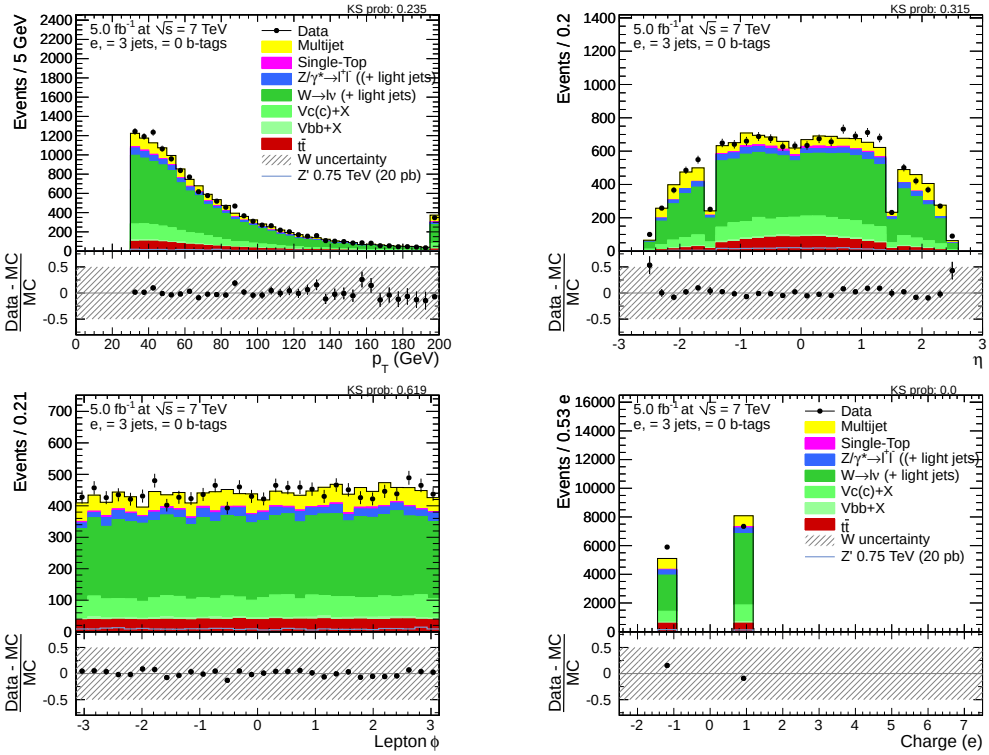

Figure 7.11: Distribution of electron p_{T} (top left), pseudorapidity η (top right), azimuth angle ϕ (bottom left) and charge (bottom right) in electron-plus-jets events with three jets and no b-tag.

A number of kinematic distributions of the reconstructed electron are shown in figure 7.11.

The p_{T} of the electron is well described by the simulation except for a small tendency of the simulation to predict a harder spectrum, similar to the muon p_{T} distribution. The electron η distribution agrees well between data and simulation. The data are above the simulation at the edge of the endcap region ($2.4 < |\eta| < 2.5$), which can be explained by the multijet model that only explicitly takes events from the conversion-enriched control region into account. The electron charge distribution shows the same disagreement as in the muon channel, an overestimation of positively charged electrons with respect to negatively charged electrons.

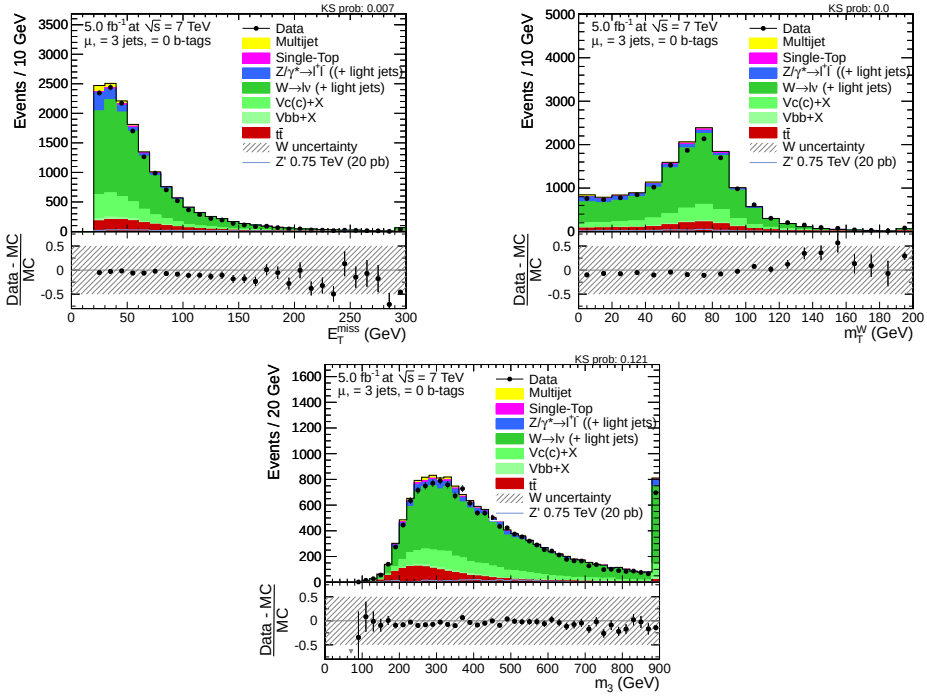

Figure 7.12: Distribution of missing transverse energy (top left), transverse W boson mass (top right) and invariant mass of the three reconstructed jets with highest p_{T} after adding the four-momenta vectorially (bottom) in muon-plus-jets events with three jets and no b-tag.

Two properties related to the modelling of the missing transverse energy, the $E_{\mathrm{T}}^{\mathrm{miss}}$ distribution and the transverse W boson mass, are shown in figures 7.12 and 7.13 for the muon and electron channels, respectively. In both channels, the simulation describes the $E_{\mathrm{T}}^{\mathrm{miss}}$ spectrum reasonably well in the region of low $E_{\mathrm{T}}^{\mathrm{miss}}$, but slightly overestimates the fraction of events with higher $E_{\mathrm{T}}^{\mathrm{miss}}$ values. The data-simulation agreement of the transverse W boson mass distribution is good up to $m_T^W \sim 100$ GeV, i.e. in the region of the Jacobian peak due to the production of a W boson. Events with no real W boson, most importantly events from multijet production, tend to have small values of the transverse W boson mass, especially in the muon channel. The good agreement in the region of low M_T^W is therefore an independent confirmation that the number of multijet events is estimated correctly. Beyond 100 GeV, the simulation underestimates the number of events. The difference between data and simulation may be explained by an imperfect modelling of the $E_{\mathrm{T}}^{\mathrm{miss}}$ resolution as events with a W boson can only have transverse mass values larger than the W boson mass if the $E_{\mathrm{T}}^{\mathrm{miss}}$ vector is not measured accurately, with the assumption that the lepton momentum is well measured. The small disagreement is however

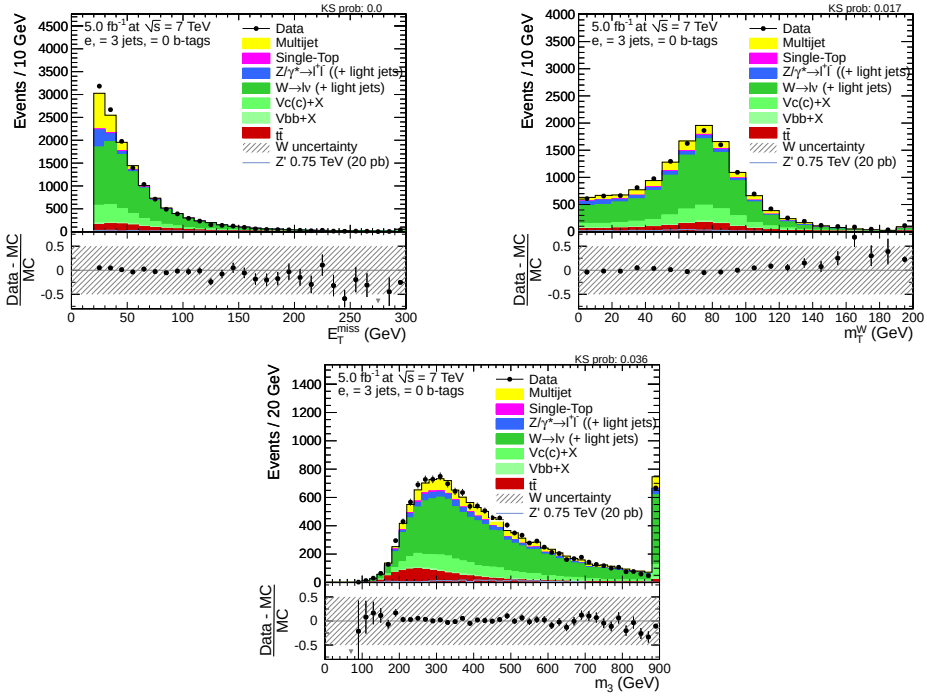

Figure 7.13: Distribution of missing transverse energy (top left), transverse W boson mass (top right) and invariant mass of the three reconstructed jets with highest p_{T} after adding the four-momenta vectorially (bottom) in electron-plus-jets events with three jets and no b-tag.

not expected to affect the results of the analysis since the number of events in the tail of the distribution is small and since there is no correlation between $m_{\mathrm{t\bar{t}}}$ and the transverse W boson mass.

In addition, the invariant mass of the three-jet system (m_3) is also shown in figures 7.12 and 7.13. The m_3 distribution has distinct shapes for events from $\mathrm{t\bar{t}}$ production, where it peaks at ~ 250 GeV in three-jet events, and events from W-plus-jets production, for which the peak is around $300 - 350$ GeV. Though the simulation prefers slightly higher values of m_3, the agreement of the m_3 distributions data and simulation is good, indicating that the composition of the event sample is well simulated.

In summary, the comparison of data and simulated events in events with three jets of which none is b-tagged shows overall good agreement and validates the modelling of the kinematic distributions of W-plus-jets events.

7.3.3 Validation of event yields in data control regions using the lepton charge asymmetry

Another possibility to study W-plus-jets events is to make use of the charge asymmetry in pp collisions. In the selected event sample, only W-plus-jets events and the relatively small number of t-channel single top events contain a higher fraction of positively than negatively

charged leptons, whereas all other background processes including multijet events are charge-symmetric. By subtracting events with negatively charged leptons from events with positively charged leptons, i.e. by assigning events with negative lepton charge a weight of $w = -1$, a pure sample of W-plus-jets events can be created. This sample can then be used to validate the simulation of W-plus-jets events. An important drawback of this method is that the statistical uncertainties are considerable since the asymmetry is only of the order of $A = \frac{N^+ - N^-}{N^+ + N^-} \sim 0.15$, depending on the lepton rapidity.

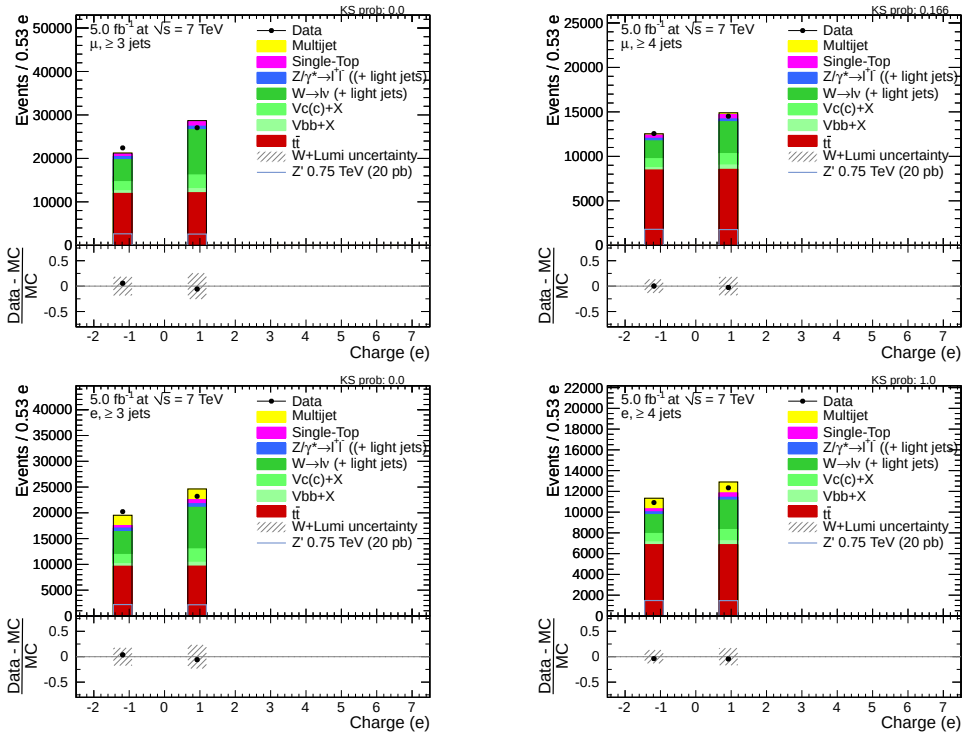

Figure 7.14: Distribution of the lepton charge in muon-plus-jets events with at least 3 jets (top left) and at least 4 jets (top right) and in electron-plus-jets events with at least three jets (bottom left) and at least four jets (bottom right).

A comparison of the measured lepton charges in data and simulation is given in figure 7.14. It generally turns out that the observed charge asymmetry is smaller in data than estimated in simulation, especially for events with three selected jets. As the lepton charge asymmetry in inclusive W-plus-jets events was found to agree well with simulation in a dedicated measurement [137], this indicates that the simulation does not very well reproduce the charge asymmetry in events with several jets. Despite these differences, the multiplicity of b-tagged jets gives a unique handle on the contribution of W-plus-jets events with heavy-flavoured jets in the phase space of 3 and more selected jets that is under consideration.

In figure 7.15, the b-tagged jet multiplicity is shown separately for muon- and electron-plus-jets events with either exactly three jets or with at least four jets. As expected from the distributions of the lepton charges, the yields of charge-subtracted events in data are in general smaller than predicted from simulation. Apart from the global underestimation of the yield, the distributions show a reasonable agreement within statistical uncertainties. In events with at least one b-tagged jet, the event yields after the charge subtraction are expected to be dominated

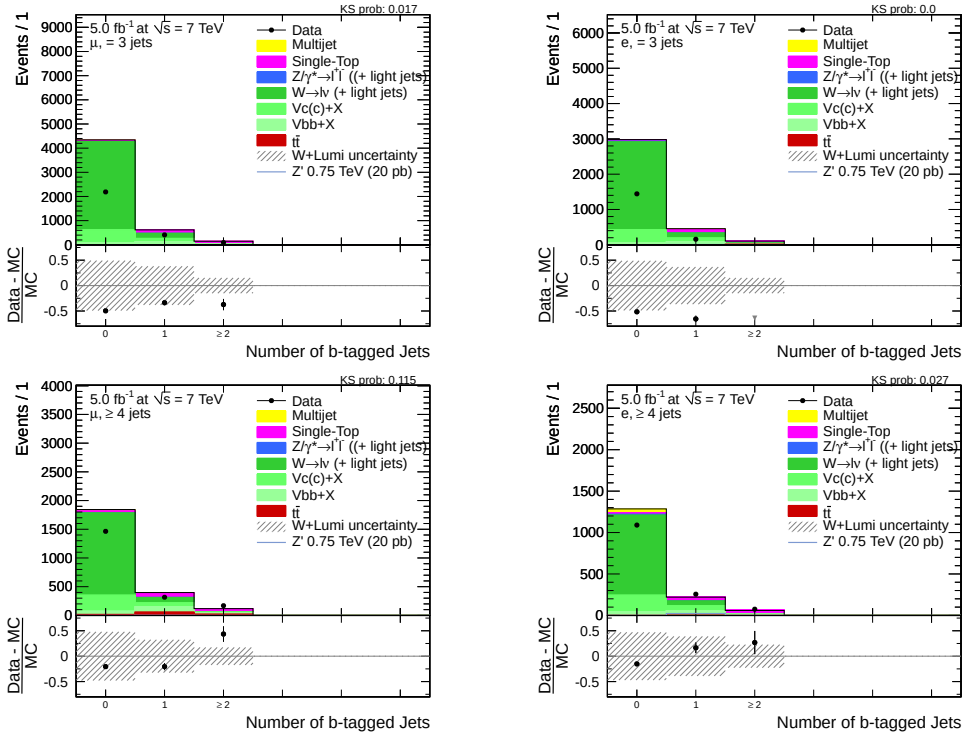

Figure 7.15: Distribution of the number of b-tagged jets in muon-plus-jets (top left) and electron-plus-jets (top right) events with three selected jets and in muon-plus-jets (bottom left) and electron-plus-jets (bottom right) events with at least four selected jets. A negative event weight is assigned to events with negatively charged leptons, i.e. the distribution from events with negatively charged leptons is subtracted from the distribution with positively charged leptons.

by events from W boson production in association with heavy-flavoured jets. Since the relative ratios of data and simulation are similar for all b-tagged jet multiplicities, there is no trend that would indicate a global underestimation or overestimation of the rate of such events in both events with 3 jets and at least four jets within statistical uncertainties.

To summarise, the lepton charge asymmetry is exploited to test the modelling of W-plus-jets events enriched in heavy-flavoured jets. Due to the global overestimation of the charge asymmetry in the simulation, the results are only used as a cross check and not to estimate event rates or the shape of kinematic distributions. The results nevertheless show that the yields of W-plus-jets events with heavy-flavoured jets are compatible with the prediction from the MADGRAPH simulation.

7.4 Top quark pair production and other background processes

The production of two top quarks in association with jets is the major, irreducible background. Therefore, no sidebands exist for the measurement of the $m_{\mathrm{t\bar{t}}}$ distribution, and the events are

Table 7.5: Expected and observed event yields for the 8 categories used in the statistical evaluation.

Yields	$\mathrm{t\bar{t}}$	W/Z+LF	W/Z+HF	Single top	Multijet	Data	Sum BG
μ 3j1t	5612	559	1168	550	164	8465	8052
μ 4j0t	2988	5726	1979	202	195	10714	11089
μ 4j1t	7802	390	906	423	104	9664	9626
μ 4j2t	6093	10	162	228	152	6697	6646
e 3j1t	4307	432	941	428	491	6932	6597
e 4j0t	2395	4729	1626	158	1398	10008	10307
e 4j1t	6183	309	742	345	504	7946	8083
e 4j2t	4770	7	134	184	210	5309	5306

necessarily taken from simulation. Top quark pair events are simulated with the MADGRAPH event generator, and the expected $m_{\mathrm{t\bar{t}}}$ shapes and the distributions of other observables are taken from this simulated event sample. To check that the simulation of $\mathrm{t\bar{t}}$ events is reliable, the modelling of various observables is checked in regions dominated by $\mathrm{t\bar{t}}$ production below, e.g. events with at least four jets of which at least one is b-tagged.

The production of single top quarks, most importantly in the tW channel and the t channel, contributes only a small expected fraction of background events and is hence also modelled with simulated events generated with POWHEG. The MADGRAPH simulation, which yields compatible event distributions, was shown to well reproduce the kinematic properties of t channel single top quark events when compared to the data and to other event generators [138]. The contribution from diboson events ($ZZ/WW/WZ$-plus-jets) is neglected due to their tiny contribution after the event selection in accordance with other $\mathrm{t\bar{t}}$ analyses in the lepton-plus-jets final state carried out within the CMS collaboration [139].

7.5 Comparison of data with simulated events

In this section, the data are compared with simulated events. First, the numbers of observed events in the different event categories will be compared with the numbers of expected events from the different simulated samples. Then, the distributions of basic kinematic quantities like jet transverse momenta or charged lepton pseudorapidities will be investigated in the signal region. Finally, data-simulation comparisons of properties relevant for the reconstruction of the $\mathrm{t\bar{t}}$ system will be carried out.

7.5.1 Event yields

The expected and observed event yields in the 8 event categories used for the statistical interpretation are listed in table 7.5. The last two columns show the event yields in the data and the sum of the expected yields from all background processes. In addition, the expected event yields are

Table 7.6: Expected fractions of selected events at in the 8 categories used in the statistical evaluation for six benchmark Z′ simulation samples .

Yields [%]	**Z′ 0.5 TeV**	**0.75 TeV**	**1.0 TeV**	**1.25 TeV**	**1.5 TeV**	**2.0 TeV**
μ 3j1t	1.0	1.4	1.5	1.4	1.2	0.8
μ 4j0t	0.3	0.6	0.8	0.8	0.7	0.7
μ 4j1t	0.9	1.7	2.0	2.0	1.6	1.3
μ 4j2t	0.7	1.5	1.6	1.4	1.1	0.8
e 3j1t	0.7	1.2	1.3	1.3	1.1	0.7
e 4j0t	0.2	0.5	0.7	0.7	0.7	0.6
e 4j1t	0.6	1.4	1.8	1.7	1.6	1.3
e 4j2t	0.5	1.2	1.4	1.3	1.1	0.8

separately shown for events from $\mathrm{t\bar{t}}$ production, from single top production, from multijet production, and from the production of a W or Z boson in association with either light-flavoured jets (LF) or at least one heavy-flavoured jet (HF), i.e. a c jet or b jet.

In events with at least four jets and either 1 b-tag or at least 2 b-tags, the agreement of the event yields from data and simulation is very good as they agree within statistical uncertainties for both the electron- and muon-plus-jets selection. Both categories are dominated by $\mathrm{t\bar{t}}$ production. About 90% of the events with at least 2 b-tags and about 80% of the events with at least 1 b-tag are expected to be from $\mathrm{t\bar{t}}$ production. Events due to single top, W/Z+HF and multijet production contribute similar but small fractions in events with at least 2 b-tags. In events with 1 b-tag, the production of a W/Z boson in association with light-flavoured jets becomes important as well, and the highest expected background contribution apart from $\mathrm{t\bar{t}}$ production is due to W/Z+HF production with a fraction of $\sim 10\%$ of the expected events.

The highest background fraction ($\sim 50\%$) in events with 4 jets and no b-tags is from W/Z boson production in association with light-flavoured jets followed by $\mathrm{t\bar{t}}$ production ($\sim 25\%$) and W/Z+HF production ($\sim$ 15–20%). Multijet production also significantly contributes in the electron channel ($\sim 14\%$), whereas multijet production in the muon channel and single top production only make up a fraction of the total expected events at the per cent level. The total number of data events in both lepton channels is about 3% lower in data than in the simulation, indicating a good agreement given the considerable systematic uncertainties of the event rates.

In events with 3 jets of which at least one is b-tagged, the dominant background contribution is from $\mathrm{t\bar{t}}$ production ($\sim 70\%$ of the events), followed by the production of a W/Z boson in association with heavy-flavoured jets ($\sim 15\%$). The rest of the background composition is made up by similar fractions of W/Z boson production in association with light-flavoured jets, single top production, and multijet events, each contributing $\sim 5-7\%$ of the events except for multijet events in the muon channel with a fraction of only about 2%. There are about 5% more observed than expected events in both the muon and the electron channel. This difference in event yields is covered by the systematic uncertainties that are assigned to the background rates, e.g. W boson production in association with heavy flavours, and generally W boson production with three selected jets.

The expected fractions of Z′ events in the categories used for the statistical evaluation are given in table 7.6 for a number of different Z′ masses. The total event selection efficiency is highest for $m'_{\mathrm{Z}} \sim 1$ TeV with $\varepsilon \sim 11\%$. As discussed above, for events with smaller masses, the requirements on the jet and lepton momenta reduce the selection efficiency; for events with higher masses, the lepton isolation requirements and the selection of at least 3 jets in the case of jet merging lead to a reduced selection efficiency. Except for $m_{\mathrm{Z}'} \sim 500$ GeV, the highest fraction of Z′ events appears in the event category with 4 jets and 1 b-tag. This category is also relatively pure in $\mathrm{t\bar{t}}$ events, which is the irreducible background. The next most populated categories are events with 4 jets and 2 b-tags, which is also the event category with the highest fraction of $\mathrm{t\bar{t}}$ events, and events with 3 jets and at least 1 b-tag. Events with 4 jets of which none is b-tagged contain only a small fraction of Z′ events at low mass (0.5% in total), but become more important at high Z′ mass with efficiencies of up to 1.5%. The reason for the increased fraction of events with no b-tags at high $m_{\mathrm{Z}'}$ is that the b-tag efficiency is reduced for high jet p_{T}.

7.5.2 Basic kinematic quantities

In this section, the distribution of several kinematic quantities will be compared between data and simulated events. The comparison aims at validating the modelling of the individual reconstructed objects like charged leptons and jets as well as the description of the according kinematic distributions by the event generators.

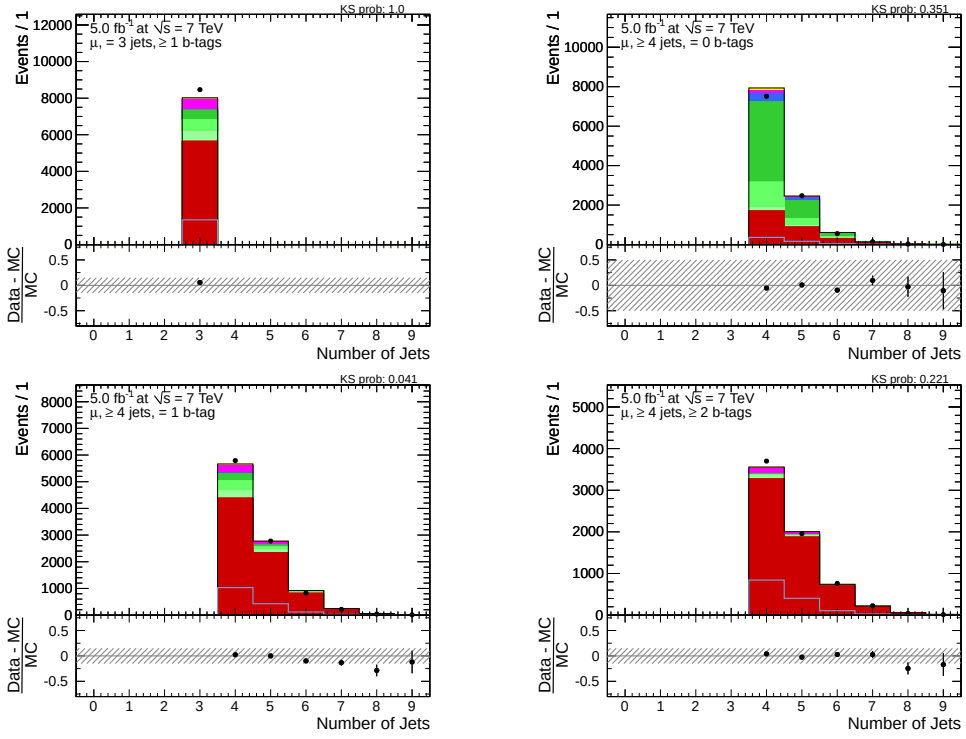

Figure 7.16: Distribution of the number of selected jets for events with 3 jets and at least 1 b-tag (top left) and at least 4 jets and either 0 b-tags (top right), one b-tag (bottom left) or at least two b-tags (bottom right) in muon-plus-jets events.

Figure 7.16 shows the distribution of the number of selected jets for all four event categories of the muon-plus-jets selection. For events with at least four jets, the jet multiplicity is rapidly falling for simulated events with no b-tags, which are dominated by W-plus-jets events. Data and simulation agree well, verifying the description of the jet multiplicity by the simulated W-plus-jets sample. For events with at least one b-tagged jet, which are dominated by $\mathrm{t\bar{t}}$ production, the agreement between data and simulation is reasonable, though there is a reduced fraction of observed events with higher jet multiplicity. This difference is most notable in events with at least 7 jets, where the simulation overestimates the number of events by 15–20%.

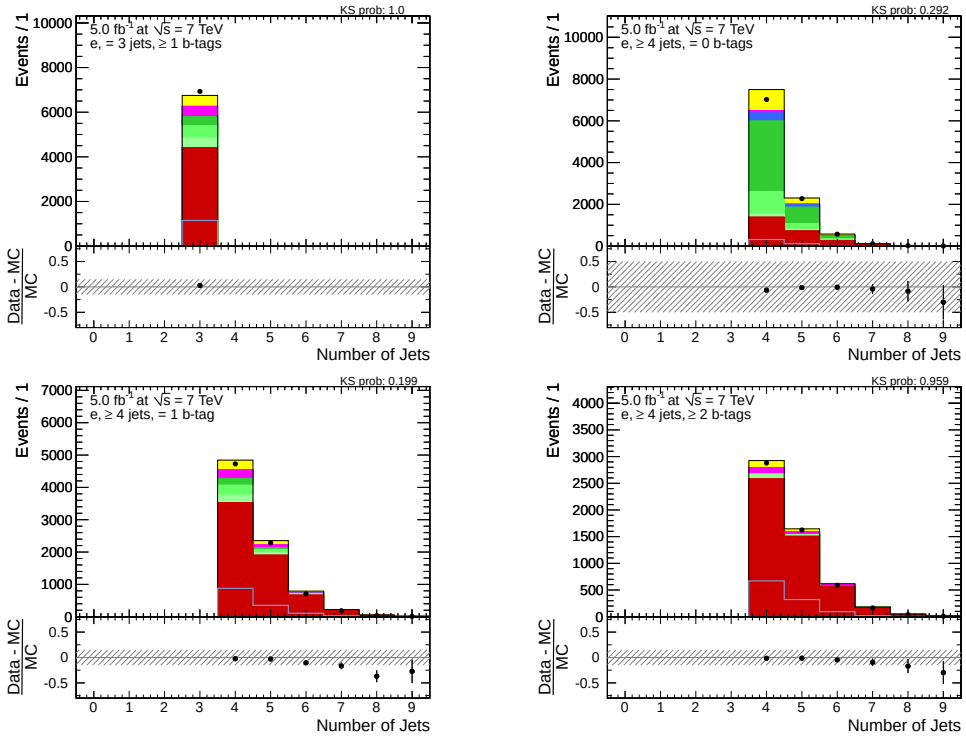

Figure 7.17: Distribution of the number of selected jets for events with 3 jets and at least 1 b-tag (top left) and at least 4 jets and either 0 b-tags (top right), one b-tag (bottom left) or at least two b-tags (bottom right) in muon-plus-jets events.

The jet multiplicity distributions in the electron channel are shown in figure 7.17. The most significant differences between the electron channel and the muon channel that could affect the description of the number of jets are the different multijet background and the higher lepton p_{T} criterion in the electron channel. The distributions of data and simulated events show the same trend as in the muon channel, i.e. the simulation slightly overestimates the number of data events at higher jet multiplicities, whereas the general level of agreement between data and simulation is good, e.g. in the W-plus-jets dominated region of 4 jets of which none is b-tagged.

The differences between data and simulation in the $\mathrm{t\bar{t}}$-dominated event categories can however be explained by systematic uncertainties. To study this in more detail, the impact of the most important systematic uncertainties on the number-of-jets distribution in $\mathrm{t\bar{t}}$ events with at least four jets is shown in figure 7.18 for the muon channel. The influence of uncertainties related to the generation of events is investigated with the help of the normalised ratio of $\mathrm{t\bar{t}}$

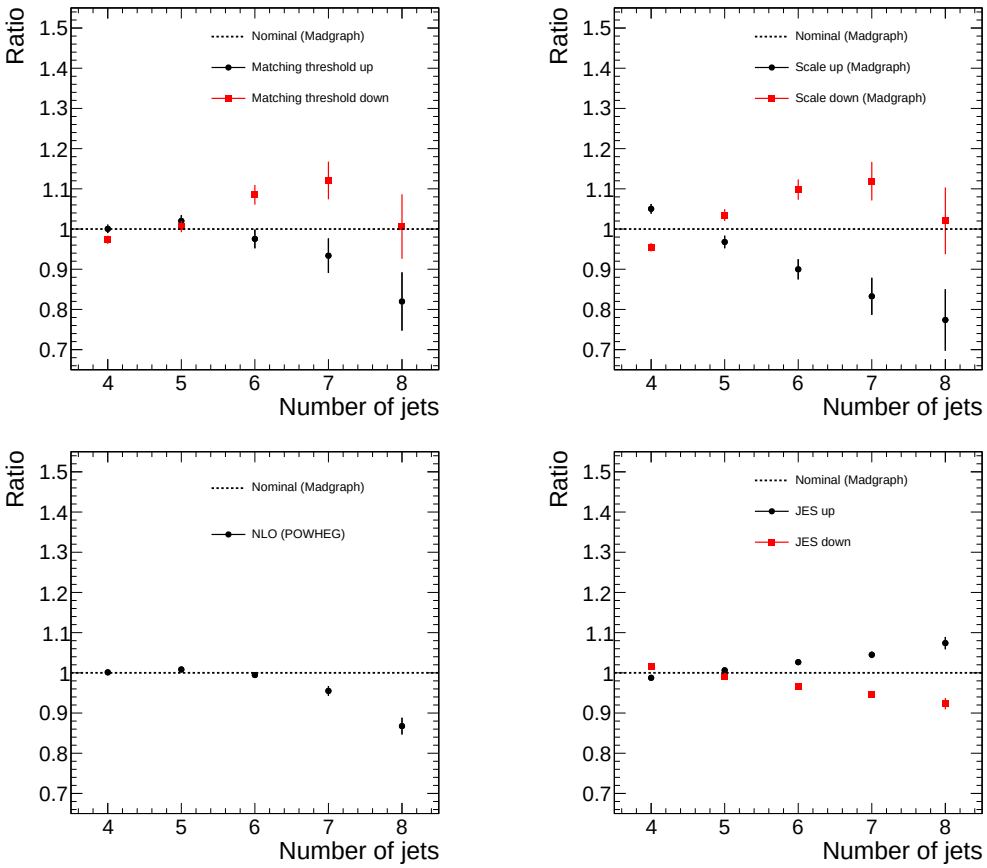

Figure 7.18: Comparison of the distributions of the number of selected jets from the nominal $t\bar{t}$ simulation (MADGRAPH) and from samples with variations of the matching threshold (top left), with variations of the renormalisation and factorisation scales (top right), from the NLO generator POWHEG (bottom left), and for events with variations of the jet energy scale within uncertainties (bottom right). The plots show the ratio with respect to the nominal sample for events with at least four jets in the muon channel.

samples with varied generator settings or the NLO generator POWHEG with respect to the nominal $\mathrm{t\bar{t}}$ sample from MADGRAPH simulation. Both for a lower matching threshold between the matrix element generator and the parton shower and for increased renormalisation and factorisation scales, the fraction of events with higher jet multiplicities is reduced by 10–20%. This reduction is of a similar size as the differences between data and simulation. The same trend is observed for the number-of-jets distribution from the POWHEG $\mathrm{t\bar{t}}$ sample, where the estimated fraction of events agrees well with the MADGRAPH sample for events with 4–6 jets and then falls by 5–15% for 7 and more jets.

From the experimental side, the uncertainty on the jet energy scale also significantly affects the jet multiplicity distribution. The 1σ variation towards a lower jet energy scale reduces the fraction of events with 7 or more jets by 5–10% and may hence also explain the observed differences. Other systematic uncertainties that may affect the shape of the jet multiplicity distribution, e.g. the uncertainty on the b-tag efficiency or a change of the background composition, lead too considerably smaller shape variations. In summary, each studied systematic uncertainty may be responsible for at least a significant fraction of the difference between data and simulation, and either the individual uncertainties or a combination of them can well accommodate the small observed differences in the jet multiplicity distributions.

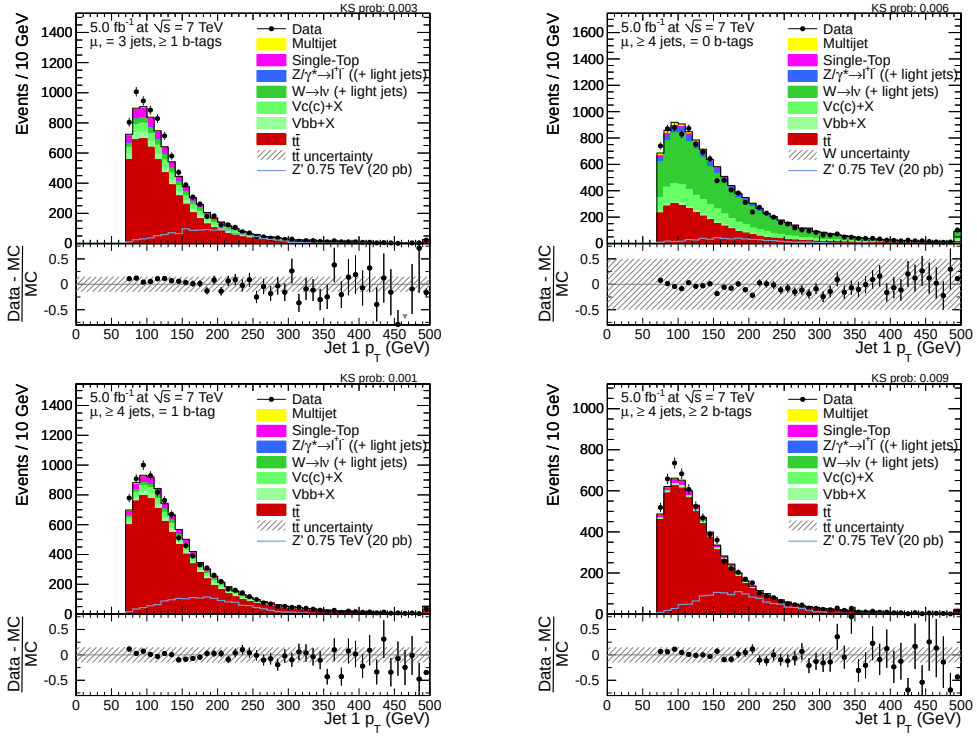

Figure 7.19: Distribution of the leading jet p_{T} for events with 3 jets and at least 1 b-tag (top left) and at least 4 jets and either 0 b-tags (top right), one b-tag (bottom left) or at least two b-tags (bottom right) in muon-plus-jets events.

The distribution of the transverse momentum of the leading jet in muon-plus-jets events is shown in figure 7.19. The leading jet p_{T} distribution peaks near 100 GeV for $\mathrm{t\bar{t}}$ production and W boson-plus-jets production; the distribution is harder for W-plus-jets events than for $\mathrm{t\bar{t}}$ events. There is reasonable agreement for events with 4 jets and no b-tags and for events with 3

jets and at least 1 b-tag. The p_{T} distribution is slightly softer in data than in simulation in both categories. For events with at least 4 jets and at least one b-tag, there are more data events at low jet p_{T} than simulated events. There is no indication that this general difference is due to an underestimation of a certain background sample, most importantly because events with at least 2 b-tags are expected to be very pure in $\mathrm{t\bar{t}}$ events.

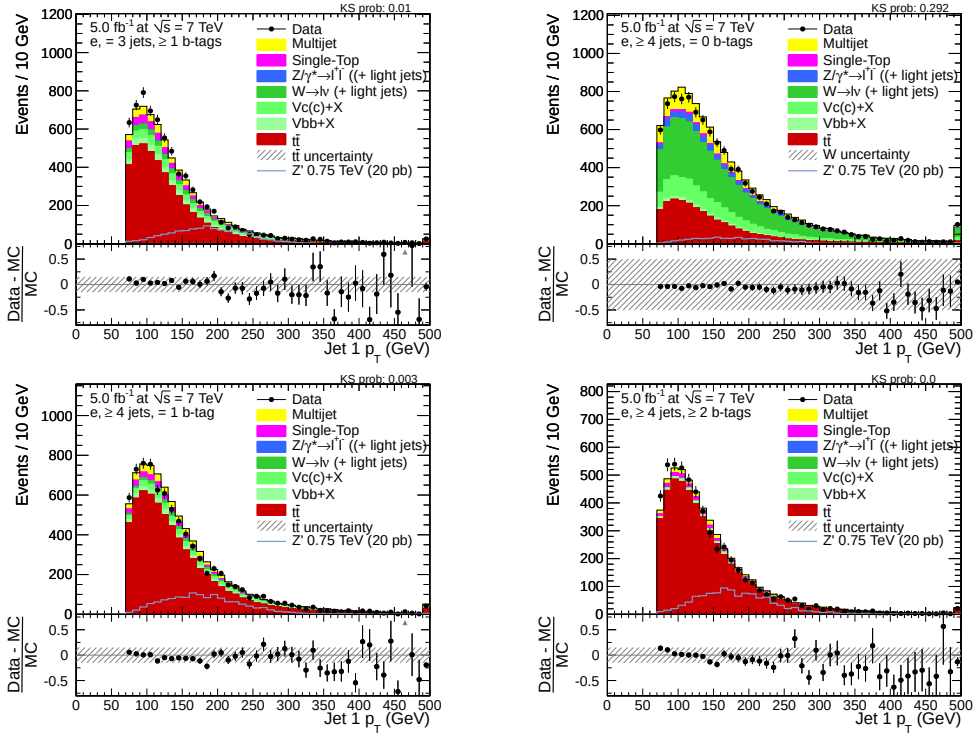

Figure 7.20: Distribution of the leading jet p_{T} for events with 3 jets and at least 1 b-tag (top left) and at least 4 jets and either 0 b-tags (top right), one b-tag (bottom left) or at least two b-tags (bottom right) in electron-plus-jets events.

Figure 7.20 shows the leading jet p_{T} distribution in the electron channel. The level of agreement between data and simulation is similar to the muon channel. Events with 4 jets of which none is b-tagged, which are dominated by W-plus-jets production, show good agreement, whereas the p_{T} spectrum is softer in data compared to the simulation in events with 3 or 4 jets and 1 b-tag or at least 2 b-tags, which are dominated by $\mathrm{t\bar{t}}$ production.

If one further investigates the differences in the muon and the electron channel by separately studying events with a different number of jets, one finds that the differences are more pronounced in events with at least 5 jets, which contain a yet higher fraction of $\mathrm{t\bar{t}}$ events. This indicates that the difference between data and simulation may be related to the lower observed fraction of data events with high jet multiplicity discussed before.

To verify that the small differences between data and simulation are covered by systematic uncertainties, the impact of the most important systematic uncertainties on the shape of the leading jet p_{T} is discussed in the following. Figure 7.21 shows the normalised ratio of events from samples corresponding to variations of systematic uncertainties and events from the nominal MADGRAPH $\mathrm{t\bar{t}}$ sample as a function of the leading jet p_{T}. Like for the jet multiplicity,

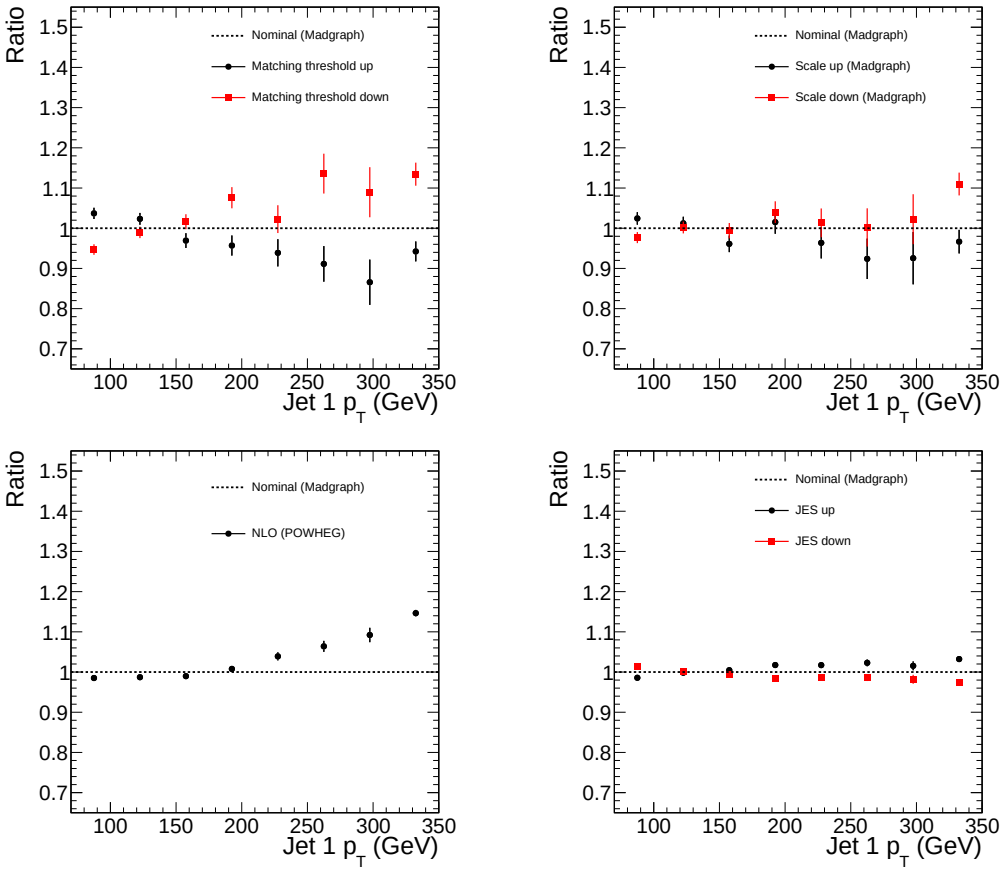

Figure 7.21: Comparison of the distributions of the leading jet p_{T} from the nominal $\mathrm{t\bar{t}}$ simulation (MADGRAPH) and from samples with variations of the matching threshold (top left), with variations of the renormalisation and factorisation scales (top right), from the NLO generator POWHEG (bottom left), and for events with variations of the jet energy scale within uncertainties (bottom right). The plots show the ratio with respect to the nominal sample for events with at least four jets.

the systematic variations significantly affect the leading jet p_{T} distribution. An increase of the matching threshold and of the renormalisation/factorisation scales leads to a softer spectrum, with the matching threshold providing the largest shape variations of $\sim \pm 5\%$ in the region of the jet p_{T} threshold and $\sim \mp 10\%$ for jet $p_{\mathrm{T}} \sim 300$ GeV. The leading jet p_{T} distribution from the NLO generator POWHEG also exhibits differences to the MADGRAPH simulation. The NLO and LO simulations agree well in the low p_{T} region, but POWHEG predicts a higher fraction of events with high jet p_{T}. This difference can be explained by POWHEG providing the hardest extra jet radiation beyond the $\mathrm{t\bar{t}}$ decay chain, but it is not supported by the observed data. Finally, the jet energy scale uncertainty also affects the leading jet p_{T} spectrum, with the downward 1σ variation of the jet energy scale uncertainty providing a shape difference that is in line with the difference between data and simulation, though of a smaller size than the uncertainties related to the MADGRAPH event generation. Like for the jet multiplicity, the differences between data and simulation in the leading jet p_{T} spectrum can be explained by systematic uncertainties related to the event generation, the jet energy scale, or a combination of them.

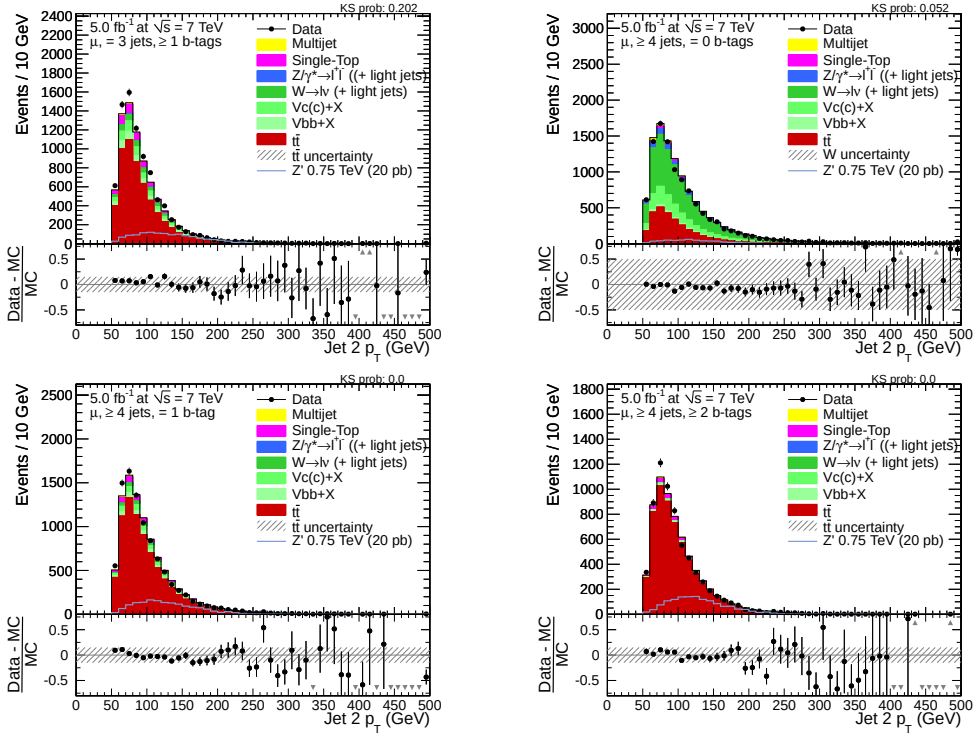

Figure 7.22: Distribution of the second leading jet p_{T} for events with 3 jets and at least 1 b-tag (top left) and at least 4 jets and either 0 b-tags (top right), one b-tag (bottom left) or at least two b-tags (bottom right) in muon-plus-jets events.

Figures 7.22 and 7.23 show the p_{T} distribution of the second leading jet in the muon channel and the electron channel, respectively. Similar to the leading jet p_{T}, the distributions agree reasonably well in events with 3 jets and at least 1 b-tag and 4 jets and no b-tag, with the data exhibiting a slightly softer p_{T} spectrum. In events with 4 jets and either one or at least two b-tags, the data are above the expectation at low jet p_{T}. This difference is of similar size and shape as in the leading jet p_{T} distributions. As above, the difference between data and simulation is covered by the uncertainties due to event generators and the jet energy scale, though it is again

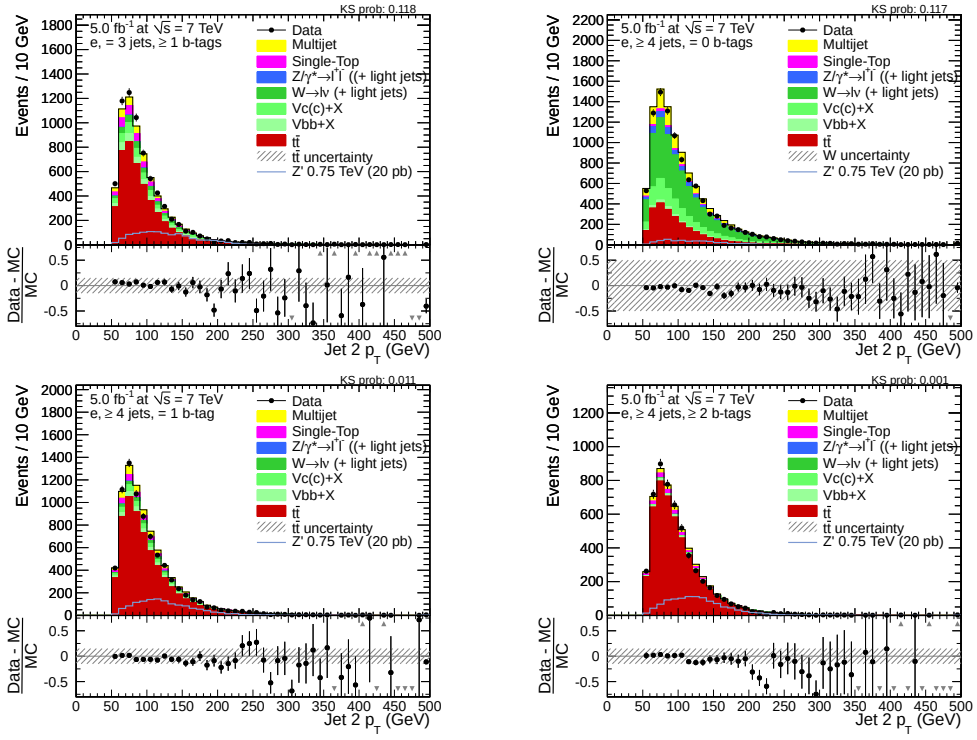

Figure 7.23: Distribution of the second leading jet p_{T} for events with 3 jets and at least 1 b-tag (top left) and at least 4 jets and either 0 b-tags (top right), one b-tag (bottom left) or at least two b-tags (bottom right) in electron-plus-jets events.

interesting to note that the difference is more pronounced in the $\mathrm{t\bar{t}}$-dominated phase space.

The spectrum of the third leading jet p_{T}, which is continuously falling for all background contributions, is shown in figure 7.24 for the muon channel and in figure 7.25 for the electron channel. The level of agreement between data and simulation is of similar quality as for the spectra of the two leading jets. The agreement is good for events with three jets and at least one b-tag and of acceptable quality in events with 4 jets and no b-tag. In the four-jet event categories with at least one b-tag, there is again a small enhancement of data events compared to the simulation in the region of low jet p_{T}, which is present in both lepton channels.

The distribution of the p_{T} of the fourth leading jet is displayed in figure 7.26 for muon-plus-jets events and in figure 7.27 for electron-plus-jets events with at least 4 jets. The agreement of data and simulation is good in events with no b-tag in both lepton channels, whereas there is again a small overshoot of data at low jet p_{T} for events with at least one b-tag. The distributions of the transverse momenta of the additional jets show similar characteristics as for the leading four jets, i.e. the data events have softer jet p_{T} spectra and the event yields are above the simulation in the region of low p_{T}.

The general description of the jet p_{T} distributions is at least reasonable in the phase space dominated by W boson production in association with jets, e.g. for events with three or four jets and no b-tag, but shows some differences in the $\mathrm{t\bar{t}}$-dominated phase space, especially in events with a higher number of jets. Though roughly compatible within uncertainties of the jet energy scale, this trend indicates that the modelling of the p_{T} spectra and the number of

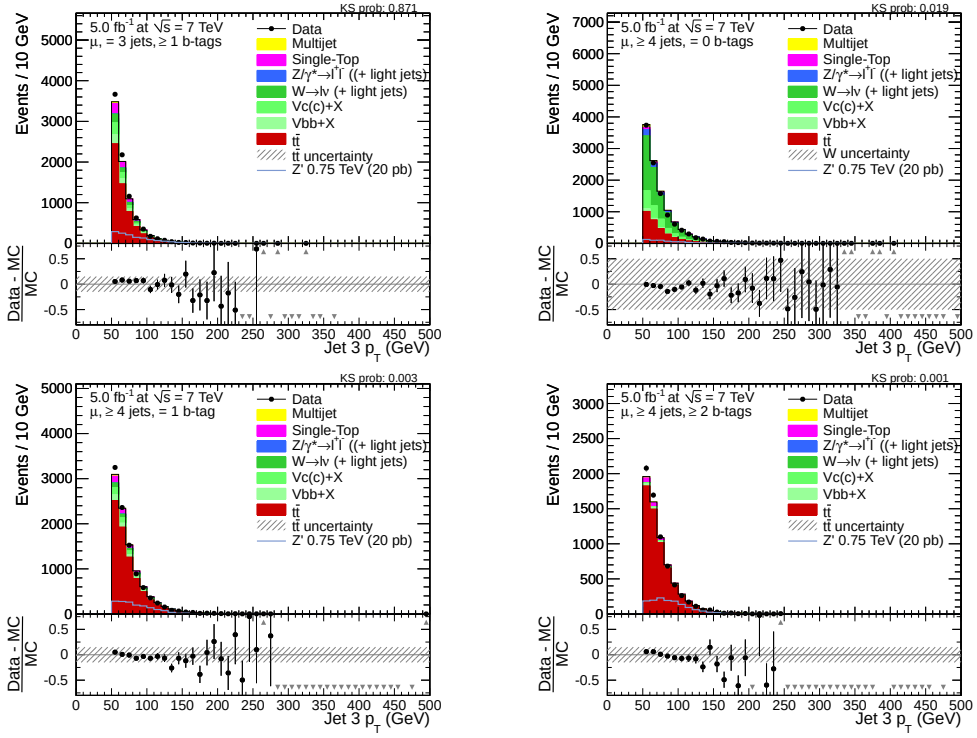

Figure 7.24: Distribution of the third leading jet p_{T} for events with 3 jets and at least 1 b-tag (top left) and at least 4 jets and either 0 b-tags (top right), one b-tag (bottom left) or at least two b-tags (bottom right) in muon-plus-jets events.

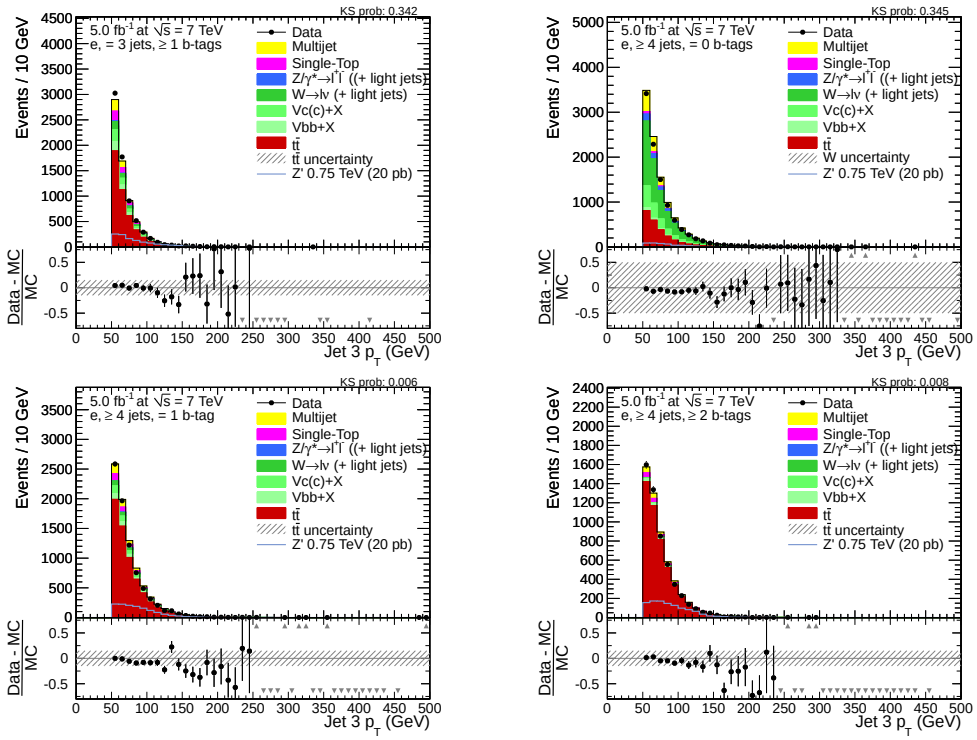

Figure 7.25: Distribution of the third leading jet p_{T} for events with 3 jets and at least 1 b-tag (top left) and at least 4 jets and either 0 b-tags (top right), one b-tag (bottom left) or at least two b-tags (bottom right) in electron-plus-jets events.

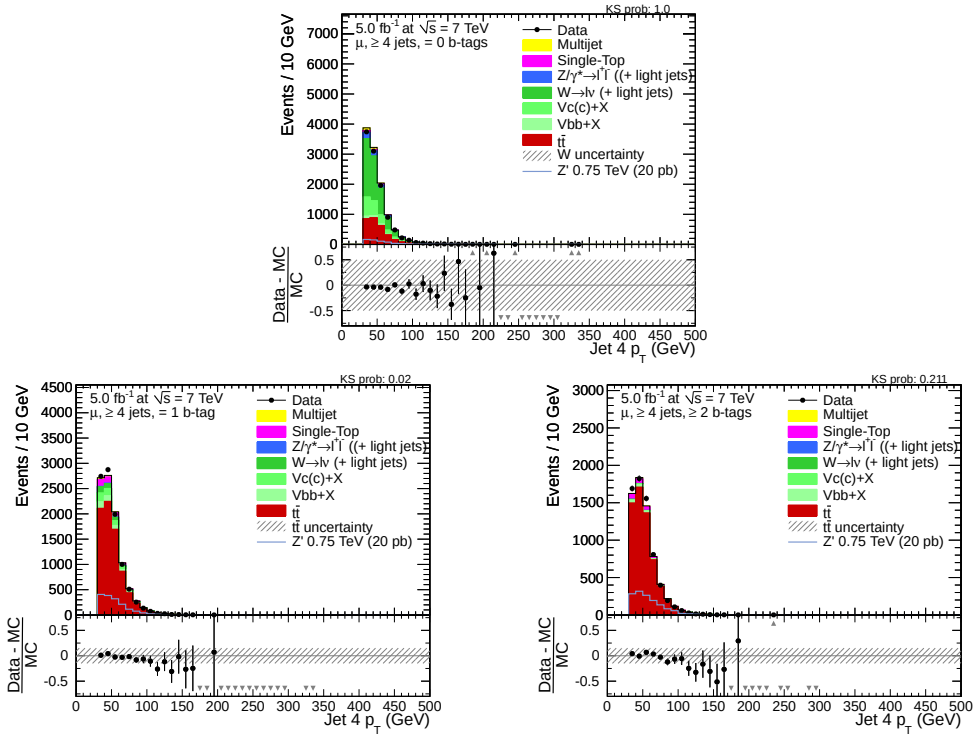

Figure 7.26: Distribution of the fourth leading jet p_{T} for events with at least 4 jets and either 0 b-tags (top), one b-tag (bottom left) or at least two b-tags (bottom right) in muon-plus-jets events.

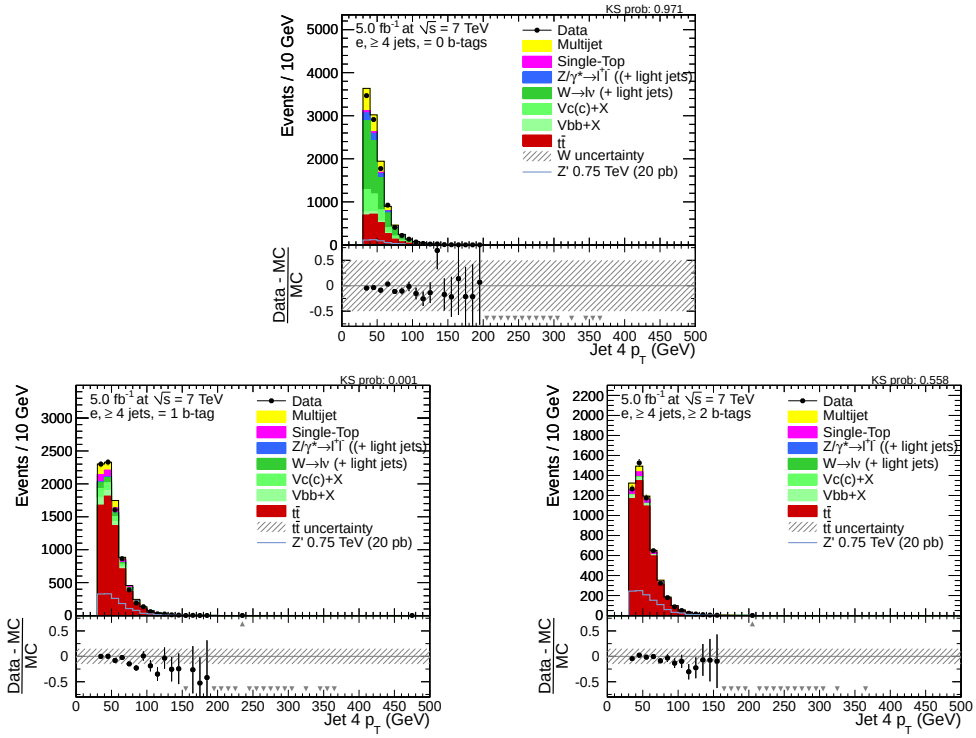

Figure 7.27: Distribution of the fourth leading jet p_{T} for events with at least 4 jets and either 0 b-tags (top), one b-tag (bottom left) or at least two b-tags (bottom right) in electron-plus-jets events.

additional jets in $\mathrm{t\bar{t}}$ events is not perfectly tuned to the data. This is taken into account in the statistical evaluation by including the discussed generator uncertainties.

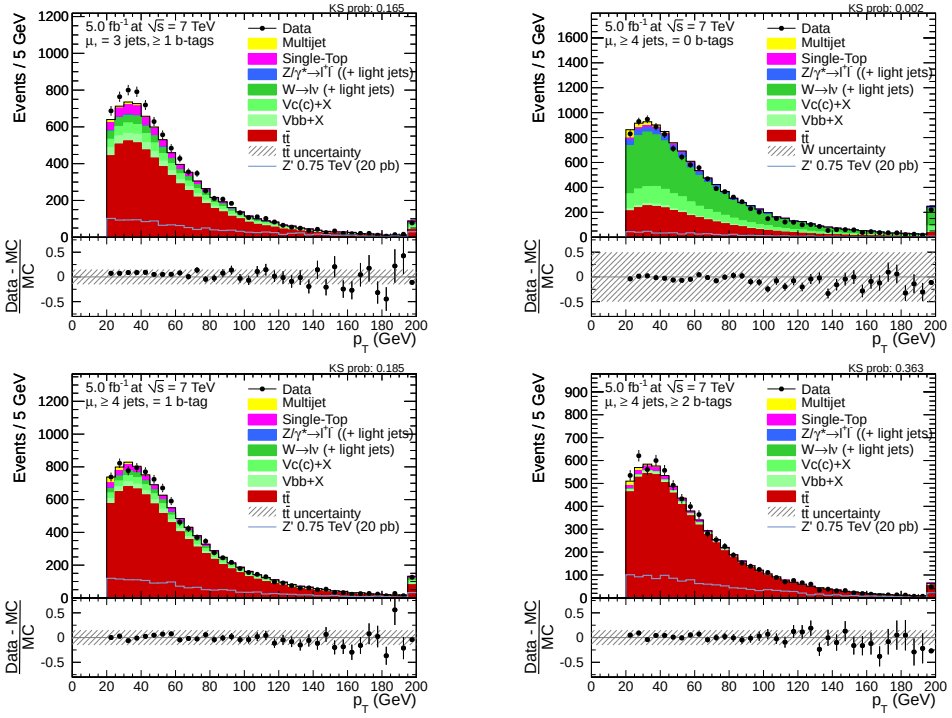

Figure 7.28: Distribution of the transverse momentum p_{T} of the muon for events with 3 jets and at least 1 b-tag (top left) and with at least 4 jets and either 0 b-tags (top right), one b-tag (bottom left) or at least two b-tags (bottom right) in muon-plus-jets events.

Figure 7.28 shows the distribution of the muon p_{T} for the four event categories in the muon channel. The distribution reaches its maximum at $\sim 30-35$ GeV for the combined background contribution in all categories. On average, the muon p_{T} is expected to be higher for W-plus-jets events than for $\mathrm{t\bar{t}}$ events. The simulated event samples generally describe the data well. There is a tendency of the simulated events to have a higher muon p_{T} than data events, though this difference is insignificant for the event categories dominated by $\mathrm{t\bar{t}}$ production.

The distribution of the muon η is shown in figure 7.29 for the muon channel. As discussed in the previous chapter (figure 5.1), muons from $\mathrm{t\bar{t}}$ and single top production are produced more centrally than muons from W-plus-jets production. Studying the muon η distribution can therefore both indicate whether the relative fractions of $\mathrm{t\bar{t}}$ and W-plus-jets events are correctly predicted, and whether the muon trigger and selection efficiencies are well described. In all four event categories, data and simulation agree well. In the categories dominated by $\mathrm{t\bar{t}}$ production, there is a slight excess of data around a muon $|\eta| \sim 2.0$, which however only contributes a small number of events in total. Moreover, the muon pseudorapidity distributions for events from Z' production are also expected to be very central. A more pronounced overshoot of data over simulation in the endcap region can be found in events with 3 jets and at least one b-tag. The enhancement is compatible with a slightly enhanced fraction of W-plus-jets events and can explain the difference between data and simulation that is observed in the total event yields in this event category. As written above, this difference is well covered by the systematic uncertainties on the event yields of W-plus-jets production in events with three jets.

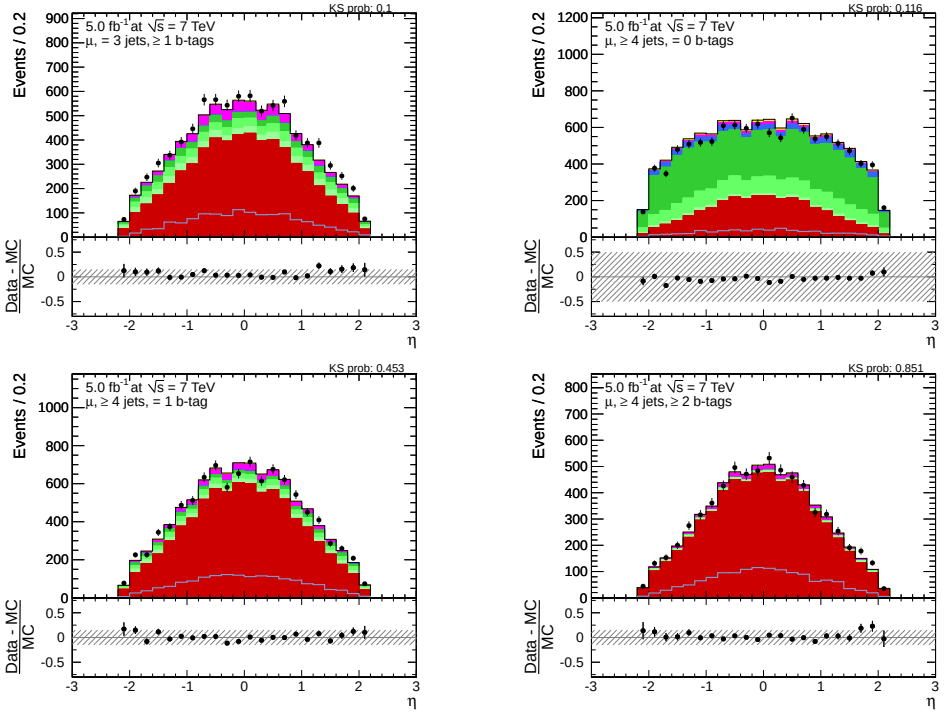

Figure 7.29: Distribution of the pseudorapidity η of the muon for events with 3 jets and at least 1 b-tag (top left) and with at least 4 jets and either 0 b-tags (top right), one b-tag (bottom left) or at least two b-tags (bottom right) in muon-plus-jets events.

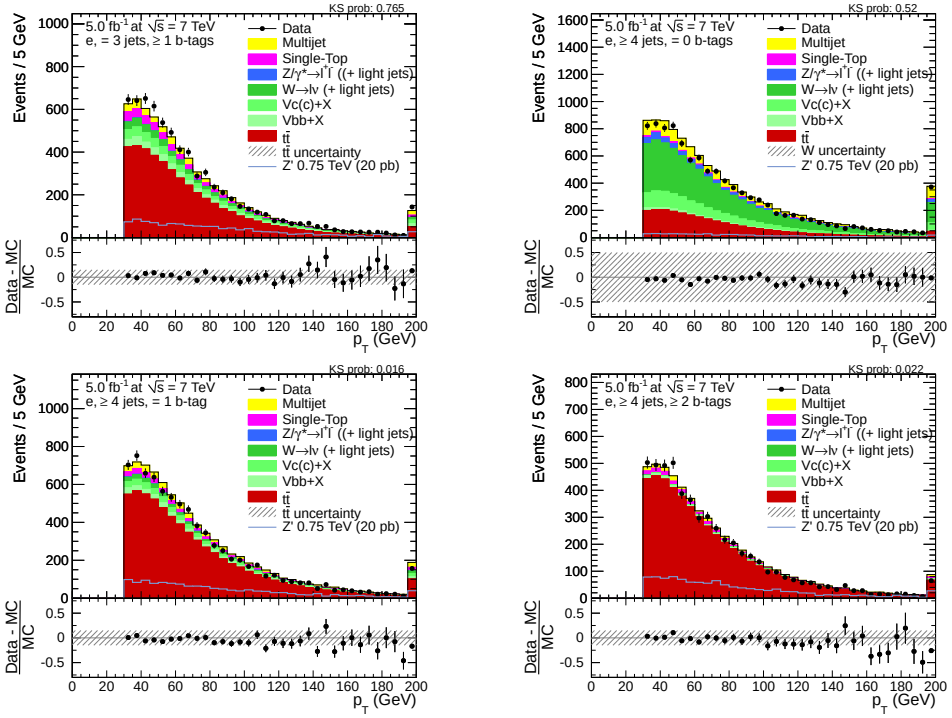

Figure 7.30: Distribution of the transverse momentum p_{T} of the electron for events with 3 jets and at least 1 b-tag (top left) and with at least 4 jets and either 0 b-tags (top right), one b-tag (bottom left) or at least two b-tags (bottom right) in electron-plus-jets events.

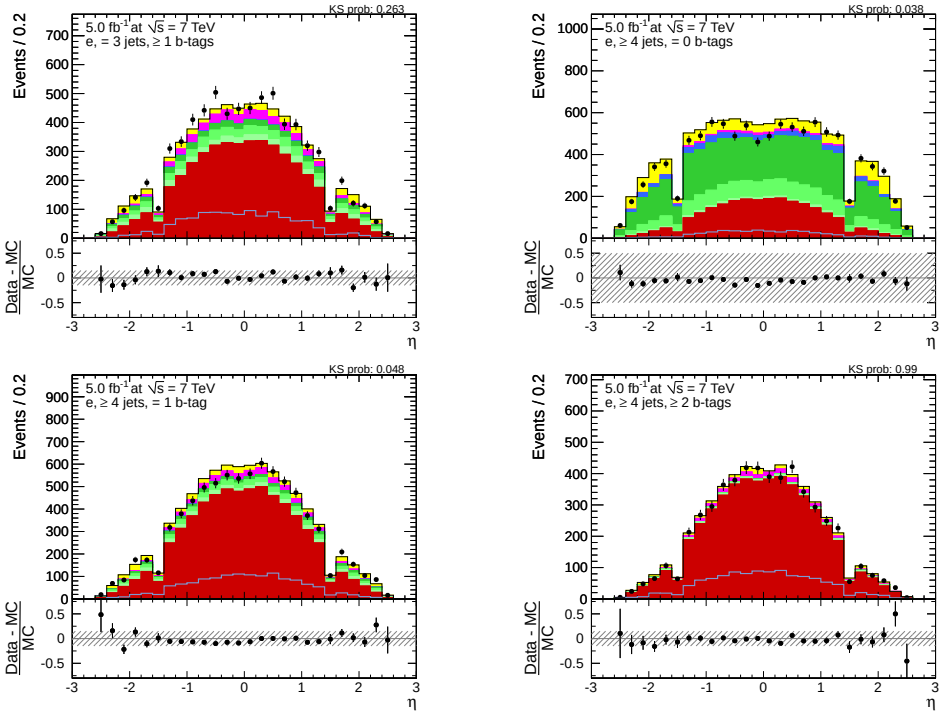

Figure 7.31: Distribution of the pseudorapidity η of the electron for events with 3 jets and at least 1 b-tag (top left) and with at least 4 jets and either 0 b-tags (top right), one b-tag (bottom left) or at least two b-tags (bottom right) in electron-plus-jets events.

The electron η distributions are displayed in figure 7.31 for the four event categories in the electron channel. The distribution of the electron η has a comparable shape to the distribution of the muon η, except for a drop at $|\eta| \sim 1.5$ due to the transition region between the ECAL barrel and endcap. There is reasonable agreement between data and simulated events, especially if taking into account that the shape of the electron η distribution for multijet events is subject to significant uncertainties. There is also an apparent asymmetry between data events with positive and negative pseudorapidity in events with 4 jets and 1 b-tag, but this asymmetry is not present in the other event categories and therefore most probably due to a statistical fluctuation.

The data-simulation agreement of the distribution of the missing transverse energy in the muon and electron channels is discussed above without the inclusion of the requirement $E_{\mathrm{T}}^{\mathrm{miss}} > 20$ GeV, see figures 7.3 and 7.5. Since data and simulation agree well in the full range, the agreement in the selected region including the requirement of a minimum amount of $E_{\mathrm{T}}^{\mathrm{miss}}$ is good as well. There is also a small preference for a softer $E_{\mathrm{T}}^{\mathrm{miss}}$ distribution in data compared to the simulation, which is more pronounced in the muon channel. This difference between data and simulation is similar to and likely correlated with that for other kinematic quantities, e.g. the transverse momenta of the jets and the lepton.

7.5.3 Quantities related to the reconstruction of the $m_{\mathrm{t\bar{t}}}$ system

In the following, distributions of kinematic quantities will be investigated that are relevant for the reconstruction of the $\mathrm{t\bar{t}}$ system. The results of the reconstruction of $m_{\mathrm{t\bar{t}}}$ will be shown in the following chapter. In the reconstruction of the $\mathrm{t\bar{t}}$ system that is explained above, an association of jets to partons is made that allows to reconstruct intermediate particles in the $\mathrm{t\bar{t}}$ decay chain. The intermediate objects are taken from the jet-parton association that is used to reconstruct the $m_{\mathrm{t\bar{t}}}$ distribution, i.e. the association that has the minimum χ^2 value. The distributions are shown for events with four jets and at least one b-tag as this is the region where $\mathrm{t\bar{t}}$ production is dominant and in which most of the signal events are expected.

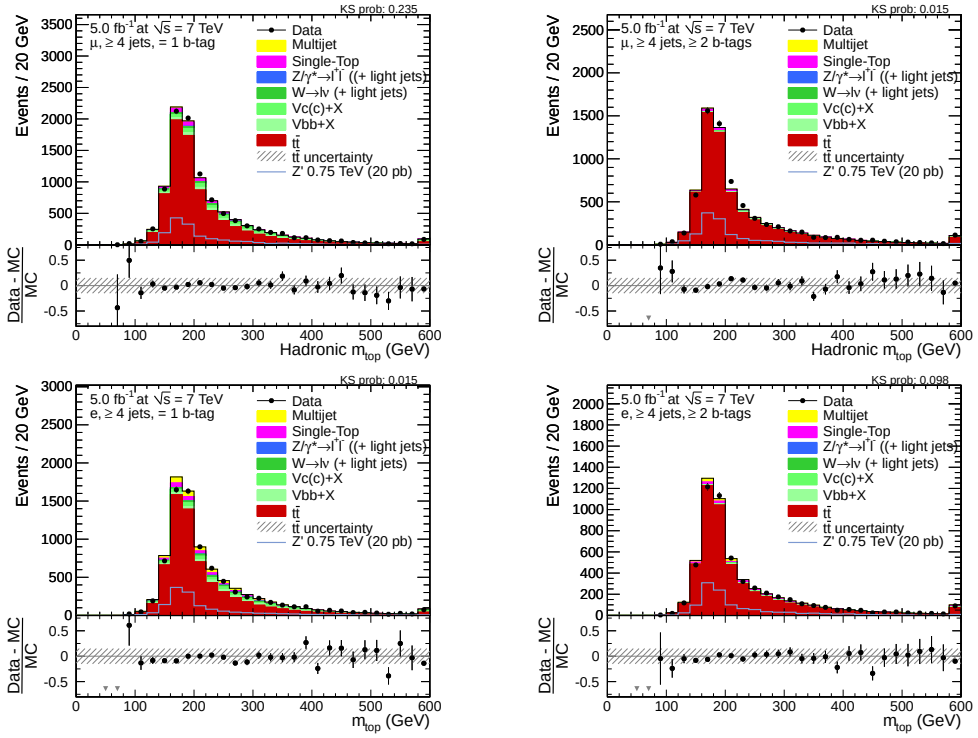

Figure 7.32: Distribution of the mass of the hadronic top quark for events with at least 4 jets and one b-tag (left) or at least two b-tags (right) in muon-plus-jets (top) and electron-plus-jets events (bottom).

Figure 7.32 shows the distribution of the mass of the hadronic top quark in events with one b-tag or at least two b-tags in the muon and the electron channel. Since the dominant contribution is from $\mathrm{t\bar{t}}$ contribution, the top quark mass distribution is expected to have a maximum at the nominal top quark mass value. There is a short tail towards lower values and a broad tail towards higher mass values due to events in which the hadronic top quark is either not fully reconstructable or where the jet-parton association is not correct. The agreement of data and simulation is therefore a measure for the correct modelling of the reconstructable fraction of events and of the energies of the jets used to reconstruct the top quark mass. The simulation describes the data distribution well, with a small tendency of the data towards higher mass values. In muon-plus-jets events with two b-tagged jets and to a lesser extent in electron-plus-jets events with one b-tagged jet and the other two event categories, there are more data events

around $m_{\mathrm{top}} \sim 200$ GeV than predicted by the simulation. This small difference between data and simulation is present in both events with one and two b-tagged jets that have a similar background composition. Therefore, the difference can rather be explained by experimental uncertainties like the knowledge of the jet energy scale and jet energy scale, which cover the differences between data and simulation.

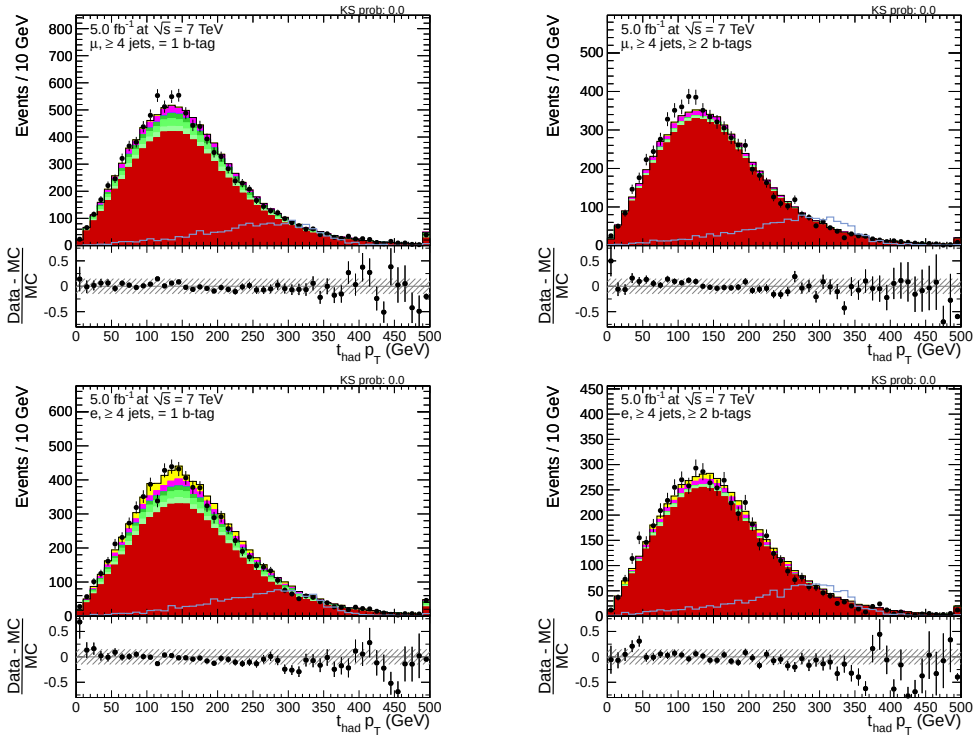

Figure 7.33: Distribution of the p_{T} of the hadronic top quark for events with at least 4 jets and one b-tag (left) or at least two b-tags (right) in muon-plus-jets (top) and electron-plus-jets events (bottom).

The p_{T} of the hadronic top quark is displayed in figure 7.33, again in the muon and electron channel for events with either one or at least two b-tags. The distribution rises from zero to a maximum at ~ 130 GeV; beyond, there is a significant tail towards higher p_{T} values. The form of the distribution is well modelled by the simulation in all four categories, except that the data distribution is slightly softer than the simulation. The top quark p_{T} is correlated with $m_{\mathrm{t\bar{t}}}$ as well as with the description of jets that do not originate from the $\mathrm{t\bar{t}}$ decay, and it is hence particularly sensitive to modelling uncertainties in event generators, which can explain the (albeit small) differences between data and simulation.

Figure 7.34 shows the distribution of the reconstructed mass of the hadronically decaying W boson in the four considered event categories. The distribution is expected to peak at the nominal W boson mass value of ~ 80 GeV with a width reflecting the jet energy resolution. Similar to the distribution of the hadronic top quark mass, there is a tail towards higher mass values due to events with missing jets, merged jets, or events with an incorrect jet-parton association. This tail is more pronounced for events with two b-tagged jets since having two b quark jets in the event reduces the probability that the two remaining jets are both from the decay of

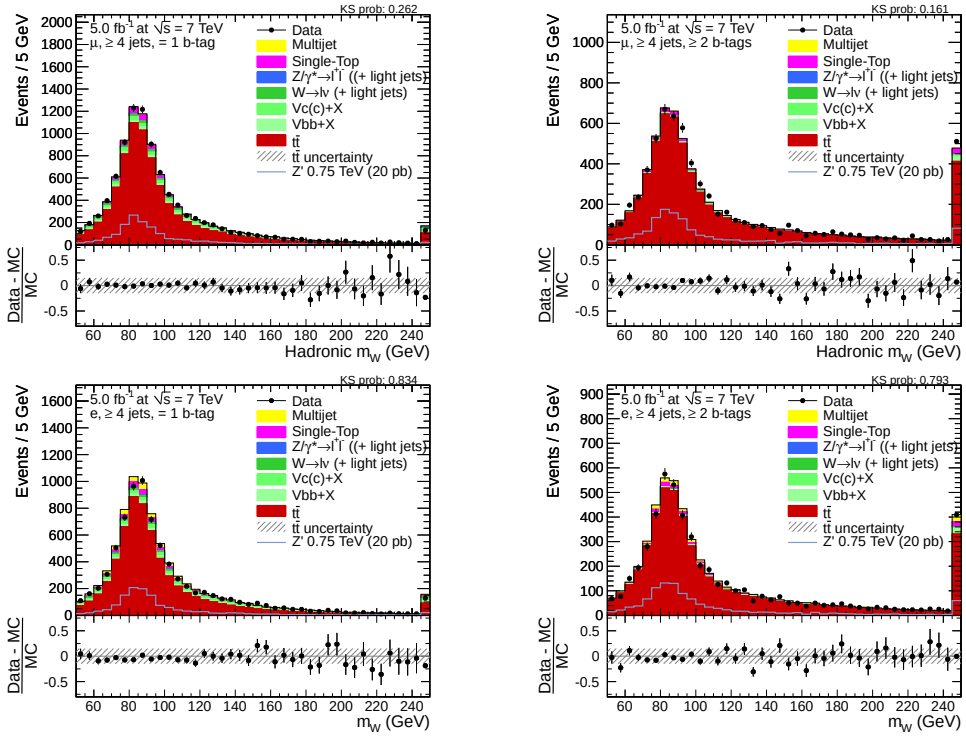

Figure 7.34: Distribution of the mass of the reconstructed hadronic W boson for events with at least 4 jets and one b-tag (left) or at least two b-tags (right) in muon-plus-jets (top) and electron-plus-jets events (bottom).

the W boson instead of from additional radiation. Data and simulated events agree well, suggesting that the jet energy scale and resolution for light-flavoured jets as well as the fraction of events with correct jet-parton associations are modelled well.

Now considering the leptonically decaying top quark, the distribution of its mass is shown in figure 7.35. Compared to the hadronic top quark mass, both peak at the nominal top quark mass value, but the distribution of mass of the leptonic top quark is significantly narrower, although both have similar intrinsic widths as seen in the previous chapter. The reason for the difference is that the probability for the single b jet from the leptonically decaying top quark to not be selected is significantly lower than the probability for at least one of the three jets from the hadronically decaying top quark to not be selected. Therefore, the tail of the distribution towards higher mass values is comparably small, especially for events with two b-tagged jets. The good agreement of data and simulation is indicative of a good modelling of the reconstruction of the neutrino as well as the lepton and the b quark jet energy scales.

As the decay of a $\mathrm{t\bar{t}}$ pair is symmetric, the p_T distribution of the leptonically decaying top quark is expected to be very similar to the p_T distribution of the hadronically decaying top quark. Figure 7.36 shows a comparison of data and simulation in the considered event categories. The maximum of the p_T distribution is also at ~ 130 GeV, and the tail towards higher mass values is compatible with that of the hadronic top quark. The comparison of data and simulation exhibits that the p_T distribution in data is a little softer than in simulation, again analogous to the hadronic top quark. The similarity of the data-simulation comparison indicates that the

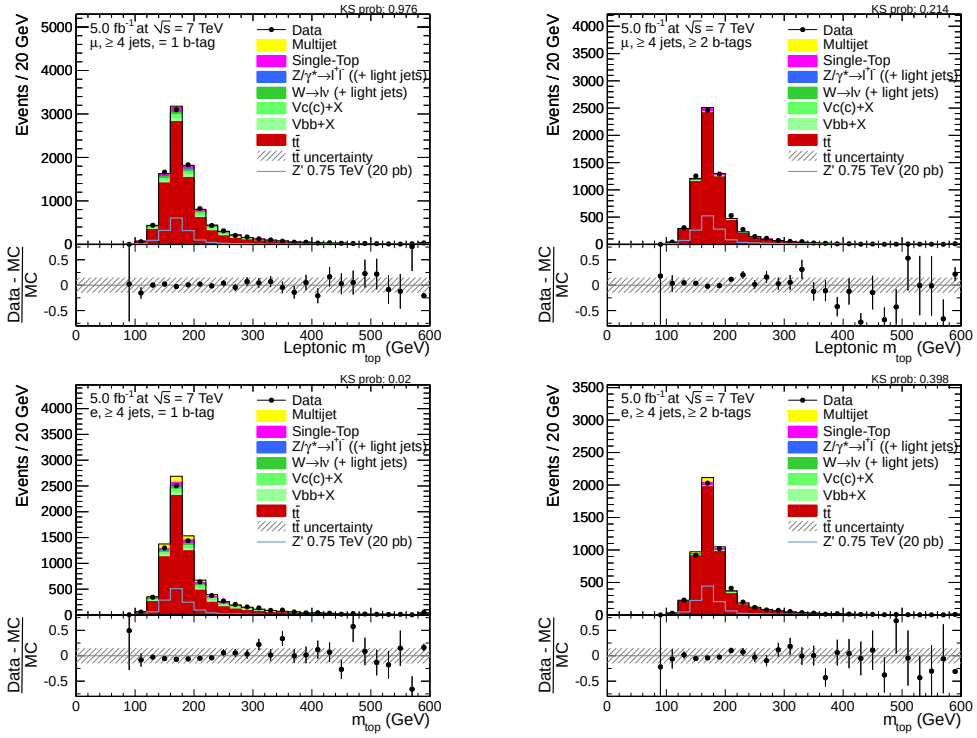

Figure 7.35: Distribution of the mass of the leptonic top quark for events with at least 4 jets and one b-tag (left) or at least two b-tags (right) in muon-plus-jets (top) and electron-plus-jets events (bottom).

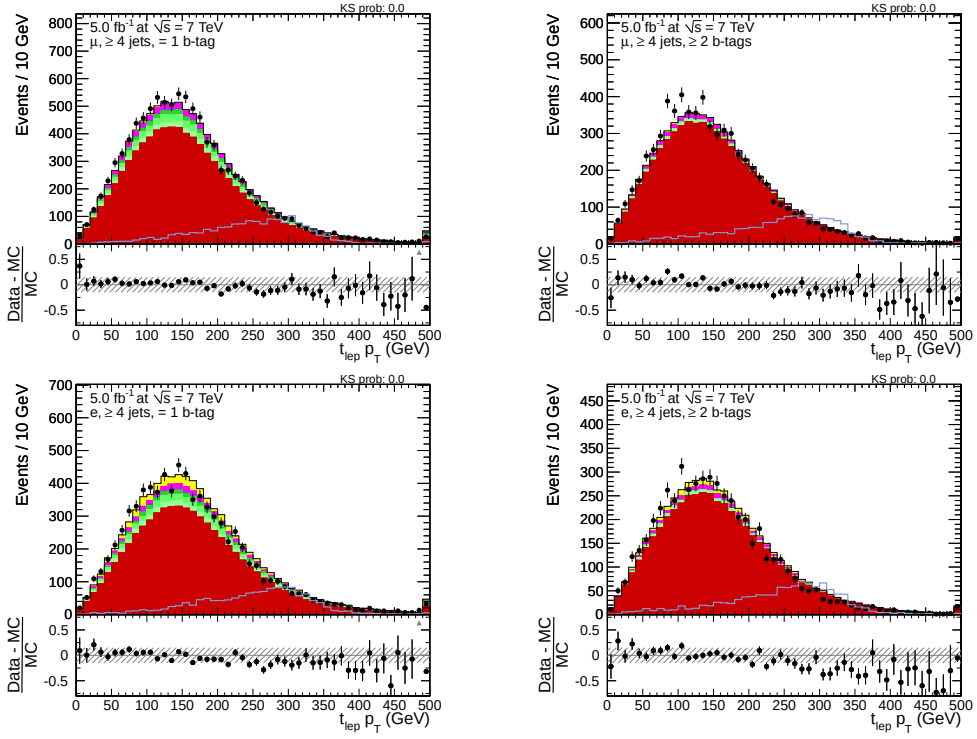

Figure 7.36: Distribution of the p_{T} of the leptonic top quark for events with at least 4 jets and one b-tag (left) or at least two b-tags (right) in muon-plus-jets (top) and electron-plus-jets events (bottom).

small differences are not due to experimental uncertainties, but that they need to be explained by uncertainties related to the description of SM $\mathrm{t\bar{t}}$ production by the used event generators.

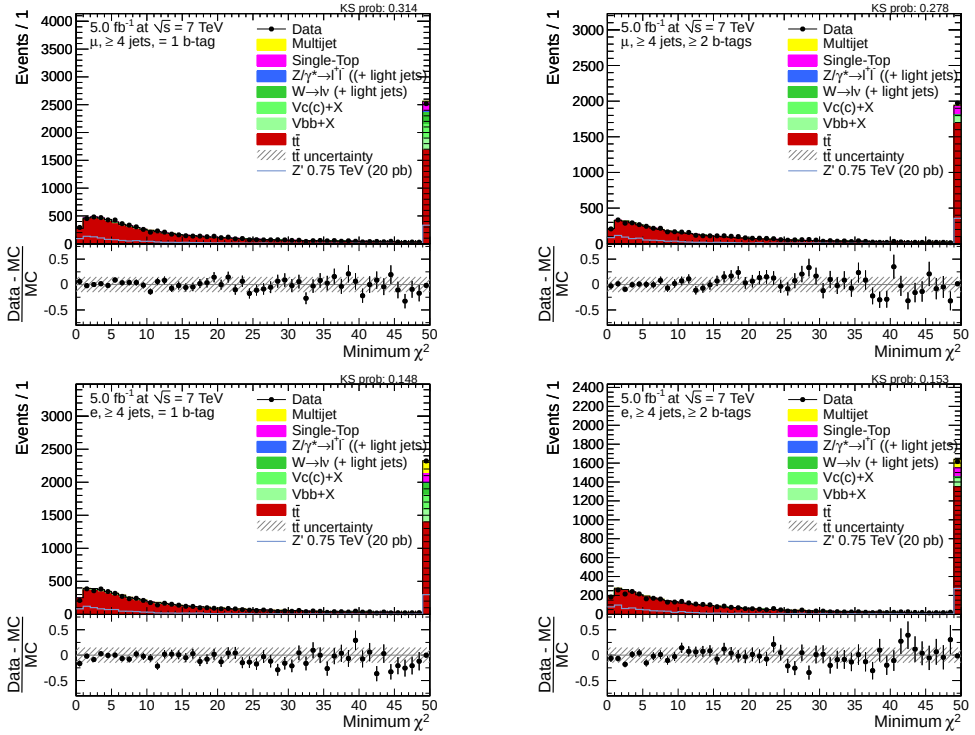

Figure 7.37: Distribution of the minimum χ^2 variable from the reconstruction of the $\mathrm{t\bar{t}}$ system for events with at least 4 jets and one b-tag (left) or at least two b-tags (right) in muon-plus-jets events (top) and electron-plus-jets events (bottom).

In the following, the focus will be on distributions related to the fully reconstructed $\mathrm{t\bar{t}}$ system. First, the distribution of the minimum χ^2 variable used in the reconstruction of the $\mathrm{t\bar{t}}$ system is shown in figure 7.37 for the considered event categories. The definition of the χ^2 variable involves the hadronic top quark, the hadronic W boson, the leptonic top quark, the p_T of the $\mathrm{t\bar{t}}$ system, and the fraction of the p_T of the selected jets and all jets. Comparing data and simulation hence probes the description of the central values and widths of the five variables. With a maximum at ~ 2.5, the χ^2 variable roughly follows a χ^2 distribution with 5 degrees of freedom, but it does not fall as fast for two reasons. First, the input resolutions do not strictly follow a Gaussian function; second, there is a significant fraction of events in which a full matching of jets to partons is not possible due to missing or merged jets. The data distributions are compatible with the simulation, underlining the good description of the variables used in the $m_{\mathrm{t\bar{t}}}$ reconstruction by the event generators and the simulation.

The distribution of the p_T of the $\mathrm{t\bar{t}}$ system is linked with the description of additional jets in $\mathrm{t\bar{t}}$ production, i.e. the number of additional jets, their p_T spectrum, and their direction. Figure 7.38 shows the $\mathrm{t\bar{t}}$ p_T distribution in the muon and electron channel for four-jet events with one or at least two b-tags. The p_T distribution rises fast and reaches its maximum at $\sim$ 25 GeV, whereafter it falls gently towards higher p_T values. In all categories, data and simulation agree well.

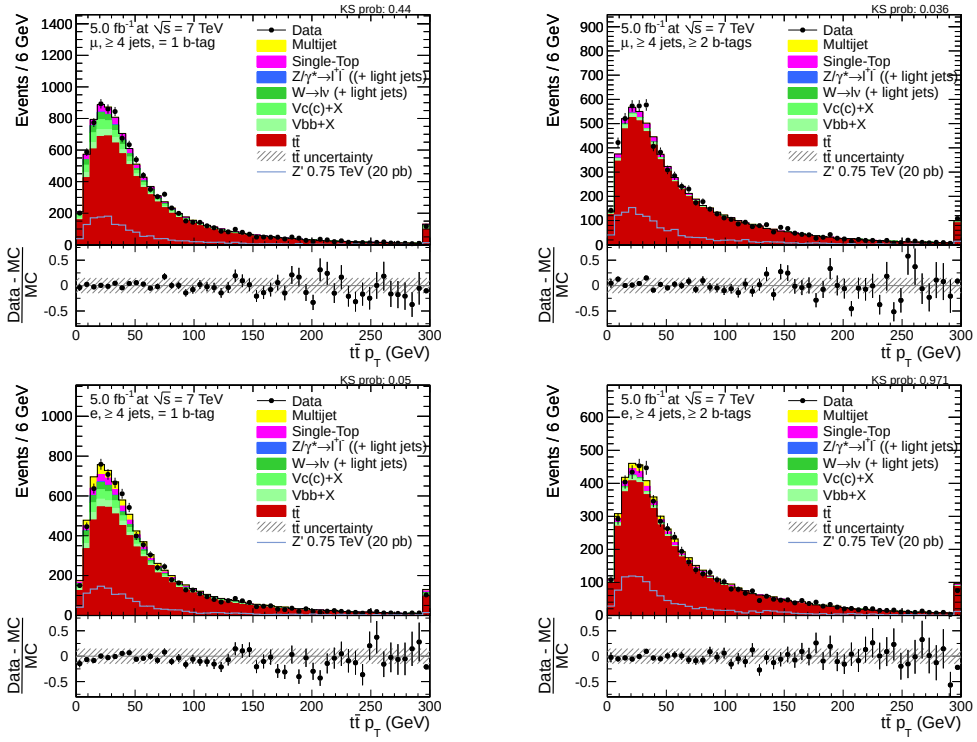

Figure 7.38: Distribution of the p_{T} of the reconstructed $\mathrm{t\bar{t}}$ system for events with at least 4 jets and one b-tag (left) or at least two b-tags (right) in muon-plus-jets events (top) and electron-plus-jets events (bottom).

In the light of the good agreement between data and simulation, the results can be compared to an analysis of the top quark forward-backward asymmetry by the D0 collaboration that shows a mismodelling of the p_{T} of the $\mathrm{t\bar{t}}$ system [2]. In the D0 analysis, the p_{T} distribution of the recorded data is significantly softer than the prediction from the sum of the background processes, amongst which the dominant background from $\mathrm{t\bar{t}}$ production is simulated with the NLO event generator MC@NLO. The discrepancies observed by the D0 analysis are not confirmed in the context of this analysis.

The rapidity y of the $\mathrm{t\bar{t}}$ system is related to the proton momentum fractions carried by the interacting partons. Figure 7.39 shows the $\mathrm{t\bar{t}}$ rapidity distribution in the four considered event categories. There is good agreement between data and simulation, confirming the description of the parton momenta within the experimental resolution.

Finally, the $m_{\mathrm{t\bar{t}}}$ distribution reconstructed from the four leading jets is shown in figure 7.40 for four-jet events with one or at least two b-tags in the muon and electron channel. For all four considered categories, data and simulation agree well. The results of the reconstruction involving the χ^2-based jet-parton association for all 8 event categories used in the statistical evaluation are shown in the next chapter.

Altogether, the simulation describes all distributions well that are related to the reconstruction of the $\mathrm{t\bar{t}}$ system. There are small differences between data and simulation in a few cases, most importantly the transverse momenta of the two top quarks, which can be explained by systematic uncertainties related to the generation of $\mathrm{t\bar{t}}$ events. These systematic uncertainties

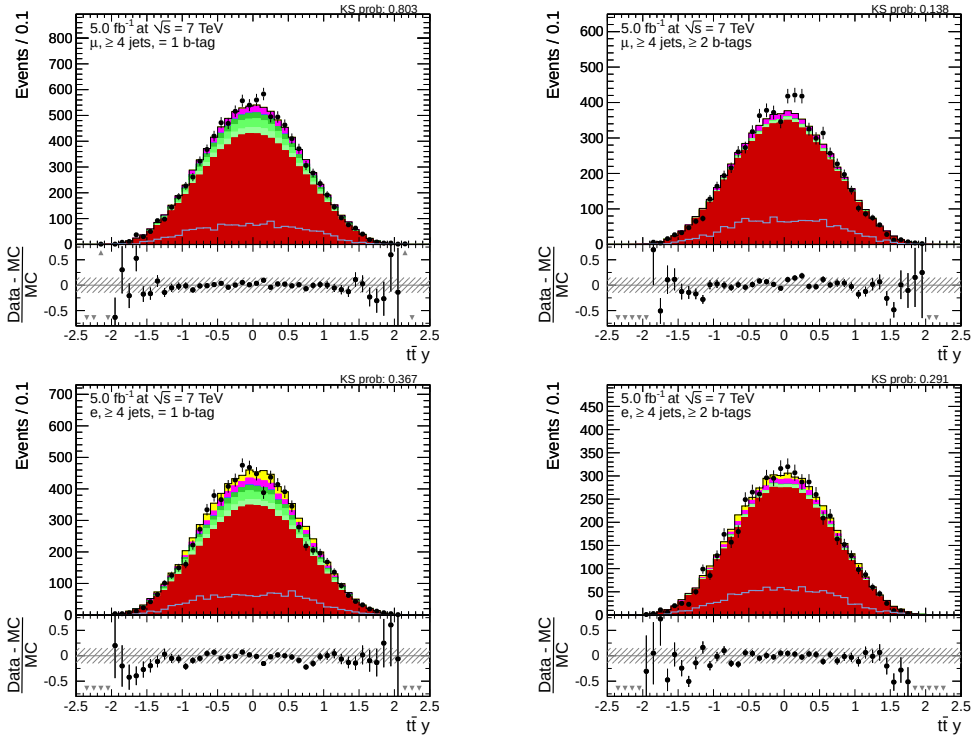

Figure 7.39: Distribution of the rapidity of the reconstructed $t\bar{t}$ system for events with at least 4 jets and one b-tag (left) or at least two b-tags (right) in muon-plus-jets events (top) and electron-plus-jets events (bottom).

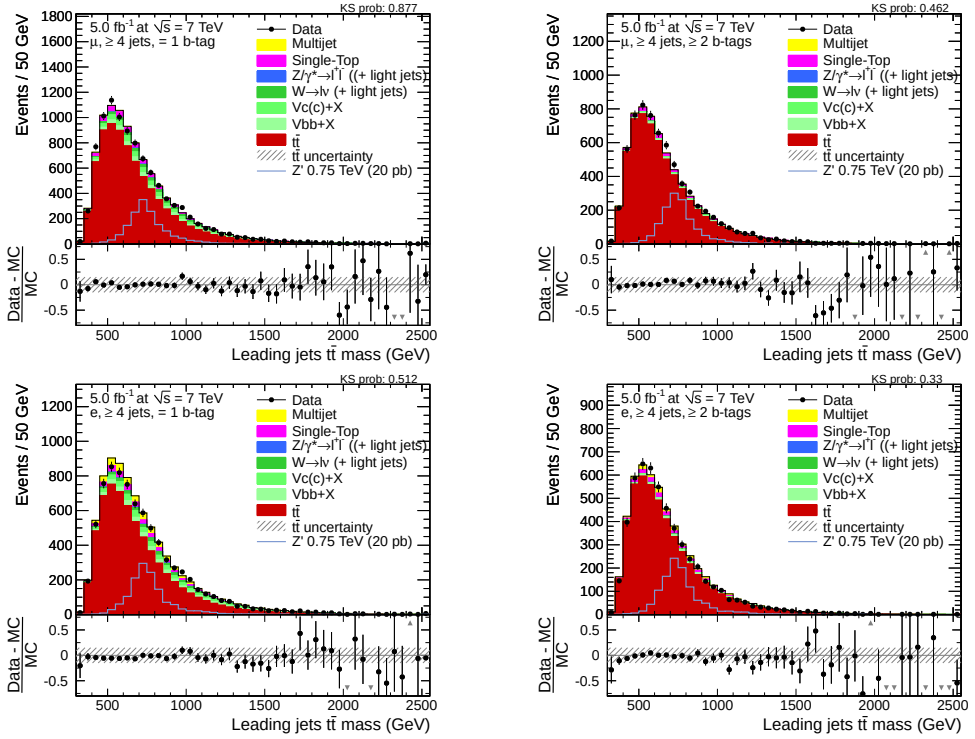

Figure 7.40: Distribution of $m_{t\bar{t}}$ using the leading-jets algorithm for events with at least 4 jets and 1 b-tag (left) or at least two b-tags (right) in muon-plus-jets events (top) and electron-plus-jets events (bottom).

originate from the choice of the matching threshold and the renormalisation/factorisation scales in the generation of simulated $\mathrm{t\bar{t}}$ events as well as from the difference between LO and NLO event generators. The uncertainties are taken into account in the statistical evaluation. The good agreement of data and simulation confirms the good performance of the reconstruction and simulation and allows the measurement of the $m_{\mathrm{t\bar{t}}}$ distributions and the search for new particles carried out in the following.

8 Statistical Evaluation

This chapter describes the measurement of the $m_{\mathrm{t\bar{t}}}$ distribution and the statistical evaluation of the search for new particles decaying to a $\mathrm{t\bar{t}}$ pair. In the first section, the systematic uncertainties that are relevant for the analysis are discussed. Then, the used statistical methods are explained. The measured $m_{\mathrm{t\bar{t}}}$ distributions are described in the following and the background model is compared with the observed data. Finally, upper limits are placed on the production cross sections for new particles decaying to a $\mathrm{t\bar{t}}$ pair that are predicted by a number of models.

8.1 Systematic uncertainties

In the following, the systematic uncertainties affecting signal and background events are discussed. Systematic uncertainties may generally affect the expected event rates for a certain physics process as well as the shape of the $m_{\mathrm{t\bar{t}}}$ distributions. The relevant systematic uncertainties can be loosely subdivided into experimental and theoretical uncertainties. Experimental uncertainties are e.g. caused by the imperfect knowledge of the detector response or the uncertainty of the amount of integrated luminosity provided by the LHC. Theoretical uncertainties arise from uncertainties on the calculations of the inclusive cross sections for the relevant background processes as well as from the description of the different background processes in event generators. In the next sections, the source of each systematic uncertainty will be described. In addition, the effect of the systematic uncertainties on the expected event rates will be discussed, starting with the experimental uncertainties.

8.1.1 b-tagging efficiencies

Uncertainties on the simulation of the b-tagging efficiency were estimated with 2011 LHC data [114]. The uncertainty on the b-tag efficiency is provided as a function of jet p_{T} and η and ranges from 2–8% for b-flavoured jets with $p_{\mathrm{T}} < 670$ GeV. For c-flavoured jets, the uncertainty is assumed to be twice the uncertainty of the b-tag efficiency as dedicated measurements of the b-tag efficiency for c-flavoured jets are experimentally more challenging. Since both b and c jets contain long-lived hadrons and therefore true sources of secondary vertices, the uncertainties are regarded as fully correlated.

To estimate the impact of the uncertainties, their effect on the considered events is calculated. The uncertainties apply to individual jets. Events are reweighted for the differences between the b-tag efficiency in data and simulation depending on the properties of the b-flavoured jets in simulation with the same technique as introduced above. The corresponding data-to-simulation

scale factors f_{b} are varied within the given uncertainties. The impact of the uncertainties can now be estimated by comparing events after the nominal corrections with events that have the reweighting for the $\pm 1\sigma$ uncertainties applied.

Table 8.1: Impact of $\pm 1\sigma$ shifts of the b-tag efficiency for b jets and c jets on the event yields for the most important background samples in all 8 categories.

Change / %	$\mathrm{t\bar{t}}$	**W+LF**	**W+b+X**	**W+c+X**	**Single top**
μ 3j1t	1/-1	0/0	2/-2	4/-4	2/-2
μ 4j0t	-6/6	0/0	-4/4	-1/1	-5/5
μ 4j1t	-1/1	0/0	1/-1	4/-4	0/0
μ 4j2t	4/-4	0/0	5/-4	7/-6	5/-5
e 3j1t	1/-1	0/0	2/-2	4/-4	2/-2
e 4j0t	-6/6	0/0	-4/4	-1/1	-5/5
e 4j1t	-1/1	0/0	1/-1	4/-4	0/0
e 4j2t	4/-4	0/0	4/-4	7/-7	5/-5

Table 8.1 shows the impact of a variation of the b-tag efficiency uncertainty within one standard deviation on the event yields for the different background samples. For events with b-flavoured jets, an increase of the b-tag efficiency reduces the number of events with 4 jets and no b-tagged jets by $\sim 5\%$, whereas the number of events with 2 b-tagged jets increases by $\sim 5\%$. The net effect on events with one b-tagged jet is comparably small (order of 1%) due to the interplay of the migration of events between the different categories.

The uncertainties on the b-tagging efficiency for light-flavoured jets, also called mistag rate, are assumed to be uncorrelated with the b-tag efficiency for b and c jets. The uncertainties of the b-tagging efficiency for light-flavoured jets have been derived dependent on jet η and p_{T} and are of the order of 11% across the considered p_{T} range. Due to the relatively small fraction of selected events with light-flavoured jets that are tagged as b jets, the impact of the b-tag efficiency uncertainty on the expected event yields is smaller for light-flavoured jets than for b and c jets. The only significant change in the number of selected events is for events from W boson production in association with light-flavoured jets, leading to variations of the expected number of events of $\sim 10\%$ for events with three or four jets of which one is b-tagged, and of $\sim 20\%$ for events with four jets and at least two b-tags.

8.1.2 Jet energy scale, jet energy resolution, and the amount of unclustered energy

Uncertainties of the knowledge of the jet energy scale σ_{jes} have been determined as a function of transverse momentum p_{T} and pseudorapidity η of the reconstructed jets using dijet and photon-plus-jet events in 7 TeV LHC data [104]. The combined jet energy scale uncertainties arise from a number of sources: the imperfect knowledge of the absolute jet energy scale; the extrapolation to high transverse momenta where the amount of available data events for a full calibration is too small; the time dependence of the corrections due to an instability in the ECAL endcap

region; η-dependent sources due to corrections for final state radiation, the uncertainty of the jet p_{T} resolution, and the statistical uncertainty of the calibration; and the modelling of pile-up interactions. The individual uncertainties are added in quadrature to yield the total jet energy scale uncertainty.

For the evaluation of the uncertainties, all jet momenta are varied according to $\pm 1\sigma$ variations of the jet energy scale. The variation of the jet energy scale simultaneously also affects the missing transverse energy. This is taken into account by computing the vectorial sum of all variations of the jet momenta and then subtracting the sum from the missing transverse energy.

Table 8.2: Impact of a $\pm 1\sigma$ shift of the jet energy scale on the event yields for the most important background samples in all 8 categories.

Change / %	$\mathrm{t\bar{t}}$	**W+LF**	**W+b+X**	**W+c+X**	**Single top**
μ 3j1t	+3/-3	+6/-6	+5/-4	+6/-6	+6/-6
μ 4j0t	+8/-8	+10/-9	+12/-10	+11/-10	+10/-9
μ 4j1t	+8/-8	+8/-7	+10/-8	+10/-9	+9/-8
μ 4j2t	+8/-8	+6/-7	+9/-8	+9/-6	+9/-7
e 3j1t	+3/-3	+5/-5	+7/-5	+4/-5	+6/-5
e 4j0t	+8/-7	+10/-9	+10/-9	+10/-10	+10/-9
e 4j1t	+8/-7	+9/-8	+8/-8	+10/-8	+9/-9
e 4j2t	+8/-7	+5/-3	+8/-8	+8/-11	+8/-8

A list of relative changes of the event yields in the different categories due to $\pm 1\sigma$ variations of the jet energy scale is given in table 8.2. The relative changes in the event yields are similar for the different simulated samples; they are of the order of 10% for four-jet events and 6% for three-jet events. The relative change in acceptance is lower for three-jet events because of the interplay of events with two or less jets and events with four or more jets: For a positive variation of the jet energy scale, a fraction of events with two jets has a third jet with sufficient transverse momentum to be selected as a three-jet event, but at the same time a fourth jet in a three-jet event can pass the selection threshold for the fourth jet.

The uncertainties of the jet energy scale resolution have been determined using dijet event samples [104]. As explained above, the relative jet energy resolution in data is 6–20% worse than in simulated events depending on jet η. The correlated effect on the missing transverse energy is calculated in the same way as for the jet energy scale uncertainties.

A third, uncorrelated uncertainty that affects the missing transverse energy is due to the amount of energy that is not clustered in jets and not due to isolated leptons. The relative uncertainty on this fraction of $E_{\mathrm{T}}^{\mathrm{miss}}$ is assumed to be 10%, motivated by measurements of the differences of the $E_{\mathrm{T}}^{\mathrm{miss}}$ resolution between data and simulation [106]. The unclustered part of $E_{\mathrm{T}}^{\mathrm{miss}}$ is calculated by vectorially subtracting all jets and isolated leptons from the reconstructed missing transverse energy. The resulting uncertainties are found to be very small and are hence neglected in the following.

8.1.3 Electron and muon trigger, reconstruction, and selection efficiencies

The uncertainties of the different parts of the lepton efficiencies are determined using the so-called tag-and-probe method in Z-plus-jets events as described above, see section 5.6.1. The statistical uncertainties of the scale factors are negligible, whereas systematic uncertainties arise from various sources.

First, there is a non-zero background fraction from events that do not have two prompt isolated leptons, i.e. events not from Z/γ^* or $\mathrm{t\bar{t}}$ production. As the expected fraction is small, a possible effect is estimated by two methods. First, instead of counting the fraction of events with probe leptons passing the selection, a two-component fit of Z-like signal and continuum background is performed to the Z boson mass distributions for events with probe leptons either passing or failing the required selection criteria. The change in the resulting data-simulation scale factors is of the order of 1%, contributing an according uncertainty. A second method of controlling the amount of possible background events is to vary the criterion of compatibility with the Z boson mass. Since background events are not expected to have a peak around the Z boson mass, the data-simulation scale factor can be derived inside and outside a window around the Z boson mass. The variations are also of the order of 1%.

Second, there may be a dependence of the scale factors on the phase space, most importantly the additional jet activity in the event. Most scale factor calculations are carried out with the requirement of the presence of at least two energetic jets, giving a similar topology to the selected phase space. However, this requirement is not applied for all calculations, giving an extrapolation uncertainty of 1%.

Finally, the assumption is made that the scale factors do not depend on kinematic properties of the lepton. As discussed in section 5.6.1, this assumption is only fulfilled to reasonable approximation, yielding an additional uncertainty of 1–2%. Altogether, the uncertainties on both the combined muon and electron efficiencies add up to 3%.

8.1.4 Integrated luminosity

The relative uncertainty on the amount of integrated luminosity is 2.2% [77]. This uncertainty affects the estimated rates of all contributions that are estimated from simulated events, i.e. $\mathrm{t\bar{t}}$, W-plus-jets, Z-plus-jets and single top quark production as well as the considered signal processes of Z′ and KK gluon production.

8.1.5 Background rates and distributions

The uncertainties on the rates of the different background processes can be clustered into three groups depending on the phase space, which will be discussed in the following:

- Irreducible background process in the considered phase space ($\mathrm{t\bar{t}}$ production).

- Reducible physical background processes that contribute in the tail of the distribution of the number of jets (W plus jets including heavy flavour jets, Z plus jets, single top production).
- Reducible background processes that have a different final state (multijet production in the muon and electron channel).

As $\mathrm{t\bar{t}}$ production is the most important background process, both the rate on the inclusive cross section and the modelling of the $m_{\mathrm{t\bar{t}}}$ distribution by event generators are included as separate uncertainties. The uncertainty of the inclusive cross section is 15%, stemming from the uncertainties of the calculation at next-to-leading order accuracy [29]. The uncertainties on the shape of the $m_{\mathrm{t\bar{t}}}$ distribution are discussed below.

The production of a W boson in association with jets is the second most important background process. While the uncertainty of the inclusive W-plus-jets cross section is of the order of 5% [35], the experimental and modelling uncertainties on the production rate for a given number of jets are significantly higher, with the relative experimental uncertainties for W-plus-jets production with at least 4 jets fulfilling $p_{\mathrm{T}} > 30$ GeV being $\sim 33\%$ [37]. To account for the differences in the jet selection, a relative uncertainty of 50% is assumed here, which is taken to be independent for events with 3 jets and at least 4 jets. By including events with 4 jets of which none is b-tagged in the statistical evaluation, the effect of these uncertainties are reduced in the statistical evaluation as they are constrained in situ, therefore not making a more precise prior uncertainty necessary. Uncertainties of the description of the $m_{\mathrm{t\bar{t}}}$ shape by event generators for W-plus-jets production are described below.

As events are categorised according to the number of identified b jets in the statistical evaluation, the description of the production of a W boson in association with b or c jets is of particular importance. There are no theoretical predictions or experimental measurements available for the considered phase space. Therefore, uncertainties of 100% are assumed for W+b+X and W+c+X production in addition to the correlated uncertainties on the W-plus-jets rates. The additional uncertainties for W+c+X and W+b+X production are treated as independent in the following. Similar to the inclusive rate for W-plus-jets production, these rather large uncertainties are constrained in situ with the help of the statistical methods introduced below.

Due to the small contribution from the other reducible background processes, no dedicated modelling uncertainties related to the event generation are introduced. To account for the potential differences in acceptance due to the description of extra jet radiation, additional rate uncertainties are included that go beyond the uncertainties on the inclusive cross section values. For single top production in all three production modes, i.e. in the t channel, tW channel, and s channel, the total uncertainty is taken to be 30%, which is significantly larger than the uncertainties on the inclusive cross sections that are of the order of 10%. The relative uncertainty of 30% includes a conservative estimate of the theoretical uncertainties on the acceptance for the three processes that are estimated using dedicated event samples with varied generator settings.

The description of the extra jet radiation in the production of a Z boson in association with jets is correlated with the extra jet production in W-plus-jets events. Therefore, the event yields for Z-plus-jets events are treated as correlated with the event yields for W-plus-jets events both for the production in association with light-flavoured jets and with at least one c jet or b jet. An

additional dedicated uncertainty of 30% is assumed to reflect uncertainties due to the inclusive cross section for Z boson production, the modelling of the missing transverse energy in Z-plus-jets events, the efficiency of the lepton selection, and the differences in the description of extra jet radiation between W- and Z-plus-jets events.

Finally, the uncertainties on the event yields of multijet events have been derived above. The uncertainties are different for the two lepton channels and for the different event categories. Their relative size ranges from 43–63% in the electron channel and from 52–73% in the muon channel. The relative uncertainties in the muon channel are higher as the expected number of multijet events in the muon channel is very small, which leads to higher statistical uncertainties in the estimation of the event yields, but only has a small effect on the statistical sensitivity. The contribution from multijet events is generally small, and the shapes of the $m_{\mathrm{t\bar{t}}}$ distribution are well described from events in the data control regions. Therefore, no dedicated shape uncertainties are taken into account for multijet events.

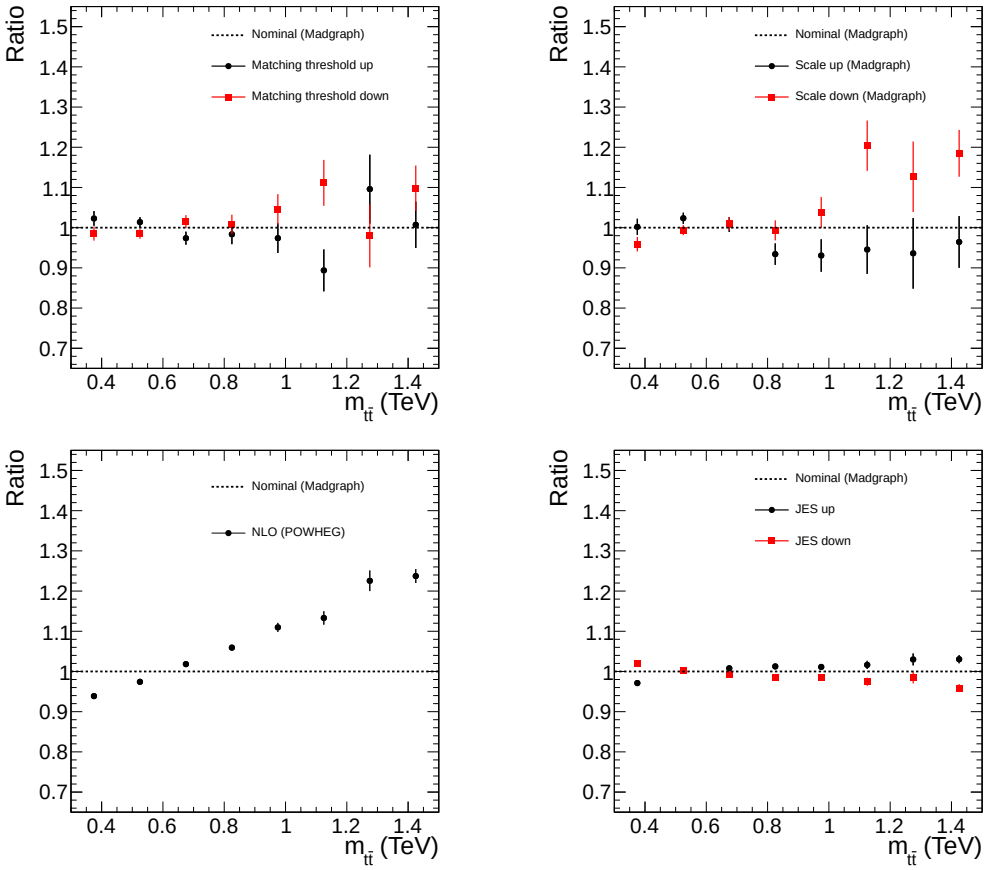

Figure 8.1: Ratio of normalised distributions of reconstructed $m_{\mathrm{t\bar{t}}}$ with variations of the matching threshold (top left), with variations of the renormalisation and factorisation scales (top right), from the NLO generator POWHEG (bottom left), and for events with variations of the jet energy scale within uncertainties (bottom right) with respect to LO simulation (MADGRAPH) for muon-plus-jets events passing all selection criteria with at least four jets.

To account for the theoretical uncertainty of the $m_{\mathrm{t\bar{t}}}$ shape in $\mathrm{t\bar{t}}$ events, distributions of events with different generator settings are compared with the nominal simulation. The settings are

simultaneous variations of the factorisation and renormalisation scales, and variations of the matching threshold; the details of the variations are given above in section 5.3. The fractions of selected events vary by about 6% for variations of the factorisation and renormalisation scales and by $\sim 3\%$ for variations of the matching threshold.

In addition, an event sample generated with the NLO generator POWHEG is used to evaluate further systematic uncertainties. Since the systematic variations of the scale and the matching threshold are made with respect to the original MADGRAPH sample, the systematic uncertainty due to the difference with the NLO generator is symmetrised for the statistical evaluation. The distributions from the MADGRAPH $\mathrm{t\bar{t}}$ sample are taken as the default, and the full difference between MADGRAPH and POWHEG is added to (subtracted from) the central distribution to define the $+1\sigma$ (-1σ) variation of the according uncertainty. A comparison of the predictions from MADGRAPH and POWHEG is shown in figure 8.1. In addition, comparisons of the nominal sample with variations due to the matching scale, the renormalisation/factorisation scales, and the jet energy scale are displayed. The relative differences in acceptance due to the NLO uncertainty are of the order of 5%, and the relative systematic variations of the $m_{\mathrm{t\bar{t}}}$ shape are of the order of $\pm 10\%$, with the NLO spectrum being harder. These shape differences are significantly larger than for variations of the jet energy scale as well as of the renormalisation and factorisation scales, as can e.g. be seen from the shift of the mean of the $m_{\mathrm{t\bar{t}}}$ distribution which is twice as high for the NLO correction. This comparison shows that the corrections from the NLO generator are of importance and that they are not covered by the other systematic variations.

Another potential systematic uncertainty arises from uncertainties of the used parton distribution functions. These uncertainties are however small when compared to the other modelling uncertainties (as can e.g. be seen in reference [57]) and are therefore absorbed in the uncertainties of the inclusive $\mathrm{t\bar{t}}$ cross section.

The effect of variations of the renormalisation and factorisation scales in W-plus-jets events is also investigated with dedicated events samples of which the details are given above. Figure 8.2 shows the ratio of the reconstructed $m_{\mathrm{t\bar{t}}}$ distributions for W-plus-jets events with varied settings of the renormalisation/factorisation scales and with the nominal settings in muon-plus-jets events. Due to the insufficient number of simulated events in the event samples with varied generator settings, the effect of the variation is parametrised by fitting a first order polynomial to the ratio of the $m_{\mathrm{t\bar{t}}}$ distributions. The fits are carried out separately for events with 3 jets and at least 4 jets as the $m_{\mathrm{t\bar{t}}}$ definition is different and as the ratios exhibit significant differences. The ratios as well as the parameters of the fitted functions are compatible between the muon and the electron channel. Therefore, the same functional parameters are used for both channels. Similarly, the ratios are compatible between W boson production in association with light-flavoured and heavy-flavoured jets. The effect of the varied generator settings is included in the statistical evaluation by reweighting the central W-plus-jets events as a function of reconstructed $m_{\mathrm{t\bar{t}}}$ with the fitted polynomials, defining the $\pm 1\sigma$ distributions of a variation of the renormalisation/factorisation scale.

As can also be seen from the ratios of the $m_{\mathrm{t\bar{t}}}$ distributions, the variation of the renormalisation and factorisation scales also has a strong impact on the event yields. The upward variation leads to a reduction of the number of events by about 50%, whereas the downward variation of the scales leads to an increase of the number of selected events by about 100%. Compared to a

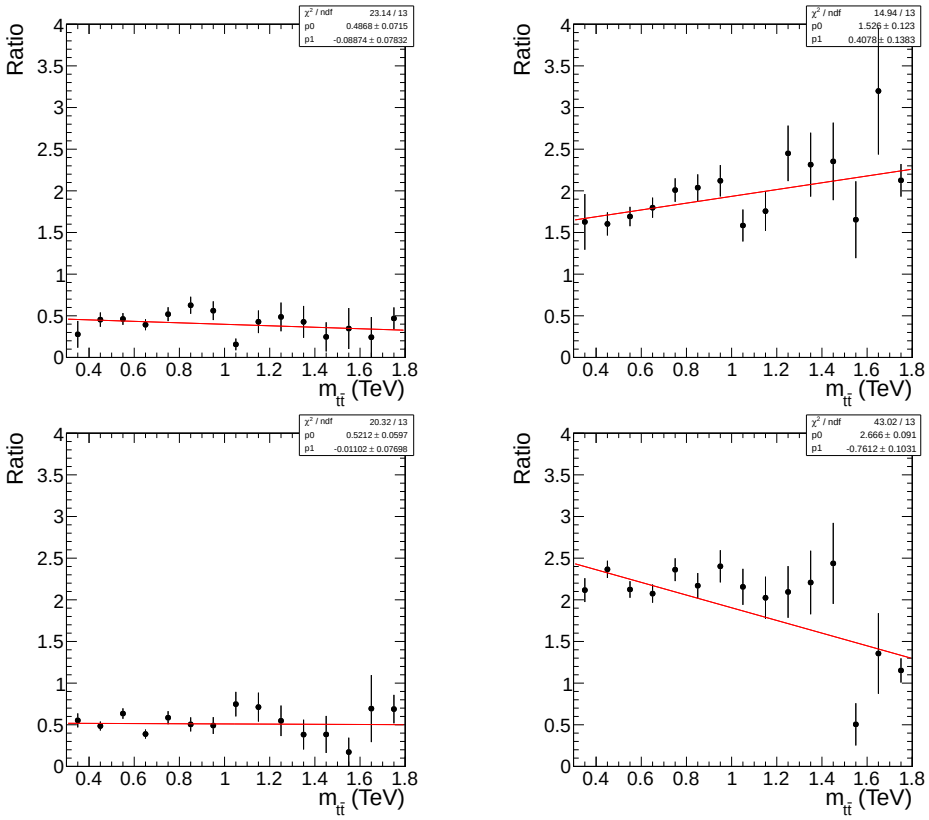

Figure 8.2: Ratio of $m_{t\bar{t}}$ distributions in W-plus-jets events with varied renormalisation/factorisation scales and with nominal settings in the muon-plus-jets channel. The shown ratios are for an upward variation of the scale in events with at least 4 jets (top left) and with 3 jets (bottom left), and for a downward variation in events with at least 4 jets (top right) and 3 jets (bottom right). Together with the ratios, a fit of a first order polynomial is displayed.

variation of the matching scale, for which the expected event yields are subject to variations of the order of 20%, both the effect on the rate and the shape of the $m_{\mathrm{t\bar{t}}}$ distribution is significantly larger for the variation of the renormalisation and factorisation scales. The effect of a variation of the matching scale is therefore well absorbed in the rate uncertainties on the W-plus-jets contribution.

The $m_{\mathrm{t\bar{t}}}$ distributions for simulated events are also subject to uncertainties due to the limited number of simulated events, which will be treated within the statistical evaluation and which is hence not discussed in detail here. Due to the high number of simulated events, e.g. a factor of 100 more simulated $\mathrm{t\bar{t}}$ events than expected in 5.0 fb^{-1} of data and at least a factor of 10 for the other simulated samples, and due to the relatively inclusive event selection, the resulting uncertainties on the event rates are small. The uncertainties may however be important in the high-mass tail of the $m_{\mathrm{t\bar{t}}}$ distribution where a low number of events is expected.

8.1.6 Summary of systematic uncertainties

The full list of considered systematic uncertainties is given in table 8.3. The uncertainties are separated by rate-changing and shape-changing uncertainties. Rate-changing uncertainties only have an effect on the yields of an event samples in one or more event categories. For example, the theoretical uncertainty on the $\mathrm{t\bar{t}}$ cross section only affects simulated $\mathrm{t\bar{t}}$ events, and uncertainties on the muon efficiencies only affect simulated samples from the muon-plus-jets selection. The horizontal lines loosely subdivide the rate-changing uncertainties into theoretical or modelling uncertainties and experimental uncertainties.

Shape-changing uncertainties have an effect both on the rate and the shape of a given distribution. Each listed source of uncertainty will be represented by an individual uncorrelated parameter in the statistical evaluation that is described in the following.

8.2 Statistical evaluation

In this section, the statistical methods for the statistical interpretation of the results will be explained, most importantly the derivation of upper limits on the production cross section for new particles. To derive upper limits on the production cross section, methods are deployed that are based on two different statistical paradigms, Bayesian and frequentist inference, or a combination of the two [136]. In the frequentist interpretation of probability, the probability of an event is its relative frequency of occurrence in repeated experiments. Bayesian inference does not require the possibility to perform repeated experiments, but needs subjective input in the form of a prior probability for a certain hypothesis to be true, where probability can be interpreted as degree of belief that is updated when performing an experiment, yielding a posterior probability for the hypothesis to be true. For practical purposes in high energy physics, the results from methods based on either paradigm however tend to give compatible results.

The main method to derive upper limits on the production cross section for new particles in this analysis is a variant of the so-called $\mathrm{CL_S}$ method, which is based on frequentist inference.

Table 8.3: List of systematic uncertainties.

Source of uncertainty	Variation
Rate-changing uncertainties	
$\mathrm{t\bar{t}}$ cross section	15%
Single top cross section	30%
W-plus-jets yield	50%
Ratio Z/W yield	30%
Fraction W/Z+b+X	100%
Fraction W/Z+c+X	100%
Multijet yield (electron)	43–63%
Multijet yield (muon)	52–73%
Integrated luminosity	2.2%
Electron efficiency	3%
Muon efficiency	3%
Shape-changing uncertainties	
$\mathrm{t\bar{t}}$ NLO generator	POWHEG
$\mathrm{t\bar{t}}$ Q^2 scale	Generator settings
$\mathrm{t\bar{t}}$ matching scale	Generator settings
W+jets Q^2 scale	Generator settings
Jet energy scale	Dependent on jet p_T, η
Jet energy resolution	6–20% per jet (dependent on jet η)
b-tag efficiency b jets ($p_\mathrm{T} < 670$ GeV)	1.6–8% (dependent on jet p_T, η)
b-tag efficiency b jets ($p_\mathrm{T} > 670$ GeV)	Twice uncertainty for $p_\mathrm{T} = 670$ GeV
b-tag efficiency c jets ($p_\mathrm{T} < 670$ GeV)	Twice uncertainty for b jets
b-tag efficiency c jets ($p_\mathrm{T} > 670$ GeV)	Twice uncertainty for $p_\mathrm{T} = 670$ GeV
b-tag efficiency for light-flavoured jets	$\sim 10\%$ (dependent on jet p_T, η)
Limited number of simulated events	Sample-dependent

The treatment of systematic uncertainties is however based on Bayesian statistics. Therefore, the method is called a *Bayesian-frequentist hybrid*. As a cross-check, limits will also be derived with a Bayesian technique. Therefore, both techniques will briefly be introduced in the following. Before that, the likelihood function is constructed that serves as the basis for both techniques of statistical inference.

8.2.1 Construction of the likelihood function

In this section, the likelihood function $\mathcal{L}(\mathrm{data}|\mu, \boldsymbol{\theta})$ is constructed step by step. The parameter of interest in this search is the production cross section for a new particle. As usual in statistical analysis, the implementation makes use of a *signal strength modifier* μ that is proportional to the production cross section for the new particle, in other terms a multiplication factor to a given cross section value σ_0, $\sigma_{Z'} = \mu \cdot \sigma_0$. The default cross section is taken to be $\sigma_0 = 1$ pb, a typical value for the expected upper limits. The effect of systematic uncertainties is encoded

with the help of nuisance parameters that are given by the vector $\boldsymbol{\theta}$. A nuisance parameter is any parameter of the physical model or the likelihood that is not a parameter of interest.

Given the observed data, the likelihood $\mathcal{L}(\mathrm{data}|\mu, \boldsymbol{\theta})$ expresses how likely a set of parameters is, with the set of parameters being the signal strength μ and the nuisance parameters $\boldsymbol{\theta}$. The definition of the likelihood is essential for the statistical methods for limit-setting and interval estimation that are introduced below.

The expected distributions of the observable $m_{\mathrm{t\bar{t}}}$ for a given process in a given event category are modelled by the expected number of events per bin n. In other words, the statistical model is based on the histograms that represent the $m_{\mathrm{t\bar{t}}}$ distributions for the different signal and background processes in the 8 different event categories. The individual signal $s_{i,k}$ and background $b_{i,k}$ expectations in a bin i and event category k are given by

$$s_{i,k}(\boldsymbol{\theta}^r, \boldsymbol{\theta}^s) = \rho_k^{\mathrm{signal}}(\boldsymbol{\theta}^r) \cdot \mathrm{n}_k^{\mathrm{signal}}(i, \boldsymbol{\theta^s}), \tag{8.1}$$

$$b_{i,k}(\boldsymbol{\theta}^r, \boldsymbol{\theta}^s) = \sum_j \rho_k^{\mathrm{background}\ j}(\boldsymbol{\theta}^r) \cdot \mathrm{n}_k^{\mathrm{background}\ j}(i, \boldsymbol{\theta}^s), \tag{8.2}$$

with the vector of *flat (or rate-changing) nuisance parameters* $\boldsymbol{\theta}^r$ and the vector of *shape-varying nuisance parameters* $\boldsymbol{\theta}^s$. ρ_k denotes a multiplicative factor that simultaneously changes the yield for all bins in a given category k. The signal-plus-background expectation in a given bin i is then the sum of the signal and background expectations $\mu s_i + b_i$.

Flat nuisance parameters do not depend on the bin i and hence only have an effect on the overall yield for a certain background in a certain event category. While a flat nuisance parameter does not change the shape of the contribution from an individual background sample, it generally does change the shape of the combined background or signal-plus-background expectation.

As prior for the rate-changing nuisance parameters, a normal distribution is used with mean 1 and the width corresponding to the relative uncertainty that is given by the associated systematic uncertainty. The normal distribution is restricted to non-negative values. If the relative uncertainty becomes large and the normal distribution would be truncated at zero, a log-normal distribution is used instead. The parameters of the log-normal distribution are chosen such that the median of the log-normal distribution corresponds to the mean of the normal distribution and such that the variance is roughly equivalent to that of the normal distribution. Compared to the normal distribution, the log-normal distribution is skewed, and its mean is shifted to higher values, whereas the most probable value is shifted to lower values. These differences need to be taken into account when interpreting the results of parameter fits.

Shape-varying nuisance parameters affect the expectation for the number of events n in each individual bin i for each signal or background sample j by adding the sum $\Delta_l^{\mathrm{background}\ j}$ of the expected differences for all nuisance parameters l,

$$n^{\mathrm{background}\ j}(i, \boldsymbol{\theta}^s) = n_{\mathrm{nominal}}^{\mathrm{background}\ j}(i) + \sum_l \left(\Delta_l^{\mathrm{background}\ j}(i, \theta_l^s) \right), \tag{8.3}$$

with $n_{\text{nominal}}^{\text{background } j}(i)$ denoting the nominal expectation for the number of events in a bin. Shape-changing nuisance parameters generally also have an effect on the overall event yield that is given by the sum of the nominal yield and the changes in a certain category.

Technically, the effect of a shape-changing systematic uncertainty is calculated from repeating the whole analysis with varied settings corresponding to $\pm 1\sigma$ variations of the systematic uncertainty under consideration, yielding modified predictions for the number of events in each bin. However, all statistical methods described below require predictions that are a continuous function of each nuisance parameter, which is accomplished by interpolating between the provided values at $\pm 1\sigma$ in each individual bin and by extrapolating beyond. The combined procedure is also called *template morphing*. Several calculation techniques for limit-setting and significance estimation involve differentiation. Therefore, all binned templates also have to be fully differentiable functions of each nuisance parameter θ_l.

A so-called *cubic interpolation* method is used that deploys a polynomial of third degree to interpolate between the three points at the nominal value $\theta_l = 0$ and the values corresponding to $\pm 1\sigma$ variations of the systematic uncertainty under consideration, $\theta_l = \pm 1$. Beyond $\pm 1\sigma$, the extrapolation is performed with a linear function, i.e. a first degree polynomial. The cubic interpolation between three input values is carried out separately for each individual bin, background process, and systematic uncertainty. In a given bin, the value is a function of the nuisance parameter θ_l and the histogram values n_0, n_+ and n_- (nominal histogram value and histogram values at $\pm 1\sigma$). The interpolated number of events is

$$n(\theta_l) = n_0 \pm \frac{1}{2}(2n_0 - n_+ - n_-)\theta_l^3 + (n_+ + n_- - 2n_0)\theta_l^2 + \frac{1}{2}(n_+ - n_-)\theta_l \tag{8.4}$$

for $|\theta_l| < 1$ and $\theta_l \gtrless 0$. By construction, the numbers of events for the input settings are given by $n(0) = n_0$, $n(1) = n_+$, and $n(-1) = n_-$. The indices for the bin i, the background sample j and the event category k are omitted. If the interpolation or extrapolation yields a negative expected number of events, $n(\theta_l)$ is set to zero.

The prior for the nuisance parameter θ_l follows a normal function with mean 0 and width 1 according to the interpretation of the $\pm 1\sigma$ uncertainties in terms of Gaussian standard deviations. An additional interpolation method is used for cross checks; it deploys a quadratic function to interpolate between the three given values. The three free parameters are fully defined by the central and $\pm 1\sigma$ values. Beyond $\pm 1\sigma$, a linear extrapolation is performed that is defined by the slope at the $\pm 1\sigma$ points.

Figure 8.3 visualises the effect of the two different morphing algorithms and compares them with a simple linear interpolation that produces a kink at the nominal value n_0. The chosen rate changes are larger than in the typical use case to emphasise the differences between the algorithms. The quadratic and cubic interpolation algorithms yield similar results for the interpolation region, i.e. for changes below one standard deviation. The differences are more pronounced in the extrapolation region, i.e. beyond one standard deviation. As the quadratic interpolation tends to amplify statistical fluctuations, the cubic interpolation is chosen as the baseline method.

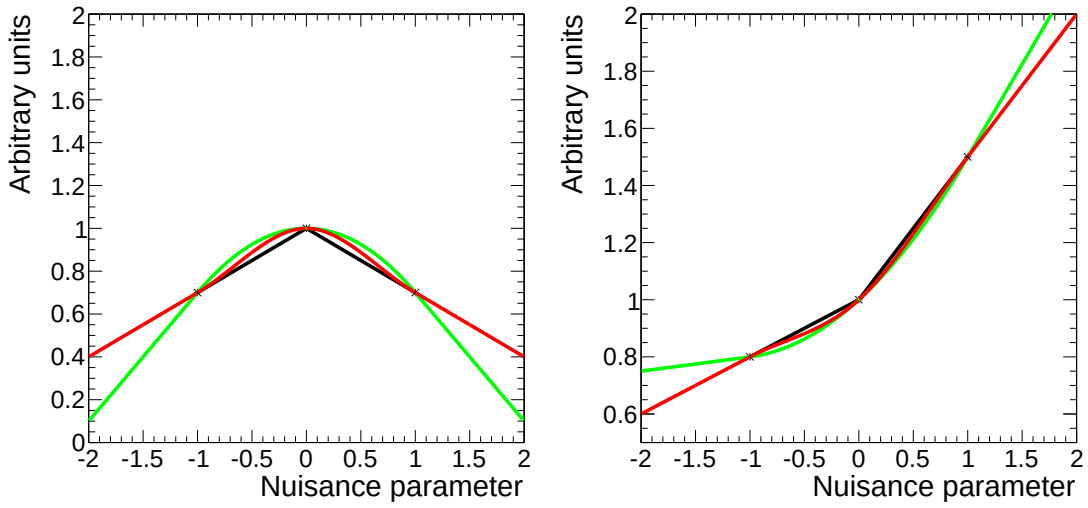

Figure 8.3: Prediction in a given bin as a function of a nuisance parameter for different interpolation algorithms with two numerical examples: $n_0 = 1$, $n_- = -0.7$, and $n_+ = 0.7$ (left); $n_0 = 1$, $n_- = -0.8$, and $n_+ = 1.5$ (right). The grey line shows a linear interpolation with a kink at n_0, the red line the cubic interpolation, and the green line the quadratic interpolation. The latter two algorithms are described in the text.

A second variant of template morphing is used for the modelling of signal templates for intermediate Z′ masses to fill up the region between the Z′ samples that are generated with a certain number of discrete Z′ mass values. For this, `RooMomentMorph` (from the `RooFit` package [140]) is used to create signal shapes for all Z′ masses between 0.5 TeV and 2 TeV that are used for the statistical evaluation. To check that the method yields correct shapes apart from visual inspection, the algorithm has been used to create a signal template for a mass of 1 TeV with the samples generated at 0.75 TeV and 1.25 TeV. The resulting shape is compatible within statistical uncertainties.

With the inputs introduced up to this point, the joint likelihood can be constructed. For simplicity, the nuisance parameters are summarised by the single symbol $\boldsymbol{\theta}$ in the following, and there is no differentiation between bins and categories. The likelihood is defined as

$$\mathcal{L}(\text{data}|\mu, \boldsymbol{\theta}) = \text{Poisson}(\text{data}|\mu \cdot s(\boldsymbol{\theta}) + b(\boldsymbol{\theta})) \cdot \rho(\boldsymbol{\theta}|\tilde{\boldsymbol{\theta}}), \tag{8.5}$$

where "data" denotes either the observed experimental data or a set of pseudo-data and $\rho(\boldsymbol{\theta}|\tilde{\boldsymbol{\theta}})$ is the joint probability density function for the nuisance parameters θ. The background-only likelihood is equivalent to the signal-plus-background hypothesis with $\mu = 0$ and only depends on the nuisance parameters $\boldsymbol{\theta}$. The product of the Poisson probabilities in all bins is given by

$$\text{Poisson}(\text{data}|\mu, \theta) = \prod_i \frac{(\mu s_i + b_i)^{n_i}}{n_i!} e^{-\mu s_i - b_i}, \tag{8.6}$$

with the observed number of events in each bin n_i.

A special kind of systematic uncertainty arises from the limited number of simulated events, leading to an uncertainty per bin and per sample that is given by the Poisson error of the number of simulated events. The explicit inclusion of this uncertainty is however highly impractical due to the high number of resulting nuisance parameters. For this reason, the systematic uncertainties due to the limited number of events are evaluated by including the relevant uncertainty in the generation of pseudo-experiments that are used for the statistical techniques in the following, i.e. by including a Poisson uncertainty due to the limited number of simulated events for each bin and sample. The spread of the measured cross sections for the considered new particles, which is set to a number of cross section values close to the expected upper limits, is compared with the spread without the inclusion of the uncertainty. In addition, the effect on the resulting upper limits is tested for the background-only model. By considering the variation in the signal cross section and in the upper limits, this procedure tests for the influence of both the limited number of simulated events in the background event samples and the signal event samples. The relative variations of the observed signal cross sections are at most of the order of several per cent, i.e. the effect of the uncertainty due to the limited number of events is small. The uncertainty is hence implemented as an additional rate uncertainty on the signal cross section, with a value corresponding to the relative variations.

The development version of the THETA package also contains an implementation of a different technique for evaluating the systematic uncertainties due to the limited number of simulated events, the so-called Barlow-Beeston technique [141]. The technique introduces nuisance parameters for each bin and event sample. However, a maximum likelihood fit is still numerically possible because the minimisation factorises for each nuisance parameter. The implementation can be further simplified by only including the total Poisson uncertainty in each bin (and not separately for each sample), leading to a quadratic equation to solve for each parameter [142]. Results with this implementation are calculated for a few example signal models, showing that the influence of the uncertainty due to the limited number of simulated events is small and that the taken approximation covers this uncertainty.

8.2.2 Prescription of the $\mathrm{CL_s}$ technique

A variant of the $\mathrm{CL_s}$ technique is used to derive 95% CL upper limits on the $\mathrm{Z'}$ cross section [143,144] . The definition of the test statistic follows a joint ATLAS-CMS recommendation and is the same as in the CMS Higgs combination [145]. However, systematic uncertainties are treated with a Bayesian-frequentist approach instead of a pure frequentist approach.

The test statistic q_μ is defined as the ratio of two likelihood functions

$$q_\mu \;=\; -2\ln\frac{\mathcal{L}(\,\mathrm{data}\,|\,\mu,\hat{\theta}_\mu\,)}{\mathcal{L}(\,\mathrm{data}\,|\,\hat{\mu},\hat{\theta}\,)},\ \text{where } 0\le\hat{\mu}\le\mu, \tag{8.7}$$

and depends on the given signal strength modifier μ. In the maximisation of the likelihood functions, the values of certain parameters are allowed to float within the constraints defined by the likelihood. The parameters that are allowed to float are indicated with a hat, e.g. $\hat{\mu}$. A likelihood fit in which all or certain parameter values are allowed to float in the maximisation

of the likelihood with given constraints is also called a *profile likelihood fit*. In the numerator, the signal strength μ is fixed, and only the nuisance parameters θ are fitted for the given μ. In the denominator, both the signal strength μ and the nuisance parameters θ are allowed to float, with the constraint that the signal strength may not exceed the signal strength μ for which the test statistic is evaluated.

Two tail probabilities are defined, the probability for the test statistic from the signal-plus-background model to be higher than the observed test statistic q_μ^{obs} for a given μ,

$$\mathrm{CL_{s+b}} = P\left(q_\mu \geq q_\mu^{obs} | \mu \cdot s + b\right), \tag{8.8}$$

and the probability for the test statistic from the background-only model to be higher than the observed test statistic,

$$\mathrm{CL_b} = P\left(q_\mu \geq q_\mu^{obs} | b\right). \tag{8.9}$$

For $\mu = 0$, the probability $\mathrm{CL_b}$ can be interpreted as a p-value to estimate the statistical significance of a possible data excess by relating the p-value to standard deviations using the one-sided tail integral of the normal distribution.

The distributions of the test statistic q_μ are generated by sampling from the priors for all nuisance parameters for either the signal-plus-background hypothesis or for the background-only hypothesis ($\mu = 0$). In addition, the entries in each bin are generated according to their Poisson probability given the expected number of events per bin. The test statistic is calculated for each such pseudo-experiment. The calculation is carried out at several values of μ between which is interpolated for the determination of the cross section limit.

The $\mathrm{CL_s}(\mu)$ value at a fixed signal strength μ is given by the ratio of two tail probabilities,

$$\mathrm{CL_s}(\mu) = \frac{\mathrm{CL_{s+b}}}{\mathrm{CL_b}}. \tag{8.10}$$

Upper limits on the production cross section for a new particle are derived by adjusting μ such that $\mathrm{CL_s} \leq \alpha$ to exclude a new particle with the given cross section at the $1-\alpha$ confidence level. For the 95% confidence level upper limits set in the following, μ is adjusted such that $\mathrm{CL_s}(\mu_{95\%CL}) = 0.05$. In the case of a fluctuation of the data towards a lower number of observed events than expected, the $\mathrm{CL_s}$ prescription avoids a too stringent limit on the production cross section of a new particle to which the data is a priori not sensitive.

The implementation of the $\mathrm{CL_s}$ technique is also done with the THETA package. As discussed, the definition of the likelihood ratio test statistic requires a minimisation. Due to the considerable number of systematic uncertainties, the minimisation needs to be carried out with a chain of numerical minimisation algorithms to yield numerically robust results. If one minimisation algorithm fails, a different algorithm is run that is numerically more robust, but takes more computing time. Since numerical techniques such as Markov chain Monte Carlos are also used in the minimisation that only yield point estimates with limited precision, a standard fit using the MINUIT minimiser is performed after a successful previous minimisation with one of the other minimisation algorithms.

8.2.3 Bayesian evaluation

Bayes' theorem connects the conditional probability $p(A|B)$ of A given B with the reverse conditional probability of B given A,

$$p(A|B) = \frac{p(B|A)p(A)}{p(B)}. \tag{8.11}$$

In the context of a search for new physics with a signal strength μ, the equation can be re-written to yield the conditional probability $p(\mu|\mathrm{data})$ of μ given the data,

$$p(\mu|\mathrm{data}) = \frac{p(\mathrm{data}|\mu)\pi(\mu)}{p(\mathrm{data})}. \tag{8.12}$$

$p(\mu|\mathrm{data})$ is called the *posterior probability* of the signal strength μ. Bayes' theorem connects this posterior probability with the conditional probability $p(\mathrm{data}|\mu)$ of obtaining the data given a signal strength μ, which is given by the likelihood function from equation 8.5 without nuisance parameters $\boldsymbol{\theta}$.

As opposed to statistical inference based on frequentist methods like the $\mathrm{CL_S}$ technique discussed above, an additional term $p(\mu)$ is introduced that is the *prior probability* of the signal strength μ.

The assignment of a prior probability can be based on prior knowledge or on a degree of belief, and it therefore generally introduces a certain degree of subjectiveness. In a physics analysis, the prior probability is supposed to be uninformative or objective, i.e. it should only contain objective information such that the cross section for the production of a new particle may not be negative. Here, a uniform distribution is used for the prior probability with the constraint $\mu \geq 0$ [131]. A uniform prior is not necessarily objective as e.g. the prior becomes non-uniform if not the cross section is measured but a related quantity that implies a different metric. For this analysis, dedicated coverage tests have been performed, showing that the choice of a uniform prior guarantees exact coverage (or over-coverage for small signal cross sections) for setting upper limits on the signal cross section for a new particle.

The probability $p(\mathrm{data})$ of obtaining the data is constant and only necessary to normalise the total probability to unity. It is therefore often neglected, and the posterior probability is simply proportional to the numerator from equation 8.12,

$$p(\mu|\mathrm{data}) \propto p(\mathrm{data}|\mu)\pi(\mu), \tag{8.13}$$

i.e. the posterior probability is proportional to the likelihood function multiplied with the prior probability.

Systematic uncertainties are introduced in the same way as above. In general, the probability $p(\mu|\mathrm{data})$ depends also on the nuisance parameters $\boldsymbol{\theta}$,

$$p(\mu, \boldsymbol{\theta}|\mathrm{data}) \propto p(\mathrm{data}|\boldsymbol{\theta}, \mu)\pi(\mu) = \mathcal{L}(\mathrm{data}|\mu, \boldsymbol{\theta})\pi(\mu), \tag{8.14}$$

with $p(\mathrm{data}|\boldsymbol{\theta}, \mu)$ given by the likelihood function defined above in equation 8.5, which includes the prior probabilities $\rho(\boldsymbol{\theta})$ for all nuisance parameters. To arrive at a posterior probability that only depends on the signal strength μ, the effect of the nuisance parameters is integrated out,

$$p(\mu|\mathrm{data}) = \frac{1}{C} \int_{\boldsymbol{\theta}} p\left(\mathrm{data}|\mu s(\boldsymbol{\theta}) + b(\boldsymbol{\theta})\right) \rho(\boldsymbol{\theta}) \pi(\mu) \mathrm{d}\boldsymbol{\theta}. \tag{8.15}$$

C denotes a normalisation constant that is obtained by requiring that the integral of the posterior probability density is 1.

The procedure of treating systematic uncertainties by integrating over the nuisance parameters is called *marginalisation*. Similar to the profiling of systematic uncertainties discussed above, the marginalisation exploits the full information about the effects of the nuisance parameters that is encoded in the likelihood function. Thereby, it reduces the influence of individual systematic uncertainties by letting the data constrain their values.

To derive an upper limit on the signal strength μ, the posterior probability $p(\mu|\mathrm{data})$ for the signal strength μ is integrated up to the desired probability, which is 95% in this case,

$$\int_0^{\mu_{95\%CL}} p(\mu \,|\, \mathrm{data}) \; d\mu \;=\; 0.95, \tag{8.16}$$

yielding the upper limit $\mu_{95\%CL}$. As above, the upper limit on the signal strength can then be converted to upper limits on the production cross section of a new particle at 95% confidence level.

For a measurement of a production cross section within a central 1σ (68.3%) confidence level interval given by $(\mu_{\mathrm{lower}}, \mu_{\mathrm{upper}})$ in terms of the signal strength μ, the posterior probability density is integrated to yield the corresponding probabilities,

$$\int_0^{\mu_{\mathrm{lower}}} p(\mu \,|\, \mathrm{data}) \; d\mu \quad = \quad 0.159, \text{ and} \tag{8.17}$$

$$\int_0^{\mu_{\mathrm{upper}}} p(\mu \,|\, \mathrm{data}) \; d\mu \quad = \quad 0.841. \tag{8.18}$$

Similarly, the central value can be calculated by integrating to 50%, and the most probable value is given by the maximum of the posterior. Instead of integrating over all nuisance parameters $\boldsymbol{\theta}$, one can leave out one nuisance parameter and instead integrate over the signal strength μ and the remaining set of nuisance parameters $\tilde{\boldsymbol{\theta}}$,

$$p(\theta_1|\mathrm{data}) = \frac{1}{C} \int_{\tilde{\boldsymbol{\theta}}, \mu} p\left(\mathrm{data}|\mu s(\boldsymbol{\theta}) + b(\boldsymbol{\theta})\right) \rho(\boldsymbol{\theta}) \pi(\mu) \mathrm{d}\tilde{\boldsymbol{\theta}} \mathrm{d}\mu, \tag{8.19}$$

yielding the posterior probability $p(\theta_1|\mathrm{data})$ for the nuisance parameter θ_1. This posterior can be compared to the prior probability to study the impact the likelihood has on the knowledge of the nuisance parameter, e.g. by deriving central 68% confidence levels for the nuisance parameter. This is often done for the background-only model, i.e. for a fixed signal strength of zero, $\mu = 0$, to investigate the compatibility of the background-only model and the data.

8.3 Measurement of $m_{\mathrm{t\bar{t}}}$ distributions

In the following, the measurement of the $m_{\mathrm{t\bar{t}}}$ distributions is discussed. First, the $m_{\mathrm{t\bar{t}}}$ distributions in data and simulated events are compared. Here, the measurement of the $m_{\mathrm{t\bar{t}}}$ distributions implies the comparison of data and simulation, including statistical compatibility tests; the measured data are not unfolded to the particle level. Then, a background-only fit to data is performed to test the compatibility of the background model, i.e. the SM predictions, with the observed $m_{\mathrm{t\bar{t}}}$ distributions. Finally, a measurement of the $\mathrm{t\bar{t}}$ cross section is performed to further validate the modelling of the most important background process.

8.3.1 Distributions of $m_{\mathrm{t\bar{t}}}$ after event selection and reconstruction

In the previous chapter, the comparison of a number of kinematic distributions is shown between data and simulated events. Now, the reconstructed $\mathrm{t\bar{t}}$ distributions are discussed that are input to the statistical evaluation. In all cases, the expected $m_{\mathrm{t\bar{t}}}$ distributions derived with simulated events are produced at the nominal values of all uncertainty parameters, i.e. only prior information is taken into account.

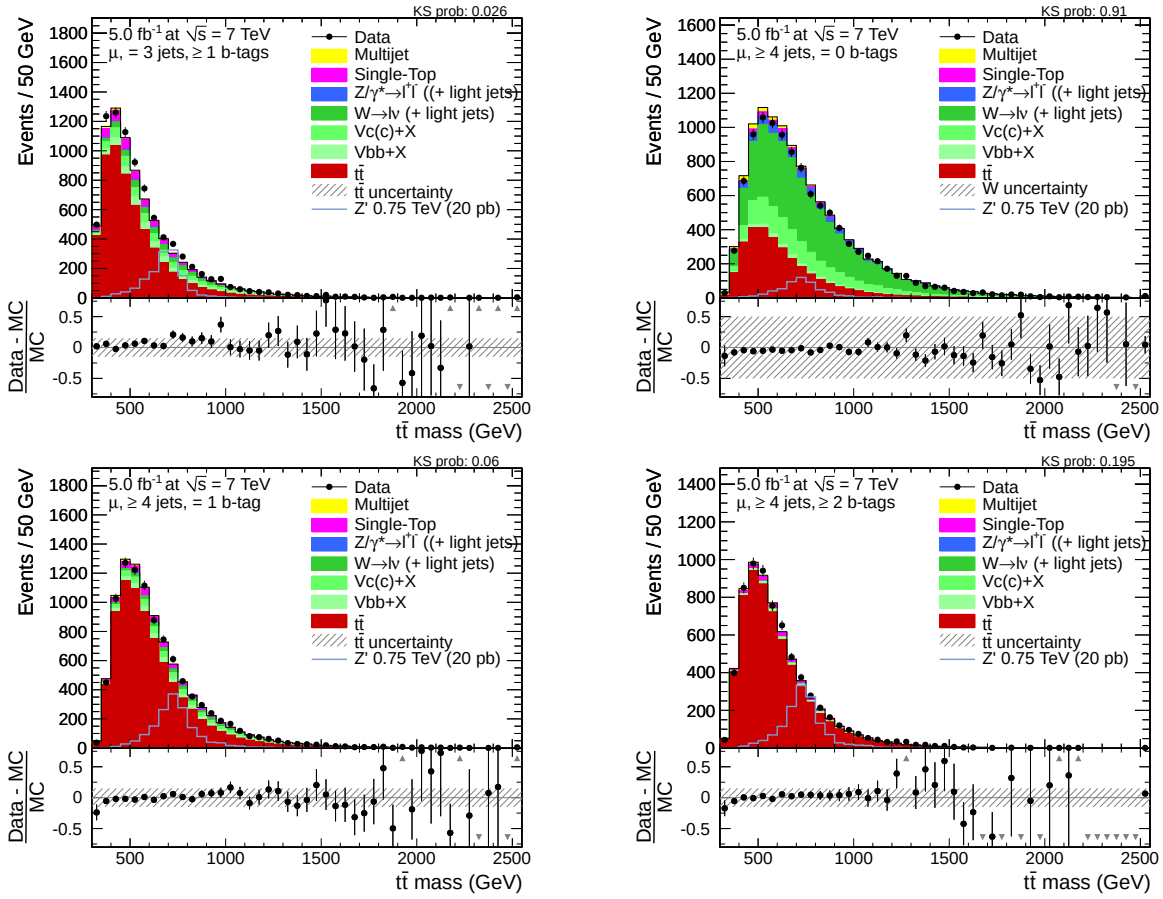

Figure 8.4: Distribution of the invariant mass of the reconstructed $\mathrm{t\bar{t}}$ system for muon-plus-jets events with 3 jets and at least one b-tag (top left) and at least 4 jets and either 0 b-tags (top right), 1 b-tag (bottom left), or at least two b-tags (bottom right).

Figure 8.4 shows the reconstructed $m_{t\bar{t}}$ distributions in the muon channel for the four event categories used in the statistical evaluation, events with 3 jets and at least one b-tagged jet and events with at least four jets and either no b-tagged jet, one b-tagged jet, or at least two b-tagged jets. The invariant $t\bar{t}$ mass is reconstructed with the χ^2-based algorithm for jet-parton association in events with at least 4 jets and with the top mass criterion in events with 3 jets. In general, there is good agreement between data and simulation, though there are a few trends discussed in the following. For events with 3 jets and at least 1 b-tag, the region of $700 < m_{t\bar{t}} < 1000$ GeV exhibits a small trend towards a higher event yield in data compared to the prediction. Similarly, in events with 4 jets of which one is b-tagged, there is a very mild surplus of data events around $850 < m_{t\bar{t}} < 1100$ GeV. The $m_{t\bar{t}}$ distributions in data also tend to be slightly harder than in simulated events for events with 4 jets and either one or at least two b-tags. In the region dominated by W-plus-jets events, i.e. events with 4 jets of which none is b-tagged, the agreement of the $m_{t\bar{t}}$ distributions in data and simulated events is excellent.

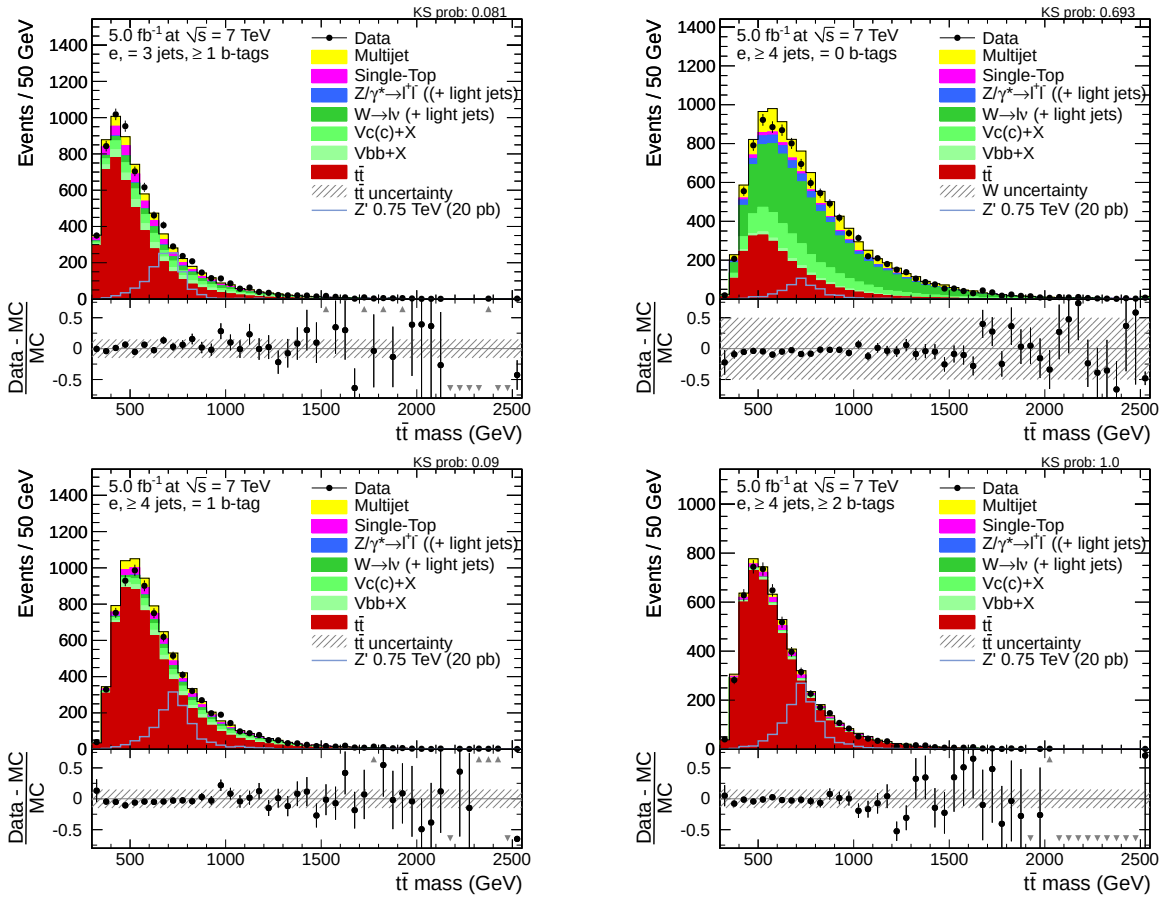

Figure 8.5: Distribution of the invariant mass of the reconstructed $t\bar{t}$ system for electron-plus-jets events with 3 jets and at least one b-tag (top left) and at least 4 jets and either 0 b-tags (top right), 1 b-tag (bottom left), or at least two b-tags (bottom right).

For the electron channel, the reconstructed $m_{t\bar{t}}$ distributions are shown in figure 8.5. The general agreement of data and the prediction is again good, with a few notable points discussed in the following. Up to the region of 1 TeV, the $m_{t\bar{t}}$ distribution in data events tends to be a bit harder than in the simulation both for events with 3 jets of which at least one is b-tagged

and for events with 4 jets of which one is b-tagged. There is no visible difference between the general shapes of the $m_{\mathrm{t\bar{t}}}$ distribution in data and simulation for the other two event categories. For events with 4 jets and either one or at least two b-tagged jets, there tend to be more data than simulated events in the region around 1 TeV and just below 1 TeV, respectively, when compared to the remainder of the distribution. This difference is however very small.

The predicted and observed event yields in the 8 categories used for the statistical evaluation have been compared above and are hence only very briefly discussed again at this point. There are mild differences between the event yields in data and simulation, which are especially present for events with 3 jets of which at least one is b-tagged with a surplus of data at the level of several per cent. These differences have been explained to be well covered by the systematic uncertainties, but should be taken into account in the interpretation of the following parameter fits to the data.

8.3.2 Comparison with background-only model

The simulated and observed $m_{\mathrm{t\bar{t}}}$ distributions and their uncertainties, as implemented in the statistical model introduced in the previous section, are used to perform a maximum likelihood fit of the background-only model to the data. The background-only likelihood is given by equation 8.5 with the signal strength parameter μ fixed to zero. In the maximum likelihood fit, the values of the nuisance parameters that represent the systematic uncertainties are allowed to float, i.e. the fit is a profile likelihood fit. The maximum likelihood fit hence yields point estimates of the central values of all parameters of the statistical model. Furthermore, the diagonal values of the covariance matrix of the fit equal the variance (or width) for each individual parameter, which is a good approximation of the central 68% confidence level interval for each parameter.

The results of the background-only fit are shown in table 8.4; listed are the fitted central values and the widths of all nuisance parameters as well as the deviation of the fitted value with respect to the input value and uncertainty, expressed in terms of Gaussian standard deviations. All fitted parameters are within one standard deviation of the input value, showing that there is good agreement between the default background-only model and the data.

By comparing the fitted width with the prior width (see table 8.3), one can determine to which extent each nuisance parameter is constrained by the data. For example, the width of the $\mathrm{t\bar{t}}$ cross section is reduced from 15% to $\sim 5\%$. Similarly, the widths of the W-plus-jets yield parameters both for events with 3 jets and at least 4 jets are reduced from 50% to 16% and 10%, respectively. The small fitted widths shows that the approach of using a relatively loose prior width for the W-plus-jets parameters is well justified. Along the same lines, the fitted widths of the W+b+X parameter (40%) and the W+c+X parameter (42%) are significantly smaller than the input widths of 100%. The widths of the parameters reflecting the yields of the other background processes change only marginally in the fit procedure.

Several shape-changing nuisance parameters are also constrained by the data. For example, the width of the b-tag parameter is reduced by more than a factor of two. This can be explained by the categorisation according to the number of b-tags by which the different shapes of the distribution of the number of b-tagged jets for variations of the b-tag uncertainty in $\mathrm{t\bar{t}}$ events lead to

Table 8.4: Fitted value of the nuisance parameter, the corresponding width after the fit, and the difference of the fitted value to the corresponding nominal value and width in terms of Gaussian standard deviations.

Uncertainty	**Fitted value**	**Fitted width**	**Deviation (σ)**
Luminosity	1.00	0.02	0.0
Muon efficiency	1.00	0.03	0.0
Electron efficiency	1.00	0.03	0.0
Single top yield	1.08	0.27	0.3
$\mathrm{t\bar{t}}$ cross section	0.98	0.05	-0.1
W+jets yield	0.87	0.10	-0.3
W+3-jets yield	0.99	0.16	0.0
W+c+X yield	1.13	0.42	0.1
W+b+X yield	1.26	0.40	0.3
Z+jets yield	0.98	0.27	-0.1
Muon multijet yield (3j1t)	0.98	0.58	0.0
Muon multijet yield (4j0t)	0.85	0.43	-0.3
Muon multijet yield (4j1t)	1.04	0.85	0.1
Muon multijet yield (4j2t):	0.74	0.46	0.4
Electron multijet yield (3j1t)	0.89	0.23	-0.3
Electron multijet yield (4j0t)	0.96	0.13	-0.1
Electron multijet yield (4j1t)	0.74	0.22	-0.5
Electron multijet yield (4j2t)	0.57	0.27	-0.7
Jet energy scale	0.47	0.60	0.5
Jet energy resolution	0.98	0.88	1.0
b-tag (b and c jets)	0.38	0.37	0.4
b-tag (light-flavoured jets)	0.55	0.67	0.6
Pile-up simulation	0.20	0.80	0.2
Matching threshold ($\mathrm{t\bar{t}}$)	-0.06	0.13	-0.1
Renormalisation/factorisation scale ($\mathrm{t\bar{t}}$)	0.12	0.13	0.1
NLO generator ($\mathrm{t\bar{t}}$)	0.35	0.21	0.4
Renormalisation/factorisation scale (W+jets)	0.04	0.10	0.0

a preferred parameter value when compared with the data. The other experimental uncertainties are only mildly constrained. All theoretical uncertainties, i.e. the three uncertainties affecting the $\mathrm{t\bar{t}}$ distributions and the variations of the renormalisation/factorisation scales for W-plus-jets production, are subject to relatively large constraints. This can be explained by the considerable effects they have on the $m_{\mathrm{t\bar{t}}}$ shapes and yields that are discussed above.

Instead of performing a maximum likelihood fit, one can also perform a Bayesian integration for each nuisance parameter to derive the posterior probability distribution for the parameter. The central values and the central 68% confidence level band for each nuisance parameter can then be obtained from the relevant quantiles, see equation 8.17. The such obtained central values and widths agree within the precision of the statistical methods, e.g. the limited number

of steps in the Markov chain used for the evaluation of the posterior probability in the case of the Bayesian integration, with the ones from the maximum likelihood fit.

The fitted values of the nuisance parameters are now used to modify the $m_{\mathrm{t\bar{t}}}$ distributions from simulated events such that they correspond to the $m_{\mathrm{t\bar{t}}}$ distributions that represent the fit result. For this, the $m_{\mathrm{t\bar{t}}}$ distributions are scaled in the exact same way as in the statistical modelling described above, i.e. the parameters representing rate-changing uncertainties affect the yields of the $m_{\mathrm{t\bar{t}}}$ distributions for individual samples and the shape-changing systematic uncertainties also affect the shapes of the individual $m_{\mathrm{t\bar{t}}}$ distributions by means of template morphing.

Figure 8.6 shows the scaled $m_{\mathrm{t\bar{t}}}$ distributions in the four event categories in the muon-plus-jets channel. After the fit, there is very good agreement between data and simulation, i.e. only statistical fluctuations are visible. The compatibility of data and simulation in the four distributions is probed by two statistical tests, a Kolmogorov-Smirnov test as introduced above and a standard χ^2 test. Whereas the KS test is only sensitive to shape differences, the χ^2 test also probes rate differences and hence provides additional and complimentary information. For both tests, the probability to obtain the test result or a lower value is given with the plot, taking only statistical variations into account. For statistically compatible samples and a sufficient number of observed events, the probabilities are expected to be distributed according to a flat distribution between 0 and 1, with a tendency for slightly higher values in the case of the KS test for binned distributions as explained above.

The observed χ^2 test probability in events with three jets and at least one b-tag is 77%, and the three probabilities in events with four jets range from 89–99%, showing high compatibility of the simulated and observed $m_{\mathrm{t\bar{t}}}$ distributions. The same conclusion can be drawn from the KS test probabilities, with a value of 84% in the three-jet category and values close to 1 in the three four-jet categories.

The data and the scaled simulated $m_{\mathrm{t\bar{t}}}$ distributions in the four event categories in the electron channel are shown in figure 8.7. Like in the muon channel, there is good agreement between the data and the simulated distributions in all event categories, and only statistical fluctuations can be identified. The observed χ^2 test probabilities show that the $m_{\mathrm{t\bar{t}}}$ distributions from data and the prediction are compatible, with the average probability being higher than 0.5 when considering all four event categories. The KS tests yield probabilities close to 1 for events with 3 jets of which at least one is b-tagged and events with four jets of which either none or one is b-tagged. For events with 4 jets and at least 2 b-tags, the probability is of the order of 40%. Taken together, both tests show that there is good agreement between the scaled $m_{\mathrm{t\bar{t}}}$ distributions from the simulation and the data.

Figure 8.8 shows the observed and scaled simulated $m_{\mathrm{t\bar{t}}}$ distributions in the muon channel with semi-logarithmic scale. This allows to visually inspect the region of high $m_{\mathrm{t\bar{t}}}$ values for deviations of data and the prediction, which may be unnoticed in the statistical tests due to the lower number of events in the tail region. The agreement of data and the simulation is however also excellent in the high $m_{\mathrm{t\bar{t}}}$ region for all four event categories.

The $m_{\mathrm{t\bar{t}}}$ distributions in the electron channel with semi-logarithmic scale are shown in figure 8.9 for the four considered event categories and with the predicted distributions scaled to

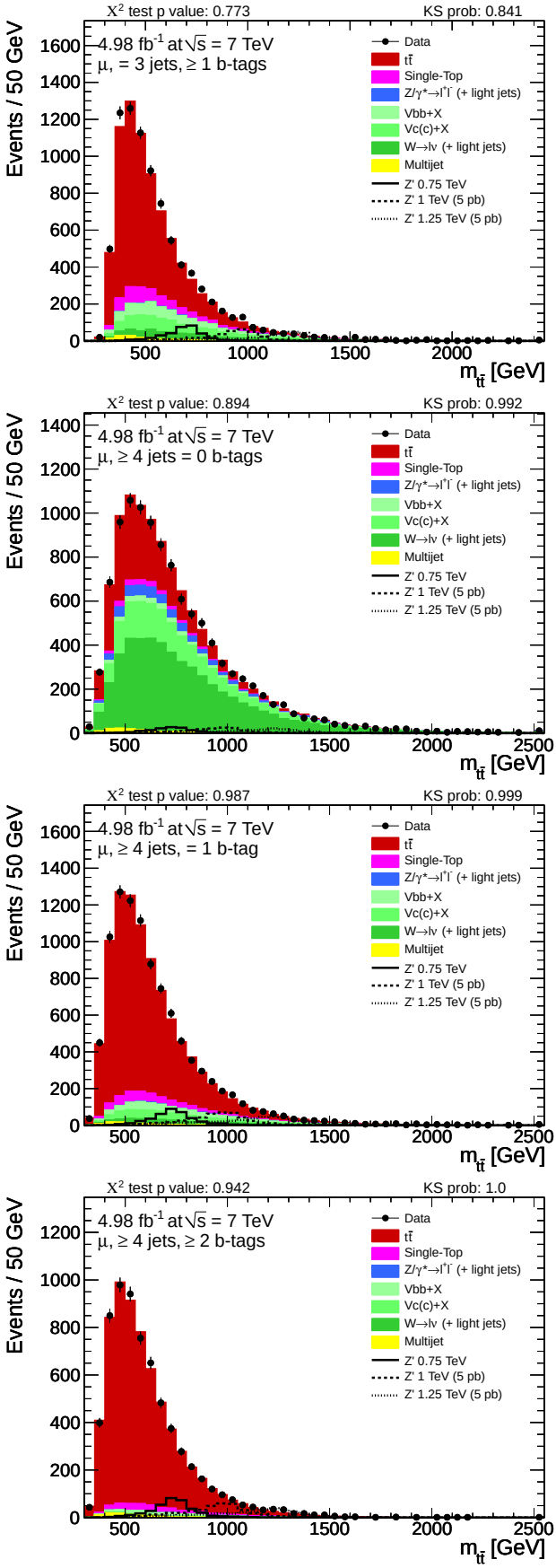

Figure 8.6: Distribution of the invariant mass of the reconstructed $\mathrm{t\bar{t}}$ system for muon-plus-jets events with 3 jets and at least one b-tag (top) and at least 4 jets and either 0 b-tags (middle top), 1 b-tag (middle bottom), or at least two b-tags (bottom), with all nuisance parameters set to the outcome of a background-only fit to data.

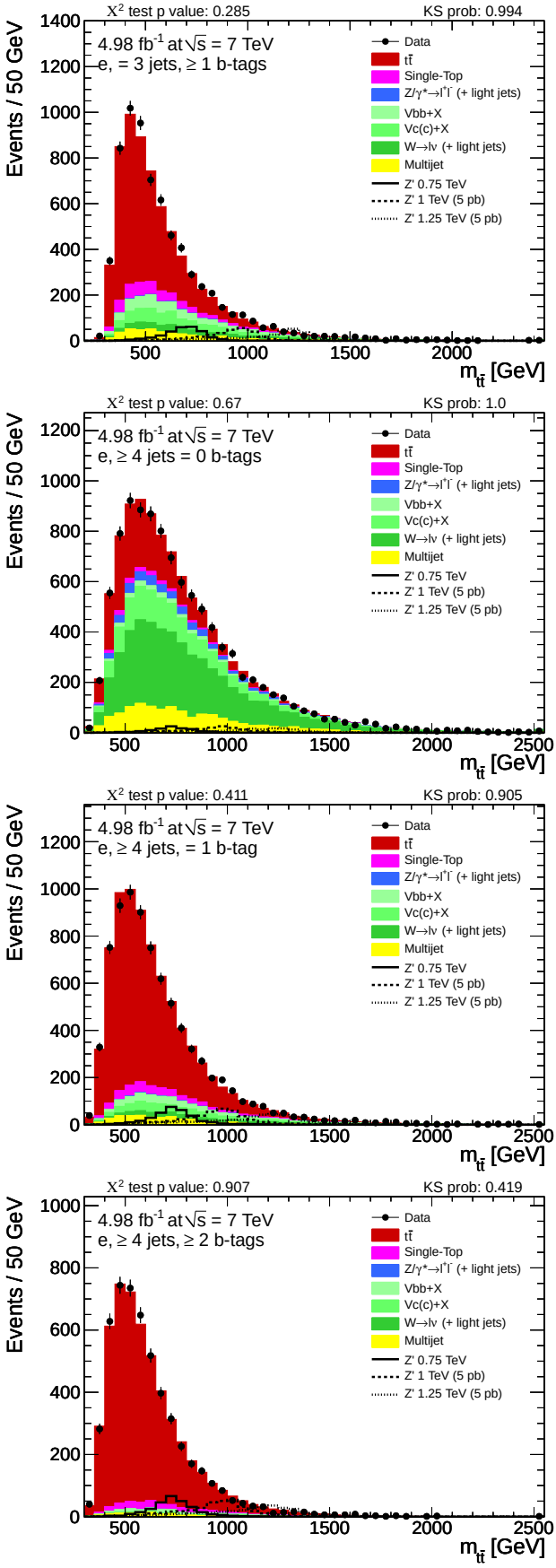

Figure 8.7: Distribution of the invariant mass of the reconstructed $\mathrm{t\bar{t}}$ system for electron-plus-jets events with 3 jets and at least one b-tag (top) and at least 4 jets and either 0 b-tags (middle top), 1 b-tag (middle bottom), or at least two b-tags (bottom), with all nuisance parameters set to the outcome of a background-only fit to data.

the results from the background-only fit. Like in the muon channel, there is also no notable difference between data and simulation in the region of high reconstructed $m_{\mathrm{t\bar{t}}}$.

In summary, the background-only model has been compared to the data in a two-step procedure. First, a background-only fit to the data is performed. The fitted values of all nuisance parameters are compatible with the expectation within one standard deviation, indicating that the default background-only model agrees well with the data and hence that the systematic uncertainties are well estimated. Second, the simulated $m_{\mathrm{t\bar{t}}}$ distributions are scaled to the outcome of the background-only fit and compared to the data. The predicted and observed $m_{\mathrm{t\bar{t}}}$ distributions agree well, which is confirmed by two statistical tests.

In line with the good agreement between data and simulation, there is no sign of an excess in the $m_{\mathrm{t\bar{t}}}$ spectra that would indicate the presence of a new particle. Below, the $m_{\mathrm{t\bar{t}}}$ distributions are used to set upper limits on the production cross section for new particles in a number of models for physics beyond the SM.

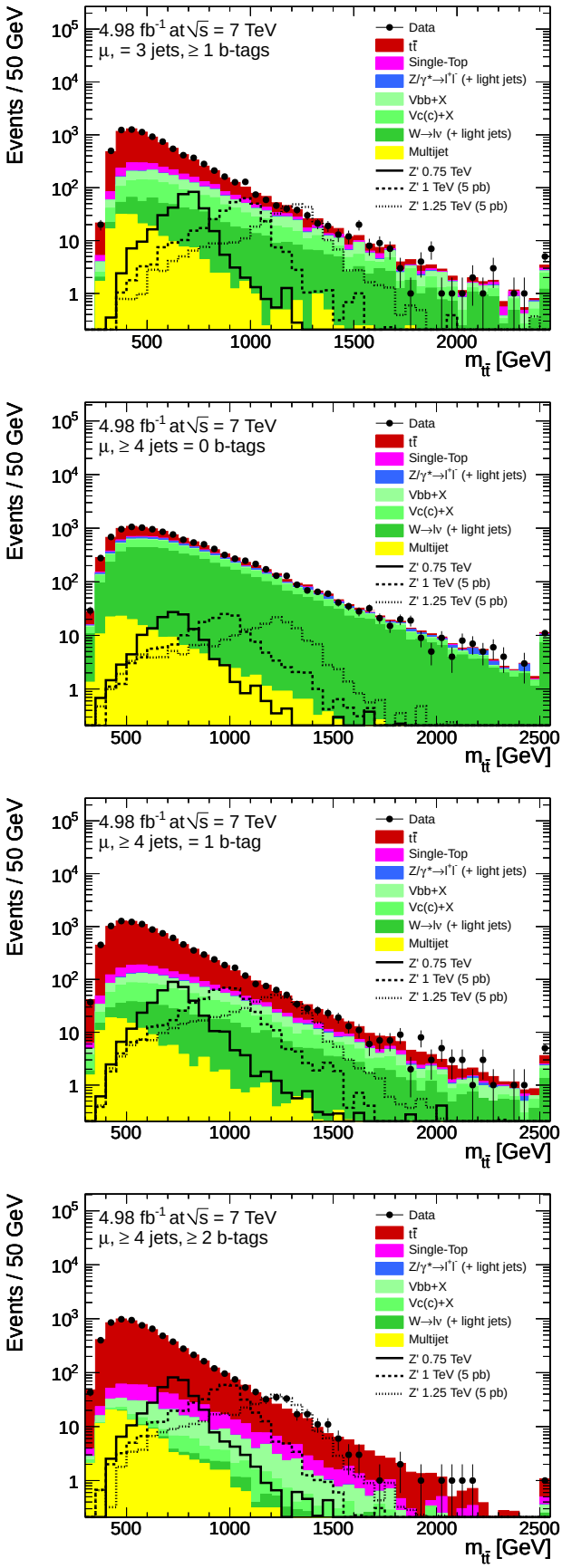

Figure 8.8: Distribution of the invariant mass of the reconstructed $\mathrm{t\bar{t}}$ system with semi-logarithmic scale for muon-plus-jets events with 3 jets and at least one b-tag (top) and at least 4 jets and either 0 b-tags (middle top), 1 b-tag (middle bottom), or at least two b-tags (bottom). The values of all nuisance parameters are set to the outcome of a background-only fit to data.

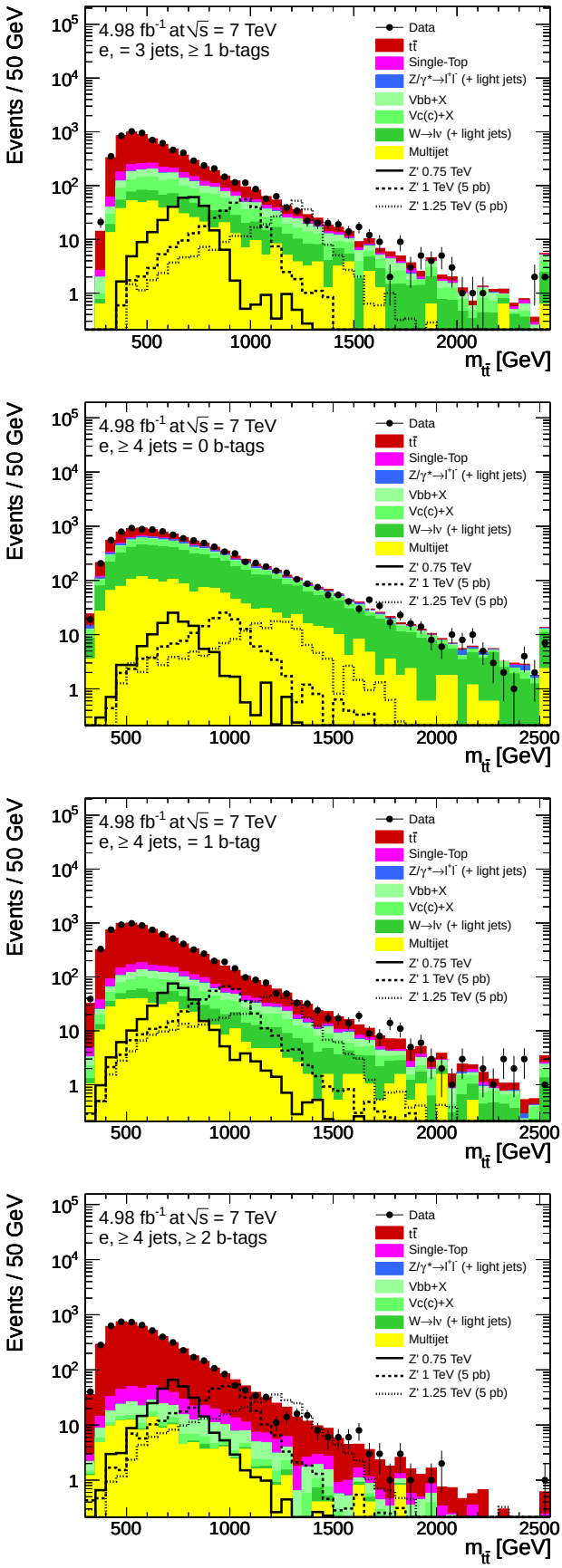

Figure 8.9: Distribution of the invariant mass of the reconstructed $t\bar{t}$ system with semi-logarithmic scale for electron-plus-jets events with 3 jets and at least one b-tag (top) and at least 4 jets and either 0 b-tags (middle top), 1 b-tag (middle bottom), or at least two b-tags (bottom). The values of all nuisance parameters are set to the outcome of a background-only fit to data.

8.3.3 Measurement of $\mathrm{t\bar{t}}$ production cross section

By using a flat prior probability instead of a normal distribution for the $\mathrm{t\bar{t}}$ production cross section, the statistical setup can be used to measure the production cross section for $\mathrm{t\bar{t}}$-plus-jets events. A Bayesian integration is performed according to equation 8.19, yielding the posterior probability density for the $\mathrm{t\bar{t}}$ cross section. From the posterior probability density, the measured $\mathrm{t\bar{t}}$ cross section and the values defining the central 68% confidence level are determined as

$$\sigma_{\mathrm{t\bar{t}}} = 154.3^{+8.3}_{-7.0}(\mathrm{stat} + \mathrm{syst} + \mathrm{lumi})\ \mathrm{pb}. \tag{8.20}$$

The central value and the uncertainties are compatible with the input cross section of 157.5 pb, which is calculated at NLO accuracy, and also with the calculations of the $\mathrm{t\bar{t}}$ production cross section at approximate NNLO accuracy given above. The high compatibility confirms the good description of the data by the background-only model. With a relative uncertainty of 5%, the measurement yields an uncertainty that is competitive with dedicated measurements of the inclusive $\mathrm{t\bar{t}}$ production cross section [113,146]. One should however take into account that minor acceptance uncertainties, e.g. the uncertainties due to parton distribution functions and due to the leptonic branching ratio of the W bosons from the top quark decay, would have to be considered for a dedicated measurement of the $\mathrm{t\bar{t}}$ production cross section.

8.4 Upper limits on production cross sections of new particles

Finally, upper limits are calculated on the production cross section for new particles. Three reference models are considered, a leptophobic topcolour Z' with a width of 1.2% of its mass, a leptophobic topcolour Z' with a width of 10% of its mass, and a specific Randall-Sundrum model implementation with a prediction for the first KK gluon, which has a typical width of 20% of its mass. The results from the search for a Z' with a width of 1.2% of its mass are derived from simulated event samples with a width of 1% of the Z' mass, but can be used to set model-independent upper limits on the production cross section for Z'-like resonances with a width that is small compared to the detector resolution, i.e. $\Gamma/m_{\mathrm{Z}'} \ll 10\%$. The upper limits on the production cross sections for the Z' model with higher width and for the KK gluon can also be used as good approximations for models that predict particles with similar widths, i.e. they can also be interpreted in a model-independent way.

8.4.1 Narrow-width Z'

Figure 8.10 shows the upper limits on the production cross section for a narrow-width Z' as a function of Z' mass. The expected and observed upper limits are derived with the previously introduced $\mathrm{CL_s}$ prescription. In addition to the median expected limits, the central $\pm 1\sigma$ and $\pm 2\sigma$ bands of the expected limits are shown. The expected upper limits range from $\sim$ 3 pb

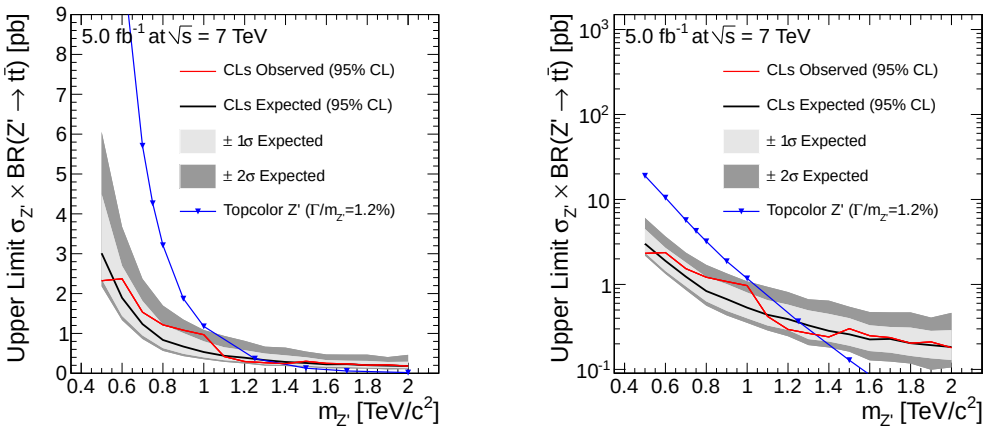

Figure 8.10: Expected and observed upper limits at 95% confidence level on the production cross section of a narrow-width Z′ as function of Z′ mass derived with a $\mathrm{CL_s}$ method in standard (left) and semi-logarithmic (right) depiction. The light (dark) grey bands show the $\pm 1\sigma$ ($\pm 2\sigma$) range of the expected limits.

at a Z′ mass of 0.5 TeV to $\sim$ 0.2 pb for a Z′ mass of 2 TeV, the lowest and highest mass values for which upper limits are calculated. The observed upper limits agree well with the expected limits, with most observed limits contained in the 1σ band of expected limits except for the two Z′ masses of 0.9 TeV and 1 TeV for which the observed limits are higher than the expected limits by more than one standard deviation, but well below two standard deviations. The observed limit lies just below the expected limit for $m_{\mathrm{Z}'} = 0.5$ TeV, then has a broad range up to 1 TeV where the observed limit is above the expected limit, after which the observed limit is again a bit below the expected limit before being in agreement from around 1.4 TeV. The variations are in agreement with the small differences between data and simulation before scaling the $m_{\mathrm{t\bar{t}}}$ distributions discussed above.

The derived upper limits are compared with the predicted cross sections from a topcolour leptophobic Z′ with a width of 1.2% of its mass with the leading order cross section values taken from reference [59] with an additional scale factor of 1.3 to take NLO corrections into account [147]. The expected limit and the predicted cross section curves cross close to 1.3 TeV, leading to an expected upper limit of $m_{\mathrm{Z}'} > 1.26$ TeV with the usual assumption that the expected limit curve scales exponentially between the Z′ masses of 1.2 TeV and 1.3 TeV. The observed upper limit lies slightly above the expected limit such that a Z′ with a mass of $m_{\mathrm{Z}'} \leq 1.33$ TeV for the topcolour Z′ model with a width of 1.2% of its mass is excluded at 95% confidence level.

The previous best limits on the mass of a Z′ with a width of 1.2%, $m_{\mathrm{Z}'} > 900$ GeV, have been derived by the CDF collaboration [4]. The excluded region is hence significantly extended by the presented limits. For comparison, a search by the ATLAS collaboration in the combined lepton-plus-jets and dilepton decay channels using an integrated luminosity of 2.05 fb^{-1} sets an upper limit of $m_{\mathrm{Z}'} = 880$ GeV, and the best limit derived by the D0 collaboration is $m_{\mathrm{Z}'} = 835$ GeV [3].

In addition to the plots, table 8.5 lists the model-independent limits at 95% confidence level on a new Z′-like particle that fulfils the narrow-width approximation, with the Z′ mass ranging

Table 8.5: List of expected and observed upper limits at 95% confidence level for the narrow-width Z′ model.

Mass (GeV)	Expected limit (pb)	Observed limit (pb)
500	$3.01^{+1.48}_{-0.64}$	2.32
600	$1.89^{+0.80}_{-0.45}$	2.37
700	$1.23^{+0.58}_{-0.28}$	1.53
800	$0.84^{+0.39}_{-0.20}$	1.22
900	$0.67^{+0.34}_{-0.18}$	1.08
1000	$0.53^{+0.27}_{-0.13}$	0.97
1100	$0.44^{+0.21}_{-0.11}$	0.42
1200	$0.39^{+0.19}_{-0.10}$	0.30
1300	$0.33^{+0.17}_{-0.10}$	0.27
1400	$0.28^{+0.17}_{-0.07}$	0.24
1500	$0.26^{+0.14}_{-0.07}$	0.30
1600	$0.23^{+0.11}_{-0.06}$	0.25
1700	$0.23^{+0.09}_{-0.07}$	0.24
1800	$0.20^{+0.11}_{-0.06}$	0.20
1900	$0.19^{+0.09}_{-0.06}$	0.21
2000	$0.18^{+0.11}_{-0.05}$	0.18

from 0.5 TeV to 2 TeV. The expected and observed limits are given together with the central 68% confidence level band of expected limits.

8.4.2 Validation of the limit-setting procedure

In this section, the expected and observed upper limits on the cross section for a narrow-width Z′-like particle will be discussed in more detail. The conclusions also hold for the models considered in the following, i.e. a Z′ with a width of 10% of its mass and a KK gluon.

First, the influence of systematic uncertainties on the results is studied. Compared to the expected limits without the inclusion of systematic uncertainties, the expected upper limits are higher by a factor of about 2 for $m_{Z'} = 500$ GeV, by a factor of 1.5 for $m_{Z'} = 1$ TeV, and by a factor of 1.2 for $m_{Z'} = 2$ TeV. Hence, the influence of systematic uncertainties is more pronounced for lower Z′ masses for which the background due to SM processes is high, whereas the upper limits at high mass are mostly influenced by statistical uncertainties.

The impact of individual systematic uncertainties is studied by rederiving the expected limits without the considered uncertainty. Due to the finite accuracy of the expected limit calculation, only significant contributions at the level of more than several per cent can be distinguished from statistical fluctuations. The evaluation shows that no single uncertainty contributes more than 10% to the overall expected limit, regardless of the Z′ mass, i.e. there is no single uncertainty driving the increase of the expected limits.

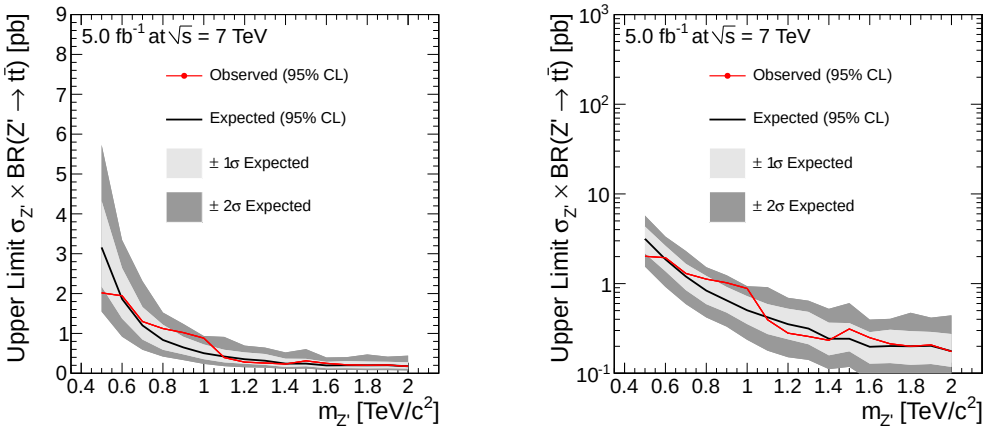

Figure 8.11: Expected and observed upper limits on the production cross section of a narrow-width Z′ as function of Z′ mass derived with a Bayesian technique in standard (left) and semi-logarithmic (right) scale. The light (dark) grey bands show the $\pm 1\sigma$ ($\pm 2\sigma$) range of the expected limits..

The dependency of the derived upper limits on the statistical technique is studied by performing the statistical evaluation with a Bayesian integration. Figure 8.11 shows the such-derived expected and observed limits for a narrow-width Z′-like particle as a function of the particle mass. The observed and expected limits are compatible with the ones obtained by the $\mathrm{CL_s}$ method within a few per cent. The most significant difference between the results of the two techniques is in the 2σ band of expected limits, which extends to lower values for the Bayesian method. This difference can be explained by the extra protection in the $\mathrm{CL_s}$ method to avoid the exclusion of cross sections to which the physics model is not sensitive, given by the term in the denominator of the $\mathrm{CL_s}$ definition in equation 8.10. On the other hand, the 2σ band extends to higher values for the $\mathrm{CL_s}$ method such that the total widths of the bands are similar, but more symmetric for the Bayesian method in a linear scale in cross section.

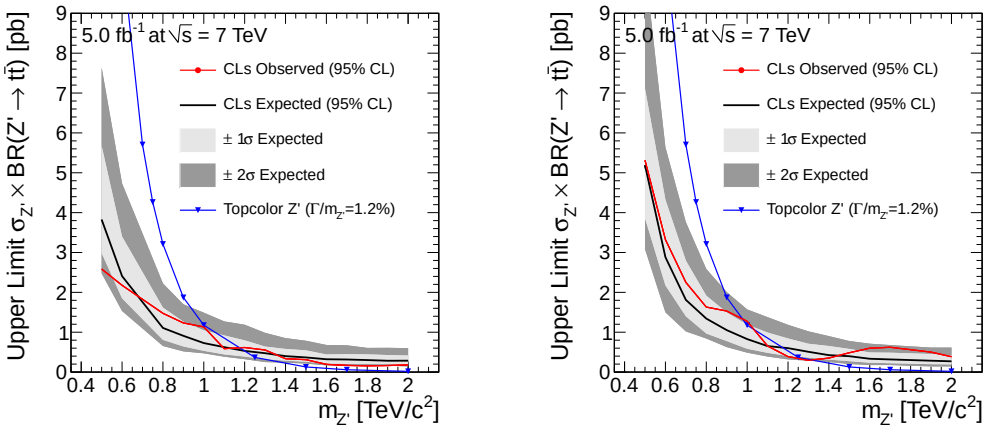

Figure 8.12: Expected and observed upper limits on the production cross section of a Z′ with a width of 10% of its mass as function of Z′ mass derived with a $\mathrm{CL_s}$ method for the muon channel (left) and the electron channel (right). The light (dark) grey bands show the $\pm 1\sigma$ ($\pm 2\sigma$) range of the expected limits.

Figure 8.12 shows the expected and observed upper limits for the same setup as above, but separately for the muon and the electron channel. The investigation of the individual lepton channels provides an estimation of how much the individual channels contribute to the final results. In addition, it serves as a cross check how much the results in the two lepton channels differ. The expected upper limits range from 5.2 pb at 500 GeV to 0.3 pb at 2 TeV in the electron channel, and from 3.8 pb to 0.3 pb in the muon channel. The higher expected limits in the electron channel at lower Z' masses are due to the higher p_{T} threshold of 30 GeV for the electron selection compared to the 20 GeV for the muon selection. At Z' masses of more 1 TeV, the differences between the different channels become small, and the electron channel provides slightly better expected limits for a mass of 2 TeV since the isolation requirement in the muon trigger reduces the signal efficiency at high masses.

The observed limits in the two lepton channels have different shapes compared to the respective expected limits. In the muon channel, the observed limit is below the expected limit for a Z' mass of 500 GeV, after which the observed and expected limit curves cross, with the observed limit being higher than the expected limit up to 1 TeV. For masses higher than 1 TeV, the observed limits are at the level of the expected limits and slightly below when approaching a mass of 2 TeV. In the electron channel, the observed limits are at the level of the expected limits for $m_{\mathrm{Z}'} = 500$ GeV and then exceed the expected limits within the 1σ band of expected limits up to 1.1 TeV. Then, there is a downward fluctuation up to a mass of 1.5 TeV, after which the observed limits exceed the expected limits within the 2σ band of expected limits.

Taken together, there is only one coherent region where the observed limits in both the muon and the electron channel are above the expected limits, the region between $0.8 < m_{\mathrm{Z}'} < 1$ TeV, leading to the combined observed upper limit that is discussed above. The differences in the relative variations outside this region are indicative of statistical fluctuations, whereas the coherence in the 900 GeV region may either be a sign of a statistical fluctuation or a systematic effect. A potential systematic effect that could explain the observed upper limits would be a shape difference due to the usage of a matched leading order event generator instead of higher-order generators, which predict harder $m_{\mathrm{t\bar{t}}}$ spectra.

8.4.3 Z' with a width of 10% of its mass

The next considered model is again a Z' that decays to a $\mathrm{t\bar{t}}$ pair, but in this case with a width of 10% of its mass. Since a width of 10% of the mass is not small when compared to the $m_{\mathrm{t\bar{t}}}$ resolution, the upper limits on the production cross section of such a Z' are therefore not as easily translatable to a large range of models as the ones discussed in the previous section. The upper limits are however indicative of the limits for generic new particles decaying to a $\mathrm{t\bar{t}}$ pair that have a larger intrinsic width.

Figure 8.13 shows the expected and observed upper limits at 95% confidence level on the production cross section for a Z'-like particle with a width of 10% of its mass, together with the predicted cross section for an according leptophobic topcolour Z' [59]. The expected upper limits range from 4.0 pb for a Z' mass of 500 GeV to 0.3 pb for a mass of 2 TeV. Compared to the narrow-width Z', the expected upper limits are a factor of 1.3–1.8 higher, but the ratio of

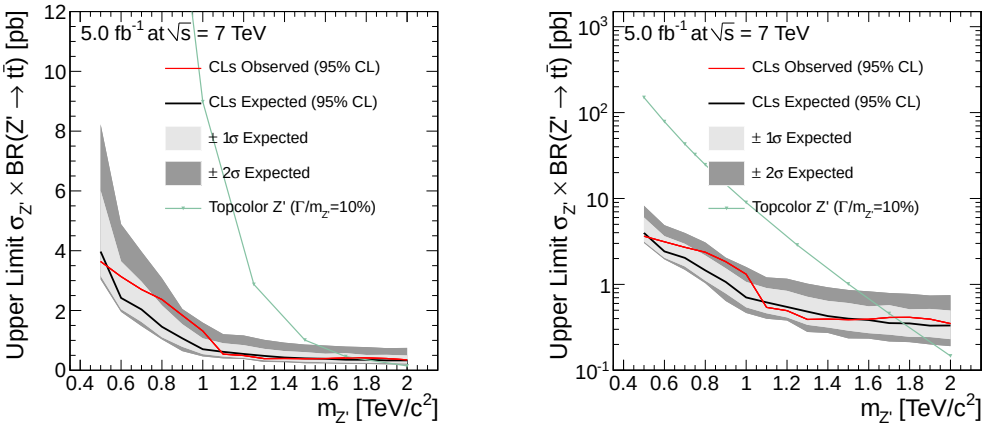

Figure 8.13: Expected and observed upper limits on the production cross section of a Z′ with a width of 10% of its mass as function of Z′ mass derived with a $\mathrm{CL_s}$ method in standard (left) and semi-logarithmic (right) scale. The light (dark) grey bands show the $\pm 1\sigma$ ($\pm 2\sigma$) range of the expected limits.

the observed and expected upper limits is similar. Like for the narrow-width Z′, the observed upper limit lies below the expected limit at 500 GeV, then exceeds the expected limits up to a Z′ mass of 1 TeV, after which the observed and expected limits are in good agreement. Due to the high correlation with the narrow-width Z′, the most significant difference between expected and observed limits is again between a Z′ mass of 800 GeV to 1 TeV, however with the observed limits being well contained in the 2σ band of the expected limits. Thus, observed and expected limits are in good agreement.

Compared to the theory prediction for the topcolour leptophobic Z′, the expected upper limit on the Z′ mass is 1.77 TeV. The observed limit is in good agreement and allows to exclude the Z′ with a width of 10% of its mass up to a mass of $m_{Z'} \leq 1.72$ TeV.

Table 8.6 lists the numerical values of the expected and observed upper limits such that they can be compared to other models that predict a Z′-like particle with a similar width. The table also contains the values of the $\pm 1\sigma$ variations of the expected upper limits.

8.4.4 Kaluza-Klein gluon

Finally, a Kaluza-Klein gluon is investigated in a Randall-Sundrum model with the model parameters set according to the model implementation in reference [50]. The considered first KK gluon has a mass-dependent width, which is of the order of 20% of its mass for the considered mass range. In contrast to the leptophobic topcolour Z′ models discussed above, the KK gluon does not exclusively decay to a $\mathrm{t\bar{t}}$ pair. The branching ratio for the decay to $\mathrm{t\bar{t}}$ is of the order of 90%, dependent on its mass. The upper limits on the production cross section for such a new particle are again derived as a function of its mass and can also be used as an approximation for new particles with similar intrinsic widths.

The expected and observed upper limits on the production cross section for the first KK gluon at 95% confidence level are shown in figure 8.14. In addition to the expected upper limits, the

Table 8.6: List of expected and observed upper limits at 95% confidence level for the 10% width Z′ model.

Mass (GeV)	Expected limit (pb)	Observed limit (pb)
500	$3.97^{+2.04}_{-0.81}$	3.64
600	$2.42^{+1.23}_{-0.38}$	3.13
700	$2.04^{+0.93}_{-0.42}$	2.70
800	$1.46^{+0.72}_{-0.35}$	2.37
900	$1.07^{+0.47}_{-0.28}$	1.84
1000	$0.70^{+0.36}_{-0.16}$	1.31
1100	$0.62^{+0.29}_{-0.16}$	0.54
1200	$0.55^{+0.30}_{-0.13}$	0.49
1300	$0.48^{+0.24}_{-0.14}$	0.39
1400	$0.43^{+0.21}_{-0.11}$	0.39
1500	$0.40^{+0.21}_{-0.11}$	0.39
1600	$0.38^{+0.17}_{-0.11}$	0.39
1700	$0.35^{+0.22}_{-0.09}$	0.41
1800	$0.35^{+0.16}_{-0.11}$	0.41
1900	$0.33^{+0.19}_{-0.09}$	0.39
2000	$0.33^{+0.16}_{-0.10}$	0.35

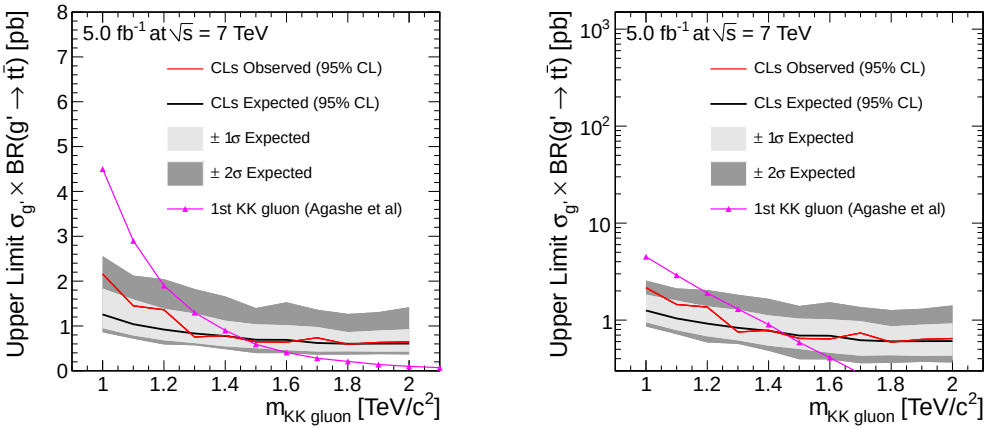

Figure 8.14: Expected and observed upper limits on the production cross section of the first KK gluon in a Randall-Sundrum model with the parameters from reference [50] as function function of the KK gluon mass derived with a CL_s method in standard (left) and semi-logarithmic (right) scale. The light (dark) grey bands show the $\pm 1\sigma$ ($\pm 2\sigma$) range of the expected limits.

Table 8.7: List of expected and observed upper limits at 95% confidence level for the KK gluon assumption.

Mass (GeV)	Expected limit (pb)	Observed limit (pb)
1000	$1.26^{+0.58}_{-0.31}$	2.16
1100	$1.04^{+0.55}_{-0.25}$	1.45
1200	$0.92^{+0.46}_{-0.24}$	1.36
1300	$0.83^{+0.45}_{-0.21}$	0.75
1400	$0.78^{+0.34}_{-0.23}$	0.79
1500	$0.69^{+0.34}_{-0.19}$	0.65
1600	$0.69^{+0.33}_{-0.23}$	0.64
1700	$0.62^{+0.36}_{-0.19}$	0.74
1800	$0.60^{+0.26}_{-0.17}$	0.59
1900	$0.61^{+0.29}_{-0.18}$	0.63
2000	$0.61^{+0.32}_{-0.18}$	0.65

expected production cross section in the considered RS model as well as the $\pm 1\sigma$ and $\pm 2\sigma$ bands of expected limits are given. The limits are given in the KK gluon mass range from 1 TeV $\leq m_{g'} \leq$ 2 TeV. Table 8.7 lists the numerical values of the observed and expected upper limits together with the $\pm 1\sigma$ variations for the considered KK gluon masses.

The expected upper limits range from 1.3 pb for a KK gluon mass of 1 TeV to 0.6 pb for a mass of 2 TeV. The observed limits are higher than the expected limit at the level of about 1.5 standard deviations for a mass of 1 TeV and about one standard deviation for KK gluon masses up to 1.2 TeV. For higher masses, the expected and observed limits agree at the level of significantly less than one standard deviation.

The comparison with the calculated cross section for the considered KK gluon yields an expected lower limit on the g' mass of 1.45 TeV. The expected and observed limits on the cross section agree well in this region, translating into an observed lower limit on the g' mass of 1.46 TeV.

Searches for colour-octet particles decaying to a $\mathrm{t\bar{t}}$ pair have been performed at the Tevatron and at the LHC. The CDF collaboration places limits on the couplings of a generic colour-octet particle in the mass range of 400 GeV $< m_{g'} <$ 800 GeV in an analysis of 1.9 fb^{-1} of $p\bar{p}$ collision data [5]. With a larger dataset of 5.3 fb^{-1}, the D0 collaboration excludes a colour-octet vector boson with a mass of less than 775 GeV [3]. The ATLAS collaboration sets a lower limit on the KK gluon mass of 1.13 TeV using 2.05 fb^{-1} of pp collision data for a KK gluon in a non-specified RS model [6].

An analysis in the full-hadronic final state with the CMS detector deploying reconstruction techniques adapted to high-p_{T} top quarks excludes a KK gluon in the same model as studied here in a small mass region around $m_{g'} \sim 1.5$ TeV with 5 fb^{-1} of data [148]. Combined with the limits obtained here, a KK gluon can be excluded with a mass of less than 1.5 TeV. The lower limits on the KK gluon mass obtained here hence significantly extend the reach of previous searches.

9 Conclusion

With 5 fb^{-1} of data recorded with the CMS detector at a centre-of-mass energy of 7 TeV at the LHC in 2011, the large number of events from $\mathrm{t\bar{t}}$ production allows to precisely analyse the production and decay of $\mathrm{t\bar{t}}$ pairs in an unprecedented energy regime. In this thesis, the invariant mass distributions of the reconstructed $\mathrm{t\bar{t}}$ system ($m_{\mathrm{t\bar{t}}}$) were measured and compared to the Standard Model predictions. With the help of the measured $m_{\mathrm{t\bar{t}}}$ distributions, searches for new particles decaying to $\mathrm{t\bar{t}}$ pairs were performed. New particles would appear as resonant contributions in addition to the non-resonant $m_{\mathrm{t\bar{t}}}$ distributions from Standard Model background processes. The focus of the data analysis extends from invariant top quark pair masses near the production threshold of $m_{\mathrm{t\bar{t}}} \sim 2 \cdot m_{\mathrm{top}}$ to the region of $m_{\mathrm{t\bar{t}}} \sim 2$ TeV.

The analysis was based on the final state of the $\mathrm{t\bar{t}}$ system with one charged lepton, i.e. either a muon or an electron, a neutrino, and four jets of which two are b quark jets. Events from $\mathrm{t\bar{t}}$ production were selected by requiring the presence of at least three energetic jets, either a muon or a neutrino, and a significant amount of missing transverse energy. The choice of the selection criteria was optimised to yield a high sensitivity in the search for new particles. This was achieved by efficiently selecting events from $\mathrm{t\bar{t}}$ production, either in the Standard Model or from models for new physics, while suppressing the contribution from reducible background events.

A full kinematic reconstruction of $\mathrm{t\bar{t}}$ events was performed with the goal of measuring $m_{\mathrm{t\bar{t}}}$ with high resolution. Therefore, all selected decay products were associated to final state particles in the $\mathrm{t\bar{t}}$ decay chain, and the goodness of the association was tested by a χ^2 method. The association was found to be correct in 50–70% of the events, depending on the generated $m_{\mathrm{t\bar{t}}}$. This led to a relative resolution of the measured $m_{\mathrm{t\bar{t}}}$ of $\sim 9\%$ in the considered region of generated $m_{\mathrm{t\bar{t}}}$.

Additional information contained in the data was exploited by categorising events according to the number of selected jets, the number of jets that are identified as b quark jets, and the lepton flavour (muon or electron). This yielded 8 independent categories in which the $m_{\mathrm{t\bar{t}}}$ distributions were measured. The categorisation improves the statistical sensitivity for finding new phenomena by taking advantage of the different signal-to-background ratios in the different event categories. Furthermore, the division into categories helps to constrain the rates of background processes and to reduce the impact of systematic uncertainties.

The relevant contributions from different background sources were studied in detail. The contributions from multijet events were estimated from control regions in data, using different techniques in the muon and the electron channel. Other background sources were simulated using event generators, including event samples with variations of uncertainties related to the event generation and the theoretical description. The modelling of W-plus-jets events was

verified by comparing kinematic distributions from data and simulation in dedicated control regions. To validate the description of the data by simulated events in the signal region, several kinematic distributions were investigated, ranging from basic properties of reconstructed objects to distributions related to the reconstruction of the $\mathrm{t\bar{t}}$ system.

The measured $m_{\mathrm{t\bar{t}}}$ distributions in all 8 event categories showed good agreement with the expectation from the background model, most importantly with the $m_{\mathrm{t\bar{t}}}$ distributions from SM $\mathrm{t\bar{t}}$ production. The compatibility was tested by performing a background-only fit involving the complete statistical background model to the data. The statistical model included all relevant systematic uncertainties from experimental and theoretical sources, which were studied in detail. The fitted values of all parameters were consistent with the input parameters, verifying the description of the uncertainties and of the $m_{\mathrm{t\bar{t}}}$ distributions. With the expected $m_{\mathrm{t\bar{t}}}$ distributions scaled to the outcome of the background-only fit to the data, statistical goodness-of-fit tests confirmed the good agreement with the observed $m_{\mathrm{t\bar{t}}}$ distributions.

Stringent limits were set on the production cross section for new particles that are predicted by a number of models for new physics. The considered masses extend from 0.5 TeV to 2 TeV, with the corresponding expected cross section limits at 95% confidence level ranging from 3 pb to 0.2 pb for the Z′ model with a width that is small compared to the $m_{\mathrm{t\bar{t}}}$ resolution. For three dedicated models, the upper limits on the production cross section as a function of the particle mass were translated into lower bounds on the mass of the particle by comparing to the predicted cross sections. A leptophobic topcolour Z′ with a width of 1.2% (10%) of its mass was excluded up to $m_{\mathrm{Z}'} = 1.33$ TeV ($m_{\mathrm{Z}'} = 1.72$ TeV) at 95% confidence level. In addition, a Kaluza-Klein gluon in a Randall-Sundrum model was excluded with a mass up to $m_{g'} = 1.45$ TeV.

When interpreted in a model-independent way, the limits on the production cross section for narrow-width new particles improve the previous exclusion limits set by the CDF and D0 collaborations as well as by the ATLAS collaboration in a large part of the considered mass range and provide the most stringent limits to date. The model-independent interpretation is of particular importance for the comparison with models for new particles that can explain the discrepancies between data and simulation observed in the $\mathrm{t\bar{t}}$ charge asymmetry measurements at the Tevatron. Among these models, there are predictions for s-channel resonances in the $m_{\mathrm{t\bar{t}}}$ region of 500 to 1000 GeV. The presented limits significantly reduce the available phase space for these models.

The observation of a new particle consistent with the Higgs boson by the ATLAS and CMS collaborations completes the set of particles predicted by the Standard Model. On the one hand, this success underlines the validity of the Standard Model; on the other hand, it reinforces the interest in models for new physics that are consistent with a 125 GeV Higgs boson. The allowed parameter space of models for new physics based on supersymmetry has been reduced significantly with 2011 LHC data, and various searches for new physics based on striking signatures have been unsuccessful so far. With the data from the 2012 LHC run, searches for new physics involving the third generation, which are typically complicated by significant background contributions from SM processes, therefore become one of the main interests of the LHC physics programme. The strategies deployed in this search, especially the categorisation of events, will play a key role in the optimisation of similar future analyses. The top quark sector and especially the $m_{\mathrm{t\bar{t}}}$ distribution remain one of the most promising regions to search for signs of new physics.

Bibliography

[1] T. Aaltonen *et al.*, "Evidence for a Mass Dependent Forward-Backward Asymmetry in Top Quark Pair Production," *Phys.Rev.* **D83** (2011) 112003, arXiv:1101.0034 [hep-ex].

[2] V. M. Abazov *et al.*, "Forward-backward asymmetry in top quark-antiquark production," *Phys.Rev.* **D84** (2011) 112005, arXiv:1107.4995 [hep-ex].

[3] V. M. Abazov *et al.*, "Search for a Narrow $t\bar{t}$ Resonance in $p\bar{p}$ Collisions at $\sqrt{s} = 1.96$ TeV," *Phys.Rev.* **D85** (2012) 051101, arXiv:1111.1271 [hep-ex].

[4] T. Aaltonen *et al.*, "A Search for resonant production of $t\bar{t}$ pairs in 4.8 fb^{-1} of integrated luminosity of $p\bar{p}$ collisions at $\sqrt{s} = 1.96$ TeV," *Phys.Rev.* **D84** (2011) 072004, arXiv:1107.5063 [hep-ex].

[5] T. Aaltonen *et al.*, "Search for New Color-Octet Vector Particle Decaying to t anti-t in p anti-p Collisions at s**(1/2) = 1.96-TeV," *Phys.Lett.* **B691** (2010) 183–190, arXiv:0911.3112 [hep-ex].

[6] G. Aad *et al.*, "A search for ttbar resonances with the ATLAS detector in 2.05 fb^{-1} of proton-proton collisions at sqrt(s) = 7 TeV," arXiv:1205.5371 [hep-ex].

[7] K. Nakamura *et al.*, "2011 Review of particle physics," *J.Phys.G* **G37** (2010) 075021.

[8] CERN Press Release, "CERN experiments observe particle consistent with long-sought Higgs boson," 2012. http://press.web.cern.ch/press/PressReleases/Releases2012/PR17.12E.html.

[9] "Combination of CDF and D0 results on the mass of the top quark using up to 5.8 fb-1 of data," arXiv:1107.5255 [hep-ex].

[10] M. E. Peskin and D. V. Schroeder, *An Introduction To Quantum Field Theory (Frontiers in Physics)*. Perseus Books, 1995.

[11] R. K. Ellis, W. J. Stirling, and B. R. Webber, *QCD and Collider Physics*, vol. 8. Cambridge University Press, 1996.

[12] e. Grojean, C. and e. Spiropulu, M., "High-energy physics. Proceedings, 17th European School, ESHEP 2009, Bautzen, Germany, June 14-27, 2009," arXiv:1012.4643 [hep-ph].

[13] S. Bethke, "The 2009 World Average of alpha(s)," *Eur.Phys.J.* **C64** (2009) 689–703, arXiv:0908.1135 [hep-ph].

[14] "Precision Electroweak Measurements and Constraints on the Standard Model," arXiv:1012.2367 [hep-ex]. http://lepewwg.web.cern.ch/LEPEWWG/.

[15] V. M. Abazov *et al.*, "Determination of the width of the top quark," *Phys.Rev.Lett.* **106** (2011) 022001, arXiv:1009.5686 [hep-ex].

[16] M. Beneke, I. Efthymiopoulos, M. L. Mangano, J. Womersley, A. Ahmadov, *et al.*, "Top quark physics," arXiv:hep-ph/0003033 [hep-ph].

[17] W. Wagner, "Top quark physics in hadron collisions," *Rept.Prog.Phys.* **68** (2005) 2409–2494, arXiv:hep-ph/0507207 [hep-ph].

[18] A. Quadt, "Top quark physics at hadron colliders," *Eur.Phys.J.* **C48** (2006) 835–1000.

[19] W. Bernreuther, "Top quark physics at the LHC," *J. Phys.* **G35** (2008) 083001, arXiv:0805.1333 [hep-ph].

[20] A. Martin, W. Stirling, R. Thorne, and G. Watt, "Parton distributions for the LHC," *Eur.Phys.J.* **C63** (2009) 189–285, arXiv:0901.0002 [hep-ph].

[21] M. Dobbs, S. Frixione, E. Laenen, K. Tollefson, H. Baer, *et al.*, "Les Houches guidebook to Monte Carlo generators for hadron collider physics," arXiv:hep-ph/0403045 [hep-ph].

[22] J. H. Kuhn and G. Rodrigo, "Charge asymmetry of heavy quarks at hadron colliders," *Phys.Rev.* **D59** (1999) 054017, arXiv:hep-ph/9807420 [hep-ph].

[23] N. Kidonakis and B. D. Pecjak, "Top-quark production and QCD," arXiv:1108.6063 [hep-ph].

[24] P. Baernreuther, M. Czakon, and A. Mitov, "Percent level precision physics at the Tevatron: first genuine NNLO QCD corrections to qqbar $\to$ ttbar + X," arXiv:1204.5201 [hep-ph].

[25] V. Ahrens, A. Ferroglia, M. Neubert, B. D. Pecjak, and L. L. Yang, "Precision predictions for the t+t(bar) production cross section at hadron colliders," *Phys.Lett.* **B703** (2011) 135–141, arXiv:1105.5824 [hep-ph].

[26] M. Beneke, P. Falgari, S. Klein, and C. Schwinn, "Hadronic top-quark pair production with NNLL threshold resummation," *Nucl.Phys.* **B855** (2012) 695–741, arXiv:1109.1536 [hep-ph].

[27] M. Cacciari, M. Czakon, M. L. Mangano, A. Mitov, and P. Nason, "Top-pair production at hadron colliders with next-to-next-to-leading logarithmic soft-gluon resummation," *Phys.Lett.* **B710** (2012) 612–622, arXiv:1111.5869 [hep-ph].

[28] N. Kidonakis, "Next-to-next-to-leading soft-gluon corrections for the top quark cross section and transverse momentum distribution," *Phys.Rev.* **D82** (2010) 114030, arXiv:1009.4935 [hep-ph].

[29] J. M. Campbell and R. Ellis, "MCFM for the Tevatron and the LHC," *Nucl.Phys.Proc.Suppl.* **205-206** (2010) 10–15, arXiv:1007.3492 [hep-ph].

[30] S. Chatrchyan *et al.*, "Combined results of searches for the standard model Higgs boson in pp collisions at sqrt(s) = 7 TeV," *Phys.Lett.* **B710** (2012) 26–48, arXiv:1202.1488 [hep-ex].

[31] "Feynman diagrams for top physics talks and notes," D0 public web, November, 2011. http://www-d0.fnal.gov/Run2Physics/top/top_public_web_pages/top_feynman_diagrams.html.

[32] N. Kidonakis, "Next-to-next-to-leading-order collinear and soft gluon corrections for t-channel single top quark production," *Phys.Rev.* **D83** (2011) 091503, arXiv:1103.2792 [hep-ph].

[33] N. Kidonakis, "Two-loop soft anomalous dimensions for single top quark associated production with a W- or H-," *Phys.Rev.* **D82** (2010) 054018, arXiv:1005.4451 [hep-ph].

[34] N. Kidonakis, "NNLL resummation for s-channel single top quark production," *Phys.Rev.* **D81** (2010) 054028, arXiv:1001.5034 [hep-ph].

[35] K. Melnikov and F. Petriello, "Electroweak gauge boson production at hadron colliders through O(alpha(s)**2)," *Phys. Rev.* **D74** (2006) 114017, arXiv:hep-ph/0609070.

[36] C. Berger, Z. Bern, L. J. Dixon, F. Febres Cordero, D. Forde, *et al.*, "Precise Predictions for W + 4 Jet Production at the Large Hadron Collider," *Phys.Rev.Lett.* **106** (2011) 092001, arXiv:1009.2338 [hep-ph].

[37] S. Chatrchyan *et al.*, "Jet Production Rates in Association with W and Z Bosons in pp Collisions at sqrt(s) = 7 TeV," *JHEP* **1201** (2012) 010, arXiv:1110.3226 [hep-ex].

[38] S. Badger, J. M. Campbell, and R. Ellis, "QCD corrections to the hadronic production of a heavy quark pair and a W-boson including decay correlations," *JHEP* **1103** (2011) 027, arXiv:1011.6647 [hep-ph].

[39] G. Aad *et al.*, "Measurement of the cross section for the production of a W boson in association with b-jets in pp collisions at sqrt(s) = 7 TeV with the ATLAS detector," *Phys.Lett.* **B707** (2012) 418–437, arXiv:1109.1470 [hep-ex].

[40] CMS Collaboration, "Measurement of associated charm production in W final states at $\sqrt{s} = 7$ TeV," CMS Physics Analysis Summary CMS-PAS-EWK-11-013, 2011. http://cdsweb.cern.ch/record/1369558.

[41] H. Ita, Z. Bern, L. Dixon, F. Febres Cordero, D. Kosower, *et al.*, "Precise Predictions for Z + 4 Jets at Hadron Colliders," *Phys.Rev.* **D85** (2012) 031501, arXiv:1108.2229 [hep-ph].

[42] S. Dimopoulos, S. Raby, and F. Wilczek, "Supersymmetry and the Scale of Unification," *Phys.Rev.* **D24** (1981) 1681–1683.

[43] C. T. Hill and E. H. Simmons, "Strong dynamics and electroweak symmetry breaking," *Phys.Rept.* **381** (2003) 235–402, arXiv:hep-ph/0203079 [hep-ph].

[44] C. T. Hill, "Topcolor: Top quark condensation in a gauge extension of the standard model," *Phys.Lett.* **B266** (1991) 419–424.

[45] C. T. Hill, "Topcolor assisted technicolor," *Phys.Lett.* **B345** (1995) 483–489, arXiv:hep-ph/9411426 [hep-ph].

[46] R. M. Harris, C. T. Hill, and S. J. Parke, "Cross section for topcolor Z'(t) decaying to t anti-t," arXiv:hep-ph/9911288.

[47] N. Arkani-Hamed, A. G. Cohen, and H. Georgi, "Electroweak symmetry breaking from dimensional deconstruction," *Phys.Lett.* **B513** (2001) 232–240, arXiv:hep-ph/0105239 [hep-ph].

[48] B. C. Allanach, C. Grojean, P. Z. Skands, E. Accomando, G. Azuelos, *et al.*, "Les Houches physics at TeV colliders 2005 beyond the standard model working group: Summary report," arXiv:hep-ph/0602198 [hep-ph].

[49] L. Randall and R. Sundrum, "A Large mass hierarchy from a small extra dimension," *Phys.Rev.Lett.* **83** (1999) 3370–3373, arXiv:hep-ph/9905221 [hep-ph].

[50] K. Agashe, A. Belyaev, T. Krupovnickas, G. Perez, and J. Virzi, "LHC Signals from Warped Extra Dimensions," *Phys.Rev.* **D77** (2008) 015003, arXiv:hep-ph/0612015 [hep-ph].

[51] B. Lillie, L. Randall, and L.-T. Wang, "The Bulk RS KK-gluon at the LHC," *JHEP* **09** (2007) 074, arXiv:hep-ph/0701166.

[52] A. Fitzpatrick, J. Kaplan, L. Randall, and L.-T. Wang, "Searching for the Kaluza-Klein Graviton in Bulk RS Models," *JHEP* **0709** (2007) 013, arXiv:hep-ph/0701150 [hep-ph].

[53] N. Arkani-Hamed, S. Dimopoulos, and G. Dvali, "The Hierarchy problem and new dimensions at a millimeter," *Phys.Lett.* **B429** (1998) 263–272, arXiv:hep-ph/9803315 [hep-ph].

[54] Z. Dong, T. Han, M.-x. Huang, and G. Shiu, "Top Quarks as a Window to String Resonances," *JHEP* **09** (2010) 048, arXiv:1004.5441 [hep-ph].

[55] D. Dicus, A. Stange, and S. Willenbrock, "Higgs decay to top quarks at hadron colliders," *Phys. Lett.* **B333** (1994) 126–131, arXiv:hep-ph/9404359.

[56] W. Bernreuther, M. Flesch, and P. Haberl, "Signatures of Higgs bosons in the top quark decay channel at hadron colliders," *Phys. Rev.* **D58** (1998) 114031, arXiv:hep-ph/9709284.

[57] R. Frederix and F. Maltoni, "Top pair invariant mass distribution: a window on new physics," *JHEP* **01** (2009) 047, arXiv:0712.2355 [hep-ph].

[58] S. Moretti and D. Ross, "On the top-antitop invariant mass spectrum at the LHC from a Higgs boson signal perspective," *Phys.Lett.* **B712** (2012) 245–249, arXiv:1203.3746 [hep-ph].

[59] R. M. Harris and S. Jain, "Cross Sections for Leptophobic Topcolor Z' decaying to top-antitop," *Eur.Phys.J.* **C72** (2012) 2072, arXiv:1112.4928 [hep-ph].

[60] B. Lillie, J. Shu, and T. M. P. Tait, "Kaluza-Klein Gluons as a Diagnostic of Warped Models," *Phys. Rev.* **D76** (2007) 115016, arXiv:0706.3960 [hep-ph].

[61] S. Chatrchyan *et al.*, "Measurement of the charge asymmetry in top-quark pair production in proton-proton collisions at sqrt(s) = 7 TeV," *Phys.Lett.* **B709** (2012) 28–49, arXiv:1112.5100 [hep-ex].

[62] G. Aad *et al.*, "Search for New Physics in the Dijet Mass Distribution using 1 fb^{-1} of pp Collision Data at sqrt(s) = 7 TeV collected by the ATLAS Detector," *Phys.Lett.* **B708** (2012) 37–54, arXiv:1108.6311 [hep-ex].

[63] S. Chatrchyan *et al.*, "Search for Resonances in the Dijet Mass Spectrum from 7 TeV pp Collisions at CMS," *Phys.Lett.* **B704** (2011) 123–142, arXiv:1107.4771 [hep-ex].

[64] Y. Bai, J. L. Hewett, J. Kaplan, and T. G. Rizzo, "LHC Predictions from a Tevatron Anomaly in the Top Quark Forward-Backward Asymmetry," *JHEP* **03** (2011) 003, arXiv:1101.5203 [hep-ph].

[65] E. Alvarez, L. Da Rold, J. I. S. Vietto, and A. Szynkman, "Phenomenology of a light gluon resonance in top-physics at Tevatron and LHC," *JHEP* **1109** (2011) 007, arXiv:1107.1473 [hep-ph].

[66] E. Alvarez, "Enhancing the sensitivity to New Physics in the top-antitop invariant mass distribution," arXiv:1205.5267 [hep-ph].

[67] U. Baur and L. H. Orr, "Searching for $t\bar{t}$ Resonances at the Large Hadron Collider," *Phys. Rev.* **D77** (2008) 114001, arXiv:0803.1160 [hep-ph].

[68] C. Degrande, J.-M. Gerard, C. Grojean, F. Maltoni, and G. Servant, "Non-resonant New Physics in Top Pair Production at Hadron Colliders," *JHEP* **1103** (2011) 125, arXiv:1010.6304 [hep-ph].

[69] CERN, "The CERN accelerator complex." http://public.web.cern.ch/public/en/research/AccelComplex-en.html, 2012.

[70] e. Evans, Lyndon and e. Bryant, Philip, "LHC Machine," *JINST* **3** (2008) S08001.

[71] G. Bayatian *et al.*, "CMS Physics Technical Design Report Volume I: Detector Performance and Software," Technical Design Report CMS, 2006. http://cdsweb.cern.ch/record/922757/.

[72] R. Adolphi *et al.*, "The CMS experiment at the CERN LHC," *JINST* **3** (2008) S08004.

[73] S. Chatrchyan *et al.*, "Precise Mapping of the Magnetic Field in the CMS Barrel Yoke using Cosmic Rays," *JINST* **5** (2010) T03021, arXiv:0910.5530 [physics.ins-det].

[74] S. Chatrchyan *et al.*, "Performance and Operation of the CMS Electromagnetic Calorimeter," *JINST* **5** (2010) T03010, arXiv:0910.3423 [physics.ins-det].

[75] CMS Collaboration, "ECAL detector performance, 2011 data," CMS Detector Performance Summary CMS-DP-2012-007, May, 2012. http://cdsweb.cern.ch/record/1457922.

[76] CMS Collaboration, "Single-particle response in the CMS calorimeters," CMS Physics Analysis Summary CMS-PAS-JME-10-008, 2010. http://cdsweb.cern.ch/record/1279141.

[77] CMS Collaboration, "Absolute calibration of the luminosity measurement at CMS: Winter 2012 update," CMS Physics Analysis Summary CMS-PAS-SMP-12-008, 2012. http://cdsweb.cern.ch/record/1434360.

[78] CMS Collaboration, "Absolute calibration of the CMS luminosity measurement: Summer 2011 update," CMS Physics Analysis Summary CMS-PAS-EWK-11-001, 2011. http://cdsweb.cern.ch/record/1376102.

[79] S. van der Meer, "Calibration of the effective beam height in the ISR," Tech. Rep. CERN-ISR-PO-68-31, CERN, Geneva, 1968.

[80] H. Bretz, M. Brodski, M. Erdmann, R. Fischer, A. Hinzmann, *et al.*, "A Development Environment for Visual Physics Analysis," *JINST* **7** (2012) T08005, arXiv:1205.4912 [physics.data-an].

[81] J. Alwall, A. Ballestrero, P. Bartalini, S. Belov, E. Boos, *et al.*, "A Standard format for Les Houches event files," *Comput.Phys.Commun.* **176** (2007) 300–304, arXiv:hep-ph/0609017 [hep-ph].

[82] "Physics eXtension Library." https://forge.physik.rwth-aachen.de/projects/pxl/wiki/.

[83] R. Brun and F. Rademakers, "ROOT: An object oriented data analysis framework," *Nucl.Instrum.Meth.* **A389** (1997) 81–86.

[84] F. Cossutti, "Tuning and optimization of the CMS simulation software," *J.Phys.Conf.Ser.* **219** (2010) 032005.

[85] S. Agostinelli *et al.*, "GEANT 4–a simulation toolkit," *NIM* **A506** (2003) 250–303.

[86] W. Adam, V. Adler, B. Hegner, L. Lista, S. Lowette, *et al.*, "PAT: The CMS physics analysis toolkit," *J.Phys.Conf.Ser.* **219** (2010) 032017.

[87] Thomas Müller, Jochen Ott, Jeannine Wagner-Kuhr, "theta - a framework for template-based modeling and inference," 2010. http://www-ekp.physik.uni-karlsruhe.de/~ott/theta/files/theta.pdf.

[88] O. Actis, M. Erdmann, R. Fischer, A. Hinzmann, M. Kirsch, *et al.*, "Visual Physics Analysis (VISPA): Concepts and First Applications," arXiv:0810.3609 [physics.data-an].

[89] O. Actis, M. Brodski, M. Erdmann, R. Fischer, A. Hinzmann, *et al.*, "Visual physics analysis VISPA," *J.Phys.Conf.Ser.* **219** (2010) 042041.

[90] L. Moneta, K. Belasco, K. S. Cranmer, S. Kreiss, A. Lazzaro, *et al.*, "The RooStats Project," *PoS* **ACAT2010** (2010) 057, arXiv:1009.1003 [physics.data-an].

[91] CMS Collaboration, "Particle–flow event reconstruction in CMS and performance for jets, taus, and $E_{\mathrm{T}}^{\mathrm{miss}}$," CMS Physics Analysis Summary CMS-PAS-PFT-09-001, 2009. http://cdsweb.cern.ch/record/1194487.

[92] W. Adam, B. Mangano, T. Speer, and T. Todorov, "Track reconstruction in the CMS tracker," Tech. Rep. CMS-NOTE-2006-041. CERN-CMS-NOTE-2006-041, CERN, Geneva, Dec, 2006. http://cdsweb.cern.ch/record/934067/.

[93] V. Khachatryan *et al.*, "CMS Tracking Performance Results from early LHC Operation," *Eur.Phys.J.* **C70** (2010) 1165–1192, arXiv:1007.1988 [physics.ins-det].

[94] S. Cucciarelli, M. Konecki, D. Kotlinski, and T. Todorov, "Track reconstruction, primary vertex finding and seed generation with the pixel detector," Tech. Rep. CERN-CMS-NOTE-2006-026, CERN, Geneva, Jan, 2006. http://cdsweb.cern.ch/record/927384/.

[95] CMS Collaboration, "Commissioning of the particle-flow reconstruction in minimum-bias and jet events from pp collisions at 7 TeV," CMS Physics Analysis Summary CMS-PAS-PFT-10-002, 2010. http://cdsweb.cern.ch/record/1279341.

[96] CMS Collaboration, "Commissioning of the particle-flow event reconstruction with leptons from J/ψ and W decays at 7 TeV," CMS Physics Analysis Summary CMS-PAS-PFT-10-003, 2010. http://cdsweb.cern.ch/record/1279347.

[97] V. Khachatryan *et al.*, "Measurements of Inclusive W and Z Cross Sections in pp Collisions at sqrt(s)=7 TeV," *JHEP* **1101** (2011) 080, arXiv:1012.2466 [hep-ex].

[98] S. Chatrchyan *et al.*, "Performance of CMS Muon Reconstruction in Cosmic-Ray Events," *JINST* **5** (2010) T03022, arXiv:0911.4994 [physics.ins-det].

[99] CMS Collaboration, "Performance of muon identification in pp collisions at $\sqrt{s}$ = 7 TeV," CMS Physics Analysis Summary CMS-PAS-MUO-10-002, 2010. http://cdsweb.cern.ch/record/1279140.

[100] CMS Collaboration, "Commissioning of the particle-flow event reconstruction with the first LHC collisions recorded in the CMS detector," CMS Physics Analysis Summary CMS-PAS-PFT-10-001, 2010. http://cdsweb.cern.ch/record/1247373.

[101] CMS Collaboration, "Electron reconstruction and identification at $\sqrt{s} = 7$ TeV," CMS Physics Analysis Summary CMS-PAS-EGM-10-004, 2010. http://cdsweb.cern.ch/record/1299116.

[102] M. Cacciari, G. P. Salam, and G. Soyez, "The Anti-k(t) jet clustering algorithm," *JHEP* **0804** (2008) 063, arXiv:0802.1189 [hep-ph].

[103] CMS Collaboration, "Jet energy scale performance in 2011," CMS Detector Performance Summary CMS-DP-2012-006, May, 2012. http://cdsweb.cern.ch/record/1454659.

[104] S. Chatrchyan *et al.*, "Determination of Jet Energy Calibration and Transverse Momentum Resolution in CMS," *JINST* **6** (2011) P11002, arXiv:1107.4277 [physics.ins-det].

[105] CMS Collaboration, "Jet energy resolution in CMS at $\sqrt{s} = 7$ TeV," CMS Physics Analysis Summary CMS-PAS-JME-10-014, 2010. http://cdsweb.cern.ch/record/1339945.

[106] S. Chatrchyan *et al.*, "Missing transverse energy performance of the CMS detector," *JINST* **6** (2011) P09001, arXiv:1106.5048 [physics.ins-det].

[107] CMS Collaboration, "MET performance in 2011 CMS data," CMS Detector Performance Summary CMS-DP-2012-003, Apr, 2012. http://cdsweb.cern.ch/record/1454656.

[108] CMS Collaboration, "Missing transverse energy performance in minimum-bias and jet events from proton-proton collisions at $\sqrt{s} = 7$ TeV," CMS Physics Analysis Summary CMS-PAS-JME-10-004, 2010. http://cdsweb.cern.ch/record/1279142.

[109] CMS Collaboration, "CMS MET performance in events containing electroweak bosons from pp collisions at $\sqrt{s} = 7$ TeV," CMS Physics Analysis Summary CMS-PAS-JME-10-005, 2010. http://cdsweb.cern.ch/record/1294501.

[110] S. Chatrchyan *et al.*, "Measurement of the Top-antitop Production Cross Section in pp Collisions at $\sqrt{s} = 7$ TeV using the Kinematic Properties of Events with Leptons and Jets," *Eur.Phys.J.* **C71** (2011) 1721, arXiv:1106.0902 [hep-ex].

[111] CMS Collaboration, "Tracking and primary vertex results in first 7 TeV collisions," CMS Physics Analysis Summary CMS-PAS-TRK-10-005, 2010. http://cdsweb.cern.ch/record/1279383.

[112] CMS Collaboration, "Commissioning of b-jet identification with pp collisions at $\sqrt{s}$ = 7 TeV," CMS Physics Analysis Summary CMS-PAS-BTV-10-001, 2010. http://cdsweb.cern.ch/record/1279144.

[113] S. Chatrchyan *et al.*, "Measurement of the $t\bar{t}$ Production Cross Section in pp Collisions at 7 TeV in Lepton + Jets Events Using b-quark Jet Identification," *Phys.Rev.* **D84** (2011) 092004, arXiv:1108.3773 [hep-ex].

[114] CMS Collaboration, "b-jet identification in the CMS experiment," CMS Physics Analysis Summary CMS-PAS-BTV-11-004, 2011. http://cdsweb.cern.ch/record/1427247.

[115] CMS Collaboration, "Algorithms for b jet identification in CMS," CMS Physics Analysis Summary CMS-PAS-BTV-09-001, 2009. http://cdsweb.cern.ch/record/1194494.

[116] CMS Collaboration, "Performance of b-jet identification in CMS," CMS Physics Analysis Summary CMS-PAS-BTV-11-001, 2011. http://cdsweb.cern.ch/record/1366061.

[117] J. Alwall, P. Demin, S. de Visscher, R. Frederix, M. Herquet, *et al.*, "MadGraph/MadEvent v4: The New Web Generation," *JHEP* **0709** (2007) 028, arXiv:0706.2334 [hep-ph].

[118] T. Sjostrand, S. Mrenna, and P. Z. Skands, "A Brief Introduction to PYTHIA 8.1," *Comput.Phys.Commun.* **178** (2008) 852–867, arXiv:0710.3820 [hep-ph].

[119] S. Frixione, P. Nason, and G. Ridolfi, "A Positive-weight next-to-leading-order Monte Carlo for heavy flavour hadroproduction," *JHEP* **0709** (2007) 126, arXiv:0707.3088 [hep-ph].

[120] S. Alioli, P. Nason, C. Oleari, and E. Re, "NLO single-top production matched with shower in POWHEG: s- and t-channel contributions," *JHEP* **0909** (2009) 111, arXiv:0907.4076 [hep-ph].

[121] E. Re, "Single-top Wt-channel production matched with parton showers using the POWHEG method," *Eur.Phys.J.* **C71** (2011) 1547, arXiv:1009.2450 [hep-ph].

[122] T. Sjostrand, S. Mrenna, and P. Z. Skands, "PYTHIA 6.4 Physics and Manual," *JHEP* **0605** (2006) 026, arXiv:hep-ph/0603175 [hep-ph].

[123] P. Bartalini, R. Chierici, and A. De Roeck, "Guidelines for the estimation of theoretical uncertainties at the LHC," CMS Note CERN-CMS-NOTE-2005-013, Sep, 2005. http://cdsweb.cern.ch/record/888430/.

[124] R. K. Ellis, "An update on the next-to-leading order Monte Carlo MCFM," *Nucl.Phys.Proc.Suppl.* **160** (2006) 170–174.

[125] CMS Collaboration, "Measurement of the inelastic pp cross section at $\sqrt{s}$ = 7 TeV with the CMS detector," CMS Physics Analysis Summary CMS-PAS-FWD-11-001, 2011. http://cdsweb.cern.ch/record/1373466.

[126] G. Antchev, P. Aspell, I. Atanassov, V. Avati, J. Baechler, *et al.*, "First measurement of the total proton-proton cross section at the LHC energy of $\sqrt{s}$=7 TeV," *Europhys.Lett.* **96** (2011) 21002, arXiv:1110.1395 [hep-ex].

[127] J. M. Butterworth, A. R. Davison, M. Rubin, and G. P. Salam, "Jet substructure as a new Higgs search channel at the LHC," *Phys.Rev.Lett.* **100** (2008) 242001, arXiv:0802.2470 [hep-ph].

[128] D. E. Kaplan, K. Rehermann, M. D. Schwartz, and B. Tweedie, "Top Tagging: A Method for Identifying Boosted Hadronically Decaying Top Quarks," *Phys.Rev.Lett.* **101** (2008) 142001, arXiv:0806.0848 [hep-ph].

[129] CMS Collaboration, "Search for heavy narrow resonances decaying to $\mathrm{t\bar{t}}$ in the muon+jets channel," CMS Physics Analysis Summary CMS-PAS-EXO-11-055, 2011. http://cdsweb.cern.ch/record/1376673.

[130] CMS Collaboration, "Search for high-mass resonances decaying to $\mathrm{t\bar{t}}$ in the electron+jets channel," CMS Physics Analysis Summary CMS-PAS-EXO-11-092, 2011. http://cdsweb.cern.ch/record/1423037.

[131] K. Nakamura *et al.*, "Review of particle physics," *J.Phys.G* **G37** (2010) 075021.

[132] J. Bauer, *Prospects for the Observation of Electroweak Top Quark Production with the CMS Experiment.* PhD thesis, May, 2010. http://cdsweb.cern.ch/record/1308713/.

[133] CMS Collaboration, "Search for resonances in semi-leptonic top-pair decays close to production threshold," CMS Physics Analysis Summary CMS-PAS-TOP-10-007, 2010. http://cdsweb.cern.ch/record/1335720.

[134] S. Chatrchyan *et al.*, "Measurement of the Inclusive W and Z Production Cross Sections in pp Collisions at sqrt(s) = 7 TeV," *JHEP* **1110** (2011) 132, arXiv:1107.4789 [hep-ex].

[135] G. Aad *et al.*, "Measurement of the production cross section for W-bosons in association with jets in pp collisions at sqrt(s) = 7 TeV with the ATLAS detector," *Phys.Lett.* **B698** (2011) 325–345, arXiv:1012.5382 [hep-ex].

[136] F. James, *Statistical methods in experimental physics*. World Scientific, Singapore, 2nd ed., 2006.

[137] S. Chatrchyan *et al.*, "Measurement of the lepton charge asymmetry in inclusive W production in pp collisions at $\sqrt{s} = 7$ TeV," *JHEP* **1104** (2011) 050, arXiv:1103.3470 [hep-ex].

[138] S. Chatrchyan *et al.*, "Measurement of the t-channel single top quark production cross section in pp collisions at sqrt(s) = 7 TeV," *Phys.Rev.Lett.* **107** (2011) 091802, arXiv:1106.3052 [hep-ex].

[139] S. Chatrchyan *et al.*, "Measurement of the Top-antitop Production Cross Section in pp Collisions at sqrt(s)=7 TeV using the Kinematic Properties of Events with Leptons and Jets," *Eur.Phys.J.* **C71** (2011) 1721, arXiv:1106.0902 [hep-ex].

[140] W. Verkerke and D. P. Kirkby, "The RooFit toolkit for data modeling," *eConf* **C0303241** (2003) MOLT007, arXiv:physics/0306116 [physics].

[141] R. J. Barlow and C. Beeston, "Fitting using finite Monte Carlo samples," *Comput.Phys.Commun.* **77** (1993) 219–228.

[142] J. Conway, "Incorporating Nuisance Parameters in Likelihoods for Multisource Spectra," arXiv:1103.0354 [physics.data-an].

[143] T. Junk, "Confidence level computation for combining searches with small statistics," *Nucl.Instrum.Meth.* **A434** (1999) 435–443, arXiv:hep-ex/9902006 [hep-ex].

[144] A. L. Read, "Presentation of search results: The CL(s) technique," *J.Phys.G* **G28** (2002) 2693–2704.

[145] CMS Collaboration, "Combined standard model Higgs boson searches with up to 2.3 fb^{-1} of pp collision data at $\sqrt{s} = 7$ TeV at the LHC," CMS Physics Analysis Summary CMS-PAS-HIG-11-023, 2011. `http://cdsweb.cern.ch/record/1399607`.

[146] G. Aad *et al.*, "Measurement of the cross section for top-quark pair production in pp collisions at sqrt(s) = 7 TeV with the ATLAS detector using final states with two high-pt leptons," *JHEP* **1205** (2012) 059, `arXiv:1202.4892 [hep-ex]`.

[147] J. Gao, C. S. Li, B. H. Li, C. P. Yuan, and H. X. Zhu, "Next-to-leading order QCD corrections to a heavy resonance production and decay into top quark pair at the LHC," *Phys. Rev.* **D82** (2010) 014020, `arXiv:1004.0876 [hep-ph]`.

[148] S. Chatrchyan *et al.*, "Search for anomalous $t\bar{t}$ production in the highly-boosted all-hadronic final state," `arXiv:1204.2488 [hep-ex]`.

Danksagung/Acknowledgements

Zunchst geht mein Dank an Prof. Dr. Martin Erdmann für die ausgezeichnete Betreuung dieser Arbeit. Die immerwährende Unterstützung, z.B. für Konferenzen und CERN-Besuche, sowie die wöchentlichen Arbeitsgruppentreffen haben das Gelingen dieser Arbeit ermöglicht.

Herrn Prof. Dr. Thomas Hebbeker danke ich für das bereitwillige Übernehmen der Zweitkorrektur sowie für die interessanten Meetings.

Ein besonderer Dank gilt allen aktuellen und ehemaligen Mitgliedern unserer D0- und CMS-Arbeitsgruppe, Andreas Hinzmann, Anna Henrichs, Daniel van Asseldonk, Dennis Klingebiel, Joschka Lingemann, Matthias Bock, Matthias Komm, Oxana Actis, Rebekka Höing, Robert Fischer und Tatsiana Klimkovich, den Mitgliedern der VISPA-Gruppe, abgesehen von den Vorgenannten Gero Müller, Hape Bretz, Marcel Rieger, Michael Brodski, Thomas Münzer und Tobias Winchen, und den weiteren Mitgliedern der Auger-Gruppe für die produktive Zusammenarbeit und die vielen Diskussionen über Physik und andere Themen während/nach der Arbeitszeit sowie beim Mittagessen.

Ohne das Bereitstellen vieler Tassen Kaffees wäre diese Arbeit nicht zustande gekommen - Danke sowohl für die moderne (Frau Jenkins, Frau Jansen) als auch die klassische Variante (Adriana Del Piero). Das gleiche gilt für die effiziente Verwaltung sowie für die GRID- und EDV-Teams.

Für das Korrekturlesen dieser Arbeit danke ich Andreas Hinzmann, Martin Erdmann und Joschka Lingemann.

I also wish to thank all CMS colleagues, who made this work possible. I'd like to express special thanks to the leaders of the top group and the relevant subgroups, i.e. the top pair BSM, the top cross section, and the top mass group (to each of which the analysis was assigned at some point) - most importantly Roberto Chierici, Petar Maksimovic (who both were 2010 analysis contacts at some point), Francisco Yumiceva, Frank-Peter Schilling, Jorgen d'Hondt, and Silvano Tosi - as well as the (more than 10) members of the review committees for the 2010 and 2011 analyses, the "low-mass" collaborators from Lyon (Viola, Stephane and Silvano) and Bristol (especially Joel Goldstein as 2011 analysis contact and Luke), and the "high-mass" collaborators from Karlsruhe (most importantly Jochen for all the theta-related efforts) and Chicago/Fermilab.

Zu guter Letzt danke ich Annika, meinen Freunden und meiner Familie für die hervorragende Unterstützung.